2022-08-01

Reflectance Spectral Characterization and Taxonomy Applications of Spacecraft Materials to Aid Space Situational Awareness

Jacqueline Andrea Reyes
University of Texas at El Paso

REFLECTANCE SPECTRAL CHARACTERIZATION AND TAXONOMY APPLICATIONS OF SPACECRAFT MATERIALS TO AID SPACE SITUATIONAL AWARENESS

JACQUELINE ANDREA REYES

Doctoral Program in Materials Science & Engineering

APPROVED:

Miguel Velez-Reyes, Ph.D., Chair

Heather Cowardin, Ph.D., Co-Chair

Stephen W. Stafford, Ph.D.

Darren Cone, M.S.

Hector Erives-Contreras, Ph.D.

Stephen L. Crites, Jr., Ph.D.
Dean of the Graduate School

Dedication

For my mom, my dad, and my sister, whom the entirety of this work would not have been completed without.

REFLECTANCE SPECTRAL CHARACTERIZATION AND TAXONOMY APPLICATIONS OF SPACECRAFT MATERIALS TO AID SPACE SITUATIONAL AWARENESS

by

JACQUELINE ANDREA REYES

B.S., University of Texas at El Paso (2017)

DISSERTATION

Presented to the Faculty of the Graduate School of

The University of Texas at El Paso

in Partial Fulfillment

of the Requirements

for the Degree of

DOCTOR OF PHILOSOPHY

Materials Science & Engineering

THE UNIVERSITY OF TEXAS AT EL PASO

August 2022

Acknowledgements

It is with utmost priority that I first acknowledge and thank my immediate family, comprised of my mother, my father, and my sister. To my mother, who has been my #1 fan since the day I arrived into existence. My mother, who was with me in all my trials, all my shortcomings, and all my achievements, who loved me regardless of the multitude of flaws that I possess and still believed in me during the countless moments that I no longer believed in myself. My mother, who saw a greatness in me that I may never comprehend, but who was vital in my ability to endeavor into the world of academics and supported me every step of the way. My mother, who sacrificed her entire career as an engineer herself, a career that she loved, to raise me and my sister, because her love for us was boundless. My mother, who never hesitated to be there when I needed her, who was there for every event, from my early days taking me to folklórico practice as a child, to band practice and competitions in middle school, high school and college, and up until this very day. My mother, who makes the *best* home-cooked meals and who's presence is a breath of fresh air. My mother, who I constantly look up to and aspire to be like one day. She is the strongest woman I will ever know in my lifetime and I am immensely blessed that I get to call her my mom, because I truly have the best one.

To my father, who did absolutely everything in his power to provide myself and my family a safe and fruitful home. My father; who taught me how to ride a bike, how to fly a kite, how to mow the lawn, and later how to drive, but most importantly, my father taught me how to view the world in ways that nobody else could. My father, who taught me how to find happiness in the simplest of things, like the clouds in the sky which we'd form into imaginary figures and discuss their rate at which they moved across the sky. My father, who'd banish all the moths that would find their way to my room as a child because they scared me, and who would carry me to and from

places when I was simply too tired to walk, and whom would spend hours playing the computer game Deimos Rising with me because it was that much fun. Saying that he'd do anything to partake in my happiness is truth in its completeness. I realize that not many young daughters in this generation can say that they have the best dad, but I hit the jackpot again, because I get to say that I have the best dad.

To my sister, Janelle, who has been my other half and my confidant since I was born. My sister; who would convince me to partake in some of the craziest things, like believing we could "drive" our electric Barbie jeep all the way to McDonald's when I was like 6 years old and she was 8 (our dad had to chase us down and then our parents *actually* drove us to get our Happy Meals). My sister; who I have the most in common with in this world, and can geek out with and spend countless hours talking about Harry Potter, or Kingdom Hearts, or Avatar the Last Bender… the list goes on. My sister, who always cheered me up when I was down, who always defended me if I needed it, and who was there for me. My sister, whom I am different from in many ways but wish I could be more like, for she has taught me that it's ok be yourself and not dwell on what others may think. My sister, who deserves all good things in the world, because without her, my life would have been colorless, boring, and extremely lonely.

To my friends, who never judged me and accepted me for all of my faults and still loved me anyway. My friends, who were the source of my laughter and never failed to be present for me when I needed them. My friends, who are a large reason of why I was able to remain sane throughout the duration of this work, for they understood and shared the toll it took on me. My friends, who reminded me of who I was when I lost sight of myself, who comforted me, who rooted for me, and who are proud of me. All time spent with my friends throughout the years of this work was like my reset button that was very much needed.

To my primary mentor, Heather, whom I am 100% certain this degree would not have been accomplished without. She was the first who told me that I could do this, even before I knew that I wanted to try. She supported me throughout every step of this research and was available to me at all times necessary. Even though I bothered her so much, she never once made me feel that I was a burden. Every conversation that I had with her never failed to make me realize why she is one of the greatest scientists I know. She was the first who taught me how to take measurements in the lab and how to analyze them before I even knew what I was doing. She fostered in me a passion to dive into this work and she serves as a constant role-model in the academic aspect of my life. I thank her for this immensely.

To my additional mentor, Dr. Miguel Velez-Reyes, who provided me the essential support needed for me to move forward in this degree program and who set time aside to guide me and present me with opportunities that served to help me grow professionally and academically. He has served as an additional role model for me in the academia setting and it is without doubt that the completion of this degree was only able to be achieved under his direction. I have learned what it takes to be a true mentor to students in a lab setting, and I one day aspire to uphold the principles that he has unceasingly modeled for me.

It is imperative to recognize and express my genuine gratitude toward the NASA Fellowship Activity Program with which I had the opportunity to partake in for the last half of my graduate studies. I was supported during the course of this research by the NASA Fellowship under award number 80NSSC18K1702. I also acknowledge the mentors that I gained during my time involved at the Air Force Research Laboratory Space Vehicles Directorate, including Ryan Hoffmann, Daniel Engelhart, and Elena Plis, who delivered a wealth of knowledge to me and took the time to give me valuable advice whenever needed.

And finally, to Namjoon, Seokjin, Yoongi, Hoseok, Jimin, Taehyung, and Jungkook, whom have individually and collectively been my primary source of motivation to complete this work. I am wholeheartedly confident that they arrived into my life four years ago at the onset of my graduate school journey for a purpose, for without them I would not have found the inspiration to keep moving forward. It was on a specific day during the endeavor of this work, when I was certain that I was going to fail, that they delivered a message to me in the form of an album titled Map of the Soul: 7, which spoke directly to the obstacles I was facing mentally and emotionally. On this day, it became too coincidental to think that these seven individuals were not instrumental in my achievement. It was through this occurrence and through their encouragement that I was confident that I could complete this work, it was through them that I knew I never walked alone, it was through them that the desert became a sea, and it was through them that the initial crawl became a walk, which then transformed into a run, and later a flight with wings. Their reinforcement is unmistakable, and it would be a disservice to overlook the credit and recognition that they deserve as a vital source of why this work was fulfilled. And to them, I say, “you got me, and I got you.”

I present this work with my heart, and with the help derived from God. Now, I look forward to what is yet to come.

Abstract

The increasing number of space missions involving successfully deployed spacecraft have resulted in an augmented density of artificial objects positioned in orbital domains near Earth. With this steady accumulation of objects in space, it has become increasingly imperative to characterize spacecraft materials, which may ultimately be contributors to the orbital debris population. In an effort to identify unique material-specific spectroscopic markers, a variety of spacecraft materials frequently utilized in the aerospace industry to construct typical spacecraft were analyzed using reflectance spectroscopy as a characterization technique for assessment on material type according to optical features. This is significant in providing information to contribute toward the comprehensive space situational awareness (SSA) aspect. Spectral measurements of selected materials analyzed in their pristine and laboratory simulated space-weathered conditions are presented in this work. These data provide a spectral characterization baseline for modern-day and historical spacecraft materials and are compared to each other to distinguish spectra of materials belonging to different classifications with an effort of grouping them according to a color index. The potential to assess materials remotely by a means of classification can provide a degree of information regarding the hazards associated with debris objects for further risk mitigation if necessary. This approach was taken by calculating color index from reflectance spectra of common spacecraft materials in their pristine conditions that fell under different family groupings. Color index was determined using various established and arbitrary filter passbands to evaluate the possibility of isolating or distinguishing materials from one another by means of optical measurements depending upon passbands chosen. From this analysis, it was found that polyimide and photovoltaic materials resulted in distinguishability from all other materials most often depending upon the color index combinations used. While the silicon-based

solar cell demonstrated effective separability from other materials when using classic filter passbands to calculate for color index, the germanium-based solar cell and polyimide exhibited better discrimination when calculating color index using theoretical filter passbands created in this study.

Table of Contents

List of Tables

List of Figures

List of Acronyms

AEDC …….……	Air Force Arnold Engineering Development Complex
AMR ……..	area-to-mass ratio
AO ……...……..	atomic oxygen
AR ……...……..	anti-reflective
ASAT ……	anti-satellite
ASD ……	Analytical Spectral Device
BED ……	the Berlin emissivity database
BRDF ……	bidirectional reflectance distribution function
CFRP ……..	carbon fiber reinforced polymer
CLLS ……..	constrained linear least squares
CT ……..	correlated target
CTE ……	coefficient of thermal expansion
DHR ……..	directional hemispherical reflectance
EDS ……	energy dispersive X-ray spectroscopy
EISCAT ……..	European Incoherent Scatter
EMR ……..	energy to mass ratio
ES-MCAT ……..	Eugene Stansbery Meter Class Autonomous Telescope
ESA ……	European Space Agency
ESASDT ……	European Space Agency Space Debris Telescope
EuReCa ……..	European Retrieval Carrier
GEO ……	geosynchronous Earth orbit
GFRP ……..	glass fiber reinforced polymer

Goldstone ……..	Goldstone Orbital Debris Radar
GRC ……	General Research Corporation
GTO ……	Geostationary Transfer Orbit
HAMR ……	high area-to-mass ratio
HAX ……..	Haystack Auxiliary Radar
HSI ……	hyperspectral imaging
HST ……	Hubble Space Telescope
HUSIR ……	Haystack Ultrawideband Satellite Imaging Radar
IR ……	infrared
ISS ……..	International Space Station
IUS ……	inertial upper stage
JAXA ……..	Japanese Aerospace Exploration Agency
JSC ……	Johnson Space Center
LDEF ……..	Long Duration Exposure Facility
LEO ……	low Earth orbit
MASTER ……	Meteoroid And Space Debris Terrestrial Environment Reference
MCAT ……	Meter Class Autonomous Telescope
MERTIS ……	Mercury Radiometer And Thermal Infrared Spectrometer
MESMA ……	Multiple Endmember Spectral Mixture Analysis
MLI ……	multi-layer insulation
MMOD ……..	micrometeoroid and orbital debris
MODEST ……..	Michigan Orbital Debris Survey Telescope
MPO ……..	Mercury Planetary Orbiter

NASA ……	the National Aeronautics and Space Administration
NDSWI ……..	Normalized Difference Surface Water Index
NDWI ……	Normalized Difference Water Index
NIR ……	near-infrared
ODPO ……	Orbital Debris Program Office
OMC ……..	Optical Measurements Center
OPM ……..	Optical Properties Monitor
ORDEM ……	Orbital Debris Engineering Model
ORU ……..	orbital replacement unit
PCA ……	principal component analysis
PCB ……	printed circuit board
PICA ……..	Phenolic Impregnated Carbon Ablator
PMA-2 ……	Pressurized Mating Adapter #2
POSA ……..	Passive Optical Sample Assembly
PTFE ……..	polytetrafluoroethylene
RSI ……..	Reusable Surface Insulation
RSO ……	resident space object
SDSS ……..	Sloan Digital Sky Survey
SDT ……	Space Debris Telescope
SEM ……	scanning electron microscope
SILC ……..	SOI In Living Color
SIRCA ……	Silicone Impregnated Reusable Ceramic Ablator
SMC ……..	Air Force Space and Missile Systems Center

SOCIT ……	Satellite Orbital Debris Characterization Impact Test
SOI ……	Space Object Identification
SSA ……	space situational awareness
SSN ……	Space Surveillance Network
SSO ……	sun-synchronous orbit
STS ……	Space Transport System (Space Shuttle)
SWIR ……..	short wave infrared
TIRA ……..	Tracking and Imaging Radar
TPS ……	Thermal Protection System
UCT ……	uncorrelated target
UF ……...	University of Florida
URSO ……	unresolved resident space objects
USGS ……..	United States Geological Survey
USSTRATCOM ……	U.S. Strategic Command
UTJ ……	Ultra Triple Junction
UV ……..	ultraviolet
VIRTIS-M ……..	Visible and InfraRed Thermal Imaging Spectrometer Mapping Channel
VIS ……	visible
XRD ……...	x-ray diffraction

Chapter 1: Introduction

1.1. JUSTIFICATION

Space situational awareness (SSA) encompasses multiple aspects of information pertaining to resident space objects (RSO's) that currently inhabit space domain. Of these, the evaluation of RSO material make-up provides key knowledge necessary to characterize an article and assess the potential risks involved for an object traveling at high velocity in orbit. If space hardware materials can be grouped into material families using a taxonomy approach by means of optical measurements, then the ability to observe materials with greater efficiency could be achieved. This could occur since materials can provide certain information regarding their properties based on what class they fall within. It can therefore be worthwhile to gain an understanding of what behavior and potential threats a material can be associated with depending on what their classification is.

In this work, reflectance spectroscopy was applied to obtain reflectance signatures for common spacecraft materials with the aim of calculating color indices using various narrow passbands throughout the visible and near-infrared regions of the spectrum. Popular astronomical filter systems, such as those from Johnson/Bessell and the Sloan Digital Sky Survey, were used to evaluate material color index, and analysis was furthered by attempting to achieve improved results in the taxonomy aspect.

Reasons for this undertaking circulate around the idea that specific materials can be discriminated according to their color indices to better distinguish matter, RSO's in particular, by material type. Though spectral features fostered by reflectance and absorption behavior throughout the visible and near-infrared are known to provide information relating to characterization, it was our aim to explore this ability when assigning a color index value to a given material based upon

their optical properties. Because color index is dependent upon flux within a given passband, all combinations of index values for established astronomical filter system passbands and arbitrary passbands were applied to evaluate material discrimination.

1.2. Problem Statement

The motivation for this investigation stems from the necessary risk assessment surrounding the orbital debris problem. If observations could more efficiently result in material identification, then proper measures can be taken toward avoiding destructive events. To illustrate, metals are generally of greater density than polymeric materials and can therefore cause an augmented magnitude of damage. Therefore, it would be imperative to differentiate between material class when detecting RSO's or orbital debris for better understanding of their destructive behavior due to their intrinsic properties.

In addition, there is drive to optimize the data housed in spectral libraries specifically for the aerospace community with greater efficacy. If material spectra can be presented in a manner where spectral features are used to determine the classification for the measured material, regardless of information of origin, that could again provide information to characterize objects via a taxonomy approach, which can then be used for reference with remote observations for risk assessment. Furthermore, if spectra can be translated into color indices more conveniently using programming, color index can also serve as a reference to discriminate materials depending upon filter passbands in use.

1.3. Objectives & Goals

The primary objective for conducting this research is to evaluate possible material classification trends that resulted from color index values derived from the reflectance signature of a given material. The first goal executed to achieve this taxonomy approach included selecting

a balanced set of materials that are commonly used in space applications which fell under the different pillars of material classifications: metals, polymers, ceramics, and composites. Once these materials were chosen, their reflectance signatures were measured (from visible to near-infrared) via spectroscopy and were evaluated depending upon the absorption and reflectance features that appeared in their given result. The second goal encompassed conducting repeatability analysis and calculating multiple color indices for each of the selected materials using different established and new, arbitrary filter passbands within the 350-2500 nm wavelength range to associate material brightness with value. The third goal was then to evaluate the outcomes of material indices in reference to one another depending upon which combination of color indices were plotted against each other. In doing so, the color-color diagram results that delivered relevant information by displaying an efficacy of material separation or distinguishability were presented and discussed to determine if taxonomy trends were present.

1.4. Summary of Contributions

Contributions for this work include the delivery of optical data in the forms of reflectance spectra and color index for each material evaluated. These include a number of metals, polymers, ceramics, and composites often incorporated in space hardware design and that pertain to much of the human-made material populating space domain. Reflectance spectra results from the visible to near-infrared wavelength regime (350-2500 nm) are presented with the focused filter passbands depicted on spectral plots for ease of assessment. All spectral features that resulted from each material measurement were investigated and elaborated upon to confirm the properties and chemical make-up for the articles tested.

For the materials selected, all color indices that were calculated for the given filter passbands will be outlined for evaluation of material brightness in the form of values which can

be referred to. Furthermore, well established astronomical filter system passbands were compared and analyzed with respect to the determined color indices which provided assessment of which passbands better discriminated materials, which can be helpful when aiming to distinguish materials from one another when using remote sensing measurements. The reflectance signatures measured for all materials of interest in this study will contribute to the NASA JSC Spacecraft Materials Spectral Database for future reference.

1.4.1. Publications and Conference Proceeding Contributions

The following manuscript publications in journals or conference proceedings produced throughout the duration of this work are listed below:

- J. A. Reyes, K. W. Fulford, E. A. Plis and et al., "Spectroscopic behavior of various materials in a GEO simulated environment," *Acta Astronautica,* vol. 189, pp. 576-583, December 2021.
- H. M. Cowardin, J. M. Hostetler, J. I. Murray, J. A. Reyes and C. L. Cruz, "Optical Characterization of DebriSat Fragments in Support of Orbital Debris Environmental Models," *Journal of the Astronautical Sciences,* 2021.
- J. A. Reyes and H. Cowardin, "Spectral characterization of spacecraft materials used in hypervelocity impact testing," in *SPIE Algorithms, Technologies, and Applications for Multispectral and Hyperspectral Imaging XXVII*, 2021.
- J. A. Reyes, R. C. Hoffmann, D. P. Engelhart, H. M. Cowardin, D. Cone, “Spectroscopic Behavior of Composite, Black Thermal Paint, Solar Cell, and Multi-layered Insulation Materials in a GEO Simulated Environment,” in *1st International Orbital Debris Conference*, Houston, TX, December 2019.
- J. A. Reyes, B. G. Miller, E. A. Plis and e. al., "Understanding optical changes in on-orbit spacecraft materials," in SPIE Proceedings Volume 11101, Material Technologies and Applications to Optics, Structures, Components, and Sub-Systems IV;, San Diego, California, 2019.

- J. Reyes and D. Cone, "Characterization of Aerospace Materials Related to Orbital Debris using Reflectance Spectroscpoy," in *International Association for the Advancement of Space Safety (IAASS)*, El Segundo, California, 2019.

1.5. LIMITATIONS

A limitation to be addressed can be attributed to the data acquisition process and analysis originating from a laboratory-based setting only. Although measurements were performed in an ideal laboratory environment to evaluate the optical properties of materials of interest, they were not compared to remote observational or simulated data as necessary corrections would need to be applied beforehand (see Chapter 5). Though that will be a noteworthy step, that was outside the aim for the investigations included in this work. This is suggested for future work.

An additional aspect that can be viewed as a limitation refers to materials in this work being measured in their pristine condition. Materials that have been exposed to space environment in orbit for a given duration may experience changes in their optical behavior depending on their chemistry. This will be addressed further in Chapter 4 of the dissertation. It is therefore of significance to optically measure materials after having been subjected to the harsh space weather to evaluate these optical changes. However, it is equally significant to have a thorough understanding of an article optically in their original state which will serve as a baseline for any alterations in spectral behavior to be compared to. The aim of this work was to take a first step approach to determine if any material classification trends could arise from their optical properties through color index. Therefore, it was necessary to first apply this approach to materials in their pristine conditions before looking at materials effected by space weather.

1.6. OUTLINE

The first half of the dissertation discusses the significant aspects that are relevant to the subject matter of space situational awareness. Chapter 2 will deliver an overview of resident space

objects (RSO's), including the influence of orbital debris and micrometeoroids. The flux of objects related to orbital debris in orbit, as well as specific destructive events that have contributed to the saturation of debris in space domain, are discussed. Materials that are frequently incorporated into space hardware components are described, while discrimination characterization, and laboratory experimentation that have simulated destructive events to characterize fragmentations are discussed.

The third chapter provides an overview of methods used to support the characterization of objects residing in space domain. These involve the use of radar systems, optical measurement instrumentation, and *in situ* analysis. Because this dissertation focuses on material reflectance signatures obtained from optical measurements, the use of spectral measurements to evaluate planetary bodies, asteroids, and human-made materials will be explained. As previously mentioned, the topic of space weathering effects on common spacecraft materials will be introduced and experimental data obtained from simulated investigations will be discussed. Material classification using remote sensing techniques, and photometric measurements using color indices are explained. The technique of spectral unmixing is referred to, and the function of spectral libraries, along with their strengths and weaknesses, will be elaborated on.

The second half of the dissertation will include all measurements acquired for material analysis and how the spectral measurements were translated to color index which was used to evaluate the result differences amongst material classifications. All reflectance spectral measurements presented in Chapter 4 have been analyzed, discussed, and fed into the desired spectral database accordingly. Measurements conducted include those that were acquired in a non-space weathered environment, as well as those that were taken while materials were subjected to space simulated weather environment.

The material taxonomy approach methods that were applied in this work will be explained in Chapter 5. All concluding results will be presented in the form of color-color diagrams with respective values per material noted. The intent behind selecting certain bandpasses to calculate color index for the materials of interest will be discussed. The outcomes that consisted of sufficient distinguishability between RSO materials using color index are presented. Plots for common space materials selected to represent various material classifications are presented in Chapter 5. Options for the application of this taxonomy approach and how it can be used in conjunction with spectral libraries are also discussed in this chapter.

The Appendix section includes reflectance signature data for additional space-related materials, including those that were associated with a Titan Transtage mock-up rocket body, multiple silicon- and germanium-based photovoltaics, a series of metal spheres in either 2 cm or 4 cm diameter, and other common space materials (Figures A.1-A.56). The additional color index plots that were generated in attempt to find material trends but not included in the main discussion are also present in the Appendix (Figures A.57-A.77). Color index values outlined for all materials evaluated and descriptions of respective material nomenclature can be found within Tables A.1-A.25 in the Appendix as well.

Chapter 2: Space Situational Awareness

When executing any mission within a specified domain, it is vital to understand the environment and surroundings in which that operation will be undertaken. For instance, fighter plane incidents occurred during World War II, the Korean war, and the war in Vietnam, where pilots were unaware of the onslaught of enemy fire in their vicinity [1]. The United States Air Force referred to this circumstance as an absence of "Situation Awareness" [1, 2]. This same notion can be related to objects deployed and positioned in an orbit in space. Therefore, Donald Rumsfeld applied this term to the subject of space domain in his 2001 report [3] where the phrase known as Space Situational Awareness was born [1]. Space Situational Awareness (SSA) applies to the capability to locate all space objects that are currently residing in space domain and their position in reference to one another. The primary resource utilized to obtain SSA data is provided through the Space Surveillance Network (SSN) [4]. There are about 30 different optical and radar detectors that are operated globally by the U.S. Army, Navy, and Air Force that can detect an object as small at 10 cm in low Earth orbit (LEO) and 70 cm in geosynchronous Earth orbit (GEO) [4, 5]. These capabilities have granted the tracking of many space articles and have contributed to a greater understanding of SSA.

Although the location of objects inhabiting the space environment is significant knowledge to ensure the safety of any one resident space object (RSO), there are additional pieces of information that can be beneficial toward the overall intelligence that contributes to SSA. As Space Force Major Bryan Sanchez, has stated, "The more objects we can characterize and identify, the greater our freedom of movement throughout space can be," [6]. Expanding upon this declaration, it is crucial to understand not only location or size of an article, but also the chemical make-up for RSOs, including orbital debris and micrometeoroids, to gain a more comprehensive understanding

regarding said objects populating space domain, and those which could be traveling at elevated velocities in orbit.

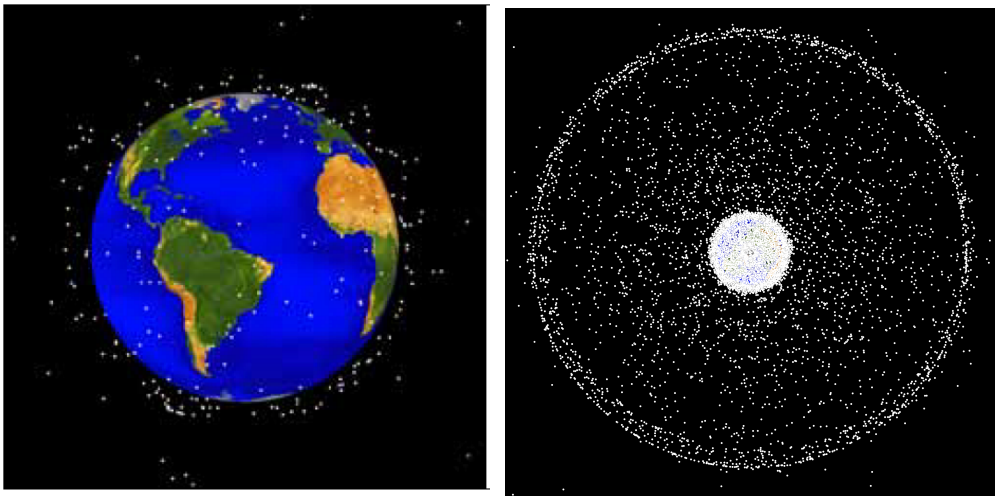

Figure 2.1: Depiction of cataloged objects represented by white marks within near-Earth orbit in 1963 (left) [7] versus 2019 (right) [8].

2.1. Resident Space Objects

The motivation for space exploration has promoted an increased population of human-made space hardware to inhabit space domains near Earth. Since the first satellite launch of Sputnik on October 4, 1957 [9], there have only been an unceasing advancement in rocket bodies and spacecraft launched and positioned in orbit. For example, the augmented flux of cataloged objects near-Earth orbit between years 1963 and 2013 can be seen in Figure 2.1. During their flight in orbit, these space articles have experienced prolonged exposure to a harsh space environment, largely contributed by atomic oxygen and ultraviolet radiation in LEO [10, 11] and electron radiation in GEO [12, 13, 14], which can lead to space material degradation. Furthermore, each RSO is sharing a realm with other space objects and micrometeoroids that they could potentially collide with, which could in turn result in material fragmentations. The likelihood of the Kessler syndrome, proposed by Kessler in 1978, where the persistent generation of debris increases the

population density of fragmentations in space domain and therefore directly increases the odds of contributing collisions and generating more debris [15], is a concept to consider. Additionally, RSO's are subject to catastrophic failure in the event that their systems unfortunately malfunction, causing singular explosive breakup events that could generate a multitude of material fragmentations [16]. These aforementioned damaging events are contributors to the existence of space junk, technically referred to as orbital debris.

2.1.1. Orbital Debris

Orbital debris is defined as any artificial material particle or material system that is residing in space domain and is no longer functional or serves a useful purpose [5]. A space realm that is in a state saturated with debris provides for an inevitable increase in the risk of an RSO facing impact by orbital debris. Debris in LEO travels at speeds of ~7-8 km/s, but can undergo collision impact at 14 km/s [17], making its impact detrimental to any object in its path. It is therefore significant to have an understanding of debris material, for an impact by a metallic substance will likely cause greater damage than that of a polymeric substance due to their differences in material properties.

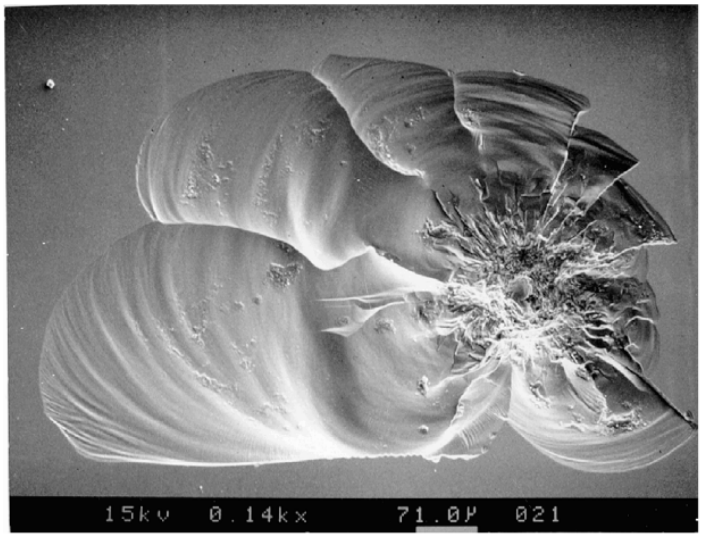

Figure 2.2: OD impact on Space Shuttle window (STS-50) [18].

Example damage caused by orbital debris impact can be seen in Figure 2.2. This is a scanning electron microscope image of a crater formation on the Space Shuttle window taken from mission STS-50 [18]. This orbital debris, estimated to measure between 100-150 μm, was chemically studied and resulted to be composed of aluminum oxide and could therefore possibly be linked to solid rocket motor ejecta [19]. This study promoted knowledge regarding new potential orbital debris hazards through characterization of impact residue.

2.1.2. Micrometeoroids

Impact hazards do not only stem from orbital debris, but are also relevant when considering the natural space environment. Micrometeoroids are small natural-occurring space particles that are derived from larger extraterrestrial forms of rock material. These miniscule natural space particulates were well studied through examinations performed on the surface of the Long Duration Exposure Facility (LDEF) upon its return from flight. The LDEF was designed of 6061-T6 aluminum alloy surface panels that were 1.6 mm thick, and after having been exposed to LEO for 5.77 years, a value of 761 impact craters were discovered on its exterior [20]. Furthermore, the orientation of the LDEF surface panels examined, being that they were zenith-facing, made for ideal exposure to the meteoroid flux environment [20] and therefore provided a worthy estimate of the extent of damage a spacecraft may encounter while in flight.

A Pressurized Mating Adapter 2 (PMA-2) cover, returned after use on the exterior of the International Space Station, faced impact by the micrometeoroid environment (Figure 2.3). After chemistry analysis acquired from scanning electron microscopy, it was determined that the impact remnant was rich in iron, nickel and sulfur elements [21]. This was indicative of damage sustained on space hardware caused by a projectile from the natural space environment and thus requires attention for risk mitigation.

To further understand the magnitude of the threats involved with the micrometeoroid and orbital debris (MMOD) setting, meteoroids can impact space objects at high speeds ranging from 12-72 km/s compared to that of orbital debris [22]. In one case, American satellite Telecom-1A faced impact damage from a micrometeoroid which ultimately left the spacecraft disabled [18]. This validates micrometeoroids to be a hazard that also must be considered in the risk mitigation of functional spacecraft positioned in near Earth space. While it has been found that meteoroid presence in near Earth space is largely related to "sporadic" meteoroids rather than meteor showers [22], the ability to determine meteoroid density is still challenging.

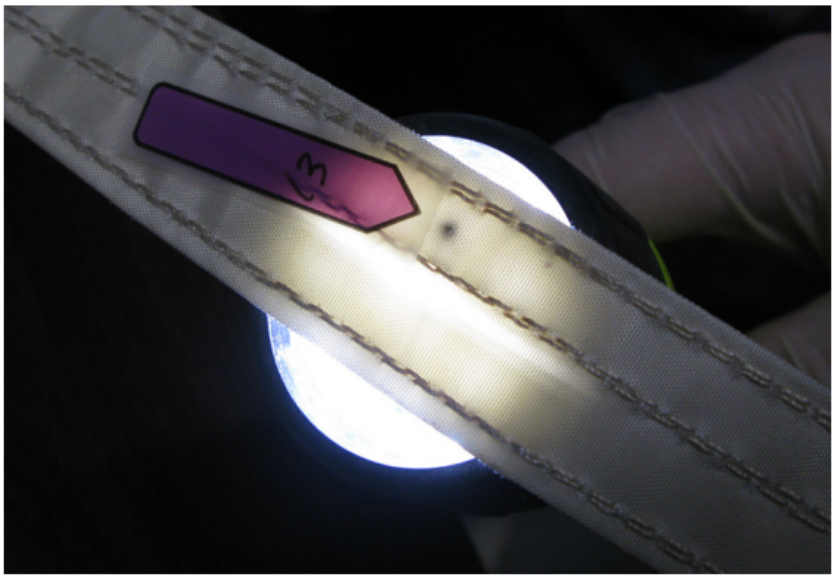

Figure 2.3: Micrometeoroid impact discovered on the returned PMA-2 cover [21].

2.2. Flux in Orbit

Although methods to characterize the MMOD population via material density can be enhanced, the systems used for modeling debris objects have provided valuable information toward gaining an overall estimate of the orbital debris environment. The National Aeronautics and Space Administration's (NASA) Orbital Debris Engineering Model (ORDEM) and the European Space Agency's (ESA) Meteoroid And Space debris Terrestrial Environment Reference

(MASTER) model both offer a data-driven representation of the MMOD status. The existence of both models is advantageous in confirming the validity of the data produced by each, enhancing the confidence in the MMOD environment assessment. Though both models serve to achieve the same objective, there are many similarities and differences between the methodologies used to generate each of these models.

2.2.1. ORDEM

ORDEM was first established by NASA's Orbital Debris Program Office (ODPO) to aid the Space Station Program Office during the mid-1980's [23]. The model has undergone several upgrades throughout its operational time. The first version of the model, ORDEM96, introduced the characterization of the debris population by various factors like altitude, size, and inclination [24], then was subsequently upgraded to ORDEM 2000 where the debris environment was refined using finite element representation [25], and then later faced an additional upgrade to ORDEM 3.0 where its capabilities were enhanced to include data out to further altitudes in GEO, incorporate material density distributions, and debris flux uncertainties [26]. Since then, ORDEM has upgraded to its current version, ORDEM 3.1, which has carried over capabilities from its previous versions but has been optimized to utilize quality data from radar, in-situ analyses, optical measurements, and latest measurement techniques that could support the enhancement of the data-driven model [23].

Debris flux is effectively modeled by ORDEM 3.1. The model provides a flux demonstration for objects in LEO and GEO that are greater than 10 μm and 10 cm, respectively [27]. The majority of data included in ORDEM 3.1 is acquired from what has been catalogued by the SSN which provides information on objects as small as ~10 cm and ~1 m in LEO and GEO, respectively [27]. ORDEM 3.1 also draws its data from the Haystack Ultrawideband Satellite

Imaging Radar (HUSIR) and from the Michigan Orbital DEbris Survey Telescope (MODEST). HUSIR is utilized to model objects in LEO between ~5 mm to ~10 cm in size, and MODEST offers the model data for objects in GEO that are within the ~10 cm to ~1 m size range [27]. An example of data taken from MODEST to support orbital debris breakup event modeling can be seen in Figure 2.4. For objects within the sub-millimeter size range (< ~3 mm) in LEO, analysis is taken *in situ* from impacts on the Space Shuttle vehicle, and the Hubble Space Telescope (HST) to deliver an estimation of the minuscule debris population.

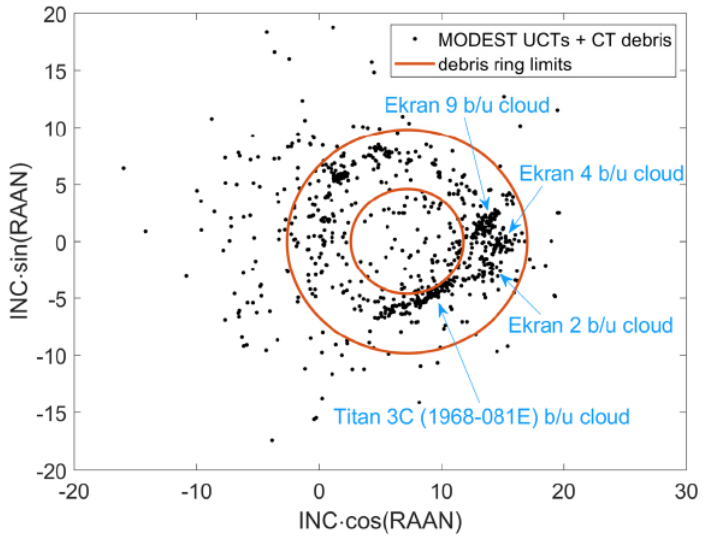

Figure 2.4: Data from MODEST 2004-2009 Uncorrelated targets (UCTs) and correlated target (CT) debris representing 4 GEO breakup clouds [27].

2.2.2. MASTER

Comparable to ORDEM 3.1, MASTER is a modeling tool that also provides information on the orbital debris population to deduce flux and spatial density [28]. For the GEO debris environment, ESA's Space Debris Telescope (SDT) is utilized for debris observations. It can detect objects that are slightly under 10 cm in size, while the 1 cm debris size population in LEO is modeled using data from the Tracking and Imaging Radar (TIRA) and the European Incoherent Scatter (EISCAT) Svalbard radar [28]. The various sources that orbital debris are generated from

can be sorted by debris size. As seen in Figure 2.5, the ≥ 1 cm debris population comprises of launch and mission related objects (TLE Background), fragments, NaK droplets, solid rocket motor slag, and multi-layered insulation (MLI) material [28].

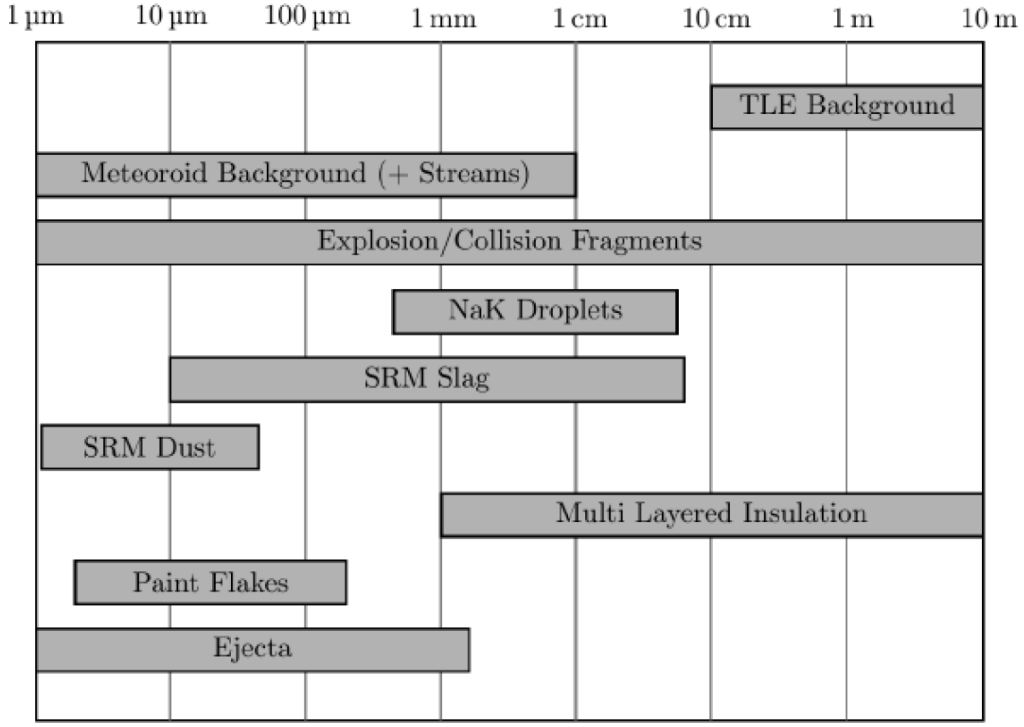

Figure 2.5: Chart outlining sources of orbital debris by size included in MASTER [28].

ORDEM and MASTER are tools that serve to achieve the same comprehensive objective, however there are details between both that are both similar and unalike, all worthy of being noted. Both models make use of the SSN as a viable resource for a broad assessment of the debris population. When pertaining to visual inspection of impacts on returned space hardware having flown in space for a lengthened stretch of time, MASTER-8 includes examinations on the Long Duration Exposure Facility (LDEF), HST, and the European Retrieval Carrier (EuReCa) to assess debris sized under 1 mm [29]. ORDEM 3.1 contains data analysis on the submillimeter population from impacts faced by the windows and radiators of the U.S. Space Transportation System (STS) vehicle (also known as the Space Shuttle) between the years of 1995 through 2011 [29]. Regarding

the size range of debris objects assessed, MASTER-8 provides flux information for debris having diameters between 1 µm to 100 m, whereas ORDEM 3.1 delivers flux data for debris between 10 µm and 1m.

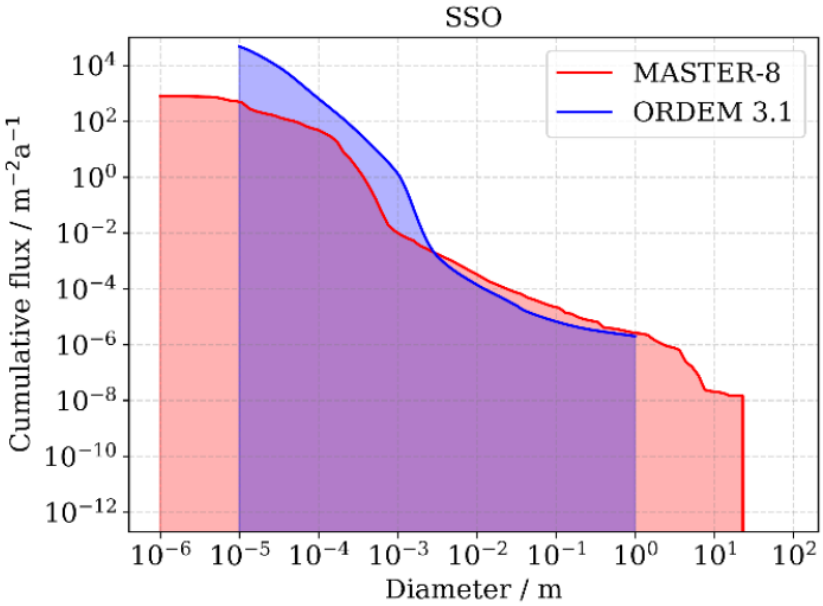

Figure 2.6: Cumulative flux in SSO of debris size range for MASTER-8 and ORDEM 3.1 [29].

To further compare the two models, simulation results for cumulative flux in sun-synchronous orbit (SSO) for the debris size range of each model has been outlined in Figure 2.6. Flux results for both models are consistent in outlining large flux values for smaller debris and lower flux of larger debris, while also producing nearly equal flux results for 1 m diameter debris, and equal flux results for 2 mm diameter debris as seen in both models [29]. Though both models resulted in large flux for small debris, the flux is almost 2 magnitudes greater in the ORDEM 3.1 model than MASTER-8.

ORDEM 3.1 and MASTER-8 have grouped debris by size using different approaches. For both models, the >10 cm debris flux is mainly attributed to the intact object population, such as launched payloads and upper stages, though regarding the micrometer-sized debris population,

MASTER-8 attributes a majority of the flux below 10 μm to solid rocket motor dust, whereas ORDEM 3.1 categorizes medium density objects to dominate the < ~500 μm population [29]. The two orbital debris models also go on to classify debris differently. The debris categories for MASTER-8 are broken down by explosion fragments, collision fragments, launch/mission-related debris, Sodium-Potassium (NaK) droplets, solid rocket motor slag and dust, paint flecks, and ejecta, and MLI fragments. ORDEM 3.1 rather categorizes its debris flux by five density groups including NaK, intact objects, low-density, medium-density, and-high density objects.

2.3. Destructive Events in Space Domain

Impact by orbital debris provokes serious risk to functional spacecraft. On May 12, 2021, when the Canadarm2 on the International Space Station (ISS) was performing a routine inspection, it was discovered that the robotic arm suffered an impact by debris (Figure 2.7), leaving a small puncture approximately 5 mm in diameter in the hardware's thermal protective cover [30, 31]. Though the Canadarm2 was lucky not to have experienced malfunction due to the debris impact, regardless of whether the debris was human-made or not, there have been events where space articles in the path of orbital debris have undergone catastrophic damage of greater severity.

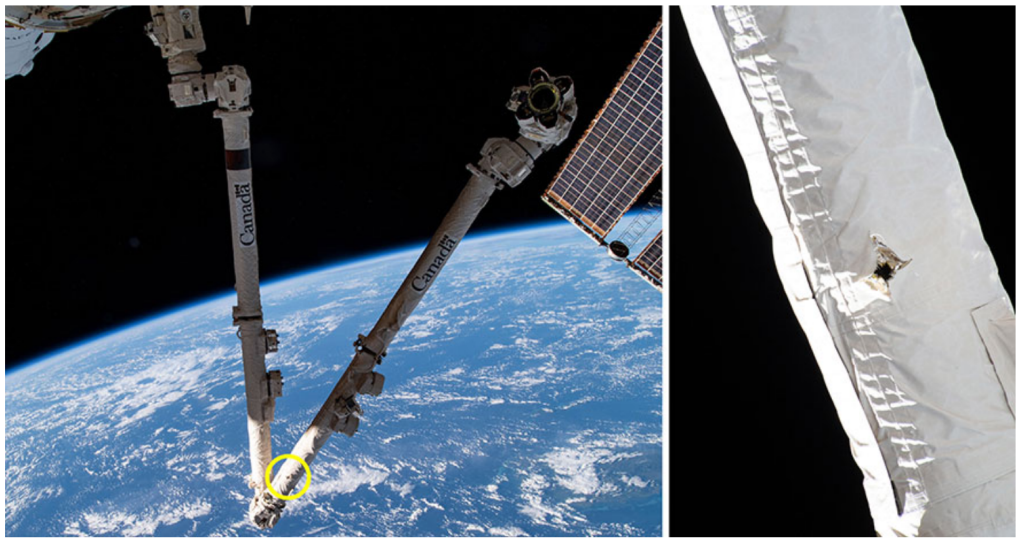

Figure 2.7: Images of damage on the Canadarm2 caused by space debris. Courtesy of *NASA/Canadian Space Agency* [30].

2.3.1. Collisions

Collision events between spacecraft that have occurred within near-Earth space domain have contributed adequately to the orbital debris population. Between 2007-2009, two distinct collision episodes occurred, resulting in three spacecraft having been subject to catastrophic fragmentation. The first event took place in early 2007, when a defunct weather spacecraft, Fengyun 1C, was annihilated after facing impact from an SC-19 missile launched kill vehicle as part of a Chinese anti-satellite (ASAT) test [32]. The second collision occurred in 2009 between the U.S. Iridium 33 and Russian Cosmos 2251 space crafts, marking the first accidental collision resulting in hypervelocity fragmentations [32, 33]. These two collision events generated an evident inflation of fragmentation debris, therefore, directly increasing the number of total objects residing in Earth orbit for the years 2007 and 2009, respectively, as seen in Figure 2.8 [34].

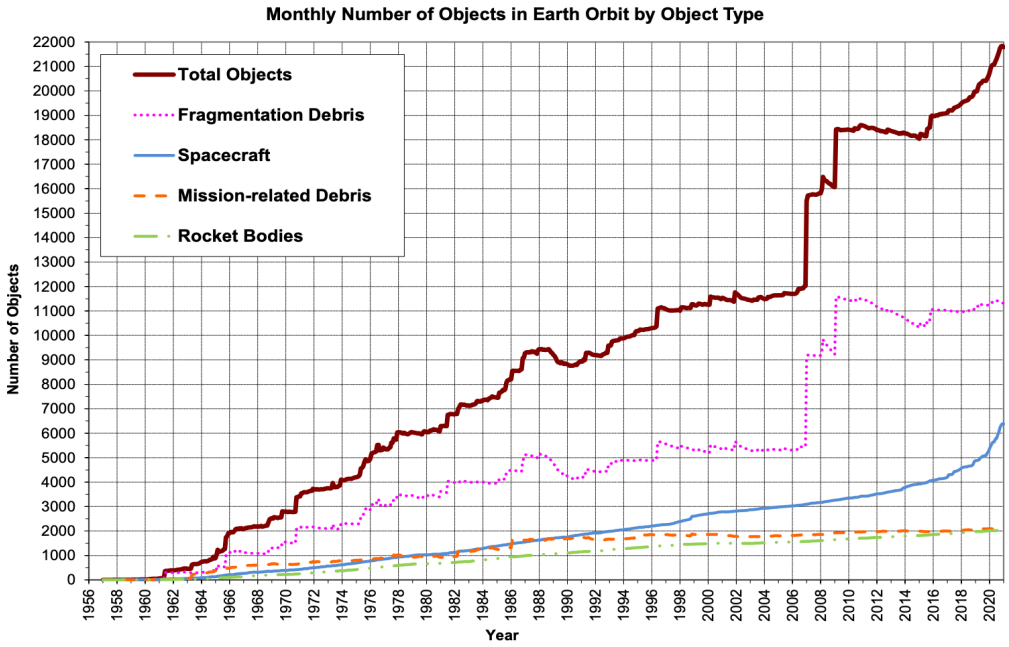

Figure 2.8: Number of objects by type residing in Earth orbit [34].

Collision events related to orbital debris are of most concern when considering the hazards associated with small orbital debris. Objects smaller than 10 cm go uncatalogued by the SSN [5, 35], leaving limited methods of *in-situ* observations for small objects (~3 cm) [35]. It can be said that the number of small orbital debris objects is more abundant than the number of large objects that are capable of being catalogued, and because these small objects go undetected, potential collisions they provoke are unpredictable [18]. Collisions can also be categorized as catastrophic. This indicates a result of fragmentation between both objects included in the event, or they can be non-catastrophic, in which case the larger impacted object results in crater morphology and only the smaller object experiences fragmentation [36].

2.3.2. Breakup Events

The Titan IIIC Transtage, an upper stage of the Titan IIIC launch vehicle developed in the 1960's, has been associated with four catalogued fragmentation events. Transtage 3C-5 (International Designator 1968-081E, U.S. Strategic Command (USSTRATCOM) SSN #3432) fragmented on 21 February 1992 after 23.4 years on-orbit [37, 38]. As of 4 July 2017, the 1968-081E breakup had 28 debris pieces associated with this fragmentation [37, 38]. Transtage 3C-17 (1969-013B, SSN #3692) fragmented again on 28 February 2018 after 49.085 years on-orbit, and the 1969-013B breakup had 18 catalogued debris pieces as of 5 July 2018 that are associated with its fragmentation event [37]. The geostationary transfer orbit (GTO) (1965-108A) and LEO (1965-082DM) events occurred on day of launch, likely due to propulsion-related events [38]. The GTO and LEO destructive events yielded 107 and 472 cataloged debris pieces, respectively, but may have produced significantly more debris than are currently cataloged [37].

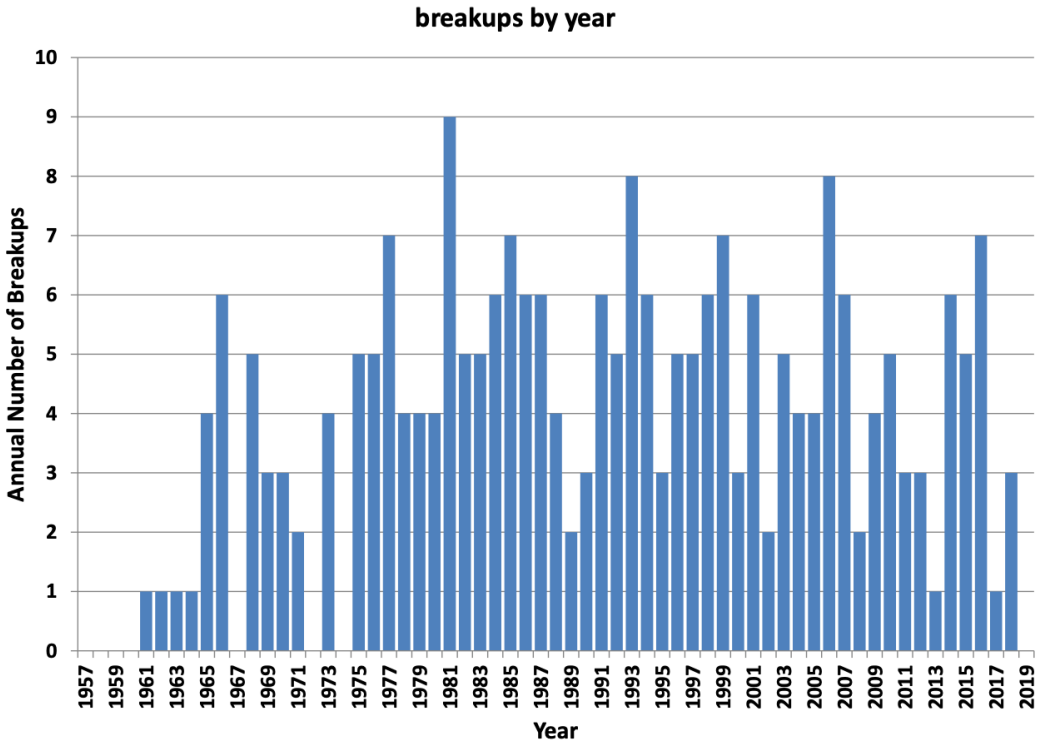

Figure 2.9: Number of breakups per year since year 1961 [16].

Breakup events that spacecraft potentially face are destructive and therefore contribute to the overall debris population inhabiting space environment. Rocket body and spacecraft explosions have been classified as the dominant contributor of orbital debris with sizes large enough to be detected [16]. There have been several breakup events having been reported in the past. These include Cosmos 862 spacecraft, Delta and Delta II rocket body second stages, Ariane 1-4 rocket bodies' third stages, to name a few, and significantly the destructive events involving the SOZ units as part of the Russian/Soviet Union Proton fourth stages which amass nearly half of all propulsion-related breakup events [16]. These destructive affairs are threatening considering that they directly contribute toward the saturation of the orbital debris population. The number of breakups that have occurred per year since 1961 can be seen in Figure 2.9. For further reading, a full overview of documented fragmentation events that have occurred as of 2018 and associated with satellites residing in orbit can be found in [16].

The aforementioned destructive breakup events, be it collision-related, propulsion-related, or others, and regardless of whether they occurred accidentally or intentionally, all lead to the production of orbital debris. With the continual accumulation of debris objects residing in near-Earth space domain, which has been outlined in Figure 2.8, there is a direct increase in the demand for understanding any hazards correlated with said fragmentations. Factors associated with the magnitude of damage that a resident space object may face when impacted by debris include debris size, speed, and material. Therefore, if debris material can be more efficiently characterized remotely, this can enhance the methods for determining any risk mitigation that should be enacted to prevent destructive events in the future.

2.4. Common Space Hardware Materials in Orbit

The artificial space fragmentations known as orbital debris are derived from a parent functional space object. Numerous satellites and spacecraft that are functional are also currently operating in near-Earth space domain, making up a part of the RSO population. These include many satellites and various configurations of spacecraft, as well as some rocket bodies and high area-to-mass ratio (HAMR) objects. Not only is it significant to characterize orbital debris materials, but it is equally as important to understand the characteristics of common functional spacecraft materials proactively in the case that these materials, both heritage and modern, are subjected to ruinous breakup events in the future. An overview of some common spacecraft materials can be found in Table 2.1.

Table 2.1: Common spacecraft material components organized per classification.

METALS	POLYMERS	CERAMICS	COMPOSITES	
			MATRIX	STRUCTURE
Aluminum alloy (6061, 6082, 5005, 5052, 7075, 2024, 1100)	Kapton®	Fiberglass	Carbon fiber reinforced polymer (CFRP)	Multi-layer Insulation (MLI)
Ti-6Al-4V	Kevlar®	Coverglasses	Glass fiber reinforced polymer (GFRP)	Si solar cell
Copper	Mylar™	Shuttle tiles	PICA (Phenolic-Impregnated Carbon Ablator heat shield)	Ge solar cell
Inconel 718 (Ni based alloy)	Teflon (PTFE)	Silica (SiO_2)	SIRCA (Silicone Impregnated Reusable Ceramic Ablator)	Beta cloth
Stainless steel (ferrous)	Thermal control paints	Titanium oxide (TiO_2)	Al-glass epoxy composite	
		Alumina	Al-carbon epoxy composite	
			Printed circuit boards (PCB)	

2.4.1. Metals

In the metals category, some common space hardware materials include various grades of aluminum alloy, titanium alloys, stainless steels, and copper. Aluminum alloys, particularly 6061 grade, are a desirable candidate for space applications due to their high strength-to-weight ratio, thermal conductivity, resistance to corrosion, affordability, and can be easily anodized [39, 40, 41]. For a metal, their density of 2.70 g/cm^3 is preferred over other metals of greater density [39, 42, 43]. Additionally, their ability to be anodized provides an oxide coating to protect against corrosion and abrasion, further making them suitable for life in space to withstand impact and

inhibit surface degradation fostered by space plasma [39, 40, 44, 45]. Structural components of CubeSats often involve aluminum alloys, particularly 6061 or 7075 [46] for these reasons.

Titanium alloy Ti-6Al-4V is another attractive metal alloy selected for use in aerospace applications. It is light in weight with a low density, yet offers high strength, high modulus, a low coefficient of thermal expansion (CTE), while having the ability to withstand elevated temperatures greater than what aluminum can [47]. Ti-6Al-4V alloy can be processed as an extra-low interstitial grade to provide less oxygen content and optimal fracture toughness down to 77 K which allows for greater ductility of the metal alloy at lower temperatures due to the interstitial elements promoting deformation by twinning [48]. Titanium alloys are used in spacecraft design in the form of brackets, fittings, propulsion tubing lines [47], and, for example, X-link sub-structural components of the Columbia Space Shuttle were a product of Ti-6Al-4V alloy which was used to connect the crew module, forward fuselage, and midbody structures of the space vehicle [49]. This titanium alloy is not uncommon to space design and is likely to continue serving as a space-grade material in the future to come.

2.4.2. Polymers

One of the most popular polymers amongst space material selection is Kapton® polyimide film. Kapton®, developed by DuPont™, is a durable and chemically inert thermoset that can withstand elevated temperature and radiation conditions [50], and has a density of 1.42 g/cm^3 [39, 51]. For these reasons it has been used widely in the space industry and has served as an effective layer of protection to many RSO's.

In addition to Kapton®, Teflon™ and DuPont™'s Mylar® are polymeric materials also used for space applications and incorporated into space thermal blankets [52]. Furthermore, DuPont™'s Kevlar® performs well as a polymer in terms of strength, having very high modulus

[53], provides effective radiation shielding [54], and is also often included as a composite counterpart [55], all serving a wide range of space-worthy material capabilities.

2.4.3. Ceramics

Ceramics are most frequently employed as heat-shield materials that can withstand the elevated heat-flux upon atmospheric re-entry. They can be composed of silica, alumina, or similar ceramic ablative materials [56, 57]. The material properties of ceramics alone as a thermal protection system can be optimized by reconstructing them into a composite material. This not only allows the ceramic to gain beneficial properties from the introduced composite material, but can also reduce its weight, offering greater efficiency of the space vehicle in which ceramics are employed. Heat-shields composed of ceramic matrix composites will be discussed further in Section 1.5.4. Composites.

Coverglasses are thin, transparent, brittle material systems incorporated as part of solar cell design, serving as their top layer to provide photovoltaic protection and hinder color darkening from the harmful ultra-violet, proton, and electron radiation that exists in space environment [58, 50]. Coverglasses are considered a vital space material component for this reason.

2.4.4. Composites

Composite materials have been on the forefront as innovative and advanced components for space applications. Of these, carbon fiber reinforced polymer (CFRP) has become an exceptionally useful candidate for space hardware. Carbon composites are manufactured having a structure of numerous carbon fibers arranged in a multi-directional orientation to achieve isotropic material properties. Similar to aluminum alloys, carbon fiber composites have a high strength-to-weight ratio [59], making them ideal for their use in space, military and commercial applications based on their tensile strength (924 ksi) and low density (1.8 g/cm^3) [39, 60, 61].

Space approved printed circuit boards (PCB's) are most likely to be include in RSO systems. They are often constructed of FR-4 epoxy composite laminate [62] or polytetrafluoroethylene (PTFE) fiberglass [63]. It is expected that these polymer-matrix composites contain quantities of organic content within their elemental composition. Material properties for FR-4 epoxy includes a density of 1.90 g/cm^3 and water absorption of 0.10% [64], whereas PTFE fiberglass laminate circuit board substrate has a density of 2.23 g/cm^3 and water absorption of 0.02% [65].

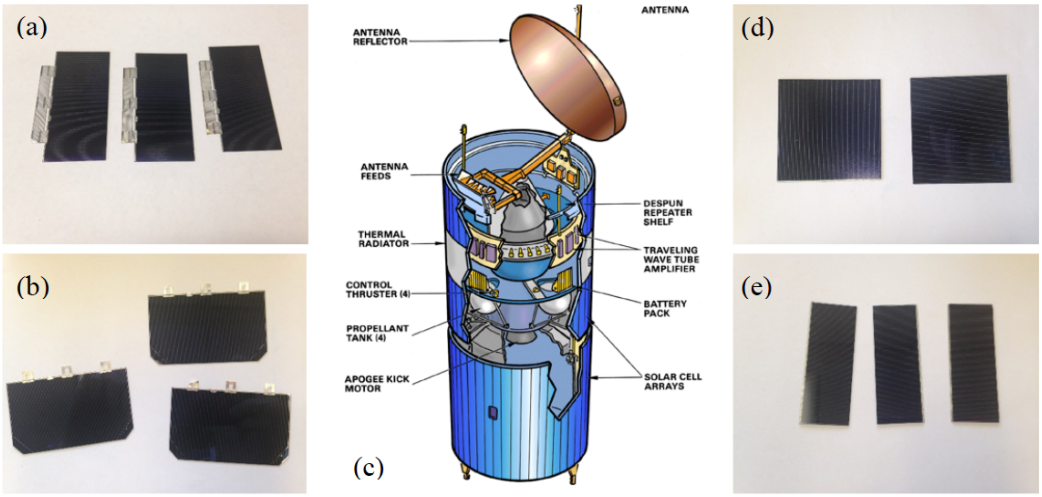

Figure 2.10: (a) GaAs/Ge cells, (b) GaInP$_2$/GaAs/Ge cells, (c) Configuration of Boeing HS-376 spacecraft [66](image credited to Boeing), (d) Silicon K4 3/4 cells, and (e) Silicon K7 cells.

Solar cells used in space hardware can be fabricated as single- or multi- junction semiconductors InGaP, GaAs, Ge or Si sub-cells (Figure 2.10) [67, 68]. Photovoltaics are vital in space design, for they provide the necessary function to power a spacecraft and are therefore repeatedly used in the space industry. Heritage spacecraft systems often use silicon-based solar cells while modern space systems are making use of multi-junction germanium based photovoltaics. For this reason, it can be expected that a bountiful quantity of solar cells are

inhabiting near Earth space regime, making it necessary to thoroughly understand their optical signatures to in turn support remote observations.

Amongst matrix material composites, Phenolic Impregnated Carbon Ablator (PICA), and Silicone Impregnated Reusable Ceramic Ablator (SIRCA) are efficient heat-shield materials, serving as a Thermal Protection System (TPS) for space vehicular design. PICA was invented by NASA in the 90's and was successful in its use on the Stardust Capsule, which reentered Earth's atmosphere at record speeds of 46,510 kmph [69, 70]. Due to its promising capacity to protect space vehicles from elevated temperatures, SpaceX moved forward in developing their own variation of the material, known as PICA-X, to be incorporated as the heat shield for their Dragon spacecraft [69, 70]. PICA is manufactured of carbon fiber impregnated with phenolic polymer resin [70] amounting to a density of ~0.26 g/cm^3 and operating temperature range of ≤1200°C [69]. The material can withstand a 15 MW/m^2 heat flux and maximum pressure around 1-1.5 atm [71].

SIRCA, similar to PICA, is a TPS ablative material, however is fabricated using Reusable Surface Insulation (RSI) as a substrate impregnated with silicone resin [72]. With a density between 0.22-0.40 g/cm^3 and ≤550°C operating temperature [69], SIRCA has been incorporated as a heat shield for use on the Mars Pathfinder and the Mars Explosion Rover spacecraft systems [71, 72]. PICA and SIRCA therefore have wide use in the aerospace industry.

Beta cloth is a heritage space material employed since the dawn of the space-age to provide protection against exposure from the harmful space environment. Beta cloth is a composite material system that is constructed of PTFE (Teflon™) coated fiberglass [73] that has been deemed a space-grade worthy material after having undergone much material property analysis after being exposed to space environment. The material had been included in an LDEF experiment, remaining

in flight for 5.7 years oriented 22° off the ram direction, receiving quantities of both atomic oxygen (AO) and ultraviolet (UV) radiation, ultimately exhibiting durability against the space elements [73, 74]. Beta cloth was furthermore successful in protecting a battery orbital replacement unit (ORU) from space exposure for 8.6 years [73]. The resourceful cloth has seen its fair share of time in space, undergoing numerous other in-situ studies. Aluminized beta cloth had flown on the Passive Optical Sample Assembly-I (POSA-I), POSA II, and the Optical Properties Monitor (OPM) long-duration flight experiments where the material optical properties were observed and color changes were noted [73, 74].

A category of space materials assigned as high area-to-mass ratio (HAMR) objects, recognized in the early 2000's by Schildknecht [75, 76], are components of space hardware and therefore have become contributors to the space debris population. Literature suggests that MLI materials are most common amongst the HAMR resident space object category [76]. MLI blankets comprise of outer layers, such as Kapton® or beta cloth, with properties that can withstand exposure to elements of space, and interior layers of various polymer counterparts, typically Kapton®, Mylar, or Teflon™, that are sandwiched together between mesh separators, like Dacron® or Nomex® netting, to form MLI [77]. MLI is often selected for spacecraft design due to its effectivity in protection from space elements while serving as an insulator of radiation-heat transfer obstructions that will impede energy flow [78].

2.4.5. Rocket Bodies

Rocket bodies are large launch vehicles necessary for the completion of space missions in deploying payloads into orbit. They have been utilized since the onset of space exploration, contributing to common hardware deemed space worthy. Launch vehicles, comprised of several stages, have been constructed using aluminum-based materials, coated in thermal control paint, or

protected with MLI (Figure 2.11). Material advancements have now led to the frequent incorporation of composites, such as carbon fiber reinforced aluminum for load bearing structures [79].

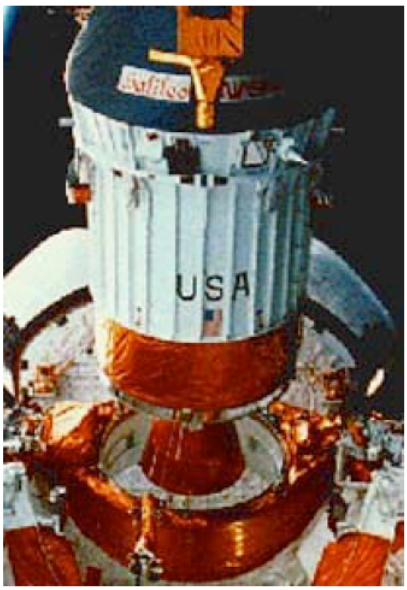

Figure 2.11: Image of the IUS rocket body (courtesy of NASA) [80].

The Titan IIIC launch vehicle's upper stage, the Titan IIIC Transtage, has been known to have undergone four breakup events during its time in flight. Due to the fragmentation generated from the destructive occurrences, it is significant to deduce the materials used for the construction of the rocket body. Therefore a mock-up of this launch vehicle component was studied to aid in the analysis of the Transtage [37]. The materials on the mock Transtage included bare iridited aluminum surfaces, white silicone paint coated surfaces, aluminum silicone painted surfaces, gold plate stainless steel foil, and glass frit (Figure 2.12) [37, 81], many of which are commonly used spacecraft and rocket body materials.

Thermal control paints frequently used to coat the external surfaces of rocket bodies are worthy of characterization optically. For example, AZ-93 (by AZ Technology) is an inorganic

white thermal control paint that offers a nonspecular white coating and enhanced thermal protection only allowing 14-16% of impinging solar radiation to be absorbed while emitting 89-93% of internal heat generated [82]. AZ-400 is an organic white thermal control paint and is used to coat surfaces such as anodized aluminum [82]. With a specialized pigment in a silicone binder, the paint can be spray deposited and with additive can form a flexible organic nonspecular white marker paint [83, 84, 85, 86]. AZ-1000-ECB is a thermally conductive inorganic black paint and retains optical properties when exposed to the space environment [87, 88].

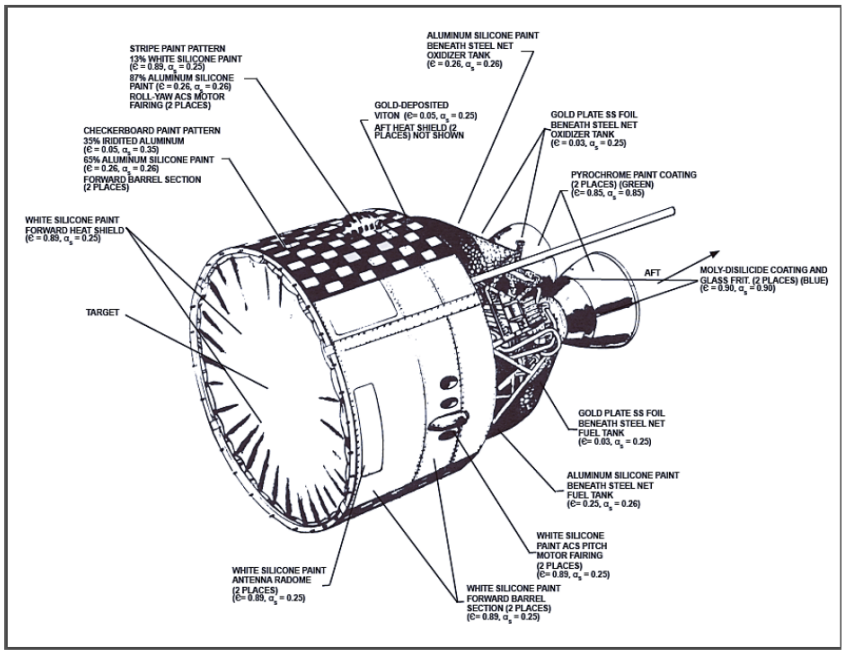

Figure 2.12: Schematic of Titan Transtage thermal control structure [37].

2.4.6. Heritage vs. Modern Space Materials

Heritage materials that have been chosen for space applications since the birth of the space era have often included aluminum alloys, polyimide films, thermal control paints, photovoltaics, and electronic systems such as circuit boards. The span of space exploration has seen several advancements in material design, which must also be taken into account when characterizing materials populating space regime in the present and future. The advancement of space materials

is concerned with their ability to perform dynamically, in respect to adaptability, self-healing, or multi-functionality [89]. For example, graphene has the ability to transform to graphane, which can aid in electric conductivity, but then can adapt back to graphene to rectify any present defects within the material [89]. Composite structures comprised of carbon nanotubes, graphenes, or the like, provide for dynamic material systems in the case of multi-functionality when incorporated with their matrix material [89], and therefore, can be expected to be more frequently utilized in space applications in the future. Additionally, solar cells have progressed in their design and while silicon-based solar cells were widely used at the onset of the space age, germanium-based solar cells are now often utilized, and photovoltaics have become more efficient with dual- and triple-junction design for their optimal solar absorption properties. It is therefore significant to take material advancements into consideration while remaining vigilant about traditional space materials when characterizing space domain.

2.5. Laboratory Tests to Understand OD Fragmentation

To gain enhanced prediction of a resulted catastrophic fragmentation event on orbit, several laboratory experiments have been conducted with the intent to achieve complete destruction of the satellite article. The following experiments not only provide sufficient awareness of what materials are used for space design, but also serve to deliver critical information regarding how such materials fractured.

2.5.1. DebriSat

To obtain a better understanding of what a typical spacecraft residing in LEO would comprise of, a mock-up satellite used as part of a debris impact study, known as DebriSat [39, 90], was constructed with common materials used in space hardware design (Figure 2.13) modeled after recent satellites observed in LEO [91, 92]. These materials, to name a few, included solar

cells, 6061 aluminum alloy in painted and unpainted forms, Kapton® polyimide film, carbon composites, and various circuit boards. The selected materials for this mock satellite applied to the category branches of heritage and modern space grade materials, provided for a worthy satellite reproduction.

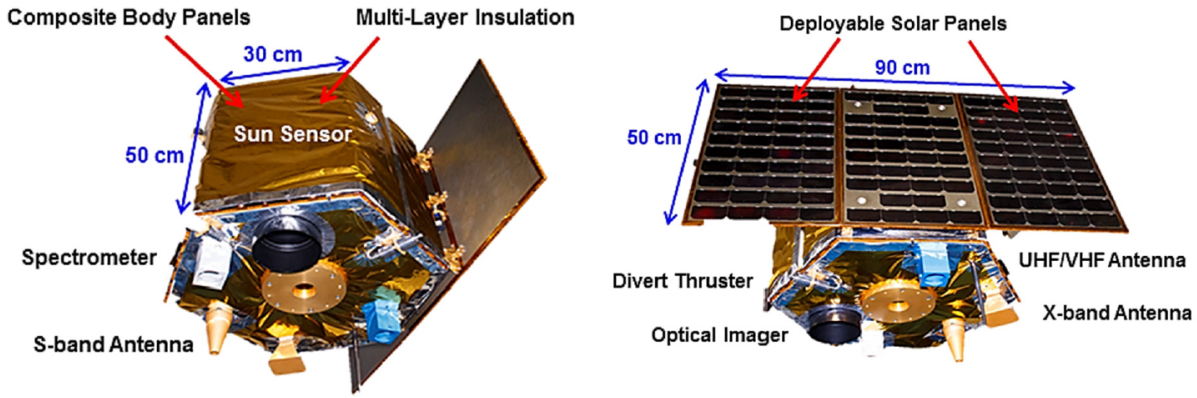

Figure 2.13: Schematic of DebriSat depicting multiple material components from different viewing perspectives [90].

The DebriSat project unfolded as a collaboration between the National Aeronautics and Space Administration (NASA) Orbital Debris Program Office (ODPO), the Air Force Space and Missile Systems Center (SMC), The Aerospace Corporation (Aerospace), the University of Florida (UF), and the Air Force Arnold Engineering Development Complex (AEDC) [39, 90]. The objective of DebriSat was to mimic a destructive breakup event that a spacecraft residing in LEO could be subjected to [39]. The project was carried out having the flight-ready satellite housed in a large chamber with walls formed of soft catch panels to collect all fragmentations of the ravaged satellite after being subjected to hypervelocity impacts [39, 90]. The impact test employed an 8.6 cm x 9 cm (570 g) nylon cap projectile with a hollow aluminum cylinder embedded in it and was delivered to strike the DebriSat target at 6.8 km/s using a two-stage light gas gun, ultimately

generating over 126,000 material fragments [39, 90, 93]. These multitude of fragments have been undergoing thorough characterization analysis since the experimental impact was executed.

The fragmentation data generated from the DebriSat project is significant toward improving current DOD and NASA breakup models, specifically in enhancing the observations of modern satellite destructive events [94]. To expand this data collection, an additional test target developed by the Aerospace Corporation was included as a pre-test shot as part of the DebriSat project. This target, named "DebrisLV" was designed as a launch vehicle upper stage and its fragments post impact were collected and are to be analyzed after the completion of DebriSat analysis [90, 94].

2.5.2. SOCIT

The DebriSat project unfolded following the Satellite Orbital Debris Characterization Impact Test (SOCIT) experiments, which similarly were a series of hypervelocity impact tests that occurred between late 1991 to early 1992 [93]. The fourth SOCIT test (SOCIT4) employed a flight ready Navy Transit satellite bus test target and took place at the Arnold Engineering Development Center Range G where the collected data analysis was overseen by the General Research Corporation (GRC) and Kaman Sciences. The SOCIT4 test target, unlike DebriSat, was a readily available satellite, known as Oscar 22, built decades before its use in the impact test [93]. It had an octagonal core with dimensions 46 cm in diameter and 25 cm in height, weighing 35 kg and designed with aluminum, copper, fiberglass, plastic, and steel [93, 95]. Though other common space-grade materials were originally incorporated in the test satellite, they were removed and excluded for various reasons. However, DebriSat in its final form was constructed of all space-grade materials, both heritage and modern, in pristine flight-ready condition, making DebriSat a more robust test target in serving orbital debris breakup models.

Furthermore, though both impact projects utilized a two-stage light gas gun, the impact projectile for DebriSat was an aluminum cylinder, whereas SOCIT employed an aluminum sphere projectile [93]. While the impacts from both experiments reached energy to mass ratios (EMR) to meet catastrophic standards, the EMR for SOCIT resulted in 81 J/g, yet the EMR for DebriSat resulted in a three-fold greater amount of 235 J/g [93]. Additionally, although foam panels were used in both experiments to collect the generated fragmentations, they were situated differently in a manner where only 65% of the SOCIT test satellite's projected area was accounted for with foam panels, nevertheless 100% of the DebriSat projected area was covered [93, 94].

Comprehensively, while there were many similarities and differences in the experiment details between DebriSat and SOCIT, both projects have contributed significantly to current orbital debris breakup models and will continue to further this data in the future. In addition to DebriSat and SOCIT, selected fragments from hypervelocity impact test, Shot CU-6470, and an explosion test (ESOC-2) were conducted and analyzed in [96]. These experiments were carried out, like DebriSat and SOCIT4, to characterize fragmentation cross-section and compare such results to existing debris models. The CU-6470 Shot and ESOC-2 destructive experiments sought to discriminate selected fragments by size, mass and shape using frequency methods [96] and further by shape broken down by flat plate, bent flat plate, curled plate, folded plate, and torn flat plate [97]. From the SOCIT4 impact test, the generated fragments have been characterized by 10 different shape categories (flat plate, curled plate, box, sphere, flake, rod, cylinder, box and plate, other, nugget) and by 2 categories of material (metals and non-metals) [98]. The DebriSat experiment characterized fragmentations by many more parameters, including material, shape, color, dimensions, characteristic length, average cross-sectional area, mass, area-to-mass ratio (AMR), volume, and bulk density [90].

2.6. SUMMARY

Space situational awareness is comprised of knowledge involving the whereabouts and risk factors of orbital debris and micrometeoroid matter in space domain. The flux of this matter can be clearly assessed through the developments of modeling the MMOD environment using data collected from various assets. Tracking the population density of space debris and micrometeoroids allows for trends to be generated and provides an estimate of what can be expected of the MMOD outlook in the future. A significant contribution toward optimizing this data is credited to the evaluations of destructive breakup events that have occurred within the history of on-orbit space hardware. In order to achieve a greater understanding of these consequential outcomes, it is first necessary to be aware of what materials are frequently used in spacecraft design. A brief summary of these have been included and broken down by relevant categories. Further, results from laboratory experiments developed to imitate in-orbit fragmentation events have been included for consideration.

Chapter 3: Methods to Characterize Space Domain

In order to have a comprehensive understanding of all objects situated in space domain, it is necessary that such articles are characterized to the highest degree possible. This can be achieved through a variety of means and methods. Factors that are of importance to characterization include object size, object shape, and object material. Furthermore, it is necessary to characterize the common spacecraft materials used since these materials ultimately make up the human-made RSO population, though articles pertaining to the natural space environment are of equal importance when working toward SSA. Asteroids and planetary bodies have been evaluated remotely through the means of spectroscopic measurements, and later, reflectance spectroscopy was employed to study human-made material matter, providing an efficacy toward remote characterization.

When discussing the ability to evaluate materials residing in orbit for a given duration, it is necessary to consider the possibility of changes in optical signature for certain objects due to the effects from space plasma, and depending upon which regime of space domain the object is occupying. Subjecting common spacecraft materials to a simulated space weathering environment and measuring their reflectance spectra responses over time delivers vital insight toward which materials are more optically affected by radiation than others.

In addition to reflectance spectra serving as a means for RSO characterization, the performance of remote observations using photometry and select astronomical filter systems can be utilized for object evaluation. The various astronomical filter bandpasses involved in each measuring system can help determine material brightness, and such magnitude can be used to calculate a color index, serving as a means to assign certain objects with for evaluation with respect to one another. These bandpasses can also serve as a guideline for deducing material brightness from reflectance spectra.

Since it is well understood that spectral measurements can provide valuable information for a given object, it is therefore advantageous to house such data within spectral libraries. There are popular public spectral databases that manage this, and their status and contributions toward the SSA community are of worthy discussion. The potential that spectral libraries have to generate and improve the current information they provide is something that should be considered for characterization applications and material references in the future.

3.1. Typical SSA Measurement Methods

The characterization techniques employed to track and identify resident space objects include *in situ* analysis, radar systems, and optical measurements. Each of these methods harness different strengths and weaknesses that make them suitable for characterizing orbital debris in various aspects. The numerous advantages they serve for SSA assessment are well defined and confirmed, and continue to provide vital pieces of information to support space safety and aid hazard mitigation.

3.1.1. Measurements *In Situ* or on Returned Surfaces

In situ measurements are most beneficial in delivering data on space debris of sizes within the extremely small-scale range. This largely includes measurements that were acquired by returned surfaces from long duration space missions or inspection of articles performed while in flight. *In situ* data collected is significant in delivering assessment to inform models that provide information for SSA purposes.

One of the main providers of characterization for orbital debris of minuscule range currently inhabiting space domain is the Hubble Space Telescope. The 11,000 kg NASA telescope with a primary mirror 2.4 meters in diameter was delivered from the Space Shuttle into orbit during April 1990 [99]. Since then, it has undergone multiple servicing missions throughout its lifetime

to support the continued deliver of quality scientific observations from the telescope. However, during several of these servicing tasks, examination of the HST surface led to the discovery of multiple MMOD impact indentations.

Residing in LEO above Earth's atmosphere, Hubble has been exposed to a space environment where orbital debris is most dominant. About 97% of Hubble's surface area was surveyed using imagery as part of the telescope's second servicing mission in 1997 [100]. This allowed for visual inspection of the telescope's exterior to provide an estimate of MMOD flux. Through the image examination (Figure 3.1), it was revealed that HST was subject to 788 potential impacts, and though the largest of these impacts measured 4.7 cm in diameter, 80% of impact impressions resulted were of less than 0.8 cm in diameter [100]. This data was then compared to surface impact data retrieved from the first HST service mission. After analyzing an identical selected area on Hubble, an initial ~5 impacts per square meter from the first servicing mission in 1993 augmented to ~20 impacts per square meter for the subsequent service mission 38 months later [100]. Though, it has been noted that the rise in impact evidence between the two servicing missions could have attributed to a degree to improved image quality for the second servicing mission.

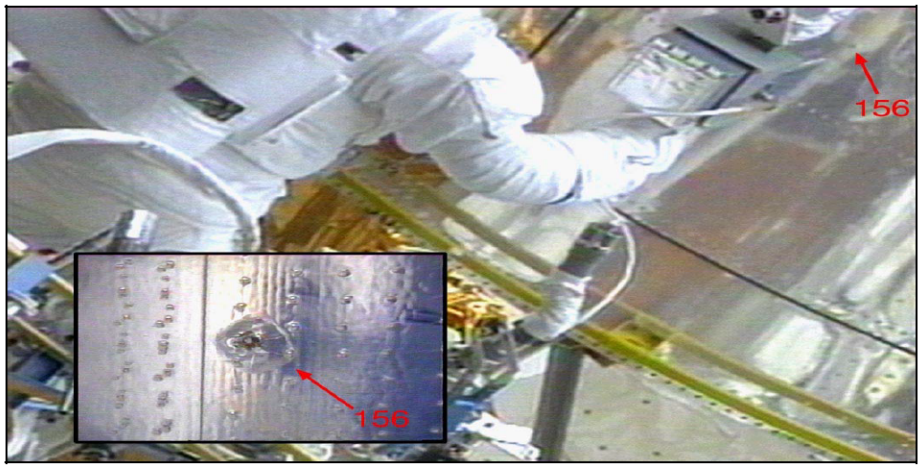

Figure 3.1: Image taken from EVA of MMOD impact on HST V2 Aft Shroud Door [100].

Similar impact characterization analyses have been performed on retrieved solar cells from the Hubble Space Telescope's first service mission. The HST solar arrays span 12 meters in length [99, 101] and, though panel exposure to MMOD was HINDERED from partial shielding of the telescope itself, there were multiple impacts FOUND on the surface of the solar arrays, some of which that could have generated from fragmentations of the HST parent body itself [102]. A result of 171 impacts ranging in size between 1-3500 μm were discovered on the 77 solar cells that were observed [103]. Employing a scanning electron microscope (SEM) and energy dispersive X-ray spectroscopy (EDS), the chemistry of impact residue resulted in a dominating quantity of Al+O from solid rocket motor debris, however, traces of Zn, S, Cl and C were also detected and associated with thermal protective paint which is composed of these elements [103].

A returned Pressurized Mating Adapter #2 (PMA-2) cover also provided *in-situ* insight pertaining to the MMOD setting. The ballistic fabric containing beta cloth PMA-2 cover was oriented on the front of the ISS to protect a docking port in mid-2013, and the article was removed early 2015 and returned on May 2015 [104]. Upon its recovery, analysis provided a resulting 26 number of impact sites on the material. Like studies performed on the HST solar cells, using EDS revealed that a majority of elemental residual detected at the impact sites, such as Fe, Ni, and Ti, suggest to be evident of high-density orbital debris [104].

As previously mentioned in Section 2.3.2 MASTER, the Space Transport System vehicle was subject to debris impact [27]. These reported impacts provided insight regarding the sub-millimeter size range of orbital debris *in-situ*. The impact sizes on the STS windows fell between 10 μm – 300 μm, whereas the impacts on the space vehicle's radiator resulted in 300 μm – 1 mm in size [27].

Similarly, as aforementioned in Section 2.2.1 Orbital Debris, the Long Duration Exposure Facility provided a plethora amount of *in-situ* orbital debris information regarding not only an estimate of debris flux via number of impacts [20], but also a description of debris chemistry. SEM and EDS were employed to analyze the impact crater surfaces discovered on the 6061-T6 aluminum LDEF tray clamps. The residual chemistry on some of these craters revealed elements such as Si, Ca, K, Fe, S, and Mg, which can be correlated to micrometeoroid composition [105].

Additional observations were performed on the LDEF witness plates composed of high-purity gold and commercial aluminum using analogous techniques to determine impact residue on these surfaces. Some impact craters contained residue largely representative of aluminum only, suggesting impact from artificial material particles [106]. Additionally, some impact sites contained evidence rich in Ti and Zn content, which are elements within thermal protective paints for spacecraft surfaces [106]. Deposits of Fe-Ni-Cr content observed on some impact craters, indicate impact from a stainless steel projectile, and surface impact sites with remnants rich in Ag and Cu correlate to electronic component materials. Traces of only Fe-Ni rich remnants deposited on other crater sites suggest impact from monomineralic projectiles like troilite, which is a constituent typical of meteorites [106]. Throughout this analysis, it was found that impact particle sizes greater than 5 μm were associated with natural material, and artificial material residue contributed to 30% of impact craters discovered on the gold surfaces [106].

3.1.2. Radar

In addition to utilizing *in-situ* observation methods to gain an understanding of the MMOD environment qualitatively in terms of chemistry, radar systems have been employed for characterizing these articles in a similar respect. The Goldstone Orbital Debris Radar (Goldstone), located in the Mojave Desert, is a radar system that has provided orbital debris data since the early

90's and has undergone several modifications over time to enhance its ability to evaluate objects in LEO within the sub-centimeter size range. The Haystack Auxiliary Radar (HAX) and the upgraded HUSIR sensor, formerly known as Haystack, both located in Massachusetts have likewise supported orbital debris environment models through the characterization of small debris in LEO via radar measurements.

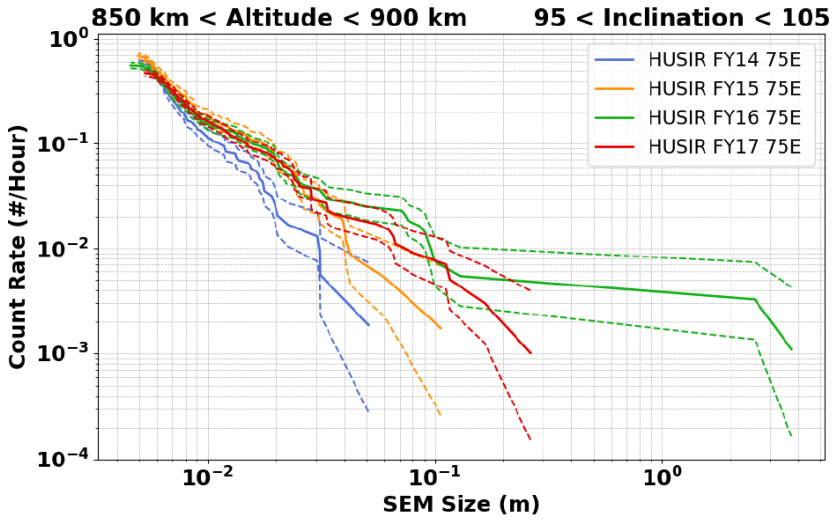

Figure 3.2: Illustration of debris size distribution pertaining to NOAA-16 and USA 109 breakup events [107].

To strengthen SSA and validate orbital debris models, the HUSIR sensor has been operated to collect observations for several hundreds of hours each year and has delivered a value of detections in the thousands per year [107]. After undergoing several upgrades to improve its service, one of which included the addition of a W-band transmitter and receiver (frequency of 92-100 GHz, 3 mm wavelength [108]), this radar can detect an object located at an altitude up to 1000 km that is as small as 5 mm in diameter [107]. HUSIR acquires its data by gathering detections of orbital debris as it passes through its fixed beam. This has provided information regarding, for example, debris size distribution between the years FY14-FY17. An increase in the number of

debris within their respective size range between FY14-FY15 and FY15-FY16, are associated with specific breakup events as seen in Figure 3.2 [107].

Though HUSIR reaches detection down to 5 mm at 1000 km altitude, Goldstone can be utilized for the detection of even smaller objects. The Goldstone radar has delivered useful data with the ability to identify an ~3mm diameter object at an altitude of 1,000 km due to its sensitivity [35]. It is considered an X-band radar with a transmitter frequency parameter of 8.56 GHz [109]. It has undergone many updates while in service to achieve this functionality and perform at enhanced detection of small objects residing in the LEO environment that other sensors may fall short of doing. For example, a collection of orbital debris located at an altitude beyond 2500 km (Figure 3.3) which is likely to be fragments associated with Project Westford [35] have been identified by Goldstone at a higher caliber than what HUSIR would have been able to accomplish.

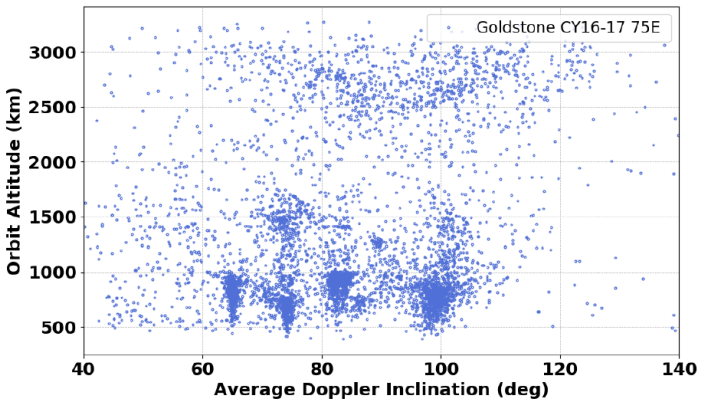

Figure 3.3: Debris data provided from Goldstone illustrated by altitude versus average Doppler inclination [35].

3.1.3. Optical

Additional techniques used for understanding the debris environment are applied through the use of telescopes to deliver optical measurements obtained from inspecting space domain. The Eugene Stansbery Meter Class Autonomous Telescope (ES-MCAT), otherwise known as MCAT,

and the Michigan Orbital DEbris Survey Telescope (MODEST) are two high-fidelity optical sensors that have the functionality to provide such orbital debris data.

MODEST has performed as a productive optical asset for observing orbital debris. The 0.6-m telescope, located in Chile, is used to monitor and assess the GEO space domain by observing any object illuminated by the sun and passing within its field of view [110]. MODEST operates with an exposure time of 5 seconds and 37.9 seconds between exposures [23]. Objects identified are categorized at correlated (CT) or uncorrelated targets (UCT), depending on their availability in the public catalog [23], and contributes orbital element data for such objects [111]. Further, these objects are discernible using astronomical filters to determine brightness. The magnitude of CT and UCT objects observed in GEO between 2007-2010 using MODEST and the R Sloan filter passband is outlined in Figure 3.4b. The R passband in the Sloan Digital Sky Survey set of astronomical filters reads the magnitude of an article viewed by an optical asset between 558-682 nm [112] and serves as a means to assess object brightness. The main objective of data presented in Figure 3.4b is to assess the number of objects fainter than 20 magnitude in GEO that can be detected.

a) 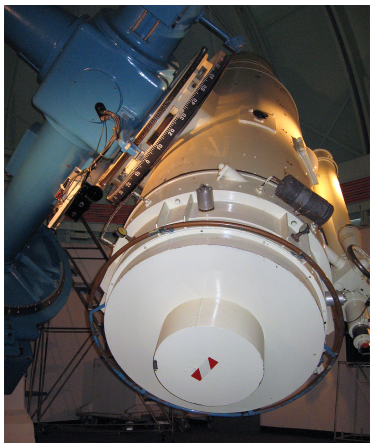

b) 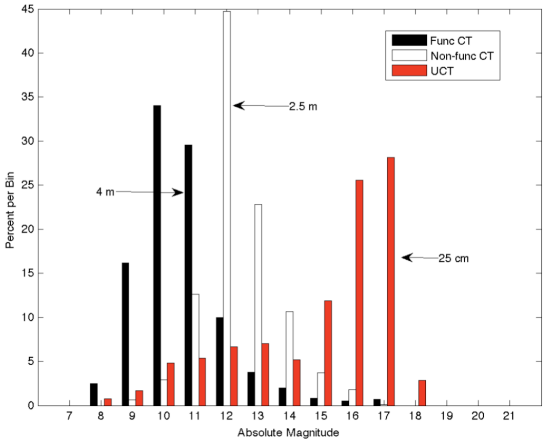

Figure 3.4: a) Image of the *MODEST* (credit NASA ODPO) [113] and b) graph of GEO objects and their R magnitudes collected by MODEST [114].

a)  b) 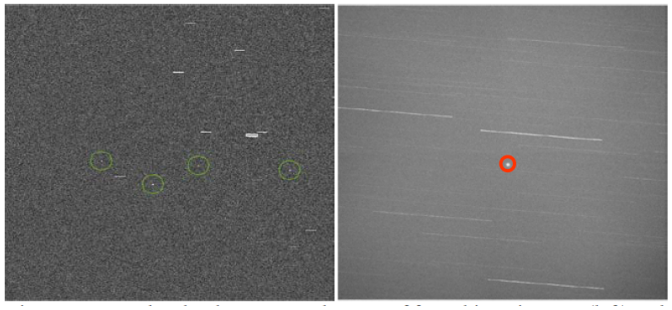

Figure 3.5: a) Image of the MCAT telescope [113]and b) image examples captured by MCAT for objects in GEO (left) and LEO (right) [115].

MCAT has been in operation starting June 2015 [116] and has produced a wealth of knowledge pertaining to SSA since then. The grand detector (Figure 3.5a) is located on Ascension Island, which allows for acceptable surveillance of LEO, GEO and GTO while also providing observations of a region not observed by other optical systems in the US [116]. MCAT is a 1.3-m telescope coupled with a 7-m ObservaDome for optimal measurement acquisition [116]. An example of images taken using MCAT of objects in GEO and LEO are presented in Figure 3.5b.

3.1.4. Space Surveillance Network

It is imperative to note that one of the most beneficial resources for SSA is through use of the Space Surveillance Network (SSN). The SSN, as previously mentioned in Chapter 2, is operated by DoD agencies and was initially assembled following the launch of Sputnik 1in the late 1950's [117]. The network utilizes a variety of both optical and radar sensors to detect, monitor, and catalog all artificial objects populated near-Earth orbital regimes.

The sensors involved, which together can perform 100,000 satellite observations within a day, are divided into three categories which include dedicated, collateral, and contributing sensors [118]. Dedicated and collateral sensors similarly pertain to a US Strategic Command controlled sensor, with dedicated sensors being of primary space surveillance activity and collateral sensors referring to activities other than space surveillance. Contributing sensors refer to those that are not

operated by DoD agencies but their collected data still serve data to SSN efforts upon request. With these combined assets exploited for use, the SSN therefore provides a quality comprehensive evaluation of resident space objects for SSA purposes.

3.2. Spectral Measurements History

In addition to the SSA characterization methods described in Section 2.1 Typical SSA Measurement Methods, a technique known as reflectance spectroscopy has proven useful in characterizing objects inhabiting space domain. Spectral measurements acquired from an RSO's reflectance response via illumination from the sun can be used to study the brightness of that object and further allow the possibility of deriving photometric data which can yield information regarding surface material. This has been seen when assessing planetary, asteroid, and orbital debris; the main sources of hazardous material that inhabit our near-Earth space realm.

Reflectance spectroscopy involves the measurement of illumination that is being reflected off a material surface. The spectra obtained can be read at various wavelengths to contribute particular knowledge of the object being measured. Reflectance data acquired within the visible region of the spectrum can provide information regarding physical properties, such as color, of the analyzed material, whereas spectral results obtained within the infrared delivers insight regarding material chemistry. This material information is deduced by analyzing the absorption features provided within the spectral measurement data plot acquired for a given material and can therefore be used for sample characterization. Further, the slope and characteristics of reflectance spectra can be affected by sample rotation, allowing for evaluation of bidirectional reflectance distribution function (BRDF) to be analyzed and used to suggest even more abundant information regarding albedo and material characterization.

3.2.1. Planetary

Spectral measurements have often been conducted to help analyze planetary bodies to study their terrain and determine composition. Enstatite is a mineral found on the surface of Mercury, or comets and asteroids that are also rich in this mineral, and has been studied by [119] using reflectance spectra to compare two synthetic polymorphs of enstatite. The two polymorphs of the mineral studied (clinoenstatite and orthoenstatite) form differently depending on thermal conditions and have different crystal structures [119]. They are low in Fe content but rich in SiO_2 and MgO, and though this chemical makeup made them difficult to discriminate between 0.4-0.9 μm in their spectra, there are features associated with the Reststrahlen bands at ~10 μm in MIR which make clinoenstatite and orthoenstatite different from one another [119]. The spectral results from this study have been used to clarify conditions regarding the surface of Mercury.

Spectroscopic techniques have also been utilized to study the Moon, Mars, Mercury, and others. where extraterrestrial volcanism has occurred to gain information regarding their geology [120]. To do this, glasses were characterized to serve as analysis of amorphous material forming from volcanic rock (Figure 3.6). Spectra were acquired on glass compositions with a focus on SiO_2 and alkali content fluctuation [120]. Since the Mercury Planetary Orbiter (MPO) spacecraft, developed from the BepiColombo mission between ESA and the Japanese Aerospace Exploration Agency (JAXA), was equipped with the MErcury Radiometer and Thermal Infrared Spectrometer (MERTIS) [121], the spectra for synthesized glasses studied by [120] were acquired within the infrared (IR) region between 7-16 μm. From these results, many conclusions were drawn such as a relationship between the shift in spectra at shorter wavelengths and increasing SiO_2 content, and features in the reflectance signature evident of the Christiansen effect [122, 123].

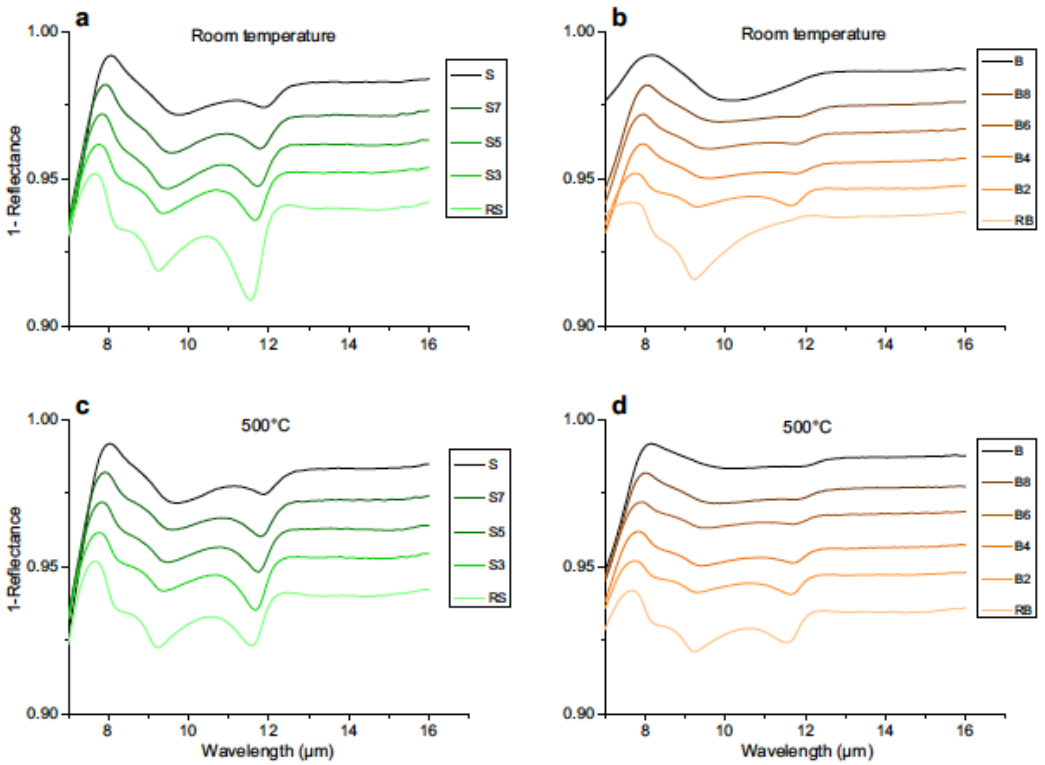

Figure 3.6: Reflectance signatures for volcano (green) and snake river (orange) glasses at room temp and 500°C [120].

Additionally, emission spectroscopy has been used by [124, 125, 126, 127] to extensively study Mars and Mercury planetary terrain. The motivation for this work is driven by providing a spectral library of emissivity measurements on planetary-like minerals and soils to help decipher the remote sensing spectral data delivered by MERTIS and by the Planetary Fourier Spectrometer (PFS) as part of the Mars Express Mission [125]. An example of this spectral data housed in the Berlin emissivity database (BED) is shown in Figure 3.7 to distinguish several subclasses of silicate by comparing the shape and position of absorption features within each respective mineral's spectra [126].

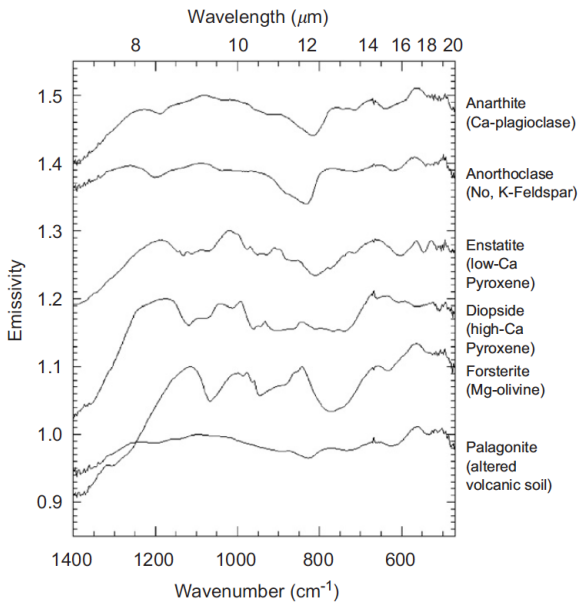

Figure 3.7: Emissivity spectra of various mineral classes [126].

3.2.2. Asteroids

Spectral reflectance has further assisted compositional examination of carbonaceous chondrites (CC's) to assess the physical properties of meteorites or asteroids and interpret their transformations. A study performed by [128] involved the spectral analysis of various packed powders representative of the Murchison meteorite. Their measurements were taken with an Analytical Spectral Device (ASD) FieldSpec Pro [129] spectrometer to acquire reflectance from 350-2500 nm. This delivered spectral results that resulted with the most densely-packed Murchison powder sample exhibiting reflectance higher in magnitude from other samples while all powder-packed variants illustrated similar absorption bands [128].

Near-infrared (NIR) spectral measurements taken on Ryugu were presented by [130] to provide observations of the asteroid's surface. A Near Infrared Spectrometer (NIRS3) aboard the Hayabusa2 spacecraft developed by JAXA was employed to deliver the reflectance signature of Ryugu's topography. When compared with one another, Ryugu differs in spectra from other

meteorite samples within the visible (VIS) region, but shares a similar absorption feature to Ivunu and MET meteorites at 2720 nm in the IR [130].

Organic compounds found on the surfaces of asteroids and comets were explored by [131] through their measurements taken in the laboratory setting on cometary-like product and under similar *in situ* conditions including high vacuum and low temperature. Motivation for this is driven by analysis captured by the Visible and InfraRed Thermal Imaging Spectrometer Mapping Channel (VIRTIS-M) that the Rosetta spacecraft is supplied with, which examined comet 67P/Churyumov-Gerasimenko [132]. Different ammonium salts were measured spectroscopically and produced absorption features agreeable with those exhibited by the comet at 3.1 µm and 3.2 µm (Figure 3.8). The method of reflectance spectroscopy has therefore been worthy of generating compositional information that can be used to study extraterrestrial terrain.

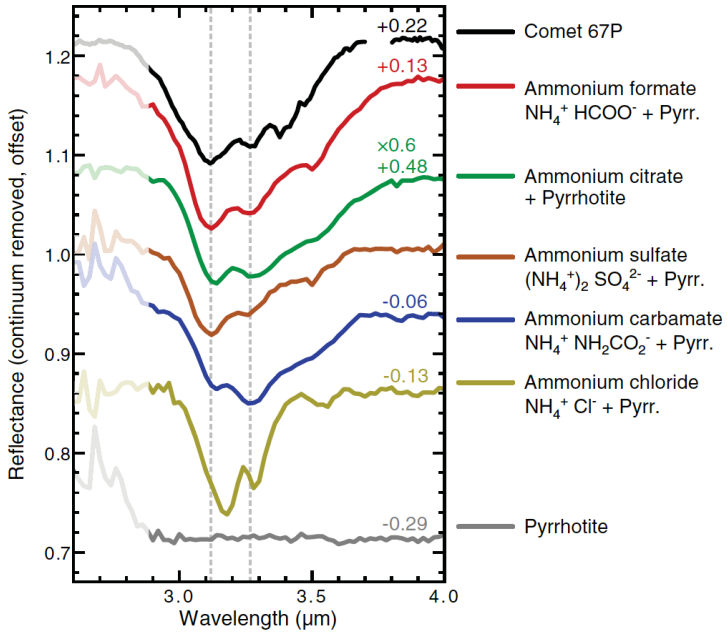

Figure 3.8: Reflectance signatures for various ammonium salts [131].

3.2.3. Rocket Bodies, Spacecraft, and Orbital Debris

In addition to extraterrestrial substances, reflective spectra have served equal purpose of deducing properties of artificial materials in space domain. This has been studied by [5, 133, 134, 135, 136, 137, 138] to name a few. The reflectance signatures for six different artificial space objects within or near GEO were investigated using a Low Dispersion Survey Spectrograph 3 (LDSS3) on a Magellan telescope in Chile [133]. The spectra for these articles resulted in similar slope trends that could still be distinguished from one another regarding magnitude [133]. It was then intended to compare this with laboratory-based measurements of several common spacecraft materials, including aluminum, solar cell, black and white paint, and MLI, which culminated in recognizable spectral features when normalized to compare with telescopic data properly [133].

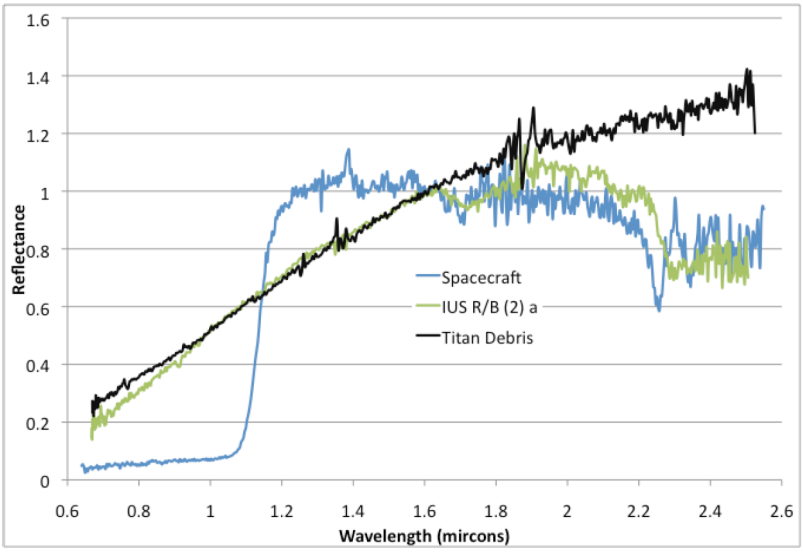

Figure 3.9: Reflectance spectra compared between spacecraft, rocket body, and orbital debris articles [135].

Additionally, [138] attempted to correlate the spectral signatures observed between rocket bodies and satellites, where it was revealed that all materials exhibited the same feature at 850 nm indicating aluminum, as well as similar trends in slope, however the reflectance behavior in the blue wavelength passband in VIS could be used to distinguish each object investigated. In a

separate study by [135], reflectivity was compared between spacecraft, rocket body, and orbital debris articles (Figure 3.9). Using a near-infrared spectrograph (SpeX) [139], the spectral results presented contrast between these objects. The debris objects observed from the Titan IIIC Transtage breakup produced a reflectance response similar to what was seen in reflectance from the inertial upper stage (IUS) rocket body within the 700-1600 nm wavelength range [135]. Beyond 1600 nm, the reflectance from the orbital debris continues to increase while the spectra from the IUS plateaus and further exhibits an absorption feature at ~2300 nm. This absorption is also demonstrated in the reflectivity of the spacecraft though the minima is shifted slightly from that of rocket body's. These absorption characteristics are due to C-H bonds which were likely present in the white paint of the IUS rocket body and in the substrate of the solar cell on the spacecraft [135]. These feature differences are key elements toward of the possibility of separating materials into different categories per their spectral reflectance.

Another work performed by [136] investigated the reflectance spectra for geostationary spacecraft Galaxy 11 using observations from a 1.6-m telescope armed with a spectrograph. Of the 265 measurements collected, 13 normalized spectra were analyzed, including a reference spectra, and while 3 of these reflectance spectra taken on the article were closely akin to that of the reference measurement, the other 9 were not. However, these 9 were similar in features to one another beyond 600 nm in wavelength, yet not below this value. This analysis approach helped assess the spacecraft spectra in comparison with that of the reference, but was limited in providing material spectral features.

Spectroscopic observations of 5 different satellites in GEO were studied using the 1.0-m ESA Space Debris Telescope (ESASDT) and compared to laboratory-based measurements by [137]. The reflectance for one of these satellites, known as Artemis, was a mixed product of its

solar cell panels serving as a winged-like structure in reference to the box-like main body of the satellite. Though the article was measured spectroscopically at 17° and 52° phase angles, it was seen that the reflectance response was similar for each of these orientations (Figure 3.10a), suggesting that the hardware's signature is dominated by the solar panel material surrounding the central body of the satellite.

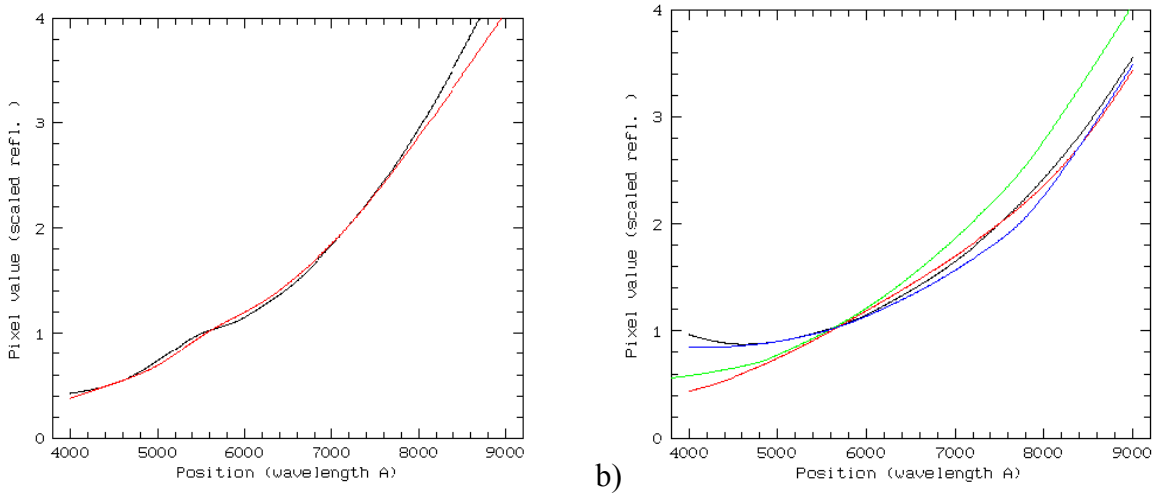

Figure 3.10: (a) spectra of Artemis satellite at 17° (black) and 52° (red) phase angles, and (b) spectra of S92005 GTO debris measured on multiple nights [137].

A debris object (S92005) in GEO was also observed spectroscopically on multiple nights (Figure 3.10b) and resulted in similar reflectance response to that of each other. This validates the reproducibility of such measurement acquisition and suggests that the surface material of such debris is not dependent on phase angle or attitude [137]. It can be additionally noted that the spectral data exhibits an increase in reflectance magnitude between 600-900 nm which can be attributed the 'reddening' phenomenon that has been seen on surface materials of spacecraft after long duration in flight [137, 140].

3.3. Space Weathering

If reflectance spectroscopy can serve as a primary measurement technique toward gaining an understanding of remote object materials, then evaluating how materials optically change *in*

situ is critical to this field of research. Much experimentation has been performed by [12, 82, 88, 141, 142, 143] where the optical behavior of commonly used spacecraft materials exhibit alterations after being exposed to a space simulated environment. It is significant that these changes are noted depending on material type and orbit altitude.

3.3.1. Plasma and the Space Environment

Resident space objects located at various altitudes in orbit are surrounded by a plasma environment composed of photon, ion, and electron constituents in vacuum conditions [88]. Articles in LEO are subjected to atomic oxygen, ultraviolet radiation, and thermal cycling [144, 145] whereas objects in GEO interact with atomic hydrogen ions and electrons [12].

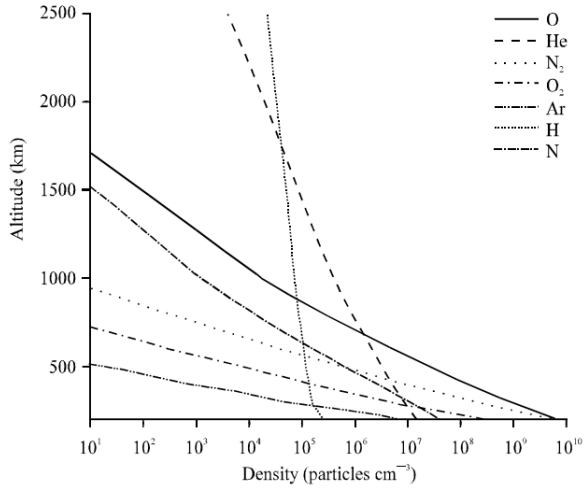

Figure 3.11: Representation for density of atomic species in LEO as a function of altitude for a year during mean solar activity [146].

The effect of atomic oxygen on spacecraft is substantial and of concern when considering space design. A spacecraft orbiting at a velocity of 7.8 km/s in LEO can experience an AO stream of ~5 eV [146]. This energy is responsible for the alterations of several material properties, one of them being optical. Further, the production of atomic oxygen is influenced by UV radiation impinging upon LEO's atmosphere [147]. An overview of the atomic species present within LEO

in terms of density with respect to altitude during mean solar activity for one year is illustrated in Figure 3.11. AO is known to be the most abundant species in LEO, making up 90% of the atmosphere at 500 km [148]. Since much spacecraft activity takes place within LEO, it is significant to understand how human-made materials are affected by this constituent. A comprehensive review on various spacecraft materials exposed to AO fluence can be found in [149].

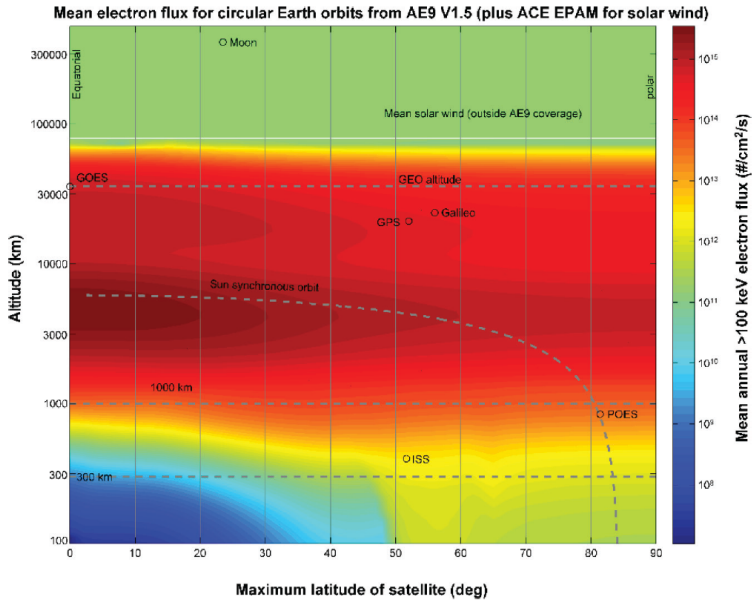

Figure 3.12: Illustration of electron flux intensities at various altitudes and orbits (dotted lines) [12].

While the prominent damaging species in LEO is atomic oxygen [150, 151], the harmful element in GEO pertains to the energy deposition caused by electrons [12, 141, 143, 39]. The highly energetic electrons in GEO are therefore responsible for material degradation over time. Electrons in GEO harness energies ranging from hundreds of eV to MeV [152]. These subatomic particles can either penetrate through a material surface and deposit that charge within it, causing arcing events, or the energy will penetrate through the material completely while releasing energy into the material upon deceleration [88]. Though metals remain unchanged upon irradiation,

surface oxides and adsorbates can be affected and cause variance in material reflective response [88]. Polymeric materials are affected to a greater degree due to the interactions between these charged particles and organic material chemistry.

Highly energetic electrons that are present in space plasma can modify polymers by causing the breakage of molecular bonds and promote the formation of radicals [12]. These radicals can then either form new bonds to lead to new material physical properties, or can create bonds that are equal to those present in the initial material and promote material recovery. The influences that a polymeric material can face due to irradiation by electrons include the alteration of said material's optical reflectance signature.

3.3.2. Space Weathering Experiments of Common Spacecraft Materials

The optical reflectance signature for commonly used spacecraft materials have been well studied via laboratory experimentation involving a GEO simulated environment. The measurements presented in Sections 3.3.2.1 MLI Components-3.3.2.3 White Thermal Control Paints were acquired at the Spacecraft Charging and Instrumentation Calibration Laboratory (SCICL) at Kirtland Air Force Base in New Mexico, USA. Materials of interest were housed in a chamber and subjected to the GEO simulated environment using high energy (~100 keV) electron radiation provided from a Kimball Physics EG8105-UD electron gun. Vacuum levels of $<10^{-6}$ Torr were reached within the chamber using turbo, mechanical, and cryogenic pumps. Electron flux was measured continuously using a Faraday cup to calculate electron dose.

Reflectance spectra were measured with a spectroradiometer coupled with an integrating sphere to provide a directional hemispherical reflectance (DHR) for materials of interest. The raw data delivered from the spectrometer was transformed to absolute reflectance appropriately [142] and an overview of the detailed procedure for measurement acquisition can be also found in [142].

3.3.2.1. MLI Components

The individual material layers used to comprise multi-layered insulation (MLI), an attractive space material, were dissected and spectroscopically studied by [142]. A total of five of these layers were analyzed, including space-facing aluminized Kapton® (front & back), spacecraft-facing aluminized Kapton® (front & back), and aluminized Mylar. Both aluminized Kapton® material samples that had their Kapton® side measured, be it spacecraft-facing (Figure 3.13a) or space-facing (Figure 3.13b), exhibited stark differences in their initial reflectance signature. This was likely caused by the grid-like netting that was present on spacecraft-facing aluminized Kapton® which affected the material's overall reflective response. Figure 3.13c represents, again, the space-facing Kapton® side of aluminized Kapton®, and was similar to the material measured in Figure 3.13b, resulting in nearly equal reflectance results as expected. Kapton® polyimide is orange in color and therefore exhibits an increase in reflection at approximately 550-600 nm.

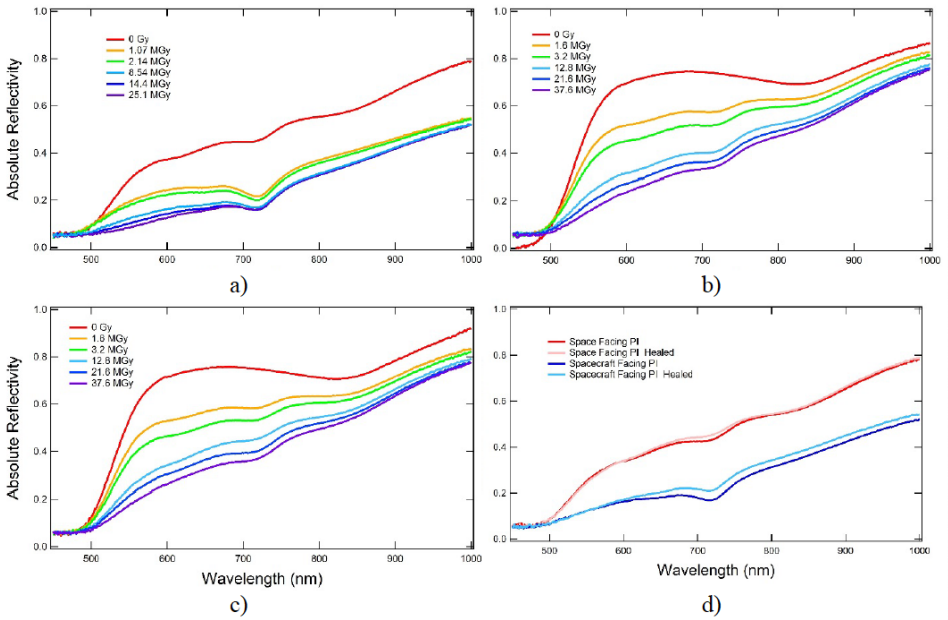

Figure 3.13: Reflectance spectra for a) spacecraft facing polyimide, b) space facing polyimide #1, c) space facing polyimide #2, and d) comparison between space facing and spacecraft facing polyimide before and after 65 hours of healing in vacuum [142].

As seen in Figure 3.13c, the various Kapton® materials measured experienced a decrease in absolute reflectance as the electron dose increased over time. This suggests absorbance changes within the material as well as chemical damage caused by the irradiation from high energy electrons [142]. It is further significant to note that this decreased reflectance response is present within the visible region of the spectrum which is the medium exploited by telescope observations. Additionally, when the space- and spacecraft-facing Kapton® materials were allowed to sit in vacuum for 65 hours after electron bombardment ceased, the polyimides optically exhibited a degree of recovery evident by the increase in reflectance (Figure 3.13d). The aluminum side of the aluminized Mylar sample included in the study did not result in absolute reflectance changes optically after having been subjected to electron bombardment, which was expected since the metallic surface was not effected chemically, however it was seen that the material experienced some level of degradation due to embrittlement [142].

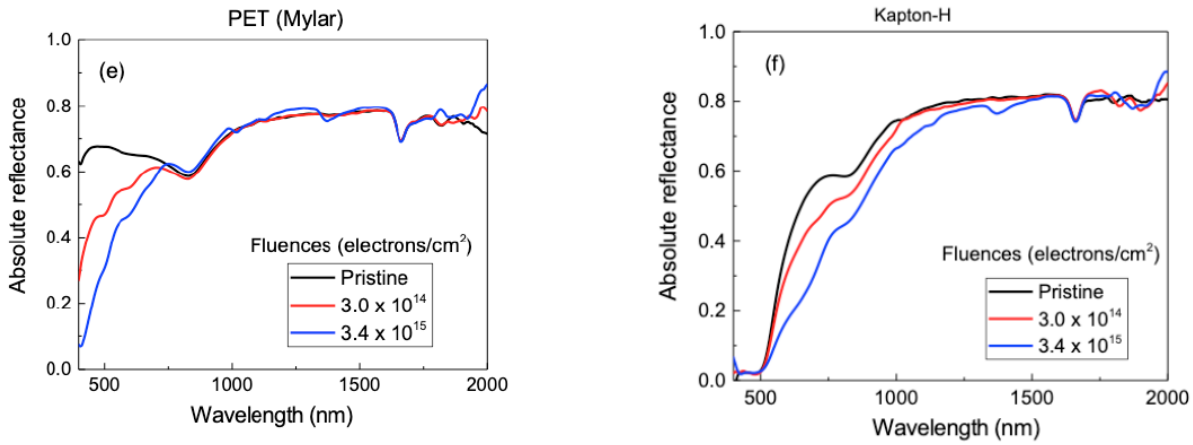

Figure 3.14: Reflectance spectra for a) Mylar and b) Kapton® in pristine and irradiated conditions [82].

In a similar study by [82], Kapton® and Mylar were exposed to a comparable high energy electron bombardment environment as that seen in [142] and yielded equally interesting results

(Figure 3.14). The Mylar sample observed resulted in reflectance that was severely reduced within the 400-800 nm wavelength range (Figure 3.14a). The nearly constant reflectance value seen post radiation for Mylar beyond 700 nm has been observed previously [153] and could be attributed to aromatic ring modification from di-substituted to mono-substituted benzene groups [154]. Increased absorption of Mylar between 400-800 nm may be due to condensation of these aromatic rings into compact carbonaceous clusters [82].

The Kapton® sample examined demonstrated evident decrease in absolute reflectance upon exposure to high energy electrons (Figure 3.14b). At 730 nm, the irradiated polyimide film yielded an absolute reflectance value a factor of ~3 lower when compared to the pristine sample. Electrons that penetrate deeply within the material can cause pervasive chemical damage to the polyimide and lead to an observed darkening of the Kapton® film within the visible region of the spectrum. The apparent reduction in reflectance at ~730 nm is caused by shrinking of the "band gap" to ~1.8 eV in the irradiated polyimide due to radiation-induced trap state presence [82].

3.3.2.2. Coverglasses

Three different types of coverglasses were also irradiated via exposure to high energy (90 keV) electron bombardment to observe material properties in a GEO simulated environment [143]. Coverglasses are a material of interest commonly used in space and military applications due to their wide use of being incorporated in solar cell structure. Though the optical properties for these coverglasses were not drastically altered upon electron irradiation, they were still worthy of analysis.

The fused silica glass, composed of SiO_2, resulted in a reflectance signature that remained stable and relatively unchanged throughout the space weathered simulation process (Figure 3.15a). Corning 0214, a borosilicate glass doped with <5% CeO_2 [143], exhibited an overall decrease in

reflectance from 500-1750 nm after having been irradiated by high energy electrons (Figure 3.15b). Adversely, the CMX coverglass, a borosilicate glass having a more complex chemistry [143], yielded results that demonstrated an increase in reflection within the same 500-1750 nm wavelength range (Figure 3.15c) after undergoing irradiation at a maximum fluence of $1.3x10^{15}$ e/cm^2.

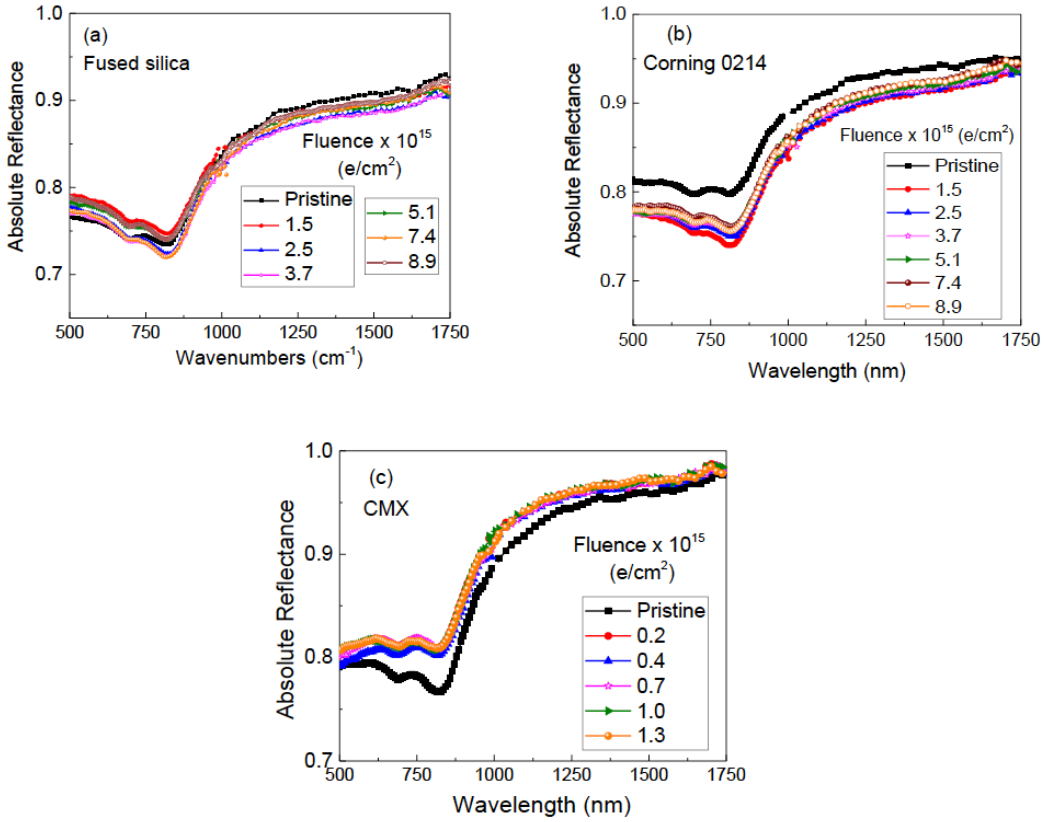

Figure 3.15: Reflectance signatures for a) fused silica, b) Corning 0214, and c) CMX coverglasses in their pristine and electron irradiated conditions [143].

3.3.2.3. White Thermal Control Paints

The use of high energy electron bombardment to produce a GEO simulated environment was also employed by [141] to study the optical behavior of various white thermal control paints. The eight paints examined, all provided by the same manufacturer, are used commonly on surfaces

of spacecraft. Detailed results describing the optical behavior of these paints after exposure to high energy electrons can be found in [141].

Overall, the AZ-3700 grade white paint was one amongst all paint samples to exhibit optical stability with no changes in reflectivity after electron irradiation (Figure 3.16). All other white paints were optically affected, resulting in evident decrease in reflection post electron induced radiation. It can be further noted that prominent absorption features appear in the irradiated spectrum for AZ-2100, AZ-93, AZW-LAII, and AZ-400, while the appearance of minor broad absorption features appear in AZ-2170 and AZ-2000 in the VIS region that were initially absent in these materials' pristine reflectance measurement. The arisen absorption features in the AZ-2100, AZ-93, and AZW-LAII paint specimen can be seen between 500-700 nm. While these samples resulted in one new absorption feature, the AZ-400 paint specimen resulted in two new absorption features, the first centered at ~550 nm and the second present at 850 nm. It can also be noted that the AZJ4020 paint sample had an absorption feature at ~1700 nm in its initial spectra, but this detail was not seen in the irradiated spectra.

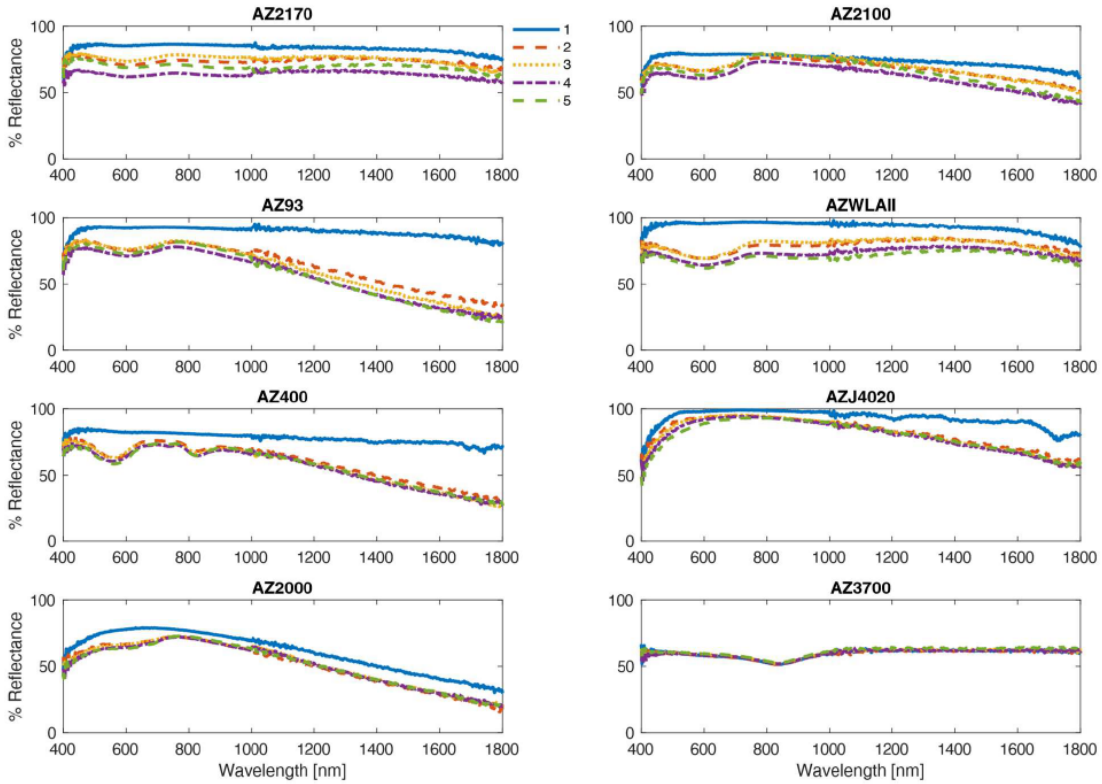

Figure 3.16: Reflectance spectra of various white thermal control paints [141].

These results were confirmed by [82] where AZ-93 and AZ-400 were exposed to 90 keV electron radiation and demonstrated a reduction in reflectance (Figure 3.17) with similar features to those presented in [141]. It was noted that there was not a substantial discoloration in the appearance of the paint samples after having undergone irradiation. This can be associated with the oxygen atoms becoming displaced near the grain surface in the ZnO pigment particles caused by radiation [155].

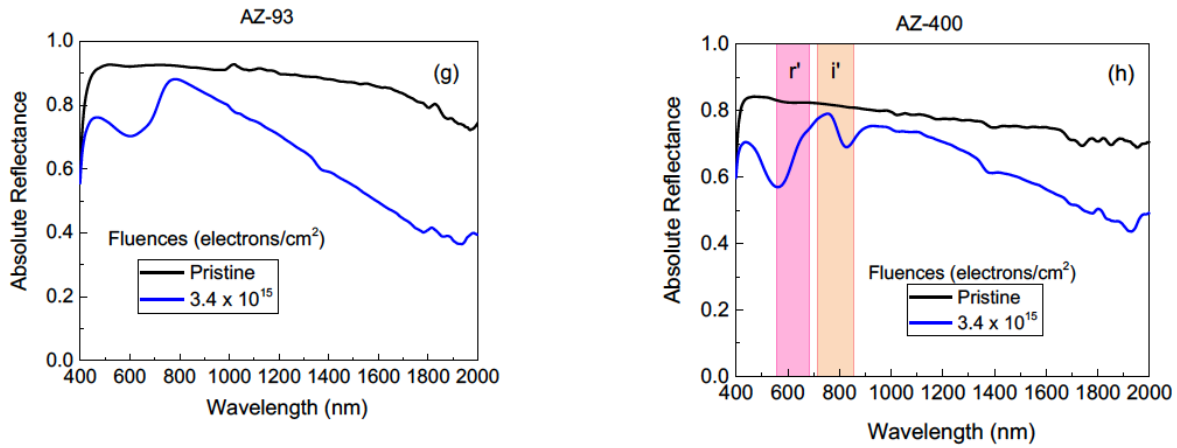

Figure 3.17: Reflectance spectra for AZ-93 and AZ-400 white thermal control paints in their pristine condition and electron exposed condition measured at 3.4 x 10^{15} electrons/cm^2 [82].

3.4. Material Classification via Remote Sensing

To further address the enhancement of SSA, resident space objects have been analyzed using remote sensing techniques that provide some level of material characterization. Remote sensing has been approached in the form of spectral data acquired from telescope instrumentation and has also been compared through similar assessments obtained in the laboratory setting. Not only do spectral measurements fall under the umbrella of remote sensing, but photometric measurements derived from spectra have also proven useful toward material classification. Further, hyperspectral remote sensing is a field of study that factors material spectral signatures into output data and has the potential to characterize RSO's in its own approach. Hyperspectral remote sensing involves object information extraction based on their radiance data obtained from sensors [156]. Particularly, through hyperspectral imagery the high spectral resolution of an unresolved object can be used to deduce material composition from its contribution to the spectra obtained [157].

3.4.1. Remote Sensing using Spectral Data

Material reflectance data has been compared to remote observations in an effort to determine material types. This was performed by [140] where materials from the LDEF measured in the lab were plotted against remote reflectance data of a rocket body after performing necessary corrections to account for atmospheric and instrument response differences. In the obtained results, the signature for a white paint and remotely observed rocket body were apparently similar; both specimen exhibiting absorption at the onset of VIS and a rise in reflectance near 400 nm, typical of white colored surfaces. This feature can be shifted when surface color is affected and becomes optically more yellow due to exposure to the space environment. This was also analyzed using a rocket body launched at a much earlier time for comparison, and described in [140].

Similar ongoing work has been conducted by groups such as [157] where spectro-temporal signatures were generated using simulation models in an effort to understand mixed spectral signatures of objects involved in hyperspectral remote sensing. This approach encompasses assigning material spectra as individual colors which produces a mixed color frame to allow for analysis of those pixels. In doing this, it is aimed to obtain insight regarding material present on unresolved objects for space situational awareness.

The need to improve remote sensing methods for SSA has been undertaken by many. A model to enhance the characterization of debris populating GEO using infrared remote sensing was described by [158]. In this work, the need to reduce uncertainties involved in remote sensing was reiterated. Because optical material measurements are an element of the overall reflectance of an observed surface remotely, the absorption and reflectance characteristics of debris is a large contributor to the uncertainties present in such models [158].

3.4.2. Laboratory-based Data for Remote Sensing

To further aid in validating remote observations, optical measurements collected in the laboratory setting have been prepared. A thorough amount of this work has been conducted by Cowardin [5] who analyzed various space materials using spectral reflectance and color index obtained in the laboratory. This work will be discussed in greater detail in Section 3.4.3.1. Published photometric data for orbital debris with a focus on high area-to-mass (HAMR) articles were compared to laboratory photometric measurements lead by Cowardin [159]. The laboratory setting used to conduct these measurements was designed to mimic a telescope set-up which involves a configuration including an illumination source, target object, and observer. Using a CCD camera for data acquisition, multiple MLI-related samples had their BVRI photometry, an optical measurement technique explained further in Section 3.4.3, analyzed at various orientations. One result of this demonstrated a fragmented solar cell material that exhibited V-R color index values that varied throughout all orientation angles studied (Figure 3.18), and similar results were yielded for an intact solar cell sample. Color index is simply defined as the difference in magnitude (brightness) for an object between two different filter passbands. All samples involved in this work demonstrated variation in color index values for the V-R filter passbands. In doing this, it was found that color index for these samples was dependent upon orientation angle [159].

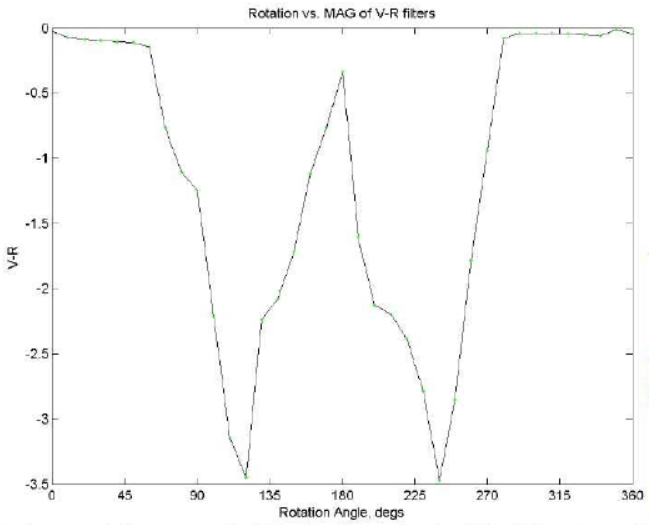

Figure 3.18: Solar cell sample plotted for V-R index at all rotation angles [159].

Laboratory-based measurements have also been thoroughly conducted by Jorgensen [134] with regards to spectral measurements of space article material surfaces with the aim of deducing all absorption/reflectance features present within an acquired material signature. Jorgensen approached material classification aims by separating the full 350-2500 nm wavelength range into three distinct regions and scrutinizing the material absorption features present in those zones. This is possible, for example, due to the chemistry differences between organic and inorganic materials. Additionally, Jorgensen investigated returned material surfaces from the LDEF that were measured in the laboratory after having been recovered.

3.4.3. Photometric Measurements using Color Indices

An optical measurement technique exploited to deduce characteristics of resident space objects involves assigning a color value with targets viewed through a telescope. This is possible when employing a filter possessing a defined wavelength passband to view desired targets. Photometric observations on satellite articles were early studied by [160]. The approach of using color index to characterize spacecraft articles derived from photometric data has been established by Murtazonv, Nosova, Kupriyanov, and Prokof'eva [161] and confirmed by [162, 163, 164]

amongst others. Acquiring color index is an advantageous method in this regard and used for many reasons; some of which involve its ability to perform even in non-ideal observation conditions since it relies less on atmosphere extinction, its associated instrumentation is more affordable, and can be collected in shorter observing time using smaller telescopes due to low resolution spectroscopic measurements [164].

Color index is defined as the difference in magnitude between two different filter passbands. In astronomical photometry, the magnitude refers to the apparent brightness resulting from an object at multiple wavelengths across the electromagnetic spectrum. Color index can therefore be calculated by:

$$f1' - f2' = -2.5 \log_{10}\left(\frac{I_{f1}}{I_{f2}}\right) = -2.5[\log_{10}(I_{f1}) - \log_{10}(I_{f2})]$$

where $f1'$ and $f2'$ represent the two filter passbands employed and I represents brightness which is determined from the sum of the area under a material reflectance curve within the given filter band. This equation has been applied by [165] to study GEO satellites, and by [166] in regards to photometric studies on LEO satellites.

Table 3.1: Comparison between UBVRI and *u'g'r'i'z* filter passband systems.

UBVRI Filter Passbands		**SDSS Filter Passbands**	
Filter	λ Range (nm)	Filter	λ Range (nm)
U	320-410	*u'*	309-400
B	350-600	*g'*	406-544
V	450-700	*r'*	588-682
R	560-1060	*i'*	705-835
I	700-1100	*z'*	839-1094

There are currently a variety of astronomical filters that have been used in conjunction with telescope observations of objects. The filters most commonly used in space applications include the UBVRI broadband system [167] and more recently the *u'g'r'i'z'* system [112]. The UBVRI filter system presented by Johnson [167] was developed to improve the efficiency of previous broadband systems and its performance has proven useful in the characterization of RSO's. This system was advanced in study by Cousins [168] specifically investigating differences in the (V-R) and (R-I) color indices, then introducing the $UBVR_CI_C$ filter system. Further refinement was also performed by Bessell [169] who compared the measurements of cool stars between the VRI filters in both Johnson and Cousins systems.

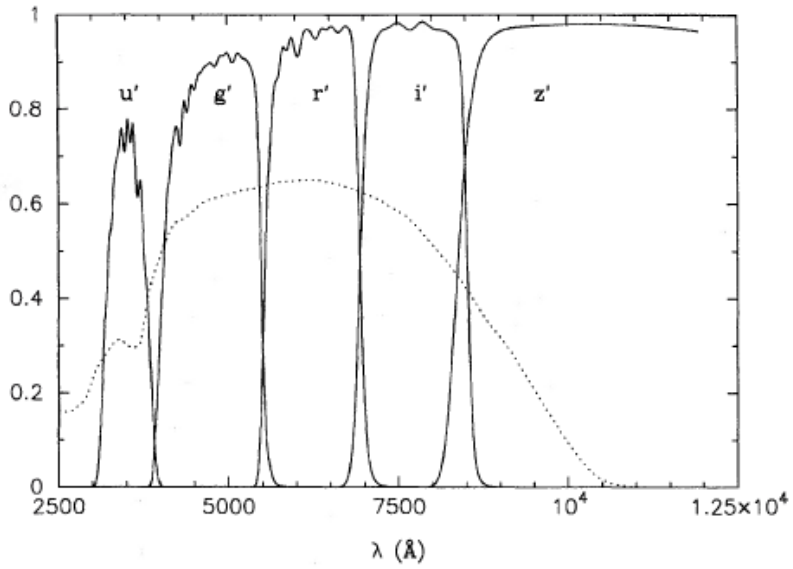

Figure 3.19 Illustration of each *u'g'r'i'z'* filter transmission (solid curves) and quantum efficiency of the CCD detector used in the SDSS system (dotted curve) [112]

Since then, the Sloan Digital Sky Survey (SDSS) has provided for improved photometric data pertaining to Galactic stars to increase intelligence in this regime [170]. The *u'g'r'i'z'* broadband filter system, defined by [112], provided notably wider bandpasses compared to those in the UBVRI Johnson/Cousins broadband system. This, along with other cutting edge features

included in the SDSS photometric system, allows enhanced performance of these filters to detect faint objects, making this a system of great interest to the SSA community.

3.4.3.1. Experiments using the UBVRI photometric system

The UBVRI photometric system has been exploited for use in attempt to aid the characterization of RSO's [5, 164, 165, 171, 172]. Much work has been performed by Payne [165] regarding the proposition of using a new filter set, known as Space Object Identification (SOI) In Living Color (SILC), designed for observing GEO satellites to support DoD efforts. Payne compared the performance of Johnson versus SILC photometry directly when observing the same GEO satellite cluster. Though the Johnson B, V, and I filters provided color data resulting in the apparent grouping of satellite classes, this was more distinguishable when using the proposed SILC photometric system.

Table 3.2: The UKIRT filter passband system [173].

UBVRI Filter Passbands

Filter	λ Range (nm)
Z	836-929
Y	979-1081
J	1169-1328
H	1492-1784
K	2029-2380

Cowardin [5] performed analysis in a laboratory setting on 14 material fragments that corresponded to various material classes and plotted their color indices using the BVRI photometric system. Space fragment materials investigated included multiple MLI components, various solar cells, glass fiber reinforced polymer (GFRP), carbon fiber reinforced polymer (CFRP), and aluminum and circuit board materials. Their B-R versus B-V indices were plotted for

photometric measurements, and this was furthered using spectral measurements in the B-R versus R-I regime. Cowardin furthered the experimentation involved with RSO's regarding area-to-mass ratio and suggested that knowledge of this from an object would aid in correlating remote and laboratory data. In addition, the light curves for these materials were also examined to determine color characteristics associated with sample shape for providing a more physical-based representation of objects.

In a study by Lederer [172], a total of 18 satellites involved in the Initial Defense Communications Satellite Program residing in GEO were remotely observed and had their photometric data collected using the Johnson/Kron-Cousins filters. It was then of interest to study a handful of selected spacecraft materials in the laboratory using Johnson/Bessell BVRI filters for comparison. It was discussed that the three different solar cells present difficulty in distinguishing them using only the visible region of the spectrum due to the colors and shape of these photovoltaics without further knowledge regarding composition. Photometric data based on associated RSO's with color data has served as a means to possibly characterize artificial materials residing in near-Earth orbit. This has also been conducted by [171] and [164] with the approach of characterizing orbital debris in GEO.

3.4.3.2. The ZYJKH Bandpasses

While [171] employed the use of the standard Johnson BVRI filter system to plot the assortment of debris observed successfully, [164] used the IR regime to understand the measurements for satellites and rocket bodies. Photometric data for the Galaxy 18 satellite and SL-12 rocket body were presented by Pearce, specifically using Z, Y, J, K, and H filters in the IR. What makes these passbands useful are their ability to provide information characteristic of articles

largely comprised of solar panels. This knowledge can therefore be applied to further distinguish between functional satellites dominated by solar panels and orbital debris of other nature.

A similar study was carried out by Frith [174] pertaining to the optical behavior of the Hughes/Boeing HS-376 spacecraft over time in flight. Multiple of these spacecraft articles were deployed in GEO and were of interest to the SSA community in terms of its characterization via photometry. The design of this particular spacecraft involved an exterior comprised of solar cells, and due to these photovoltaics exhibiting increased albedo in the IR range, the J, H, and K astronomical filters were employed for examination of this spacecraft. The J-K and H-K indices were used to determine possible trends in their values with respect to time in orbit. Of these, though discussed as preliminary conclusions, the variations provided by the J-K color index delivered more promising results than the H-K index [174].

3.4.3.3. Experiments using the SDSS Photometric System

The Sloan *u'g'r'i'z'* filter system has also been utilized to perform characteristic observations on space-related materials [82, 141, 142]. In the case of [142], the *r'-i'* color index was plotted with respect to increasing electron dose exposure during space weather simulated experiments on polyimide materials. This produced a color plot useful in illustrating the reddening effect that is exhibited by polyimides like Kapton® when irradiated with high energy electrons (Figure 3.20).

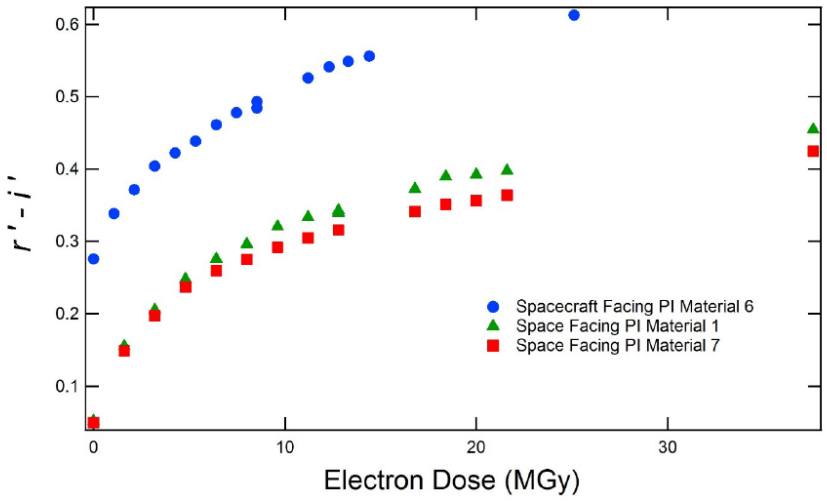

Figure 3.20: Color plot for r'-i' indices with respect to increasing electron dose for three polyimide materials [142].

A similar approach was carried out by [141] where a variety of white thermal control paints were subjected to an analogous GEO simulated environment involving electron radiation. The same *r'-i'* versus electron fluence plot was generated following these experiments. This demonstrated an upward trend in *r'-i'* color index value, some more distinguishable than others, for multiple materials measured. These upward trends in the r'-i' index, suggesting reddening, was further confirmed in [82] for Kapton®, Mylar, and AZ-93 white thermal control paint. These behavioral tendencies for popular spacecraft materials provide optical information that could be useful when performing remote observations.

3.5. Spectral Unmixing

It has been established in literature that reflectance spectroscopy and photometry are measurement techniques worthy of providing information characteristic to RSO's [135, 175, 176, 177, 136, 141, 132, 178, 168, 90]. There are additional concerns to consider regarding such data, one of which involves the problem of a spectrally mixed signature. When obtaining spectra of an observed target or sample that is comprised of multiple materials, the signature is then composed

of a mixture of the materials viewed by the sensor. This is often confronted in hyperspectral imaging (HSI) which involves spectral data and spatial imagery by using pixels to detect and classify materials. HSI has served it use in many fields of study, including topics surrounding geology, as well as surveillance and SSA. There are several models and methods used to approach the hyperspectral unmixing problem and will be discussed upon further [157, 179].

3.5.1. Fingerprint Methods and Introduction to Linear Methods

Experiments carried out by [180] entailed the potential for applying the methods of human fingerprinting to those that could aid with the ability to distinguish non-resolved RSO's from one another. In human fingerprinting, there are three levels involved that are defined as (L1) broad classification / macro characteristics, (L2) minutia, or details, and (L3) Discrete Cosine Transform Coefficients [180]. To correlate this to factors involved in characterizing RSO's, L1, L2, and L3 can be substituted for brightness and color, material spectra and article component contributions, and temporal evolution of abundance, respectively.

Further, a two-facet model concept was employed which involved assigning a satellite model a B-facet and P-facet that correspond to the body and solar panel components, respectively. The algorithms established for this two-facet model also considered that orientation of the satellite components were known, but that the surface materials and geometry of the object were unknown. After carrying out computations, it was discovered that the result delivered multi-spectral albedo-area products assigned to the body and solar panel components of the RSO and serves to characterize articles based on their observed data.

The development of better non-resolved techniques for material characterization of RSO's was again approached by Phan Dao, et. al. [181], who also meddled in the concept of a material signature being linearly mixed and could be expressed as the equation:

$$y = Sa + n$$

where y is the mixed spectra, S is the matrix of signatures in a spectral library, and a is a vector of abundance coefficients, and n is noise [181]. In then employing an algorithm to unmix the spectra, this can solve for areas of the target article (A) to help better characterize its components.

3.5.2. Traditional versus Linear Methods

Spectral unmixing is therefore defined as "the process of inverting material proportions from a combined spectrum that has distinct components that are linearly mixed" [182, 175]. This was undertaken by Abercromby and Rapp, et al., using a constrained linear least squares (CLLS) model. CLLS encompasses adding spectra linearly with respect to its distribution accounted for on the article's surface [182]. This is demonstrated in the equation:

$$S_{combined} = \sum_{i=1}^{n} p_i B_i S_i + N$$

where S represents the spectrum, i indicates the i^{th} material, p represents the proportion of the material taken from the full spectrum, B indicates the orientation factor between the incident light and the object, and N signifies noise. Since $S_{combined}$ and S_i are long vectors and p_i and B_i are scalars, this can be represented as the matrix:

$$S_c = SA$$

where A can be solved by introducing a least-squares optimization:

$$S^T S_c = S^T SA$$

and then creating a square matrix that can be invertible by multiplying S^T on both sides and isolating A. A more in-depth description of the mathematics involved to reach this equation can be found in [182]. This method can be used to face the problem of unmixing by providing a solution, however in testing this, negative proportion values were of result due to the model's attempt to

match shape which could be aimed for by adding or subtracting materials. Therefore, the *lsqnonneg* constrained least squares function in MATLAB can be applied to amend this problem by correcting negative solutions [175].

After corrections are performed, this model will generate a combined spectrum for all materials of input to its best ability. This CLLS model is different from the traditional method due to no need for the interference from the user. The traditional method for spectral unmixing requires that a user's judgement on spectral features, such as slope or absorption, present in the signature be included to match particular materials to those features, and then further match the percentage of that material to an area. The CLLS model was compared to the traditional method involving human interaction and was found to be more fit to the original remote spectral data by 10% [182].

3.5.3. Hyperspectral Unmixing

The problem of spectral unmixing has been studied by Velez-Reyes [183] in a hyperspectral remote sensing aspect. This approach is well considered due to its ability to provide high spectral resolution of unresolved resident space objects (URSO) and extract material composition data from mixed spectra. In the hyperspectral remote sensing field of study, endmembers refer to the pure materials involved in the image zone and abundances are the fraction that these pure materials are present within each pixel [176]. The *hyperspectral unmixing problem* is defined as "the problem of finding the number of endmembers, their spectral signatures, and their abundances" [157]. The constraints and challenges involved in hyperspectral unmixing have been ventured and discussed in [183] and [179].

In [183], the technique of *library-based mixing* is also considered. This involves using *Multiple Endmember Spectral Mixture Analysis* (MESMA) to select endmembers from a spectral library that could best fit like compositions within a mixed pixel, and therefore within the spectral

measurement of an article. MESMA is one means of performing spectral unmixing using a library-based approach. An obstacle involved in unmixing using spectral libraries occurs when spectral signatures may not be unique enough to certain materials and may share similar features across different classes of materials. It is additionally important to consider the optical behavioral changes that specific materials demonstrate after having been subjected to the space environment for long duration.

Simulations were conducted by Velez-Reyes and Yi with the aim to ascertain material composition on an article with a mixed signature by using spectro-temporal signatures to better characterize URSO's. This was conducted by assigning a rotating sphere with surface area comprised of different material signatures to be filmed and then having the pixels existing within the field of view for each frame analyzed with the intent of being hyperspectrally unmixed. The simulation included 7 materials and observations conducted for 12 frames. Endmember extraction was performed using different algorithms, though it was suggested that these algorithms may not operate as well for URSO's than they do for studies pertaining to the Earth. This is illustrated in Figure 3.21 where the two algorithms used, represented by red and pink markers, are still in closer result to the mixed signature rather than the true endmembers.

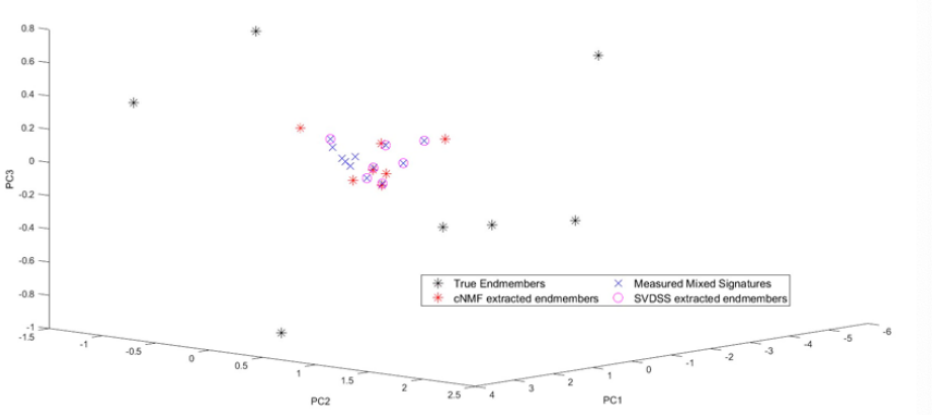

Figure 3.21: Comparison between true endmembers (blue '*' markers) and unmixed endmembers (red and pink markers) with the initial mixed signature (blue 'x' markers) [183].

Similar studies were then carried out by [179], however the simulation model incorporated an object that took on a configuration more analogous to a satellite. After assigning specific materials to various components of the modeled satellite, a mixed signature was sought using linear mixing and pixels within a captured frame were investigated. After applying unmixing algorithms to the spectro-temporal signatures generated from the simulation, it was revealed that endmember extraction was enhanced as the number of pixels per evaluated frame and endmember estimates improved, though the satellite body resulted in the highest endmember error. This leads to the proposition that article configuration could be a factor in characterizing materials of an URSO.

3.5.4. Machine Learning Techniques

On the topic of improving spectral unmixing through a library-based approach introduces the use of machine learning. An example of this was performed by [184] to detect trace residuals of chemicals on material surfaces that could appear as features within an infrared spectral signature using machine learning techniques. This concept is valid due to much chemical content for a material providing evident features in their reflectance within the infrared region of the spectrum where functional groups and chemical bonds are apparent. The aim to better detect residuals from a given spectra was carried out in the form of a challenge known as the Intelligence Advanced Research Projects Activity (IARPA) MORGOTH'S CROWN challenge. The title for this challenge was adapted from influences on JRR Tolkien's VISION of Morgoth, who represents evil, and his crown which is constructed of jewels he stole encourages him to take on a King of the World persona. The MORGOTH'S CROWN challenge involved providing participants with various material substrates and chemical residual targets that closely represented contaminated

surfaces in real-world scenarios. Further details and obstacles present in this challenge are described further in [184].

It is important to note that the MORGOTH'S CROWN challenge allowed for any algorithm methods or types to be used to train their algorithm and present spectral predictions for a total of eighteen different material substrate/chemical residual combinations. The submitted algorithms were then graded on the basis of closest match between predicted spectra and truth data. The highest scoring participants then had their algorithm tested by the challenge team to validate prediction efficacy for final assessment. A significant takeaway to be noted from this challenge pertains to the outcome that regardless of all different algorithm methods allowed and submitted, the top ten scoring participants submitted algorithms based on a machine learning or spectral average approaches [184].

Machine learning techniques have also been applied for hyperspectral imagery mapping of terrestrial topography. For example, remote sensing has been employed to study the coastline along the Arctic Ocean by [177] with the aim of testing and optimizing machine learning methods for semantic segmentation. This approach in remote sensing is beneficial for the scientific community in many aspects, one of which involves the capacity to understand the evolution of Earth's terrain, such as the Arctic coast, and another which allows the ability to remotely evaluate such terrain associated with harsh conditions that would otherwise be difficult to address safely. Furthermore, applying machine learning methods to this field has demonstrated the skill to deliver semantic segmentation of greater accuracy and with more efficiency (less time and effort involved).

The arctic coast mapping performance across using different machine learning algorithms and spectral indices were compared for evaluation [177]. One machine learning model, U-Net, was trained/modified with the incorporation of Normalized Difference Water Index (NDWI) and

Normalized Difference Surface Water Index (NDSWI) indices, and the random forest and eXtreme Gradient Boosting classic machine learning methods. Each of these individual techniques involved can also be used for semantic segmentation and the mapping involved in remote sensing imagery. The outcomes of this work revealed that after comparing the NDWI, NDSWI, random forest, and eXtreme Gradient Boost techniques with the modified U-Net machine learning technique, the latter outperformed the formers mentioned with results that matched closest to the true image elements (land and water).

The concept of machine learning has proven to aid in elemental and material analysis at great efficiency. The potential for employing machine learning to large databases for expedited evaluation of signature features is palpable. This will be further discussed and considered in Chapter 5 with regards to enhancing characterization methods of RSO's and therefore contributing larger to SSA.

3.6. Spectral Libraries

Spectral data from materials contains valuable information that can used to characterize matter optically. Reflectance measurements have been performed widely on natural materials for geological purposes, and for human-made objects, specifically those in orbit for SSA purposes. This data collected is beneficial to the science community when gathered and housed as a spectral library in the form of a database. The United States Geological Survey (USGS) and ECOSTRESS public spectral libraries are effective in storing a plethora of spectral data on various classifications of materials, while the NASA JSC Spacecraft Materials Spectral Database stores a multitude of data specific to space-grade materials.

The USGS is a publicly accessible library storing spectral reflectance data for thousands of constituents [185]. Much of the spectral data ranges from 200-2000 nm, covering the UV, VIS,

and near- to far-infrared regimes. The categories for material data, which can be filtered when navigating the database, include artificial materials, coatings, liquids, minerals, organic compounds, soils and mixtures, vegetation, and wavelength and bandpass. As of March 2022, there are currently a total of 290 artificial material data included, which is the category that would be referred to when searching for spacecraft or rocket body components. The USGS, although still including this artificial material data, is much more dense in housing minerals (1276), soils and mixtures (209), and vegetation (286), making up a total of 1771 data sets. The digital library provides an HTML description that can be accessed per material, and files for the full spectral plot, as well as those divided into UV-VIS, VIS-SWIR, SWIR, SWIR to mid-infrared, and mid-infrared to far-infrared plots. The description per material includes information, where applicable, such as material type, formula, material collection location, x-ray diffraction (XRD) and microscope analysis, and even an image of the sample for convenience.

Like the USGS, ECOSTRESS is an online digital public library that can be accessed for material spectral data. It includes data derived from Johns Hopkins University, the Jet Propulsion Laboratory, and the USGS [186, 187]. When navigating the ECOSTRESS library, materials can be first filtered by spectral type, which includes lunar, man-made, meteorites, minerals, non-photosynthetic vegetation, rock, soil, vegetation, and water. Once having narrowed down data search by spectral type, the data can be further separated by “class” and “subclass”. Also similar to USGS, the ECOSTRESS library is heavily populated of minerals, vegetation, rock, and soil, making up 3307 items of the 3447 total items included in the database, while man-made materials make up 72 of all total material items in the library as of March 2022. When viewing a spectral plot in ECOSTRESS, information such as material type, particle size, data owner, wavelength range, origin, and a general description of the target measured can be gained.

Unlike USGS and ECOSTRESS, the NASA Orbital Debris Spacecraft Materials Spectral Database [188] houses data with a specific focus on human-made materials commonly incorporated in space hardware. The spectral database came to fruition in 2019 where all previous measurements conducted by the NASA ODPO were compiled into a digital library in the form of an html file that can be accessed upon request of the curators. Materials can be filtered by cloth, epoxy, glass, metal, organic, paint, paper, plastic, polytetrafluoroethylene, rubber, or solar cell. Data can also be filtered by spacecraft, including ANDE, Falconsat, Formosat, GPS, Hubble, Hughes/Boeing HS-376, IUS, LDEF, Nanosat, POSA II, Space Shuttle, and Titan IIIC Transtage. Additionally, they can be categorized by selecting whether they were flown and exposed to space environment or not. All materials that were optically measured with data stored in the NASA Orbital Debris Spacecraft Materials Spectral Database are of human-made category. Their spectral plots range from 350 nm in VIS to 2500 nm in the infrared. Material descriptions are provided for each item housed in the digital library. The results acquired from the outcomes of the work presented in Chapter 4 will be a contribution toward the NASA Orbital Debris Spacecraft Materials Spectral Database. The material data included in this contribution range from heritage and modern spacecraft materials to rocket bodies, some of which data has already been fed into and housed in the database. This spectral library can be beneficial for the SSA community when seeking data that could serve as a baseline and be referenced for observational purposes in the future.

3.7. SUMMARY

The various assets used to aid in RSO characterization, including radar and optical instrumentation, as well as *in situ* measurements, have been discussed. The technique of reflectance spectroscopy having been employed as a viable tool toward examining the natural space environment, including asteroids and planetary bodies, and additionally the artificial materials that refer to spacecraft, rocket bodies and orbital debris, were outlined. It was then

essential to review the optical changes to materials and their potential degradation as a result of space weathering. Further, the contributions of spectral data and laboratory-based data for remote sensing were conveyed, in particular the significance behind using color indices from photometry and the different photometric systems used. Finally, the implementation of spectral unmixing and how this is supported by hyperspectral unmixing and machine learning techniques has been discussed.

Chapter 4: Laboratory-Based Measurements

It has been understood that reflectance spectra acquired from material surfaces can be used as a means to help characterize that matter. This method can be implemented for use in evaluating resident space objects (RSOs). For this reason, a variety of commonly used spacecraft materials have been selected for optical analysis in this work. Though all measurements were obtained in the laboratory setting, there were two different specific experimentation settings involved; a simulated geosynchronous Earth orbit (GEO) space weathered environment and a non-space weathered environmental setting. Each of these measurement methods and experimentation processes along with materials analyzed will be explained in detail throughout this chapter.

4.1. Laboratory Overview

For the purpose of understanding the optical behavior of space-related materials in various environmental conditions, select materials that fall within RSO categories were analyzed via spectroscopy. These material measurements were obtained using two different laboratory setups. The first, described as a non-space weathered environment, involved the material measured in atmosphere with the aim of only analyzing spectral features characteristic to common space materials. The second, described as a space simulated environment, encompassed the use of multiple instrumentation and machinery to create a state analogous to what a material would be subjected to in GEO.

4.1.1. Non-Space Weathered Environment

All materials measured in the non-space weathered environment were performed within the Optical Measurements Center (OMC) at NASA's Johnson Space Center. This provided an ideal dark lab environment and allowed for optimal reflectance response from each specific sample while minimizing the potential interference from scattered light. Instrumentation involved for this

experimental set-up included a quartz lamp illumination source and an Analytic Spectral Device (ASD) FieldSpec® Pro spectroradiometer [129]. The ASD employed is capable of providing a full-range of spectral measurements between the visible and infrared (350-2500 nm) region of the spectrum. Within the visible and near infrared (VNIR) range (350-1000 nm), the device has a spectral resolution of 3 nm, and resolution of 10 nm bandwidth in the IR (1000-2500 nm) [129]. The spectrometer system is made up of 512 and 2000 channels in VNIR and IR, respectively, which provide the full-range spectral plot for a measured sample [129]. The data collected by the instrument is then transferred and stored on a compatible laptop containing the necessary, in-house developed software used to produce absolute reflectance material spectral plots.

4.1.2. Space Weathered Environment

Materials measured in the GEO space simulated environment required a much more intricate set-up. The chamber used to provide this simulated environment is housed in the Spacecraft Charging and Instrumentation Calibration Laboratory (SCICL) at Kirtland Air Force Base in New Mexico, USA, and operated by the Air Force Research Laboratory (AFRL). Using a combination of cryogenic, turbo, and mechanical pumps, vacuum levels of $<10^{-6}$ Torr were achieved. To induce the radiation element in GEO from electrons, a Kimball Physics EG8105-UD electron flood gun was employed to provide high energy (100 keV) mono-energetic electron radiation [87]. A schematic of the experimental setup at the AFRL SCICL lab showing instrumentation involved within the chamber (in vacuum) and outside of the chamber can be referred to in Figure 4.1.

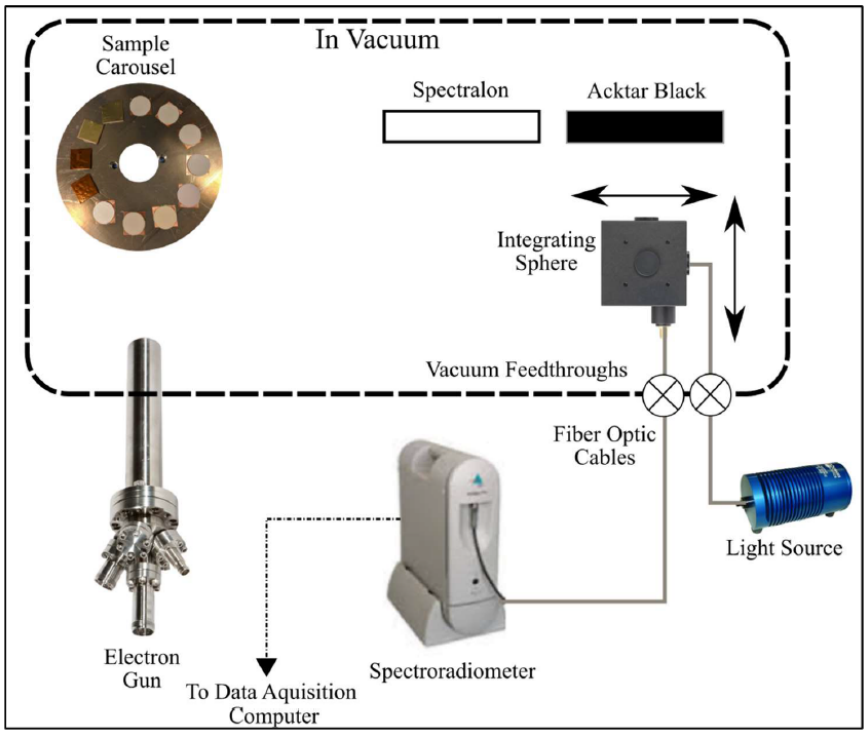

Figure 4.1: Diagram of space weathering measurement acquisition at AFRL SCICL lab [141]. *Credit: AFRL*

Like in the non-space weathered environment, reflectance spectroscopy was operated for material measurements, however in this case, rather than absolute reflectance, a directional hemispherical reflectance (DHR) was acquired for sample analysis. DHR was obtained through the use of an integrating sphere in conjunction with the spectrometer's fiber optic feed and illumination source which then provided an absolute hemispherical reflectance (HR) over the 280-2500 nm spectral range capable from the spectrometer. A Spectral Evolution SR-3501 spectrometer with a resolution of 4 nm at 280-1000 nm, 5 nm at 1500 nm, and 7 nm at 2100 nm [189], was utilized to analyze material reflected light, while an Ocean Optics (model HL-2000-HAS) halogen lamp was used to supply incident illumination.

4.2. MATERIALS OF INTEREST

The materials selected for spectral analysis are those commonly seen amongst rocket body and spacecraft fabrication, and generally pertain to RSOs. Some of the materials included in this section were analyzed in either the pristine condition while others were analyzed after exposure to the space simulated environment. The most commonly used space-grade materials were analyzed in both environmental conditions. This will be specified as necessary.

4.2.1. Rocket Body Related

The Titan IIIC Transtage, an upper stage of the Titan IIIC launch vehicle, was developed in the 1960s to lift and deliver payloads in LEO and GEO [38]. The launch vehicle was capable of numerous engine restarts and could distribute several spacecraft to orbit with high precision in a single mission, therefore deemed the world's first "space tug" [38]. The rocket body is worthy of analysis due to the four catalogued fragmentation events associated with it. Transtage 3C-5 (International Designator 1968-081E, U.S. Strategic Command Space Surveillance Network catalog number 3432) fragmented on 21 February 1992 after serving 23.4 years on-orbit [37]. Transtage 3C-17 (1969-013B, SSN #3692) fragmented on 28 February 2018, 49.085 years after life in orbit [37]. Further, as of 4 July 2017, the 1968-081E breakup had 28 debris fragments associated with the event. The 1969-013B breakup event had accrued 18 cataloged debris pieces as of 5 July 2018 that are associated with its destructive event [37]. Lastly, the LEO (1965-082DM) and GTO (1965-108A) events documented occurred on the day of launch, likely propulsion-related [37]. The LEO and GTO occurrences yielded 472 and 107 catalogued debris pieces, respectively. However, the destructive events may have potentially produced much more debris than cataloged at those times [37].

The Transtage thermal control components and coatings of the early flight test vehicle series (vehicles 1-16) are outlined in Figure 2.12. It was discovered that a test article of the Titan Transtage upper stage was in the possession of the 309th Aerospace Maintenance and Regeneration Group (AMARG) in Tucson, Arizona. Upon receiving this knowledge, the test article was comparable to the flown vehicle and therefore worthy of inspection. A total of 12 different external material surfaces (Table 4.1) of the upper stage had their reflectance response measured. Of these 12, a select few will be presented in Section 4.5.

(a)  (b) 

Figure 4.2: Transtage test article (a) at its original location and (b) as received for further lab testing [38]. *Credit: NASA*

Three different data collects were conducted on the Transtage test article and spectral measurements were compared. Data was acquired from material samples removed from the test article while in its original location (Figure 4.2a). Later the article was transported to an environmentally controlled high bay at NASA Johnson Space Center (JSC) (Figure 4.2b) for further analysis. The first data collect pertains to 12 of 28 samples that were removed from the test article in Arizona and measured in the OMC separately. The second data collect refers to measurements conducted at the NASA JSC high bay, and the third collect was a repeat of what was measured in the second collect but after each material surface was cleaned with water or isopropyl alcohol to remove dust/debris/oxidation.

Though all material characterization from the Transtage test article was conducted in the OMC (non-space weathered environment), several thermal control paints often used as coating for rocket bodies were subjected to the space weathered environment additionally. These included multiple black thermal control paints. All paint samples used for reflectance characterization were provided by AZ Technology.

Table 4.1: List of materials taken from multiple data collects of the Titan Transtage test article. Twelve materials were analyzed, but only two (denoted with *) have their results presented in this work.

Item Number	Material
001	Blue glass frit
002	Dark checkerboard surfaces
003	White checkerboard surfaces
004	Columbium metal
005	Engine shroud
006	Exposed engine bell
007	Exposed metal top
008	Gold foil
009	Green paint
010*	Red paint*
011	Strut
012*	White paint*

4.2.2. Spacecraft Related

Material measurements were conducted on various solar cells used to construct the Hughes/Boeing HS-376 spacecraft. The communications satellite (Figure 2.10c) was designed as a 2 m-diameter cylindrical bus externally constructed of multiple solar cell arrays that surround a variety of internal parts to complete the spacecraft system [37]. The materials and assembled design were chosen with intent due to their near identical physical characteristics which in turn help constrain albedo and size ambiguity [190]. Over 50 models of this satellite have been launched in GEO between 1980 and 2003 [190], therefore making it of interest to characterize the HS-376 article.

Four types of solar arrays were used on the exterior of the HS-376 satellite. These included GaAs/Ge, $GaInP_2$/GaAs/Ge, Silicon K4 3/4, and Silicon K7 cells. The GaAs/Ge and GaInP2/GaAs/Ge solar cells involve a Ge substrate, though the latter is a dual junction n/p device. The Silicon K7 and K4 3/4 are shallow junction n/p cells [190]. For the reason that solar cells are common space materials in general, they were measured in both non-space and space weathered conditions.

The silicon-based solar cell used for space-weathering experiments was a duplicate to those used on GPS satellites. Heritage spacecraft systems have incorporated silicon solar cells, which therefore alludes to a high quantity of silicon solar cells expected to inhabit space domain [88]. Furthermore, solar arrays are a necessary component that provide power to an RSO system and populate LEO and GEO in high volume. This makes it significant that their optical behavior is well understood to aid in remote observations. Solar cells used on satellites are fabricated with a sheet of coverglass placed above them for protective purposes. A CMG coverglass (provided by Qioptiq) was therefore included in optical measurements. These coverglasses are thin, transparent, brittle materials with an anti-reflective (AR) coating and doped with cerium to provide protection and inhibit color darkening from the harmful ultra-violet, proton, and electron radiation that exists in space conditions [58, 88]. Due to the transparent nature of these glasses, it was also of interest to have them backed with different materials to analyze potential behavioral differences in their spectral signatures after having been subjected to a GEO simulated environment.

Perhaps the most fruitful optical analysis of spacecraft materials in this work is dedicated to what was provided by the DebriSat project. The DebriSat experiment unfolded in a collaborative undertaking by many agencies and organizations including the NASA ODPO, the Air Force Space and Missile Systems Center, The Aerospace Corporation, the University of Florida (UF), and the

Air Force Arnold Engineering Development Complex [90]. The overall goal of this project was to design and construct a flight-ready spacecraft analogous to modern satellites deployed in LEO with the intent of subjecting the article to hypervelocity impact in order to generate and mimic a destructive breakup event in LEO. To accomplish this, the DebriSat spacecraft was placed inside a chamber with walls formed of soft catch panels where the hypervelocity impact test was carried out [39]. Ultimately, through the execution of the induced breakup event, approximately 85,000 material fragments were produced and collected by the soft catch panel walls of the chamber [39]. More details regarding the hypervelocity test, projectile used, and experiment specifics can be found in [90].

Table 4.2: List of DebriSat materials selected for optical analysis in this study.

Nomenclature	DebriSat Material
M1	Ultra Triple Junction (UTJ) solar cells
M2	Red painted 6061 aluminum alloy
M3	Magenta painted 6061 aluminum alloy
M4	Gold painted 6061 aluminum alloy
M5	Blue painted 6061 aluminum alloy
M6	Black painted 6061 aluminum alloy
M7	6061 aluminum alloy (anodized and unpainted)
M8	Carbon fiber composite: gold shimmer surface
M9	Carbon fiber composite: black, no finished surface
M10	Red circuit board
M11	Green circuit board
M12	Brown circuit board
M13	Blue circuit board

DebriSat contributed advantageous material data due to the high-fidelity structure of the article, incorporating only space-grade components and including modern space materials. An overview of materials from DebriSat selected for analysis in this work has been outlined in Table 4.2. The Ultra Triple Junction (UTJ) solar cells used to assemble DebriSat were GaInP2/GaAs/Ge in structure and were topped with an anti-reflective coverglass [90]. Many 6061 aluminum alloys were incorporated in DebriSat and they were either coated with a colored paint or were unpainted,

having only an anodized coating. Two carbon fiber composites from DebriSat were measured, one which had a gold-shimmer surface finish visually apparent and the other, which did not. These carbon fiber composites were configured with a 6061-T6 aluminum alloy honeycombed core embedded within a Toray T1000 carbon fiber composite [39]. Four different colored PCB's, each supplied by different manufacturers, were also integrated in DebriSat and therefore, were also included for optical measurements.

4.2.3. High Area-to-Mass Ratio Related

The Kapton® polyimide film is a popular polymeric material frequently incorporated with space articles, especially in MLI that has been considered to fall under the high area-to-mass ratio (HAMR) category. The polyimide is used on most space hardware currently in orbit and is anticipated to continuously be utilized in future space missions. For this reason, this material was measured in both pristine and space weathered conditions. For the space-weather simulated experiments, two flavors of Kapton® were included; Kapton® HN and Kapton® MT. Kapton® MT has three times the thermal conductivity that Kapton® HN has, as well as a higher modulus, serving an increase in strength when compared to Kapton® HN [50, 51, 88].

4.2.4. Mission Specific

In collaboration with the U.S. Air Force Falcon Orbital Debris Experiment, the NASA ODPO provided a pre-flight characterization of 10 metallic spheres to be used in optical calibration of ground-based radar systems [37]. Data taken on these spheres followed a routine of measuring the spheres at every cardinal direction in north and south hemispheres. This warranted comprehensive analysis of the objects since the variations of albedo can impact brightness. Measurements on these calibration spheres were obtained prior to their launch and deployment in orbit for a baseline of their optical signature. A total of ten of these spheres were analyzed to

provide recommendations on which spheres were best suited for flight in orbit to assist in radar system calibration [37]. Of these 10 objects, five were 4 cm in diameter and coated with an electrodeposited zinc plating (5.08E-4 cm thick) with yellow chromate, while the other five spheres were 2 cm in diameter and did not have the coating applied to them [37]. Recommendations were based on which sphere of the two different diameter groups performed well optically with the most consistent spectral response. It should be noted that these spheres were mounted using a Styrofoam™ cup to secure the spherical specimen in place.

For additional spectral analysis on various materials, a carbon fiber composite similar to what was used in DebriSat was also analyzed in the space-weather simulated environment. To support experiments on coverglasses, aluminum and copper foils were included separately in measurements involving the coverglasses since they were backed with these materials. This will be explained in greater detail in Section 3.5 Results and Discussion.

4.3. Measurement Acquisition and Setup

This section will describe the detailed measurement process for collecting reflectance measurements on materials in their respective laboratory set-ups. These involve data collected in the OMC (non-space weathered environment) and in the SCICL laboratory (space weathered environment). All materials selected for optical analysis are those commonly integrated on space-related hardware.

4.3.1. Non-Space Weathered Environment

Reflectance spectroscopy performed in the OMC involved a test configuration where the material sample was placed flat on a horizontal surface representing the origin of set-up. The illumination source and spectrometer detector's fiber optic feed were positioned approximately 45° to that of the specimen and opposite to each other (Figure 4.3). The spectrometer's fiber optic

cable was fed through and secured in a pistol grip for stability. It has an approximate 25° field of view. To ensure accurate results, a white reference material (Spectralon) panel with a highly lambertian surface and near perfect flat reflectance signature was used before and during data collections. A minimum of three measurement trials were performed for each material sample and averaged accordingly.

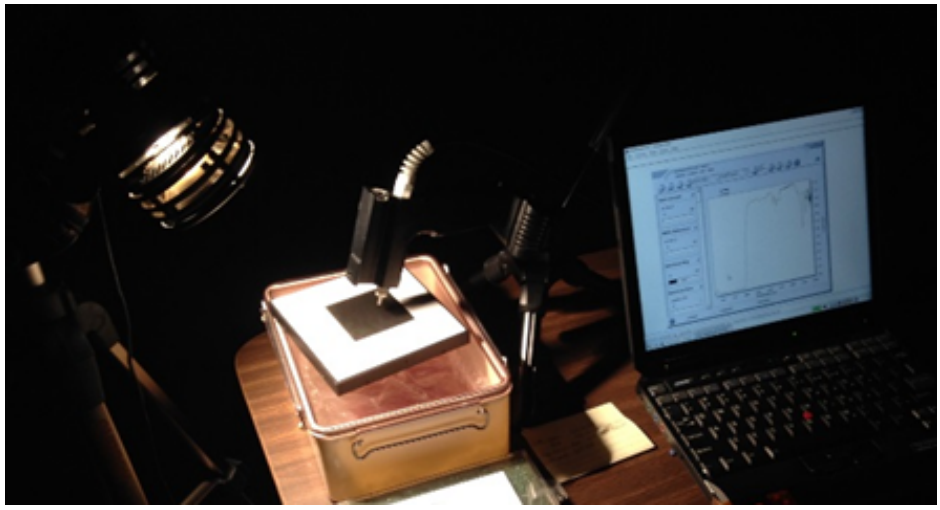

Figure 4.3: Laboratory set-up with light source and fiber optic system opposite to one another. *Credit: NASA*

4.3.2. Space Weathered Environment

Images of the measurement setup for space weathering experiments can be viewed in Figure 4.4. Material samples involved in the space-weathering experiments were mounted onto a circular plate, referred to as a carousel, that had a diameter of 8 inches (20.32 cm). The carousel plate was then mounted in a chamber and oriented where the material sample surfaces would be in direct view of the electron beam, which projected an approximate area of 4 x 4 in^2 (10.16 x 10.16 cm^2) [88]. To establish equal distribution of electron radiation, the sample carousel was rotated within the chamber during the simulated space-weathering. A Faraday cup having an orifice diameter of 0.5 cm^2 was placed at the centermost location of the carousel to monitor electron flux delivered from the beam throughout the space-weathering experiment [88].

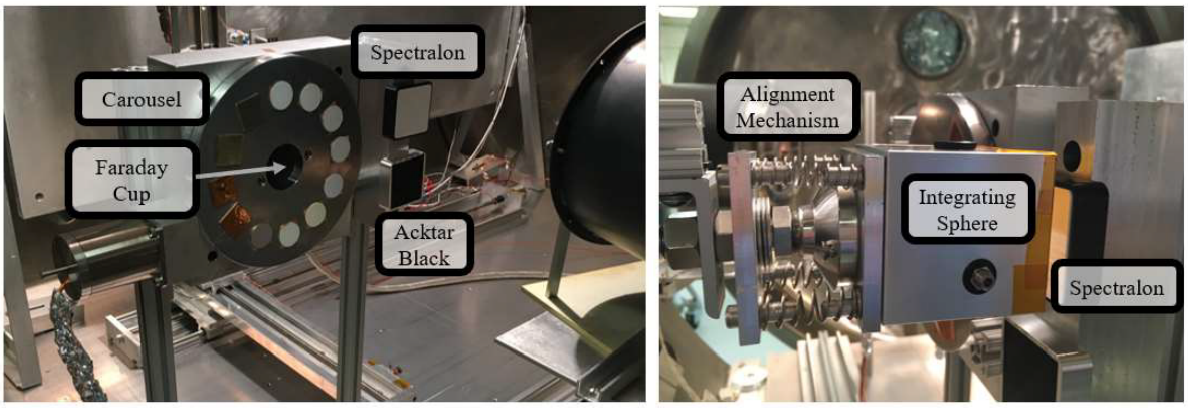

Figure 4. 4: Images of measurement setup within the Jumbo Chamber at AFRL SCICL Lab [141]. *Credit: AFRL*

The reflectance signature of each material sample that was subjected to simulated space-weathering was acquired before irradiation commenced to record the optical response of materials in their pristine conditions. As irradiation was underway, material reflectance measurements were conducted periodically until maximum electron fluence was achieved [88]. Then, upon ceasing irradiation, the materials were allowed to sit in vacuum for some time and were again spectroscopically measured to determine potential optical property changes to the different environment. The specifics regarding materials, electron fluence and time in vacuum post-irradiation are outlined in Table 4.3. Though a few of the material samples were measured on different occasions, the experimental procedures were consistent, and all samples were subjected to the same characterization methods [88].

Table 4.3: Description of materials studied in simulated GEO environment.

Material Sample	**Thickness (μm)**	**Maximum Fluence (electrons/cm^2)**	**Vacuum Exposure (hours)**
CMG	100	2.5×10^{14}	49.7
Aluminum foil	2.0×10^{3}	2.5×10^{14}	49.7
Copper tape	6.6×10^{3}	2.5×10^{14}	49.7
Kapton® HN	76.2	2.5×10^{14}	49.7
Kapton® MT	38.0	7.2×10^{13}	3.0
Solar cell	260	2.0×10^{13}	16.7
c-c composite	2.55×10^{3}	4.5×10^{13}	15.3
AZ-1000-ECB	1.75×10^{3}	4.5×10^{13}	15.3

All reflectance measurements obtained from the space weathered environment were taken within the chamber before, during and following the electron irradiation operation. To achieve this, the fiber optic cable used to deliver photons to the spectrometer was inserted into the chamber using vacuum feedthroughs (Figure 4.1). Further details regarding the material aging evolution through exposure to high energy electrons, as well as the process for acquiring spectral data within the chamber can be found in [141]. For calibration and reflectance calculations, Spectralon and Acktar black materials were used as white and black standards, respectively. During each measurement acquisition period, dark spectral readings were taken to account for noise from the instrument and provide accurate data determination.

The absolute hemispherical reflectance from raw data counts were calculated using the following equation:

$$R_{Sample_i} = \frac{(N_{Sample_i} - N_{Dark_i}) - (N_{Acktar_i} - N_{Dark_i})}{(N_{Spectralon_i} - N_{Dark_i}) - (N_{Acktar_i} - N_{Dark_i})} R_{Spectralon}$$

where N represents the spectrometer counts of the indicated measurement and $R_{Spectralon}$ is the calibrated absolute reflectance of the Spectralon [88]. The wavelength at which each measurement was taken is represented by i [142]. A reflectance spectra is then generated by plotting R_{Sample} as a function of wavelength.

The determined reflectance values for a given material were then used to calculate a color index for the sample measured. The color index of an object or material refers to the ratio of its brightness between two filter passbands. This is calculated from its reflectance spectra using the equation:

$$f_1' - f_2' = -2.5 \log_{10}\left(\frac{I_{f1}}{I_{f2}}\right) = -2.5[\log_{10}(I_{f1}) - \log_{10}(I_{f2})]$$

where f_1 and f_2 represent the two filter bands being compared, and I is the brightness determined as a sum of the area under the reflectance curve within each filter passband [88]. Brightness (I) can therefore be represented as:

$$I = \sum_{\lambda_1}^{\lambda_2} Area_f$$

where λ_1 and λ_2 correspond to the start and end of a specific filter passband, respectively. The $Area_f$ was estimated within each incremental "bin" between wavelengths within the filter band by using the trapezoid rule:

$$Area_f = \left(\frac{\left(R_f + R_{f+1}\right)}{2}\right) * (\lambda_{f+1} - \lambda_f)$$

where R_f represents the reflectance value at a wavelength within the filter passband. Total area is then summed to determine I, and I for two different filter passbands are used to ultimately determine color index.

For the space weathered environment measurement results obtained in this work, Sloan Digital Sky Survey (SDSS) filters [112] were used to evaluate optical changes in spectral brightness dependent upon irradiation exposure. This system of filters was chosen since they are considered to be more modern filters that telescope assets may make frequent use of in the near future. Brightness differences between the *r'* band (558-682 nm) and the *i'* band (705-835 nm) were determined for Kapton® HN, while brightness differences between the *r'* and *z'* bands (839-1094 nm) were determined for Kapton® MT. These specific filters were chosen since their passbands provided the largest contrast for each respective polyimide measured.

4.4. REPEATABILITY

To produce accurate measurements, steps were taken during measurement acquisition and data analysis for all experiments performed in both, non-space weathered and space weathered environment settings. After proper calibration of the ASD system was fulfilled for measurements taken in the OMC, each material sample surface studied was measured three times at minimum to obtain an average reflectance result. The standard deviation was calculated for all data sets and provided indication for accurate measurements. Only data that was properly acquired and verified to be well representative of each respective material has been presented.

Many steps were taken toward ensuring the validation of proper data results acquired in the GEO space-simulated environmental setup. This included taking dark measurements for reflectance calculations to account for noise. Spectralon and Acktar black samples were employed as acceptable reference materials. Additionally, a Kapton® HN sample was included in all test campaigns since its behavior when subjected to high energy electrons over time is well understood and can testify toward functional GEO simulated environment operation.

4.5. RESULTS AND DISCUSSION

Much investigation involved in reflectance spectroscopic measurements is heavily dependent upon the physical properties and chemical make-up of a given material. This is why spectral data can be used as a source of characterization through optical means. Some common features that appear in the reflectance response of a material are summarized in Table 4.4.

Table 4.4: Absorption/reflectance feature details present in VIS/NIR/SWIR reflectance data.

Wavelength (nm)	Feature	Cause(s)
350-700	High absorption	Black color
350-700	Relatively high absorption	Brown color
400-450	Sharp increase in reflectance	Violet and Blue colors
550	Increase in reflectance	Green color
600	Sharp increase in reflectance	Gold color
650	Sharp increase in reflectance	Red color
850	Prominent absorption dip	Aluminum content
1400	Absorption dip	O-H, first overtone
1700	Asymmetric absorption doublet	C-H, second overtone
1900	Single absorption dip	C-O, O-H, second overtone
1950	Single absorption dip	O-H, second overtone
2150	Single absorption dip	C-H
2180	Asymmetrical absorption doublet	N-H, second overtone C-H, C-O, C=O stretches
2200	Broad absorption feature	C-H, metal-OH
2300	Prominent single absorption dip	C-H, N-H stretches
2450	Low intensity absorption dip	O-H

The VIS (350-700 nm) of the electromagnetic spectrum, as expected, is responsible for the ability to detect the pigmentation of an article [39, 178]. This occurs because illumination that impinges on a material surface will excite electrons, causing them to occupy higher energy sites and result in various colors of light [39, 191]. Beyond this region, absorption present in the infrared region of a reflectance signature can be attributed toward organic content. These features will be described in detail as results are discussed in the following Sections 3.5.1 Non-Space Weathered Environment and 3.5.2 Space Weathered Environment accordingly.

4.5.1. Non-Space Weathered Environment

Though all 12 material samples derived from the Titan IIIC Transtage test article were optically measured and analyzed, data for red and white paint material surfaces are most worthy of discussion. Nomenclature for the spectral curves obtained for this test subject signify the three different data collects that occurred. Original samples refer to the material samples that were removed from the Transtage article and returned to the laboratory for separate and immediate analysis. Spectra denoted “9S” refers to the second data collect that occurred on the article as

received, while spectra denoted "9S Clean" refers to the final data collect which was a repeat of the second collect but after the surfaces were cleaned.

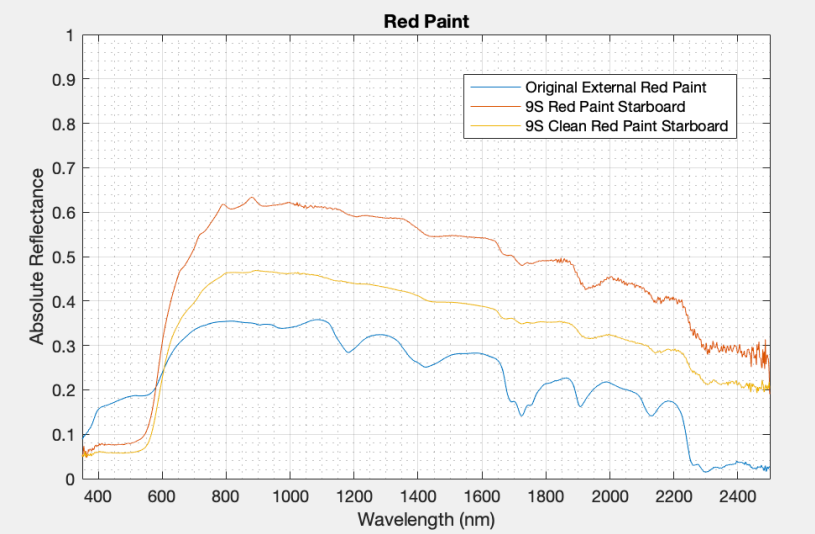

Figure 4.5: Reflectance signatures for red paint material samples taken from the Titan IIIC Transtage test article. *Credit: NASA*

The "Original External Red Paint" sample conveys evident absorption features (dips/depressions in the reflectance curve) in the IR (700-2500 nm), more so than its other red paint counterparts (Figure 4.5), though all three red paint samples show similar absorption at corresponding wavelengths. The rise in slope at 600 nm common between these paint surfaces is indicated by the red color feature associated with the paint's pigment. The absorption depressions present at 1400 nm and 1900 nm are likely associated with O-H bonding. Simultaneous presence of these two features in the signature suggests the presence of H_2O within the material's elemental composition [192]. Additionally, broad absorption in the "Original External Red Paint" sample at ~1150 nm could be due to an existence of Fe2+ due to the excitation of d-orbital electrons present in transition metal ions [192, 193]. Absorption present at ~2150 nm, as well as 1700 nm, suggests C-H bonding within the material chemistry [134].

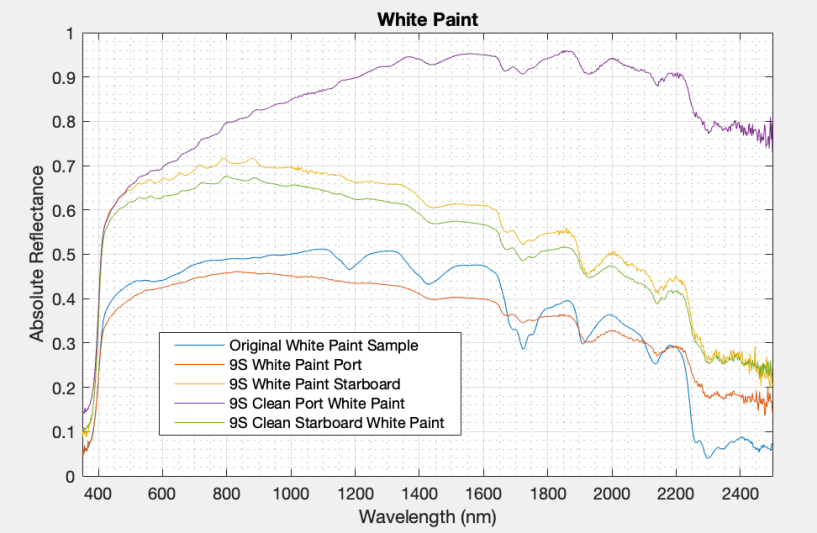

Figure 4.6: Reflectance spectra for various white paint samples taken from the Titan IIIC Transtage test article. *Credit: NASA*

Multiple, white paint material surfaces from the rocket body test article resulted in many features within their spectra (Figure 4.6). The consistency between features apparent in the multiple sample readings is sufficient. This includes the steep rise in reflectance at 400 nm with overall high reflectance in VIS to represent the white color property of the paints, followed by many organics in the IR. Features in the infrared include O-H absorbing at 1400 nm, C-H or O-H absorption at 1700 nm, C-O or O-H absorbing at 1900 nm, C-H absorption at 2150 nm, and C-H or N-H stretches at 2300 nm. Paints often contain H_2O as a solvent, and O-H/C-H bonds are generally found in paint binders, which are used to secure pigment and therefore take on polymeric properties [194, 195].

Of the other samples measured from the test article, the light checkerboard surfaces and the columbium metal were featureless, resulting in a flat spectrum throughout the entire 350-2500 nm range. The exposed metal top and strut both only exhibited broad absorption centered at 850 nm, suggesting aluminum presence. The blue glass frit and gold foil samples were also largely featureless except for their respective color property features evident in the VIS wavelength region.

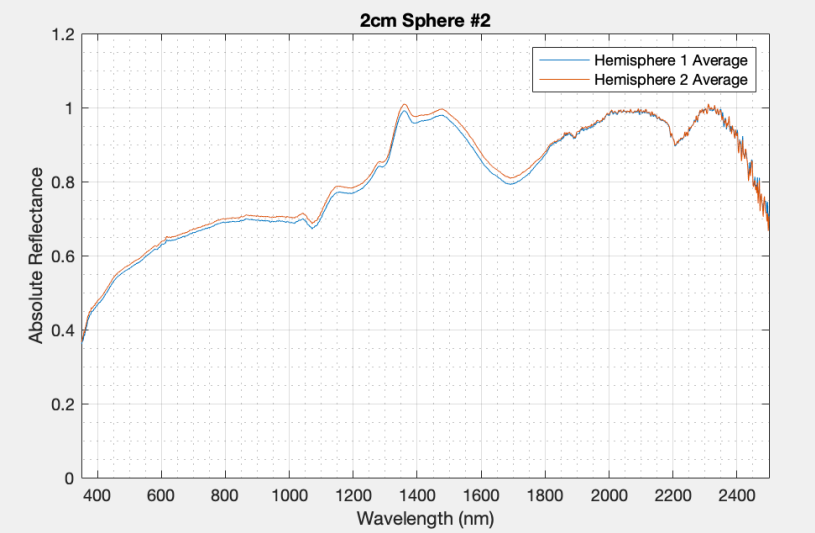

Figure 4.7: Reflectance spectral plot for 2 cm -diameter Sphere #2. Blue and red curves represent average measurements for northern and southern sphere hemispheres, respectively. *Credit: NASA*

In optically analyzing all spheres with 2 cm-diameter using consistent methods, spectral results demonstrated that the sphere labeled #2 produced the most invariable reflectance signature upon rotation. Figure 4.7 depicts the average measurements taken at each cardinal direction on the northern and southern hemispheres of the spheres represented by blue and red curves, respectively [37]. There is evident absorption present at 1700 nm in the spectra, suggesting a C-H stretch in the second overtone infrared region [134, 178, 196]. However, this feature could be due to possible interference from the Styrofoam cup used to mount the sphere. Regarding other reflectance features, the small peak present at 600 nm is a common feature seen in steels [37, 134]. Additionally, the steady parabolic increase in VIS can be associated with iron or vanadium alloyed content within steel [197]. Absorption features at 1400 nm and 1700 nm are due to O-H in the first overtone and C-H in the second overtone IR regions, respectively. The evident depression at 2200 nm could be due to metal-OH bonding [134] or C-H bonds [90, 178, 196, 198]. The absence of absorption at 850 nm commonly seen in aluminum materials can be noted, along with all aforementioned characteristics that support a more steel-like metal.

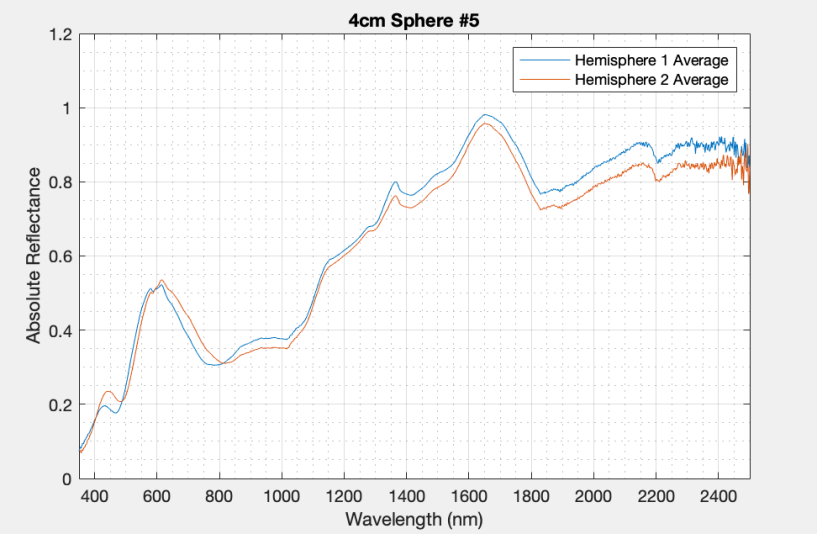

Figure 4.8: Reflectance spectral plot for 4 cm-diameter Sphere #5. Blue and red curves represent average measurements for northern and southern sphere hemispheres, respectively. *Credit: NASA*

Upon collecting measurements on all 4 cm-diameter spheres, the sphere labeled #5 resulted in the lowest standard deviation and demonstrated the most spectral consistency; its spectral response is displayed in Figure 4.8. Because the 4 cm-diameter spheres had a colored coating applied to their surface, hues of yellow, green, and blue affected the spectral curve in VIS. Increase in reflection at ~400 nm and 500 nm, are therefore attributed to these color properties. Further, the depression seen at 1400 nm is likely due to O-H bonds present, and similar to what was seen in the 2 cm-diameter sphere, the small absorption dip at 2200 nm can be due to metal-OH bonding. Again, because of the highly specular nature of these spheres, some organic features obtained could have been brought about with scattering from the Styrofoam mount, though the main objective of these analyses was to determine which spheres presented the most optically consistent results, regardless of what features were exhibited.

The germanium-based and silicon-based solar cells related to the HS 376 spacecraft resulted in spectral features that were characteristic of their nature. Germanium-based solar cells are highly absorptive throughout the full range of the VIS and IR regions (350-2400) of the

spectrum (Figure 4.9). The peak present at 850 nm corresponds with a Ge peak quantum efficiency [199]. Though not presented here, the $GaInP_2$/GaAs/Ge cells resulted in nearly analogous response to that of the GaAs/Ge cells but had an additional peak at 700 nm.

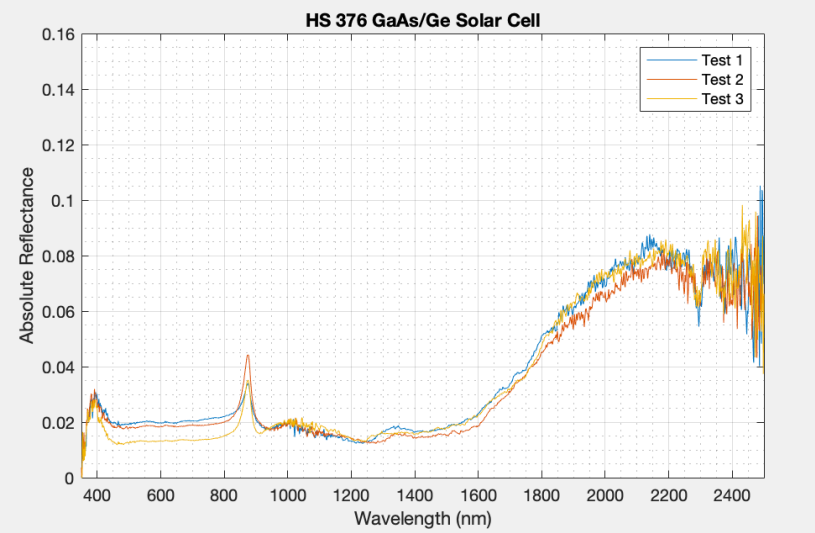

Figure 4.9: Reflectance spectra of GaAs/Ge solar cell. The three test trials acquired on this solar cell sample are shown. *Credit: NASA*

Silicon-based solar cells are also highly absorptive but are characteristic of having very high absorption in VIS followed by an increase in reflection at ~1000 nm into the IR (Figure 4.10). A doublet absorption feature is present in the Si-based solar cell's signature near 1700 nm, suggesting C-H bonding in the second overtone IR zone. The Silicon K4 3/4 cells resulted in almost identical results to the Silicon K7 cells with no additional features to note.

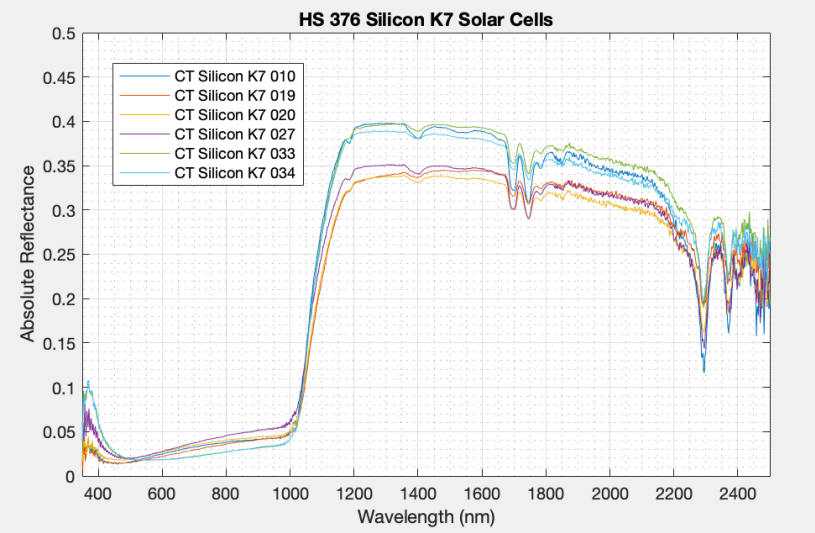

Figure 4.10: Reflectance signature of Silicon K7 solar cell samples. Average measurements acquired on six Silicon K7 cells are represented by the six curves. *Credit: NASA*

The multiple 6061 aluminum alloy samples derived from the DebriSat project were first compared (Figure 4.11). The blue-painted alloy demonstrated initial rise in reflectance at ~400 nm followed by much absorption throughout the remainder of the VIS region, characteristic of its blue color property. Gold and red-painted alloys exhibited a relatively low absorption at the onset of VIS but produced apparent increases in reflectance at 600 nm for the gold sample and 650 nm for the red-painted alloy, also alluding to its pigment. The magenta-painted alloy resulted in a notable increase in reflection at 400 nm, approximately 2.5 times that of the gold and red-painted samples, followed by absorption between 450-550 nm and then produced a significant increase in reflectance yet again at ~600 nm. This agrees with the blue and red color components that are required to produce magenta. As expected, the black-painted alloy illustrated high absorption throughout the entirety of VIS until reaching NIR (700-1300 nm) at ~800 nm. The unpainted 6061 aluminum alloy sample produced high reflectance throughout VIS, agreeing with the substantial reflectivity often perceived in bare metals [191]. The unpainted alloy therefore resulted in an optical signature causing it to stand apart from all other painted alloys.

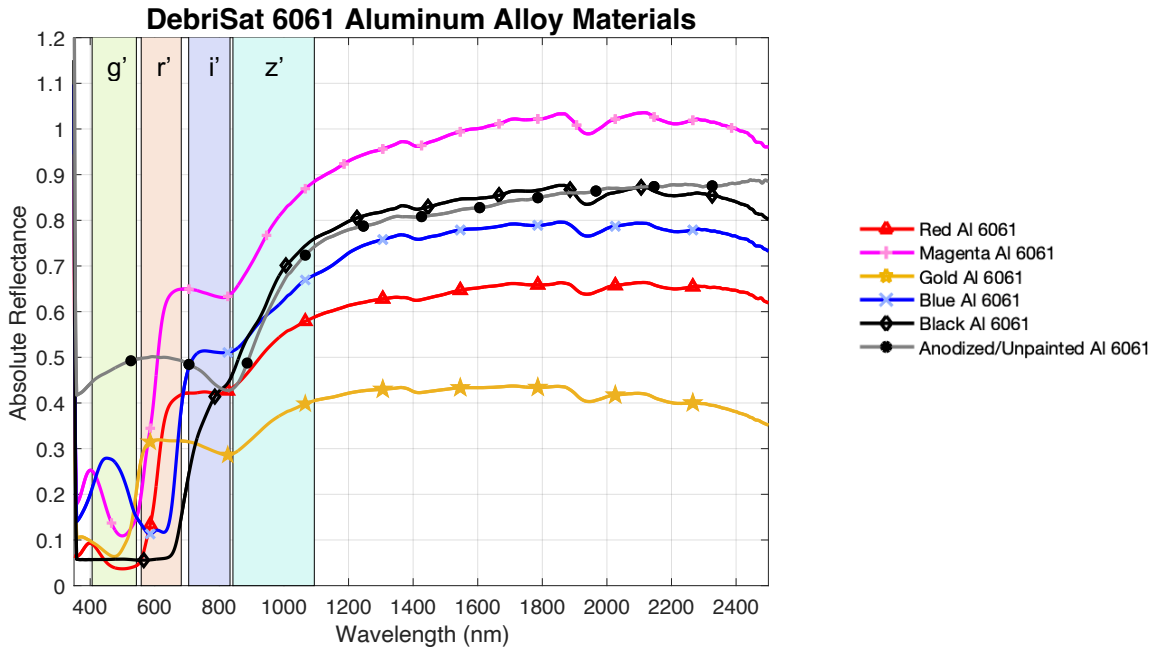

Figure 4.11: Absolute reflectance of various painted and unpainted 6061 aluminum alloy samples in their pre-impact conditions. The *g'*, *r'*, *i'*, and *z'* Sloan filter passbands are indicated in the spectral plot for future reference. *Credit: NASA*

A feature in NIR that is commonly seen in all 6061 aluminum alloy samples, regardless of having been painted or not, is the evident absorption element at 850 nm. This is a typical characteristic that is associated with aluminum content within a material and is consistent with literature [90, 134, 185, 200]. In the SWIR (1300-2500 nm) region of the spectrum, all painted aluminum alloys resulted in common absorption qualities, including an apparent absorption feature at ~1950 nm, a less pronounced feature at 1400 nm, and broad absorption at 2200 nm. The feature at 1400 nm can be due to O-H bend in the first overtone IR zone, associated with water from the chemical makeup of the sample surface [196]. Absorption present near 1950 nm is also attributed to O-H stretch, but in the second overtone IR zone, and the broad absorption feature centered near 2200 nm can be due to C-H chemical bonds [90, 134, 178, 196, 198]. It can be noted that the unpainted, anodized aluminum alloy sample did not demonstrate these same absorption characteristics in SWIR, suggesting a lack of organic content that was exhibited in the painted

alloys. It can be additionally noted that the absorption feature in the *g'* passband between the unpainted and painted metal samples can be exploited to generate a separation in color index values for these materials which can offer a step towards identifying different classifications of materials remotely [39].

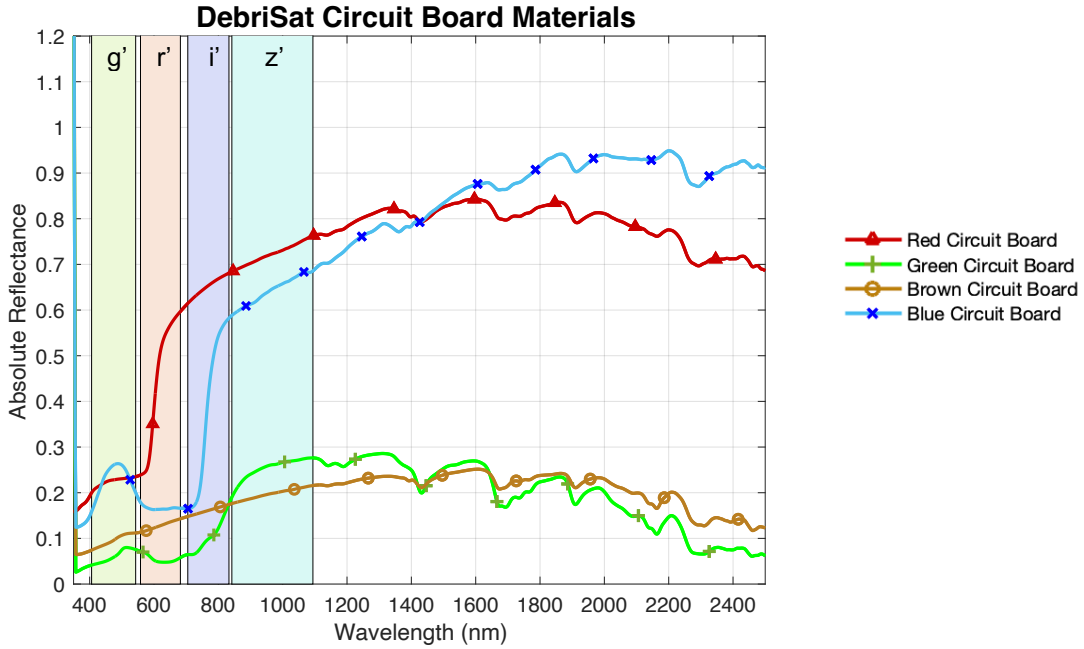

Figure 4.12: Absolute reflectance of various colored PCB samples in their pre-impact condition. The *g'*, *r'*, *i'*, and *z'* Sloan filter passbands are indicated in the spectral plot for future reference. *Credit: NASA*

Similar to the results seen in VIS for the painted 6061 aluminum alloy samples, the red, green, brown, and blue circuit boards used in DebriSat demonstrated optical properties between 350-700 nm that differentiate the materials by color (Figure 4.12). The red circuit board sample exhibited relatively high absorption at the onset of VIS before reaching ~650 nm where its signature increased. The blue and green circuit boards produced absorption throughout VIS except at 500 nm and 550 nm, respectively, where evident rise in reflectance occurred for the two materials. Adversely, the brown circuit board resulted in a signature largely absent of any noticeable features in VIS but still exhibited a level of increasing reflection. All four circuit board

samples produced common absorption features throughout the IR zone. The asymmetrical absorption doublets at ~1400 nm and ~1700 nm for the PCB's are likely associated with O-H bond vibration in the first overtone (associated with water) and C-H stretch in the second overtone (IR) region, respectively [178, 196, 39]. The prominent absorption detail at 1900 nm can be related to C-O or O-H bonds in the second overtone IR region [178, 196]. At 2180 nm, the asymmetrical absorption doublet is likely associated with N-H bends in the second IR overtone, or by C-H, C-O, or C=O stretches [178, 196]. This feature is more apparent in the green and brown circuit board samples. Absorption features located at 2300 nm and 2450 nm are associated with C-H and N-H stretches [134, 178], and OH absorption bands [201], respectively.

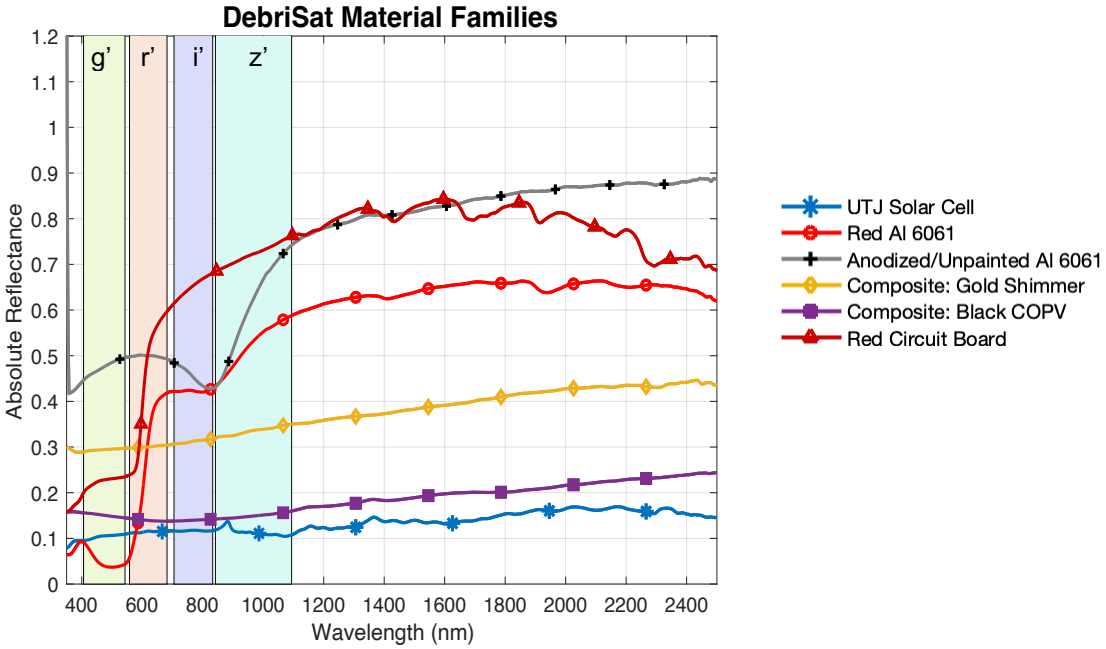

Figure 4.13: Absolute reflectance of various materials used for DebriSat in their pre-impact conditions. The *g'*, *r'*, *i'*, and *z'* Sloan filter passbands are indicated in the spectral plot for future reference. *Credit: NASA*

From the multiple DebriSat material samples analyzed, seven were selected in order to compare the reflectance signature of objects associated with different material classifications. These included a UTJ solar cell, an unpainted 6061 aluminum alloy, MLI polyimide (Kapton®),

and carbon fiber composites, one of which had a gold-shimmer surface finish and the other which did not. The red-painted 6061 aluminum alloy and red printed circuit board were also included to represent the colored alloys and circuit board categories of the DebriSat materials, respectively.

The UTJ solar cell demonstrated a consistently low reflectance curve throughout the full 350-2500 nm range of the spectrum (Figure 4.13), yet the solar cell is differentiated from all other materials by exhibiting a pronounced rise in reflectance at ~850 nm, indicating that the cell is germanium based [90]. Both composite samples produced similar reflectance responses to one another by remaining featureless throughout VIS and IR regions, though it can be noted that the composite having the gold-shimmer surface finish was two times greater in reflectance than the unfinished black COPV carbon composite, likely attributed to the gold shine on its surface. The red-painted Al alloy and red circuit board samples did not produce this increased reflection until reaching ~650 nm in VIS, as expected.

Of all materials measured, only the 6061 aluminum alloy samples resulted in absorption features at 850 nm in their reflectance signature, setting them apart as aluminum-related metals. The red-painted alloy produced absorption features between 1300-2500 nm that were absent in the unpainted alloy, differentiating painted and unpainted surfaces. The circuit board and painted aluminum alloys are the two materials that demonstrated the most evident organic features in their reflectance curves throughout the infrared range. This can likely be attributed to organic chemical content found in paints and polymer-based PCB's. Optical features present in the reflectance signature of a material in NIR and SWIR regions can be examined to differentiate between polymeric, metallic, composite, and semiconductor photovoltaic material classifications [39].

4.5.2. Space Weathered Environment

The reflectance signatures of Kapton® MT and Kapton® HN are presented in Figure 4.14 and Figure 4.15, respectively. The reflectance response of Kapton® MT was greatly affected by electron irradiation (Figure 4.14a). It can be noted, however, that the reflectivity did not waver between the irradiated and vacuum exposed conditions. Reflectivity seen in the irradiated and vacuum exposed conditions for the polyimide show an evident narrow absorption feature at ~750 nm, while absorption near this wavelength at 800 nm was broader in quality. All three reflectivity curves demonstrated strong absorption at wavelengths less than 550 nm in VIS followed by distinct rises in reflection at ~600 nm, which can be indicative of the sample having an orange physical appearance. Absorption at 1700 nm in the Kapton® MT sample in pristine, irradiated, and vacuum exposed states was also seen in the Kapton® HN polyimide sample (Figure 4.15a).

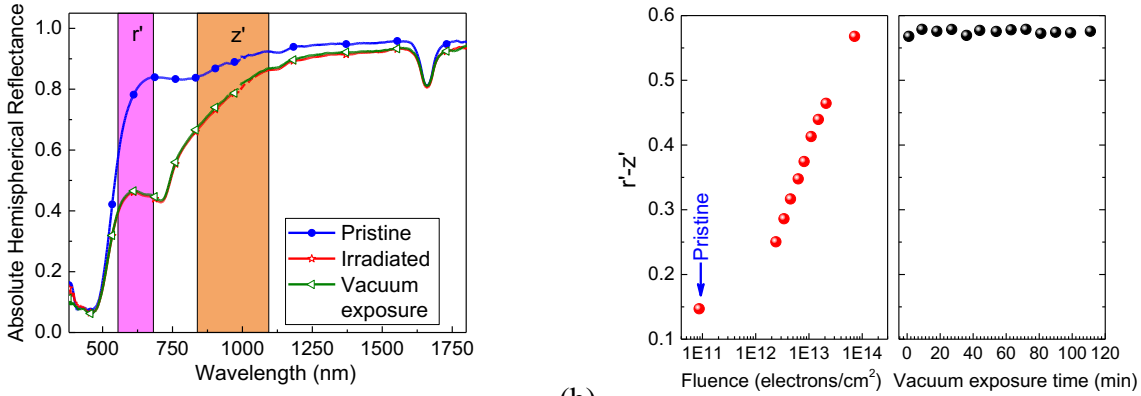

(a) (b)

Figure 4.14: (a) Absolute reflectance curves of Kapton® MT in pristine (blue), irradiated (red), and exposed to vacuum post-irradiation (green) conditions. (b) The *r'* and *z'* index using Sloan filters are displayed for Kapton® MT during electron irradiation (left) and vacuum exposure post-irradiation (right). *Credit: NASA*

Exposure to high energy electrons affected the *r'-z'* color index dramatically; resulting in an increase in value with the increase in electron fluence and ultimately reaching a value of 0.57

at a maximum fluence of 7.2 x 10^{13} e/cm^2 (Figure 4.14b). Once the irradiation exposure ceased, the Kapton® MT sample experienced no change in *r'-z'* throughout the 120 minutes of remaining in vacuum. This is contrary to what was optically exhibited from the behavior of Kapton® HN post-irradiation.

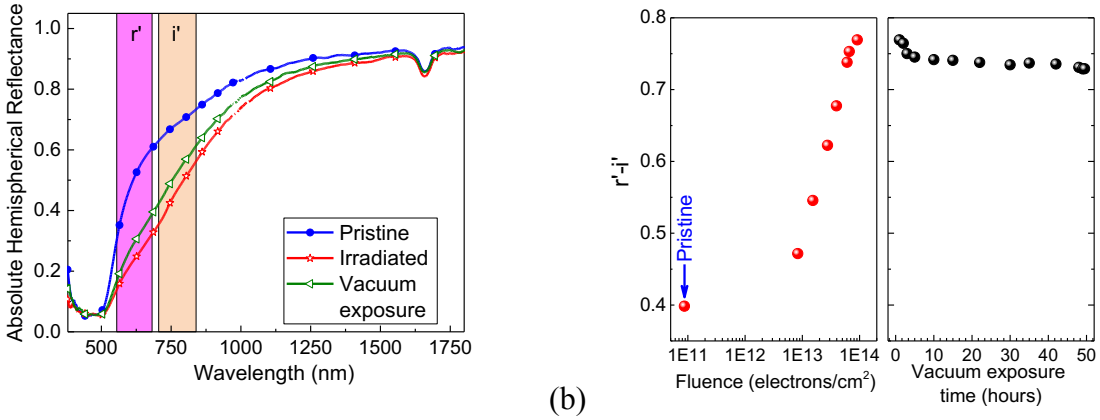

(a) (b)

Figure 4.15: (a) Absolute reflectance curves of Kapton® HN in pristine (blue), irradiated (red), and exposed to vacuum post irradiation (green) conditions. (b) The *r'* and *i'* index using Sloan filters are displayed for Kapton® HN during electron irradiation (left) and vacuum exposure post-irradiation (right). *Credit: NASA*

The Kapton® HN sample measured exhibited evident differences in reflectance values between 550-1500 nm (Figure 4.15a). Although the absorption feature at 1700 nm is shared between the two Kapton® samples measured in this study, it can be noted that the feature has less intensity in the Kapton® HN sample. This absorption characteristic is not affected by electron irradiation and indicates chemical content of the sample that would have been detected optically regardless of environmental condition. The pristine Kapton® HN material maintained the highest reflectance values in comparison to the irradiated and vacuum exposed signatures between the 350-1800 nm range, while the polyimide in its irradiated condition maintained the lowest reflectance throughout this same wavelength region. After the sample was allowed to sit in vacuum following irradiation, the material exhibited some level of recovery, resulting in reflectance values

higher than what was seen in the irradiated spectra. All three reflectivity curves demonstrate an increased slope beginning beyond 500 nm, attributed to the amber color characteristic of the polyimide, though the slope is much greater for the sample in its pristine condition.

Therefore, the aforementioned results generate large differences in brightness when comparing the passbands of *r'* and *i'* Sloan filters. This is shown by the increase in reddening with increasing electron fluence of *r'-i'* values (Figure 4.15b), with an initial value of 0.4 and increasing to 0.8 for an electron fluence of 2.5 x 10^{14} e/cm^2. Adverse to post-irradiation results of the Kapton® MT sample, Kapton® HN demonstrated recovery in optical behavior during the vacuum exposure period after irradiation. It can be noted that most of this recovery is seen in the first 6 hours of vacuum exposure.

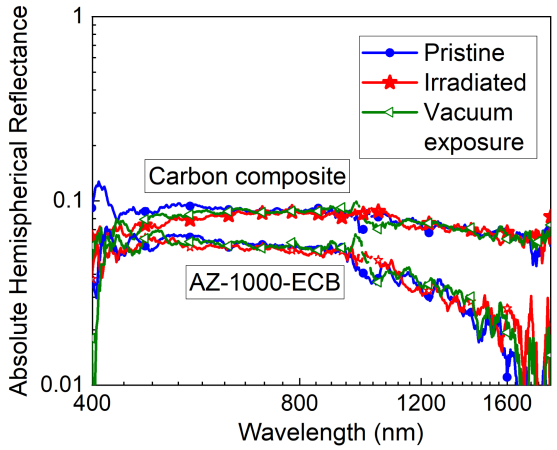

Figure 4.16: Absolute reflectance signature for carbon composite and AZ-1000-ECB black paint for pristine (blue), irradiated (red), and exposed to vacuum post irradiation (green) conditions. *Credit: NASA*

The carbon fiber-composite sample was dark black in physical appearance and for this reason resulted in high absorption throughout the VIS-NIR regions of the spectrum (Figure 4.16). Though not easily detectable, the composite had a small degree of higher reflectance between 400 to 850 nm in its pristine condition versus its irradiated or vacuum exposed post-irradiation

conditions. Within the 1000-1800 nm range in the IR, the composite produced similar optical reflectance results between all three environmental conditions measured.

Like the results obtained from the composite measurements, the AZ-1000-ECB black paint sample maintained low reflectance levels throughout the entirety of the spectrum plotted (Figure 4.16). There were no major optical behavioral differences that occurred for the paint amongst the pristine, irradiated, or vacuum-exposed measurements acquired. Note that the AZ-1000-ECB black paint and the carbon composite demonstrated an overall negative slope in their reflectance signatures when approaching IR regions of the spectrum.

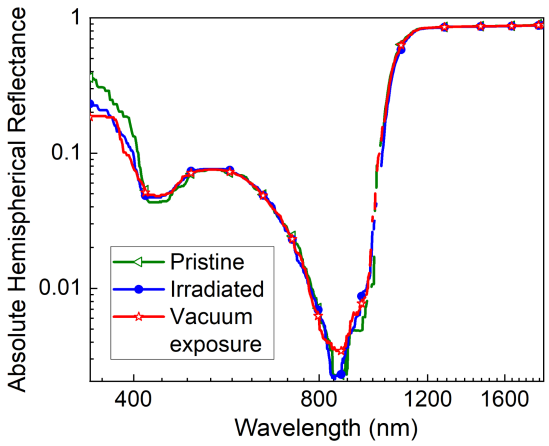

Figure 4.17: Absolute reflectance signature for solar cell coupon in pristine (blue), irradiated (red), and exposed to vacuum post irradiation (green) conditions. *Credit: NASA*

The solar cell coupon measured for this work presented a reflectance signature that is characteristic of the optical properties seen in silicon-based solar cells (Figure 4.17). This is confirmed by the significant value of absorption present in VIS between 400-1000 nm, followed by an evident increase in the reflectance curve slope beginning at ~1100 nm and maintaining higher amounts of reflectivity in the IR. Except for the region between 350-390 nm where the pristine and vacuum-exposed signatures exhibited only marginally higher reflectance than the irradiated signature, and the irradiated signature being marginally higher in reflectance at ~850

nm, the majority of the solar cell reflectivity remained largely unchanged between measurements obtained for all three conditions.

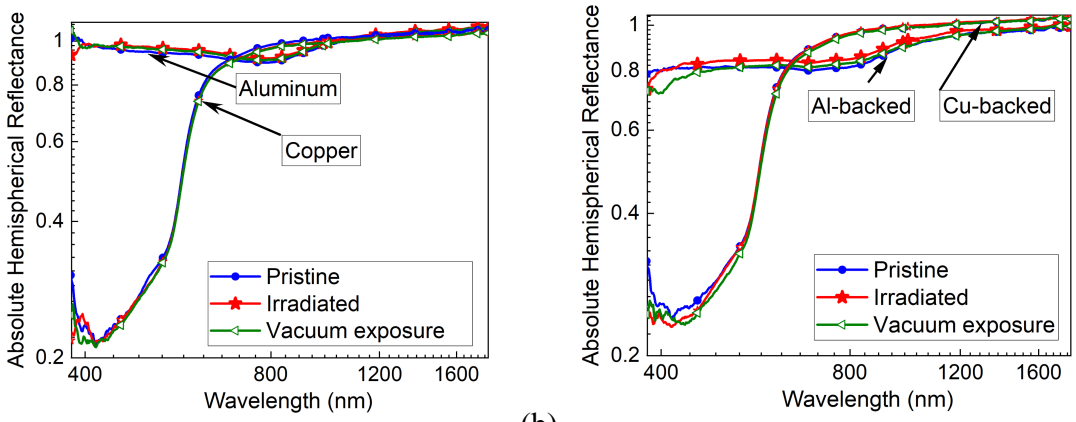

Figure 4.18: Absolute reflectance of (a) blank aluminum and copper foils, and (b) AR coated CMG coverglasses backed with aluminum and copper foils, in their pristine (blue), irradiated (red), and vacuum exposed (green) conditions. *Credit: NASA*

The CMG coverglass samples were backed with two different materials (aluminum and copper) to evaluate potential optical effects involved between the transparent and backed materials. For this reason, the backed materials had their surfaces measured in their bare state (Figure 4.18a) and when topped with a sheet of coverglass (Figure 4.18b). As expected, the bare aluminum sample produced a level of absorption near 850 nm consistently throughout the three different measurement readings. It should be recognized that the reflectance response of the aluminum sample maintains a reflectance magnitude close to 1.0, serving as a favorable mirror. After the aluminum sample underwent high energy electron bombardment, there was a marginal increase in reflection throughout the 450-1800 nm range. After irradiation ceased and the sample was allowed to sit in vacuum for 49.7 hours, its reflectance signature was only scarcely lower than the irradiated measurement and higher than the pristine measurement. These results were not seen in any other samples included in the space-weathered environment observations.

An evident steep rise in the reflectivity slope at ~600 nm exhibited by the bare copper sample in VIS is agreeable with its orange color property (Figure 4.18a). The copper sample demonstrated high reflectance near 1.0 in the near IR beyond 1000 nm. The signature for this material did not waver throughout the various environmental conditions it was subjected to for the experiment. In comparison to the bare aluminum sample, the copper material, though maintaining a stable reflectance throughout the GEO space-weathered simulation and reaching near perfect reflectivity (1.0) beyond 800 nm, does not act as a favorable, mirror-type metal due to its color signature, which interferes with the ability to detect reflectance features in VIS that could potentially be produced by an overlaid material such as coverglass. It is significant to deduce these color differences when employing ground-based observations as described in [202, 203], where (V-Rc) color index for the GAIA spacecraft indicated reddening that was contrary to the Planck spacecraft that was used as an observational reference for GAIA but caused an inaccurate comparison.

The copper-backed CMG coverglass sample yielded reflectivity results (Figure 4.18b) identical to what was demonstrated in the bare copper sample (Figure 4.18a). The aluminum-backed CMG sample resulted in evidently lower absolute reflectance with values of ~0.8 in VIS and ~0.95 in the IR regions of the spectrum (Figure 4.18b), contrary to the near perfect reflectance (almost 1.0 between 350-1800 nm) that was exhibited in the bare aluminum sample (Figure 4.18a).

Any wavelengths in Figure 4.18 that display a reflectance marginally exceeding unity are indicative of the sample resulting in reflectance slightly more than what was produced by the Spectralon reference material in the IR. Spectralon material ideally serves as a reference since they are spectrally flat, Lambertian reflectors. Therefore, one reason for a material producing reflectance in excess of unity can be attributed to the nature of a sample producing a more specular

response than what was generated by the Spectralon, indicating a degree of saturation in reflected light being delivered to the detector. An additional possibility for this to occur can be due to using a Lambertian reflector that has been utilized for extended time and is therefore due for proper manufacturer refurbishment to renew its surface and remove any potential artifacts that could be causing interference with the Spectralon material.

4.6. SUMMARY

An overview of the laboratory settings for measurement acquisition and experiment setups and methods was outlined. The space-grade related materials selected for evaluation in this study had their reflectance signature results plotted and presented as figures within the chapter. This data was focused within the visible and near-infrared regions of the spectrum and included reflectance signatures for materials in their pristine conditions. Additionally, a select number of materials were measured in a GEO- simulated, space-weathering environment and had their results reported. All materials investigated have been described. A discussion of each of these material results was elaborated upon for greater understanding.

Chapter 5: Material Discrimination Approach Methods

This chapter focuses on the characterization of commonly used space-related materials optically via their color indices. The objective is to study discrimination using color indices. This was encouraged from a materials taxonomy standpoint that gives reason for the particular number and type of materials selected that belong to different classes or material groupings. The material color indices were calculated using the spectral reflectance measurements included in Chapter 4. Various filter passbands used for color index calculations are explored, as well as theoretical passbands to study potential passbands with better material discrimination capabilities.

5.1. Overview of Taxonomy

It has been well established that spectroscopy and analysis of material reflectance behavior can be used for material characterization [5, 80, 82, 178, 204]. However, there is room to enhance spectral data within spectral libraries that can advance the ability to group/sort materials that possess similar optical features into families. If this can be accomplished by utilizing data provided from reflectance spectra and color index then this could potentially advance the efficiency in material assessment based on physical properties in general, such as density.

This aim would entail identifying optical trends between material spectral features that suggest information regarding density or other intrinsic physical material properties that can be used to distinguish materials by classification. For example, polymeric materials demonstrate a large number of absorption features in the IR due to the nature of their chemistry, compared to the absence of these features seen in metals and ceramics, as well as select composites. Polymers are softer materials compared to those of higher density that fall within other classifications. If certain materials, such as polymers, can be isolated when plotting color index after deriving those values from their spectral reflectance, then that can be a step forward toward providing a means of analysis focused on risk assessment when observing orbital debris.

Taxonomy refers to the ability to organize matter into groups by means of classification. Methods regarding material classification by related optical means have been attempted by [205] for the ultraviolet (230 nm)-visible (700 nm) region using principal component analysis (PCA) for textile fibers. Similarly, such efforts have also been made by [206] for urban materials with a focus on mineral classification. However, classification analysis within the SDA branch of study has been performed by [207] with a focus on using Johnson/Bessell filters to assess materials of certain area-to-mass ratio (AMR). This can be expanded for specific space-grade materials throughout the VIS, NIR, and SWIR regions of the spectrum using select astronomical filter passbands with intention to deliver color index values from reflectance signatures as a means for taxonomy.

With the large variations in artificial space materials (not just in composition, but also in coated/painted surfaces), it becomes increasingly difficult to correlate optical measurements of targets from ground-based assets to that of nearly 1,000 laboratory acquired measurements [188] available [39]. If RSOs can be sorted into metals, polymers, ceramics, etc., from their reflectivity curve, this can support the improvement of spectral libraries in a manner where input spectra of unknown origin can be appropriately matched by class and therefore allows for a degree of suggested properties to be associated with the nature of the article. Thus, having knowledge of taxonomy-based relationships between orbital debris materials that are observed remotely can be advantageous when deducing hazards associated with a given material, which is traveling at elevated speed in orbit, if information related to that object's density can be provided.

5.2. Attempting Material Classification via Laboratory Measurements

A first attempt at identifying optical trends with a focus on material taxonomy using SDSS/Sloan astronomical filter passbands was undertaken in [39] The data used in this study was strictly pertaining to materials used in the construction of the DebriSat article. The 14 materials

that were optically measured (Table 4.2) provided a substantial variety and fell under several different branches of material classifications. The organization of the material classifications is presented in the form of a hierarchal diagram in Figure 5.1. Selected materials that represented these different material groups had their reflectance signature presented in Figure 4.13.

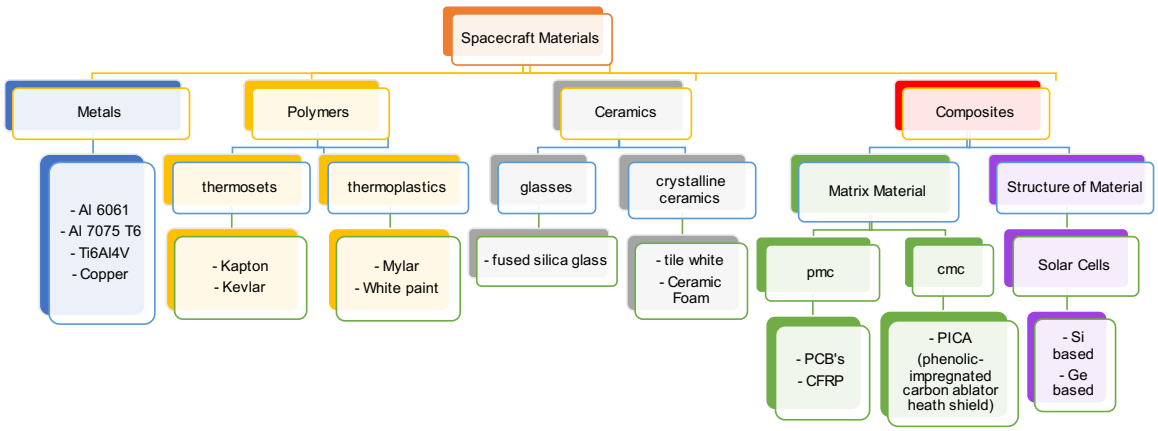

Figure 5.1: Material classification hierarchical diagram listing all materials included in taxonomy analysis via optical measurements.

In an effort to group these materials into families by color value, color indices were calculated for each material using Sloan filters. When color index *r'-i'* was plotted against the *g'-i'* index (Figure 5.2a), the painted 6061 aluminum alloys have *g'-i'* and *r'-i'* values greater than 0.76 and 0.09, respectively. All circuit board materials analyzed, regardless of color, resulted in *r'-i'* values between 0.039-1.07 and *g'-i'* values between 0.49-1.09, causing them to be clustered in a group on the *r'-i'* versus *g'-i'* color plot. Plotted at the lower left corner of the *r'-i'* versus *g'-i'* plot are the remaining materials, including solar cell, unpainted anodized 6061 Al alloy, and composite samples, which averaged a value of 0.156 in distance between these points on the color-color diagram.

Distance values between color indices for this work were calculated using the *Euclidian metric* equation [208]:

$$d_e((i,j),(h,k) = \sqrt{(j-i)^2 + (k-h)^2}$$

where variables $i, j, h,$ and k represent the different filter passbands used to create the two different color indexes used to plot against each other on color-color diagrams. The first color index passbands would be represented by the i and j variables, and the second color index passbands would be represented by the h and k variables in the *Euclidian metric* equation.

The solar cell and composites demonstrated a consistently low reflectance response throughout the *g', r'*, and *i'* filter passbands (Figure 4.13). It can be noted that the unpainted anodized 6061 aluminum alloy sample resulted in a color index that separated the metal from all other painted alloys on the *r'-i'* versus *g'-i'* plot, with an average distance of 1.958 between it and all other aluminum alloy indices. This can be attributed to the reflectivity curve of the unpainted 6061 Al alloy demonstrating higher reflectance values within the *g'* passband (Figure 4.11). This information can be used to help differentiate between painted and unpainted aluminum alloy surfaces optically. Distance values between all material indices can be found for each plot in the Appendix (Table A. 2).

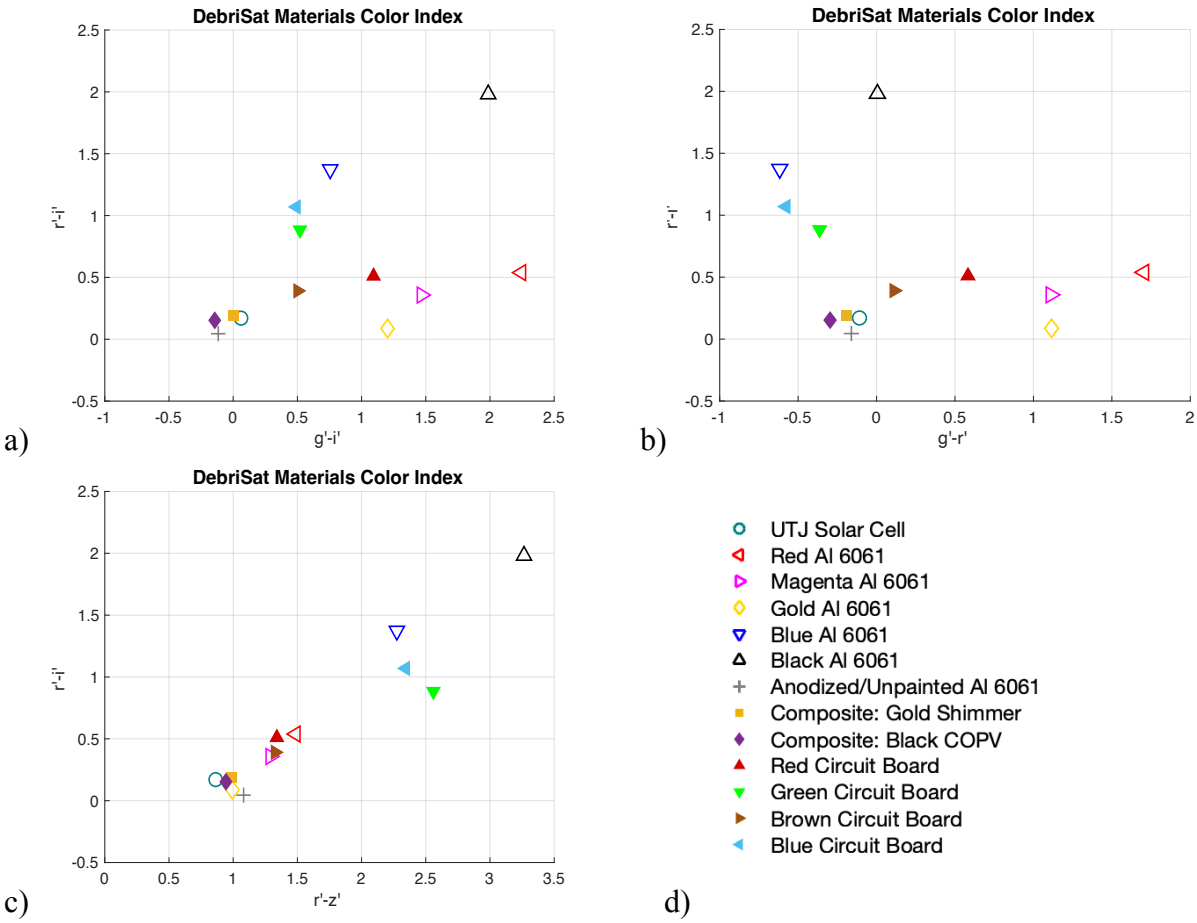

Figure 5.2: The a) *r*'- *i*' versus *g*'- *i*' color index plot, b) *r*'- *i*' versus *g*'- *r*' color index plot, and c) *r*'- *i*' versus *r*'- *z*' color index plot using SDSS filters for all measured DebriSat material samples in this study. Legend (d) outlines the materials and stars being plotted. *Credit: NASA*

In addition to the *r'-i'* versus *g'-i'* plot, color indices were calculated and plotted for *r'-i'* versus *g'-r'* (Figure 5.2b) and *r'-i'* versus *r'-z'* (Figure 5.2c) to compare and understand trends from their respective results. It can be seen that these two color plots did not yield results that were as effective in supporting the grouping of materials via taxonomy. For both the *r'-i'* versus *g'-r'* and *r'-i'* versus *r'-z'* color plots, the painted 6061 Al alloys resulted in color values that were varyingly scattered throughout the plot, located amongst materials of other classification which increased difficulty in arranging the samples by metal or polymeric categories. The average distances between the unpainted 6061 Al alloy and all other painted Al alloy points on Figure 5.2b

and Figure 5.2c were also not as large, resulting in an average distance of 1.573 and 1.163, respectively. The solar cell, unpainted Al alloy, and composites demonstrated color indices that caused for them to remain located near each other for all color plot demonstrations (Figure 5.2a, Figure 5.2b, Figure 5.2c). Values for the distances between this clustering of materials resulted in 0.156 for Figure 5.2a, 0.140 for Figure 5.2b, and 0.144 for Figure 5.2c. Note that the gold painted 6061 aluminum alloy produced color values that were similar to those of the solar cell, unpainted aluminum alloy, and composites, with an average distance value between it and the others of 0.110 for the *r'-i'* versus *r'-z'* color plot therefore, making this plot unsuited for arranging materials per classification using color indices. Of the three color index plots generated to represent the optical behavior of selected DebriSat material samples using Sloan filter passbands, the *r'-i'* versus *g'-i'* plot presented results that were most supportive in grouping materials with similar properties together.

To extend this approach, an added number of materials were included to the color index analysis generated for DebriSat; materials which met a wider variation that specifically fell under the various material classification hierarchy (Figure 5.1). Additional materials included 7075 T6 aluminum alloy, Ti6Al4V, copper, Kapton, Kevlar, Mylar, fused silica glass, white tile, ceramic foam, PICA, and silicon based solar cell. A comprehensive list of all materials included in the taxonomy analysis via optical measurements are listed with detail in Table 5.1.

Table 5.1: Materials included in taxonomy application listed and described.

Material Sample	Density (g/cm^3)	Class
6061 aluminum alloy	2.70	Metal (alloy)
7075 T6 aluminum alloy	2.81	Metal (alloy)
Copper	8.93	Metal
Ti6Al4V	4.43	Metal (alloy)
Kapton	1.42	Polymer (thermoset)
Kevlar	1.47	Polymer (thermoset)
Mylar	1.39	Polymer (thermoplastic)
Circuit Board Green		Polymer matrix composite
Circuit Board Blue	1.90-2.23 (depending on	Polymer matrix composite
Circuit Board Brown	laminate)	Polymer matrix composite
Circuit Board Red		Polymer matrix composite
PICA	0.224-0.321	Ceramic matrix composite
Fused Silica Glass	2.20	Ceramic
Ceramic Foam	0.70	Ceramic
Solar cell coverglasses (CMG,	2.54-2.60	Composite structure
CMO, CMX)		(layers)
CFRP	1.80	Composite

5.2.1. Reflectance Spectra per Classification

Material spectra have been acquired for the various metals, polymers, ceramics, and composites that are more often seen in the aerospace industry. In this section, the reflectance signatures in the spectral plots for these materials are separated by classification, with each plot depicting each Sloan *griz* passband respectively. The derived color index results that are to be presented in the following sections. Also to note is any spectra that may have resulted in absolute reflectance greater than values of unity. This is due to the nature of said material being highly specular, delivering a saturated reflectance response to the detector and simply being greater than the lambertian response calibrated by the Spectralon.

Metals often result in a reflectance response that is rather featureless in the IR regime with the absence of organic features. One of the more significant features to be considered is the absorption feature present at 850 nm that can discriminate aluminum-based metals from other metals. This is shown in Figure 5.3a where the two aluminum alloys have an absorption feature at 850 nm while the copper and titanium alloy do not. Copper can be isolated from other metals due

to its characteristic red-orange optical hue, and this is represented by absorption at the onset of VIS with an increase in reflection near 600 nm. Other than color features in VIS and the aluminum absorption feature in NIR, the reflectance signatures for the metals were predominantly featureless in the IR. This behavior is typical of unpainted metals.

It can be deduced that polymeric materials are clearly different in reflectance response than materials belonging to other classifications. The reason for this is evident in the substantial amount of absorption feature in the infrared region of the spectrum. From the multiple polymers selected for measurement, there are quite a few absorption features present at specific wavelengths that are shared between the various polymers (Figure 5.3b). For example, at 1900 nm, all polymers exhibit some level of absorption, though it is most prominently seen in the Kapton, Kevlar, and white paint materials, and noted as a doublet from the Mylar sample. There are also a number of absorption features that are specific to certain polymers. For example, the Kevlar sample demonstrated prominent absorption at ~1500 nm, whereas the other polymer samples were absent of this characteristic. Further, though all selected polymers exhibit some degree of absorption at ~1650 nm, it is apparent that Mylar exhibits this to the highest magnitude when compared. As previously analyzed in Section 4.5.1, the four printed circuit boards (PCB's) measured resulted in analogous absorption responses throughout the IR.

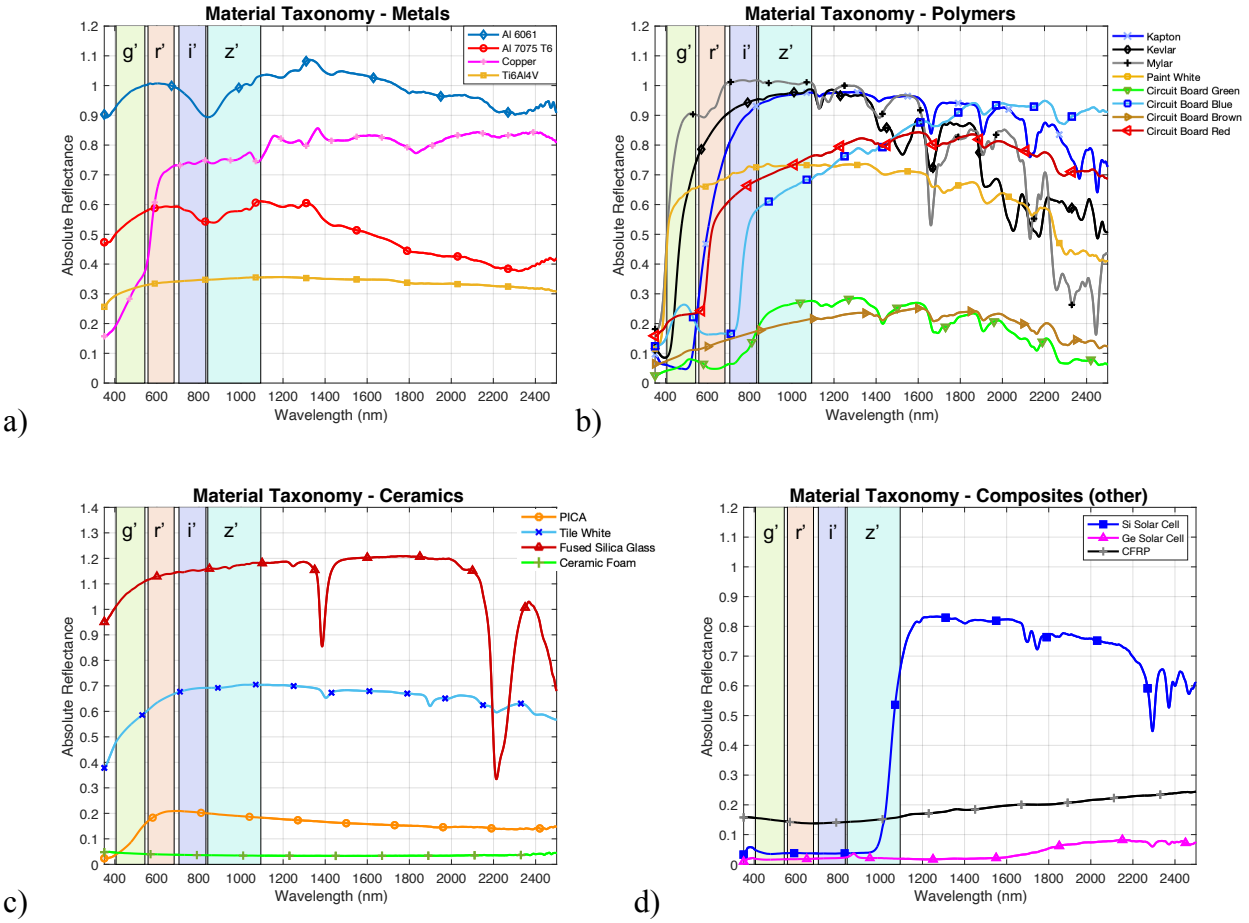

Figure 5.3: Absolute reflectance spectra for various materials divided into a) metals, b) polymers, c) ceramics, and d) composite structure. Sloan *griz* passbands depicted within the 400-1100 nm regime. *Credit: NASA*

The selected polymer materials for analysis provided multiple spectral features in the VIS regime. The Kapton and red PCB samples show increased reflection at 650 nm, and white paint and Mylar samples resulted in high reflectance at the onset of VIS before 400 nm. The blue and green PCBs reflected in VIS at 450 nm and ~525 nm to coincide with their optical color property as well.

Analysis of the selected ceramics in this study showed that they are similar to metals in optical behavior due to lacking numerous organic absorption features in IR and maintaining relatively constant reflectance throughout the 350-2500 nm range (Figure 5.3c). The fused silica

glass sample was an exception for only two strong absorption features present at ~1400 nm and 2200 nm due to O-H and C-H bonds, respectively. There is weak spectral absorption present for the white tile material at 1400, 1900, and 2200 nm, though not as evident as the clear organic feature presence in polymeric materials. The PICA and ceramic foam materials remained featureless throughout the full measurement range and exhibited much lower reflectance values relative to the other two ceramics measured.

Though PICA and the printed circuit boards are technically considered composite materials, they are being analyzed as ceramics and polymers respectively due to the detector measuring the characteristics of a material surface. PICA is a ceramic matrix composite, and the PCBs are polymer matrix composites. This indicates that the composite material introduced is embedded within the material matrix, therefore making it worthy to analyze PICA as a ceramic and the circuit boards as polymers. Therefore, the materials analyzed as composites are related to composite structure in terms of their configuration. These included solar cells with either Si or Ge substrate components, and CFRP, which although a polymer matrix composite, is comprised of fibers woven in a specific orientation to strengthen said material.

The silicon-based photovoltaic responded as expected (Figure 5.3d), with high absorption throughout VIS and up to 1000 nm, followed by a sharp increase in reflection at 1000 nm, while demonstrating absorption features at 1700 nm and throughout the 2250-2500 nm range. Also consistent with its typical response are reflectance results from the solar cell of germanium substrate, producing extremely high absorption throughout the full 350-2500 nm range with a sole, small peak feature at 850 nm. Lastly, the carbon fiber reinforced polymer (CFRP) composite maintained a relatively low reflectance with no additional features to note.

Due to the obvious nature of polymers producing reflectance signatures high in organic feature content compared to other materials, and since polymers are in general lower in density than materials of other categories, the aim was to find any optical trends to use in performing risk assessment of materials that could be labeled as orbital debris, thus providing an ease of understanding these potential hazards through observations for space situational awareness. Since a common way of characterizing objects via observations is performed through color-color diagrams, it was worthy to potentially identify optical trends using said plots to possibly better discriminate between various materials. This was first explored in [39], and will be furthered in Sections 5.2.2 and Section 5.2.3.

5.2.2. Astronomical Filter Comparisons

All color-color diagrams presented in this and the following section display color index values that were derived from the reflectance spectra presented in Figure 5.3. Additionally, the color indices for our perfectly lambertian material Spectralon are included in the color-color diagrams to serve as a reference. The color-color diagrams generated use the Sloan filters since they have narrow and non-overlapping passbands, making them, in some ways, preferred for remote observations. Furthermore, they have not been as thoroughly explored as Johnson/Bessell filters that have been well utilized and developed over a longer period of time. For this reason, the *g', r', i'*, and *z'* Sloan filter passbands are denoted on reflectance plots in Section 5.2.1 for convenience.

Although the aim for this taxonomy is to determine material trends using Sloan filter passbands, it was first sought to compare the original results from [39] with comparable Johnson/Bessell filter passbands to evaluate any differences. The Sloan *r'* passband range is from 558-682 nm, and the Johnson filter most closely related is that of V, ranging from 450-700 nm.

Similarly, the *i'* passband (705-836 nm) and *g'* passband (406-544 nm) from Sloan can be closely, though not ideally, compared to the R (560-1060 nm) Bessell filter and the B (350-600 nm) Johnson filter. Hence, the *r'-i'* versus *g'-i'* color plot was compared to the V-R versus B-R color plot (Figure 5.4). From this comparison, many things can be noted.

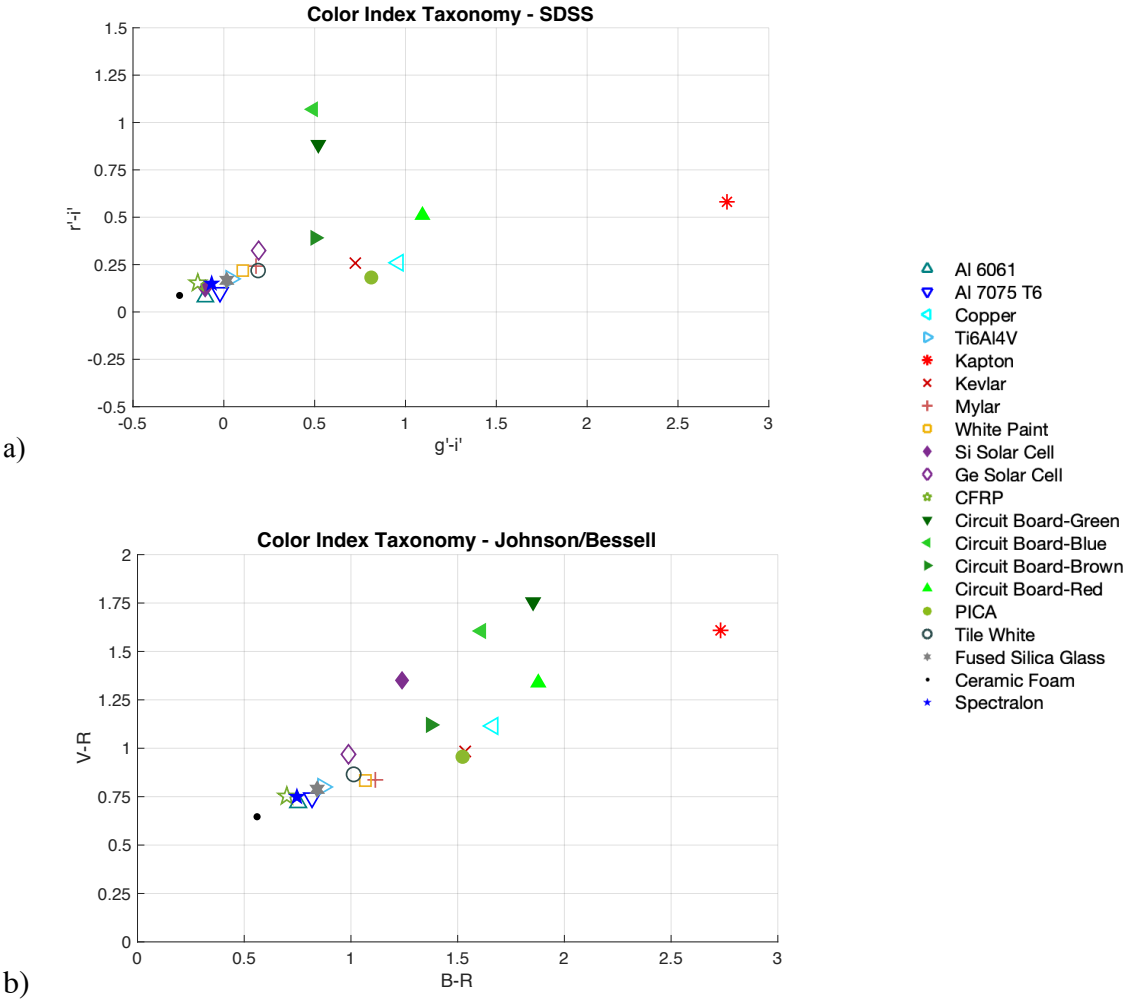

Figure 5.4: Color-color diagrams using a) Sloan Digital Sky Survey (SDSS) filter passbands, and b) Johnson/Bessell filter passbands. *Credit: NASA*

From a material trends standpoint, the SDSS plot (Figure 5.4a) produced more clusters than the Johnson/Bessell plot (Figure 5.4b). This can be seen in the separation between the circuit board materials from most others, and the Kapton sample is more isolated, resulting in a *g'-i'* index value

over twice as what resulted from the B-R index. The smallest distance between Kapton and any other material on the *r'-i'* versus *g'-i'* diagram resulted in a distance of 1.678 between it and the red circuit board, whereas the smallest distance for Kapton and other materials on the V-R versus B-R diagram concluded in a distance value of 0.891 between it and the green circuit board, therefore making Kapton greater in separation for the *r'-i'* vs. *g'-i'* plot. All distance values between indices for Figures 5.4a and 5.4b can be found in Table A. 8 and Table A. 9 in the Appendix. On another note, the scatter for discriminating between the circuit boards is better for *r'-i'* than for *g'-i'* when comparing between the SDSS indices, but in analyzing the Johnson/Bessell indices, there is scatter between the PCBs in both V-R and B-R indices, as well as for materials throughout the plot overall. This comparison was first performed to gain an understanding of to what degree a material color value is dependent upon the set of astronomical filters used and passband range has a substantial effect on these outcomes.

5.2.3. Material Patterns via Color-Color Diagrams

The objective to potentially isolate materials belonging to certain classifications will be discussed in this and the following section. This section will focus on assessing the usage of a combination between SDSS and Johnson/Bessell filter sets with UKIRT filter passbands serving as a guide for passbands in the IR to further compare their use in successfully isolating specific materials. Though astronomical filter sets are selected based upon response from the detector, the use of incorporating filter qualities from different measuring systems has been explored previously. This has been done by [209] to design a filter that resembled the function of a Sloan *z'* passband but that performed for the Wide Field Camera, as well as by [210], which used SDSS filters along with J-band photometry independently to produce color-color diagrams to better evaluate simulated quasar colors with respect to redshift. Therefore, the use of UKIRT passbands

that represent significant portions of the IR regime will serve as a guide and will be explored and incorporated in a theoretical sense.

The first combinations of filter passbands were selected for color-color diagrams with a focus on isolating solar cell materials. Of all combinations of the Johnson/Bessell UBVRI and UKIRT ZYJHK filter passbands, the Z-R versus Z-H and I-Y versus H-K color-color diagrams provided results that performed well in separating photovoltaics from all other materials. The Z-R vs. Z-H plot exhibits the clustering of all materials measured where the average Z-R is 1.79 and the average Z-H is 1.32, with the exception of the silicon solar cell that has a Z-R value of 2.42 and a Z-H value of 4.57 (Figure 5.4a). The distance between the silicon solar cell index and the closest material (CFRP) index resulted in a value of 3.016. Additionally, the I-Y versus H-K color-color diagram showed much clustering of materials in the -0.3 - +0.35 range for H-K and at an I-Y average of -1.44 with the exception of the silicon and germanium solar cells, as well as the green circuit board. For this diagram, the distance between the silicon solar cell and its nearest material index (blue circuit board) resulted in 0.661, and the distance between the germanium solar cell and the material closest to it in color index (CFRP) resulted in a value of 0.862. It can be further noted that the silicon and germanium photovoltaics are separated from one another, having an overall distance of 1.501 between them, with the silicon-based solar cell resulting in an I-Y value of -0.65 and an H-K value of 0.01, while the germanium solar cell had I-Y and H-K values of -1.57 and 1.20, respectively.

a)

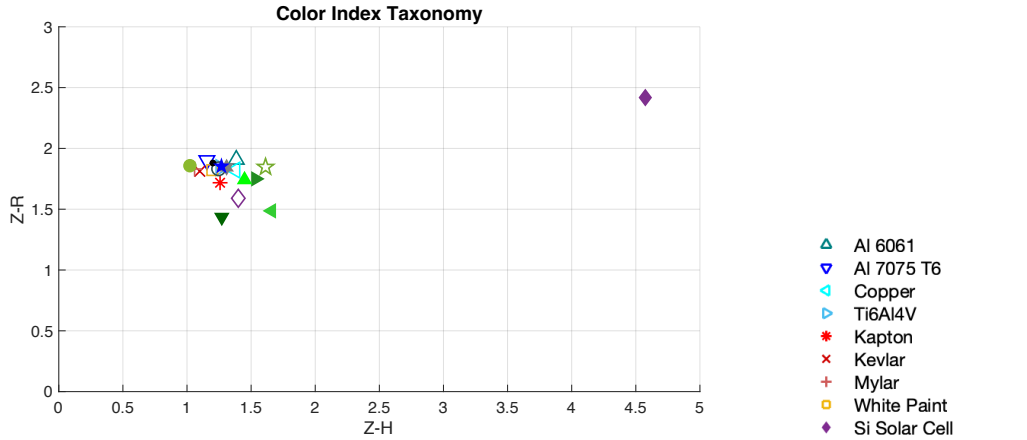

b)

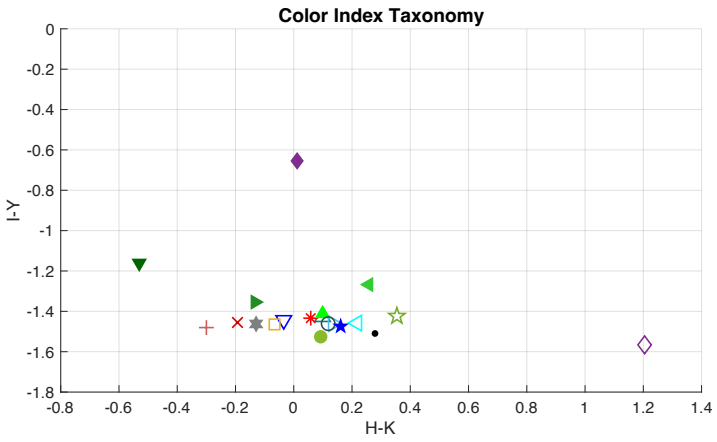

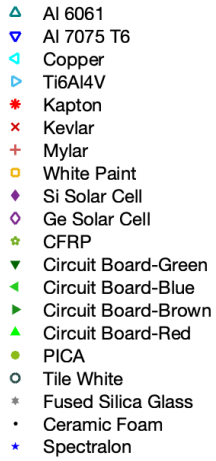

Figure 5.5: Color-color diagrams for a) Z-R and Z-H color indices, and b) I-Y and H-K color indices according to their respective filter passbands. *Credit: NASA*

a)

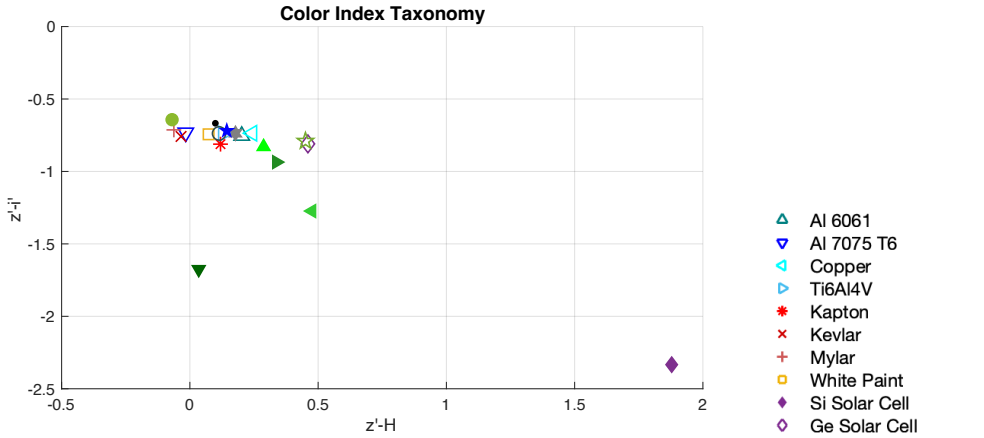

b)

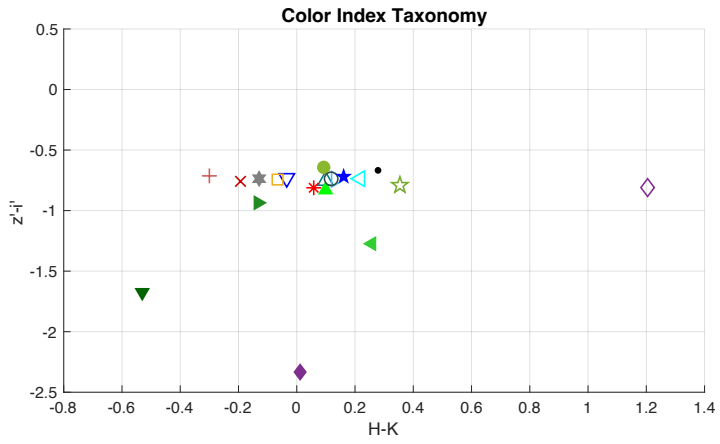

Figure 5.6: Color-color diagrams for a) *z'-i'* versus *z'*-H color indices, and b) *z'-i'* versus H-K color indices according to their respective filter passbands. *Credit: NASA*

To further evaluate these trends in color values for photovoltaics, Sloan filters with passbands comparable to Johnson/Bessell filters used in color-color diagrams for Figure 5.5 were used to generate plots in Figure 5.6, which resulted in similar material trends. The *z'-i'* versus *z'*-H diagram demonstrated the isolation of the silicon solar cell sample, having a *z'-i'* index of -2.33 and a *z'*-H color value of 1.88 (Figure 5.6a). The silicon solar cell and the material it was closest in value to (blue circuit board) resulted in 1.758 for this color-color diagram. Both solar cell samples were isolated separately for the *z'-i'* versus H-K color-color diagram, where the Si and Ge photovoltaic resulted in a H-K value of 0.01 and 1.20 (Figure 5.6b), respectively. The

distance between the Si solar cell and the material closest in color index value (green circuit board) was determined to be 0.852, while the distance between the Ge solar cell and material nearest in color index (CFRP) resulted in 0.851.

Promising results in isolating the photovoltaic materials were found in color-color diagrams of Z-Y vs. Z-H, and *z'*-Y vs. *z'*-H, when considering comparison between the UKIRT Z band and Sloan *z'* band. These two aforementioned plots are included in Figure 5.7. For the Z-Y versus Z-H diagram, the distance between the silicon solar cell and the material nearest in color index (blue circuit board) resulted in a large value of 3.545. Similarly, for the *z'*-Y vs. *z'*-H color plot, the silicon photovoltaic demonstrated a distance of 1.491 between it and the blue circuit board, which was the material closest in color index value to itself, though exhibiting isolation to a lesser degree than what was seen in the Z-Y versus Z-H plot.

a)

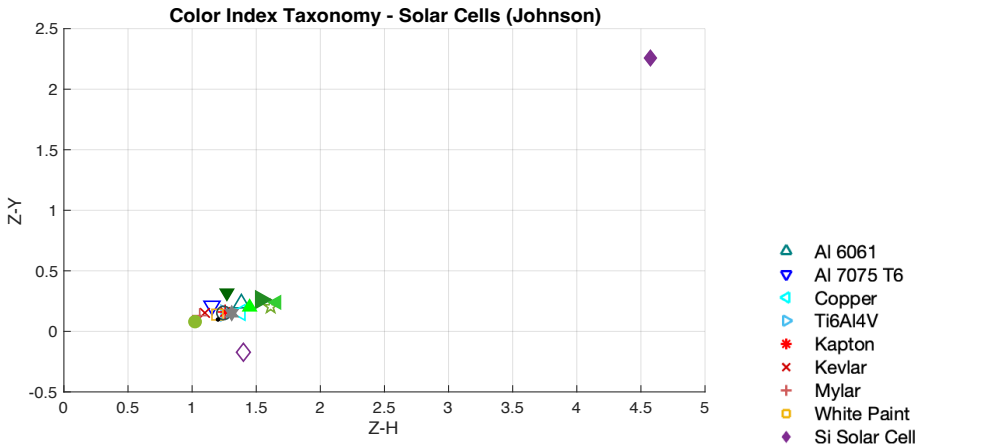

b)

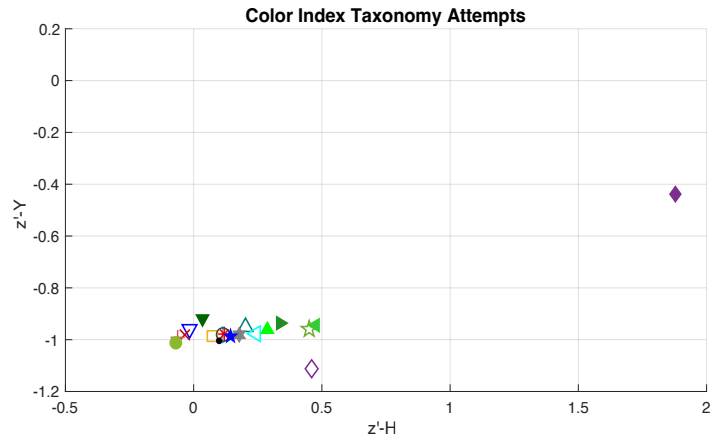

Figure 5.7: Color-color diagrams for a) Z-Y versus Z-H color indices, and b) *z'*-Y vs. *z'*-H color indices according to their respective filter passbands. *Credit: NASA*

Color indices can be used to isolate Kapton, a common space material that is used individually or included in multi-layer insulation (MLI) structure. Examples of this analyzing are in the V-R versus B-R Johnson/Bessell filter color-color diagram (Figure 5.4b), as well as the Sloan *r'-i'* versus *g'-i'* diagram (Figure 5.4a). Though the color value of Kapton could not be distinguished from the *r'-i'* and V-R indices, there is much separation in index from other materials for the *g'-i'* and B-R indices. Kapton resulted in a *g'-i'* value of 2.77 and a B-R value of 2.73.

a)

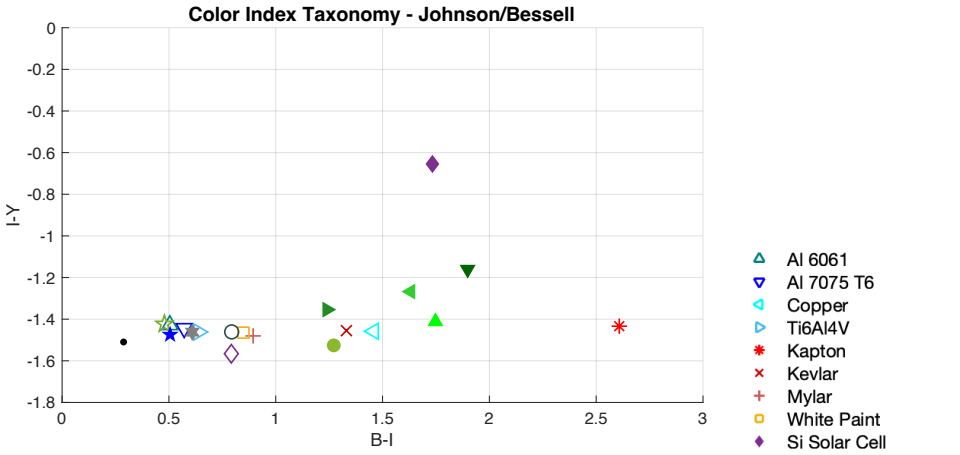

b)

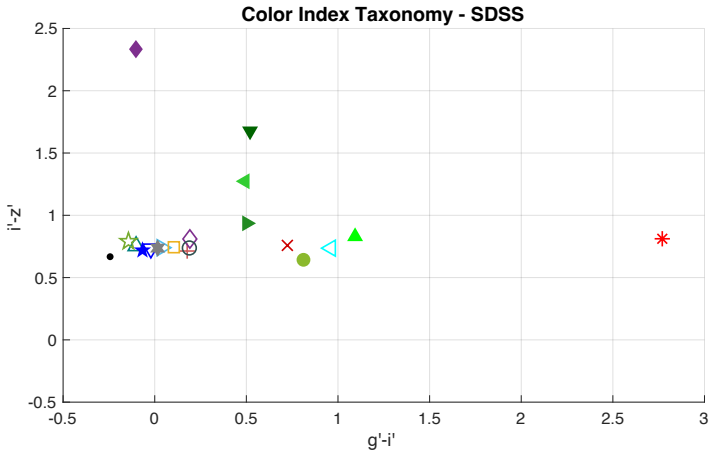

Figure 5.8: Color-color diagrams for a) I-Y versus B-I color indices, and b) *i'-z'* and *g'-i'* color indices according to their respective filter passbands. *Credit: NASA*

Kapton can also be isolated by color to some degree in generating I-Y versus B-I and *i'-z'* versus *g'-i'* diagrams (Figure 5.8). As previously seen, the Sloan *g'-i'* index works well in providing separation of Kapton from all other materials included in analysis. The distance between the polyimide and the red circuit board, which was the material closest in color index, resulted in 1.676 in value for the *i'-z'* versus *g'-i'* color-color diagram. For the I-Y versus B-I plot, the distance between Kapton and the material nearest in color index (green circuit board) had a value of 0.760, demonstrating much less separation of Kapton with all other materials than what can be seen in the *i'-z'* versus *g'-i'* diagram. Though to a lesser degree than what resulted from the B-R index,

Kapton still resulted in a much higher value between all materials measured, with a B-I of 2.61, while the other materials did not result in a B-I value greater than 1.90. The I-Y and *i'-z'* indices were not useful in isolating Kapton but did result in separation of the silicon solar cell, which had an I-Y value of -0.65 and an *i'-z'* value of 2.33.

5.2.4. Material Discrimination Attempts using Various Narrow Passbands

In an effort to attempt separating materials by color index further, a set of narrow passband regions were designated for exploring combinations of indices that could potentially provide better scatter or trends from materials of various classifications. These passbands are not representative of any current astronomical measuring system and were used only to provide various color-color diagram results of the selected materials measured. The wavelength regions chosen for this analysis were of variable range, depending upon which presumed magnitude within those ranges would yield better results, and are designated as either "V" or "IR" to represent the visible and infrared regions of the electromagnetic spectrum these variable passbands fell within. The nomenclature and corresponding wavelength range for these theoretical passbands are outlined in Table 5.2. A total of 20 different wavelength ranges were selected for this study and were explored with intentional combination depending on spectral features in the material reflectance signature.

Table 5.2: Passband variables used in attempt to better identify material trends optically.

Passband Variable Nomenclature	Wavelength Range (nm)	Passband Variable Nomenclature	Wavelength Range (nm)
V1	400-500	IR7	1500-1600
V2	400-600	IR8	1600-1700
V3	600-800	IR9	1800-2000
V4	700-800	IR10	2000-2100
IR1	800-900	IR11	2100-2200
IR2	900-1000	IR12	2200-2300
IR3	1000-1100	IR13	2200-2450
IR4	1100-1200	IR14	2300-2450
IR5	1200-1300	IR15	2350-2450
IR6	1400-1500	IR16	2400-2500

The first round of material discrimination attempts via color index from a taxonomy standpoint were focused on isolating the aluminum materials from all others. This was endeavored since it is well understood that aluminum materials exhibit characteristic absorption at 850 nm while other materials lack this feature. In being strategic with select passbands that could potentially provide this aim, a total of 10 color-color diagrams were generated. They are listed in Table 5.3. Though passbands were selected to compare the region centered around 800-900 nm with other regions of the spectrum, it remained difficult to isolate both aluminum materials together. The plots that provided best results in regard to scatter and material isolations are shown in Figure 5. 9 and Figure 5.10. All other generated color-color diagrams for taxonomy attempts are to be included in the Appendix, along with a table detailing all material color index values.

Table 5.3: Selected passbands for generating color-color plots to isolate aluminum materials.

Attempt	Color Index 1 (x-axis)	Color Index 2 (y-axis)	Attempt	Color Index 1 (x-axis)	Color Index 2 (y-axis)
1	IR1-IR14	IR1-IR2	6	IR1-IR13	IR3-IR1
2	IR1-IR13	IR1-IR2	7	V2-IR13	V2-IR5
3	IR1-IR14	IR1-IR3	8	V1-IR3	V1-IR1
4	IR3-IR13	IR3-IR1	9	IR4-IR13	V2-IR1
5	V2-IR13	V2-IR1	10	IR1-IR13	V2-IR4

The values generated for the V2-IR13 color index resulted in sufficient scatter amongst the materials and had distinguished values for Mylar (-0.67) and the Si solar cell (3.26), while all other materials fell within a -0.14 to 2.05 range. Note that the V2-IR1 index provided separation of Kapton with a value of 1.24 and its nearest neighboring material color index, the blue circuit board with a distance value of almost 1.0 (0.906) between them, while the combination of the V2-IR5 and V2-IR13 indices separated the silicon solar cell from other materials as well. For the V2-IR1 versus V2-IR13 color-color diagram, the silicon solar cell had a distance of 1.495 between it and the material closest in index (germanium solar cell), while the V2-IR5 versus V2-IR13 plot

demonstrated a distance value of 1.794 between the silicon and the polyimide (Kapton), its nearest neighboring material index.

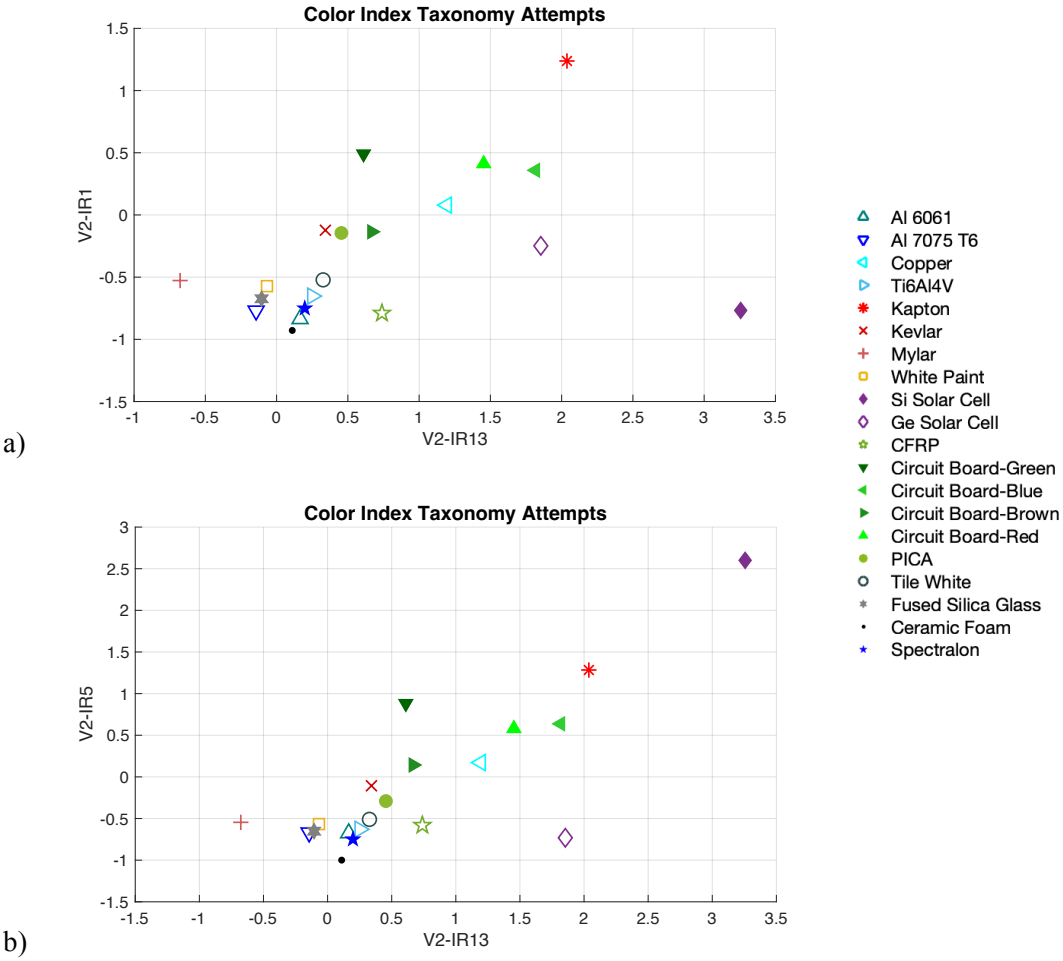

Figure 5. 9: Color-color diagrams for a) V2-IR1 versus V2-IR13 color indices, and b) V2-IR5 versus V2-IR13 color indices according to their respective filter passbands. *Credit: NASA*

Additionally, it was found that the V1-IR1 versus V1-IR3 index provided not only good repeatability in both indices but also the simultaneous isolation of the polyimide and silicon solar cell materials (Figure 5.10). While the silicon solar cell was only isolated in the V1-IR3 regime, with a color index value of 2.47 and distance of 1.617 between it and the green circuit board, the Kapton sample was isolated for both indices with a V1-IR3 value of 3.18 and a V1-IR1 value of

3.14. Kapton also resulted in having a substantial distance value of 2.216 between it and the green circuit board, the material closest in index to it. This color-color diagram also resulted in values for both aluminum materials that were nearly equal, with a distance of 0.112 between their values, while the previous diagrams described in Figure 5. 9 were not as effective in this regard and had distance values of 0.315 and 0.309 for Figures 5.9a and 5.9b, respectively. It can be noted that this color index attempt using these passbands can be compared to the narrow passbands provided by the SDSS system. Therefore, the *g'-z'* versus *g'*-Y color-color diagram was generated, and through comparison, though similar, did not yield the same results in effectively isolating the silicon solar cell material while also not exhibiting the same degree of separation for the polyimide. For quantitative purposes, the distance between the silicon solar cell and its nearest neighboring material index (green circuit board) resulted in 0.517 in value, a large value of 1.100 less than what was seen in the V1-IR1 versus V1-IR3 diagram. Furthermore, the polyimide material had a distance of 1.575 between it and the silicon solar cell for the *g'-z'* versus *g'*-Y diagram, while the distance value between it and the green circuit board resulted in 2.216 for the V1-IR1 versus V1-IR3 plot (Figure 5.10), a difference of 0.614 between these nearest neighbor material index distance results.

a)

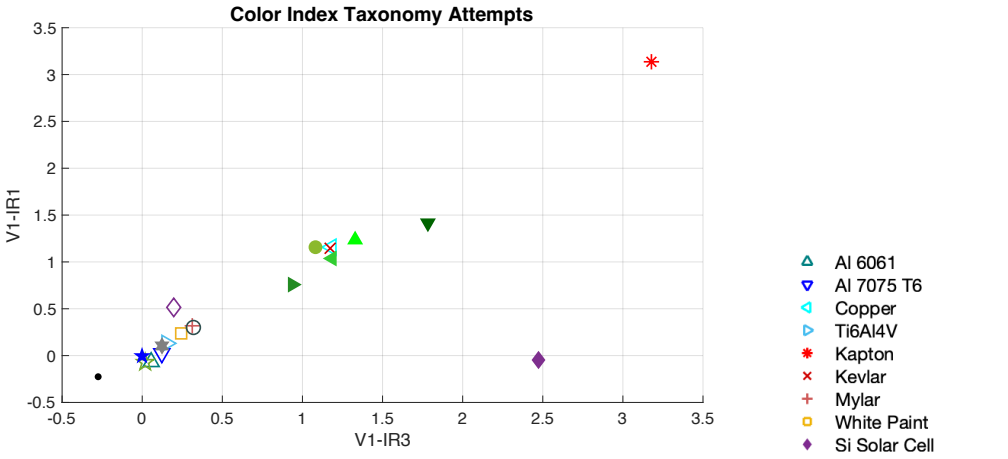

b)

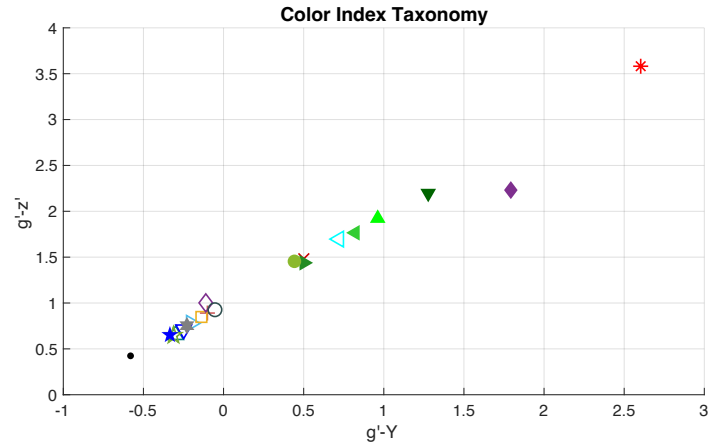

Figure 5.10: Color-color diagrams for a) V1-IR1 versus V1-IR3, and b) *g'-z'* versus *g'*-Y color indices according to their respective filter passbands. *Credit: NASA*

The next aim was to explore the possibility of isolating polymer-based materials from those of other classifications. A similar analysis approach was carried out for this and the selected passband combinations, which are listed in Table 5.4. Plots most worthy of discussion are included in Figure 5.11 and Figure 5.12. All other color index plot attempts are included in the Appendix (Figures A.57-A.77).

Table 5.4: Selected passbands for generating color-color plots in an attempt to isolate polymer-based materials.

Attempt	Color Index 1 (x-axis)	Color Index 2 (y-axis)	Attempt	Color Index 1 (x-axis)	Color Index 2 (y-axis)
1	IR1-IR13	IR4-IR13	6	IR4-IR16	V3-IR16
2	IR1-IR8	IR4-IR13	7	IR1-IR16	V1-IR16
3	IR1-IR4	IR8-IR13	8	IR2-IR16	V1-IR16
4	V1-IR4	IR8-IR13	9	IR2-IR11	V1-IR11
5	IR4-IR16	V1-IR16	10	V1-IR2	V1-V3

a)

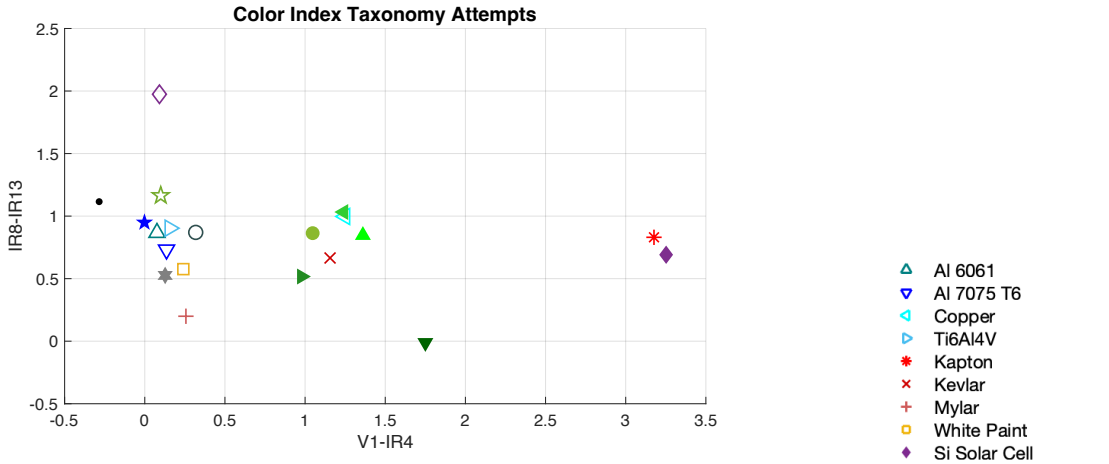

b)

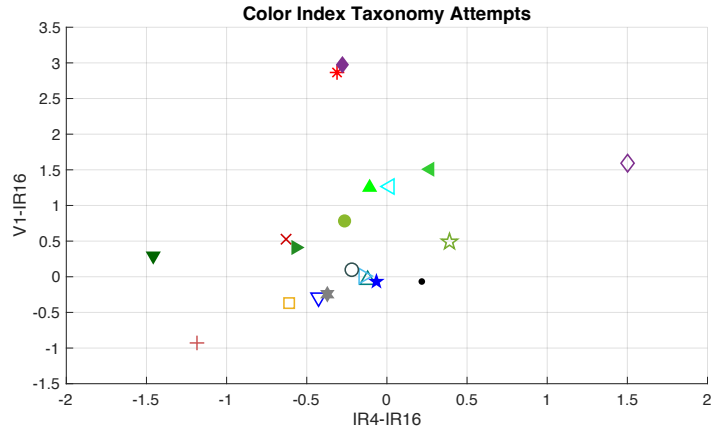

Figure 5.11: Color-color diagrams for a) IR8-IR13 versus V1-IR4, and b) V1-IR16 vs. IR4-IR16 color indices according to their respective filter passbands. *Credit: NASA*

The resulting color values for the IR8-IR13 versus V1-IR4 color-color diagram (Figure 5.11a) provided isolation of the silicon solar cell and Kapton materials together, as well as isolation of the Ge solar cell, the green circuit board material, and ceramic foam. The silicon solar cell and

polyimide were 0.159 value in close distance with each other but had values of 1.658 and 1.656 from the green circuit board, respectively. The germanium solar cell was isolated due to the IR8-IR13 index value (1.97), with a distance value of 0.810 between it and the CFRP (nearest neighbor), while the other materials were isolated due to having distinguished values in the V1-IR4 index. All color values for these materials in the V1-IR4 index are included in the Appendix (Table A. 7). It can be additionally noted that this color-color diagram allowed for some material clusters to occur, with most circuit boards (except for green) and Kevlar, PICA, and copper to be centered in the plot with V1-IR4 values between 0.98-1.36 and IR8-IR13 values between 0.52-1.03. The cluster of materials (except for the germanium solar cell) having a V1-IR4 color index less than 0.5 had an average distance value of 0.417 between them, while the material cluster with a V1-IR4 index between 0.75-1.5 had an average distance value of 0.313 between them.

Although the V1-IR16 versus IR4-IR16 color-color diagram (Figure 5.11b) did not provide as much separated grouping as seen in Figure 5.11a, it is interesting to note that materials were individually isolated once more. The silicon solar cell and Kapton materials delivered color index values that were near equal to each other in both IR4-IR16 and V1-IR16 indices, with a distance of 0.114 between these indices, though they could be separated from other materials by having V1-IR16 indices greatest in value compared to all other materials, with Kapton resulting in 2.87 and the Si solar cell having a value of 2.97 for said index. The germanium solar cell and green circuit board were isolated due to their IR4-IR16 values being 1.50 and -1.46, respectively. The germanium solar cell was separated by 1.236 from the blue circuit board (nearest in color index) and the green circuit board had a distance of 0.861 from Kevlar, which was the material closest to it. The Mylar sample also describes some level of separation in regard to both indices calculated,

having a V1-IR16 value of -0.93 and an IR4-IR16 value of -1.18, and a distance value of 0.802 between it and the white paint, its closest material in color index.

From the additional color-color diagrams generated in an attempt to isolate or group materials, the V3-IR16 vs. IR4-IR16 plot resulted in the isolation of four materials, including both solar cells, the green circuit board material, and Mylar (Figure 5.12a). The green circuit board, Mylar, and germanium solar cell were distinguished by their IR4-IR16 values being -1.46, -1.18, and 1.50, respectively. The green circuit board was separated by a distance value of 0.900 between it and the brown circuit board material, while the Mylar was 0.864 in distance from the Kevlar, and the Ge solar cell resulted in a 1.234 distance value from the blue circuit board to show a greater degree of separation. The silicon solar cell had a larger difference in the V3-IR16 index, resulting in a value of 2.29, and was 1.674 in distance from the blue circuit board, which was the material closest to it in color index value for this color-color diagram.

With greater success, the V1-IR16 versus IR2-IR16 color-color diagram resulted in the isolation of five materials (Figure 5.12b), including both solar cells, Kapton, Mylar, and the green circuit board. The Kapton and Si solar cell materials demonstrated greater separation from other materials in V1-IR16, though their values were nearly the same, as previously seen in Figure 5.11b. The polyimide was 1.522 in distance from the blue circuit board, while the silicon solar cell was 2.009 in distance from the germanium solar cell. The green circuit board, Mylar, Ge solar cell, and Si solar cell exhibited separation from other materials in the IR2-IR16 index. The green circuit board and Mylar sample resulted in much lower color values than the majority of other materials, with an IR2-IR16 value of -1.42 for the green circuit board and -1.24 for Mylar. The green circuit board was 0.821 in distance from the material closest to it in color index (Kevlar), and the distance value between Mylar and the white paint, its nearest neighboring material in color index, resulted

in 0.847. On the other hand, the two solar cells had much greater IR2-IR16 values with the Si solar cell resulting in 2.78 and the Ge solar cell resulting in a value of 1.32. The solar cells were 2.009 in distance from one another; the germanium solar cell being the material nearest to the Si solar cell in index, while the germanium solar cell had a 0.937 value in distance away from the blue circuit board, its nearest neighboring material in index.

a)

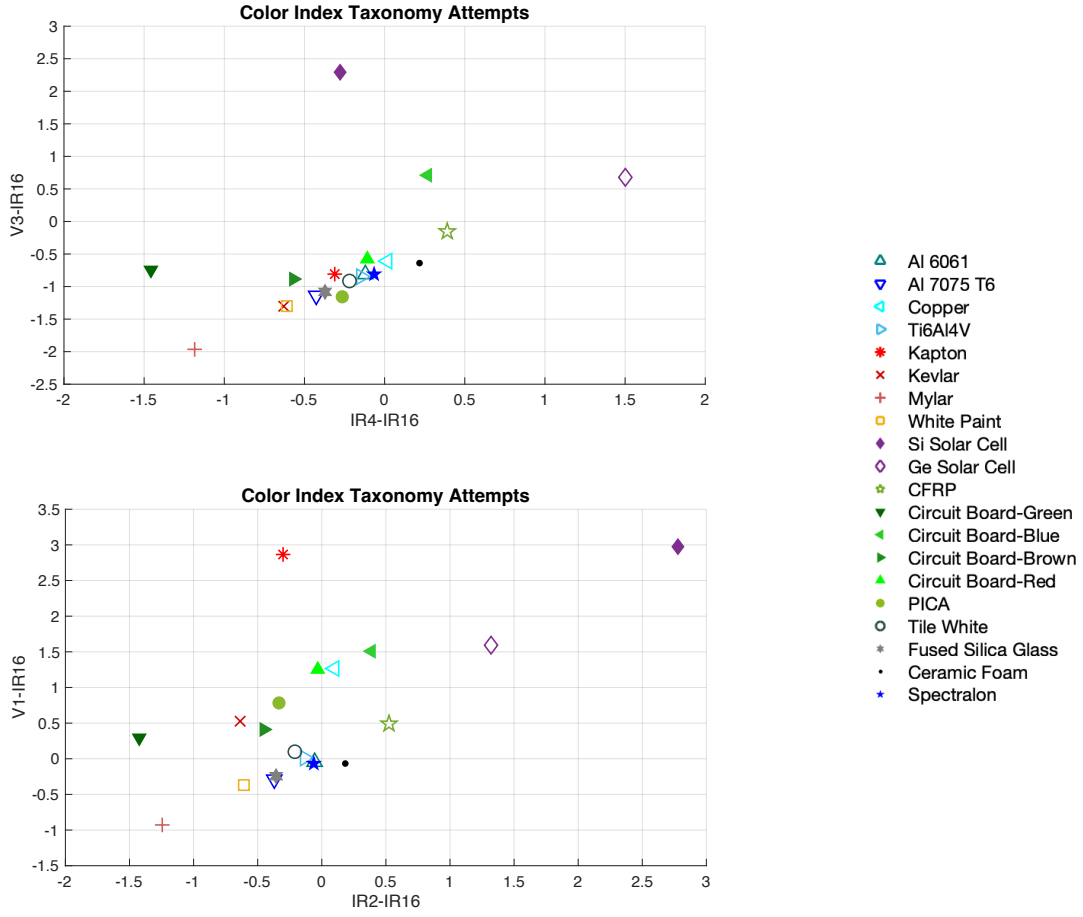

b)

Figure 5.12: Color-color diagrams for a) V3-IR16 versus IR4-IR16, and b) V1-IR16 vs. IR2-IR16 color indices according to their respective filter passbands. *Credit: NASA*

Finally, it was sought to possibly discriminate materials that produced a featureless spectral reflectance signature compared to those with many features. With this in mind, passband variables were selected with the intention to generate 10 color-color diagrams. The descriptions for selected

passband variables are described in Table 5.5. All corresponding diagrams outlined in Table 5.5 are included in the Appendix (Figures A.70-A.77) except for those displayed in Figure 5.13.

Table 5.5: Selected passbands for generating color-color plots to isolate materials with featureless reflectance spectra.

Attempt	Color Index 1 (x-axis)	Color Index 2 (y-axis)	Attempt	Color Index 1 (x-axis)	Color Index 2 (y-axis)
1	V1-IR12	V1-IR6	6	V4-IR5	V1-IR5
2	V1-IR15	V1-IR6	7	V4-IR11	V1-IR5
3	V3-IR12	V3-IR6	8	V1-IR14	V1-IR5
4	V3-IR16	V3-IR10	9	V4-IR11	V1-IR7
5	IR2-IR10	V3-IR10	10	IR1-IR11	IR1-IR5

a)

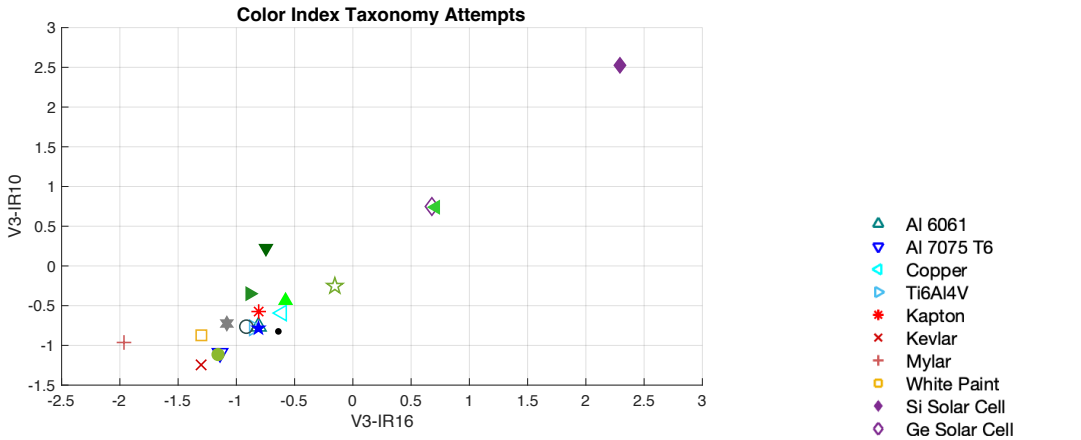

b)

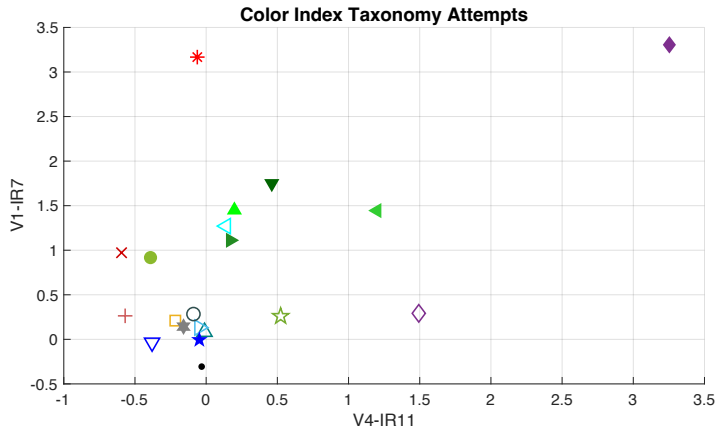

Figure 5.13: Color-color diagrams for a) V3-IR10 versus V3-IR16, and b) V1-IR7 versus V4-IR11 color indices according to their respective filter passbands. *Credit: NASA*

Although of the 10 attempts at finding color index trends amongst materials that maintain a rather featureless reflectance spectra did not result in ideal results, 2 of the 10 plots will be

discussed for their ability to isolate a group of materials different from those previously described. The V3-IR10 versus V3-IR16 color-color diagram resulted in values that permitted the isolation of the silicon solar cell and Mylar sample, in addition to isolation of the germanium solar cell and the blue circuit board, though these two latter materials resulted in index values almost identical to one another, with a distance value of 0.033 between them (Figure 5.13a). The distance between the silicon solar cell and the material closest to it in index (blue circuit board) resulted in a distance of 2.386, and the Mylar was at 0.670 from the white paint, the nearest neighboring material in index to it. The germanium solar cell and blue circuit board, being almost equal in color index for this diagram (Figure 5.13a), were at a distance of 1.303 and 1.317 between them and the material closest to them in color index value (CFRP), respectively. All four materials were discriminated due to their V3-IR16 values with Mylar resulting in -1.96, the silicon solar cell resulting in 2.29, and the germanium solar cell and blue circuit board resulting in values of 0.68 and 0.71 respectively. However, the two solar cells and blue circuit board had much greater values in the V3-IR10 index compared to all other materials; the silicon solar cell had a value of 2.53, the germanium solar cell resulted in a value of 0.75, and the blue circuit board was 0.74.

The V1-IR7 versus V4-IR11 color-color diagram demonstrated material color values that provided discrimination of the two solar cells, Kapton, and the blue circuit board (Figure 5.13b). The silicon solar cell and Kapton materials were evidently greater in V1-IR7 value than all other materials, resulting in 3.31 and 3.17 values, respectively. The silicon solar cell was also much different in V4-IR11 with a value of 3.25 and had a large distance value of 2.771 between it and the blue circuit board, the material closest to it in index. Otherwise, the blue circuit board and germanium solar cell were greater in the V4-IR11 index with values of 1.20 and 1.49, respectively.

The germanium solar cell was at 0.971 in distance from the CFRP, while the Kapton was greater in separability at a distance of 1.512 from the green circuit board.

To further evaluate the comparative outcomes between the 20 color-color diagrams presented beyond Section 5.2.2, general statistics on the data for color index distances were performed and presented in Table 5.6. From the table, it can be seen that the *z'*-Y versus *z'*-H color-color diagram demonstrated the lowest minimum distance between color indices, with a distance value of 0.006 that occurred between the polyimide and white tile materials. Similarly, the V1-IR16 versus IR2-IR16 theoretical color-color diagram demonstrated the largest maximum distance value between all color indices, with a distance of 5.605 between the silicon-based solar cell and the Mylar sample. This suggests the largest scatter between material indices from all color-color diagram plots evaluated. Additionally, the diagram with the smallest standard deviation was demonstrated in the I-Y versus H-K color plot with a value of 0.359, where the average distance value between all indices resulted in 0.419. Contrarily, the V3-IR10 versus V3-IR16 diagram presented the largest standard deviation of 1.266, where the average distance between indices for this plot was 1.281.

Table 5.6: Overview of statistics regarding color index distances for each respective color-color diagram presented beyond Section 5.2.2.

	Color-color diagrams	Min	Max	Median	Mean	Standard Deviation
1	*r′-i′* vs *g′-i′*	0.023	3.053	0.660	0.765	0.699
2	V-R vs B-R	0.029	2.375	0.633	0.723	0.518
3	Z-R VS Z-H	0.015	3.595	0.275	0.574	0.937
4	I-Y VS H-K	0.016	1.782	0.283	0.419	0.359
5	*z′-i′* vs *z′*-H	0.016	2.579	0.264	0.522	0.646
6	*z′*-i' vs H-K	0.017	1.939	0.339	0.561	0.503
7	Z-Y vs Z-H	0.010	4.166	0.240	0.608	1.106
8	*z′*-Y vs *z′*-H	0.006	2.031	0.198	0.366	0.498
9	I-Y VS B-I	0.025	2.321	0.670	0.738	0.522
10	*i′-z′* vs *g′-i′*	0.022	3.251	0.716	0.858	0.731
11	V2-IR1 vs V2-IR13	0.092	3.941	1.120	1.299	0.868
12	V2-IR5 vs V2-IR13	0.042	5.037	1.244	1.461	1.113
13	V1-IR1 vs V1-IR3	0.014	4.820	1.209	1.324	1.085
14	*g′-z′* vs *g′*-Y	0.014	4.484	1.050	1.210	1.038
15	IR8-IR13 vs V1-IR4	0.037	3.562	1.092	1.242	0.881
16	V1-IR16 vs IR4-IR16	0.060	4.007	1.294	1.429	0.908
17	V3-IR16 vs IR4-IR16	0.019	4.353	0.886	1.201	0.984
18	V1-IR16 vs IR2-IR16	0.024	5.605	1.287	1.561	1.133
19	V3-IR10 vs V3-IR16	0.021	5.504	0.806	1.281	1.266
20	V1-IR7 vs V4-IR11	0.062	4.936	1.194	1.494	1.168

5.3. Relating Color Indices and Spectral Signatures

From all color index values that were calculated using traditional, modern, and theoretical filter passbands, and were plotted on color-color diagrams (Figures 5.4-5.13), the materials that exhibited most frequent and/or effective distinguishability between them and all other materials via color index were the silicon solar cell, the germanium solar cell, and the polyimide (Kapton). The silicon solar cell demonstrated the most separation using classic filters to calculate their color indices as seen from the Z-Y versus Z-H color-color diagram (Figure 5.7), which resulted in a distance value of 3.545 between it and the blue circuit board.

For a better visualization of how this data is derived from the material spectral signatures, the reflectivity curve for the silicon solar cell is plotted (Figure 5.14) with the carbon fiber reinforced polymer (CFRP) reflective signature superimposed to better compare the color index outcomes of these signatures. Therefore, it is seen that there are large variations in flux for the silicon solar cell, where the area under the reflectivity curve is evidently much less within the Z passband versus the Y and H passbands, though the flux is relatively the same between all three passbands (Z, Y, and H) for the CFRP material.

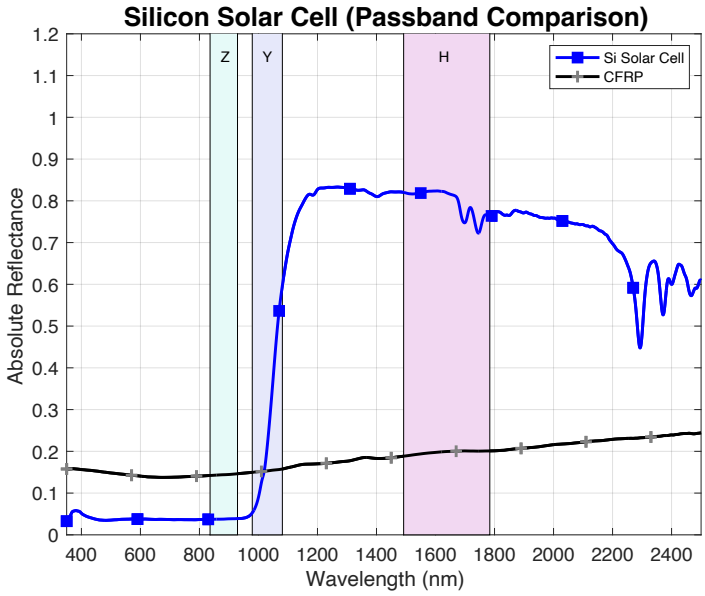

Figure 5.14: Reflectivity curves for silicon solar cell material, and CFRP material for comparison, with Z, Y, and H filter passbands depicted within the graph. *Credit: NASA*

For the germanium solar cell, most distinguishability between it and the material closest to it on the color-color diagrams evaluated in this chapter was seen in the V1-IR16 versus IR4-IR16 plot, which made use of variable/theoretical passbands for calculating material color indices. In this case the germanium solar cell resulted in a distance of 1.236 between it and the material nearest it on the respective color-color diagram. Again, this can be viewed visually in

Figure 5.15, where the Ge-based solar cell demonstrated differences in flux between the three depicted passbands, leading to its unique color index value and distinguishability in the respective color-color diagram.

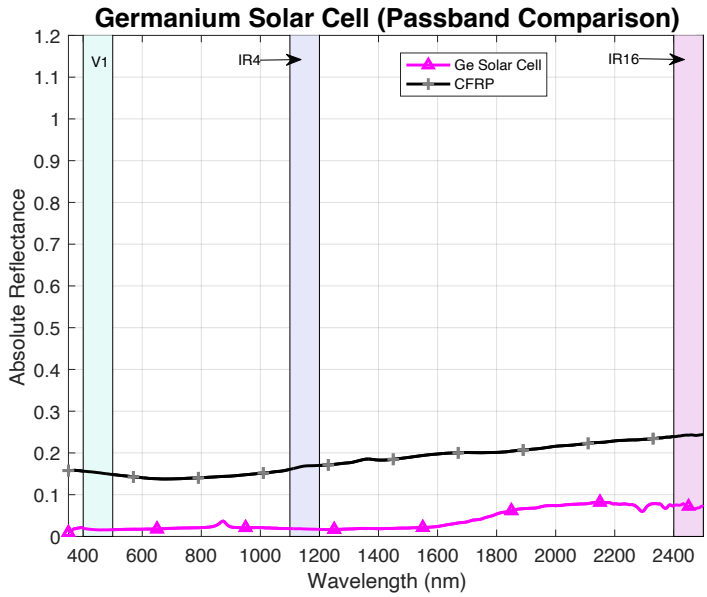

Figure 5.15: Reflectivity curves for germanium solar cell sample, and CFRP material for comparison, with V1, IR4 and IR16 passbands depicted within the graph. *Credit: NASA*

Finally, the polyimide (Kapton) exhibited most isolation in the V1-IR1 versus V1-IR3 color-color diagram (Figure 5.10a), which used variable/theoretical passbands to calculate indices and resulted in a distance of 2.216 between it and the material closest to it in index value (green circuit board). The V1, IR1, and IR3 passbands are depicted on the Figure 5.16 spectral plot along with reflectivity curves for the polyimide and CFRP materials. This schematic shows there are stark differences in the flux between the V1 and the IR1 and IR3 proposed passbands for the Kapton sample, where the area under the curve is much smaller within the VI passband versus the IR1 and IR3 passbands. Compared to the CFRP material, which has a relatively flat spectra between the 350-2500 nm range, and therefore showed fewer differences between the three

aforementioned passbands, the polyimide had larger variation between these passbands and therefore exhibited greater distinguishability in color index for the V1-IR1 versus V1-IR3 diagram.

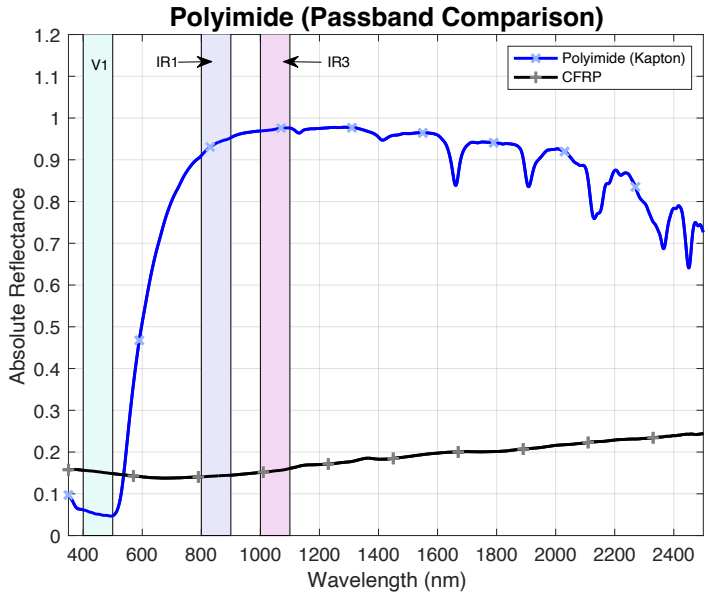

Figure 5.16: Reflectivity curves for the polyimide (Kapton) sample, and the CFRP material for comparison, with the V1, IR1 and IR3 passbands depicted within the graph. *Credit: NASA*

Of the color-color diagrams using modern filter passbands for color index, the *r'-i'* versus *g'-i'* plot demonstrated greatest separation between Kapton and the material nearest it in index, with a distance value of 1.678, however the *i'-z'* versus *g'-i'* diagram was almost as effective in isolating the polyimide with a distance value of 1.676 between it and its nearest neighboring material in index.

However, it should be emphasized that the reason taxonomy applications were explored for color index specifically is due to the use of characterizing objects using color values via remote observations. Knowing this, it should be noted that color index is not only dependent on material composition based on absorption features present in material spectra, but also dependent on phase angle and rotation factors involved in observations. Until there is a greater supply of color index

data and analysis available within the SSA community, the aim for this work was to share the indices and filter passbands that may be more useful than others in distinguishing materials, as well as those that do not perform to satisfaction in the distinct separation of material type. It is evident that it is more useful to classify materials using reflectance spectra alone, and this can be done more effectively due to compositional features that are represented within spectra. However, the goal was to take one step into bridging the gap between lab-based measurements and remote observational methods.

Additionally, of note is that the color index values provided in this work are based on laboratory measurements and not remote observations. Too compare these data to data captured remotely, additional necessary corrections should be performed. For this reason, the values for the Spectralon material were included since the color values for Spectralon and solar color values are analogous to serving as references for the target measurements or observations. Therefore, the material color index values explored in this analysis are only to serve as a first step in potentially identifying trends between common spacecraft materials that comprise much of space domain. Results could potentially serve as a guide for which passbands may provide better results for specific materials than others. Although again, methods were carried out as a first-step basis and much work can be performed in the future to further improve this assessment.

Regarding outcomes of the ability to perform discrimination of materials via color index, there was no universal combination of filter passbands that were applied in this work that ideally separated all materials, though all possible combinations of filter passbands using the Johnson/Bessell UBVRI, SDSS *ugriz*, and UKIRT ZYJHK systems were explored. However, there were certain filter passbands and color indices that were found to provide distinctions for individual materials. Some focused on Kapton and Mylar polymeric materials, silicon and

germanium solar cells, as well as circuit board materials. Furthermore, comparisons were made between the use of the more common astronomical filter passbands used for observations. It is also understood that filter systems are selected based on their performance depending on the detector, yet this work only used the filter passband ranges as a guide for identifying the ability to distinguish materials once more.

Regardless, reflectance spectra are related to material chemistry, producing absorption and reflectance features in VIS and IR regions of the spectrum that correspond to chemical bonds present within the material's structure. For this reason, polymers demonstrate greater amounts of absorption features in NIR and SWIR than most bare metals, aluminum absorbs light at 850 nm, and solar cells will exhibit characteristic features in the NIR/SWIR regime depending on their substrate and stacked structure. Since there is an evident relationship between reflectance spectra and chemistry, and since chemistry can be related to material density, it was sought to explore the uses of reflectance spectra for common space-grade materials that could further the knowledge of material trends optically.

5.4. Options for Application and Spectral Libraries

From a reflectance spectroscopy standpoint, materials can be classified from one another via spectra alone, without performing the additional step of calculating a color index from spectral data. Though this is well understood, methods for performing such analysis can also be improved. On the topic of data driven models, spectral libraries serve to house a multitude of material and mineral reflectance data and catalogue a wide variety of constituents. Some of the most popular spectral libraries that provide this data are ECOSTRESS [186] and USGS [185]. While these two platforms effectively house spectral data for an assortment of human-made/artificial materials,

they currently provide a single spectral plot per material, and are in some ways heavily geared toward minerals, vegetation, and other natural materials.

Also, reflectance spectra are not often grouped and analyzed by density or other intrinsic, physical material properties from spectral features for easier assessment of determining material classifications. Though previous attempts have been made to improve spectral libraries in various aspects, by [211, 212] for example, the delivery of spectral library objectives can be furthered in terms of 1. Providing a focus for spacecraft and rocket body material spectral data for the SSA community to refer to and 2. Operating with greater efficiency to provide output information regarding material classification and associated hazards for SSA risk assessment. The latter of these objectives can be explored through the advantages provided by machine learning.

5.5. SUMMARY

In this chapter, approaches were taken to evaluate the possible discrimination of materials depending on their optical properties through calculating color indices from spectral reflectance. The materials selected for this study were chosen via a taxonomy approach to assess any patterns for material discrimination through the presented color-color diagrams. Color-color diagrams were generated using various astronomical filter passbands included in the classic Johnson/Bessell system, the modern Sloan filter system, and passbands to represent the infrared spectral regime. In addition, proposed theoretical passbands were created to assess if material discrimination could be better promoted through making use of other passband ranges. It was found that of the group of materials included in spectral measurements, the silicon and germanium solar cells and the polyimide (Kapton) materials resulted in the best separation from all other materials via color index depending upon which combinations of filter passbands were employed for study. While the silicon solar cell demonstrated better separation/discrimination through use of established

astronomical filters, the germanium solar cell and the polyimide (Kapton) materials demonstrated better separation using the theoretical passbands proposed within this work.

Chapter 6: Conclusions and Future Work

6.1. SUMMARY

It is significant to understand the need for characterizing resident space objects in order to strengthen the objectives reached through space situational awareness. Resident space objects have been described, with a focus on micrometeoroids and orbital debris. Through understanding what potential hazards are associated with the MMOD environment and the necessary risk assessment involved, it is then critical to comprehend what is the flux of these objects in orbit. The tools used to model and provide a comprehensive estimate of the flux of cataloged objects that reside in space domain were described. Further, a number of destructive collisions and breakup events that have occurred between RSO's were detailed to emphasize the threat of an increased debris population generated from such occurrences. A variety of common space hardware materials were noted for the reason that orbital debris fragmentations are derived from a functional parent space object. A summary of noteworthy laboratory tests that have been conducted with the intent to better understand orbital debris fragmentation events was explained.

From understanding the vulnerabilities involved surrounding MMOD, the numerous methods used to characterize space domain were specified. This included *in situ*, radar, and optical measurement strategies. This dissertation work focused on optical measurements conducted via reflectance spectroscopy, therefore it was worthy to discuss the research that involves the analysis of planetary bodies, asteroids, and human-made articles including rocket bodies, spacecraft, and orbital debris. It is then fundamental to recognize how spectral measurements are used to characterize materials remotely, but further, how they can be utilized to evaluate the changes in optical behavior of RSO's when subjected to the harsh space environment for a given duration. An analysis of the space environment and previous space weathering experiments performed for

common spacecraft materials were described. In addition, material classification via remote sensing was noted, including remote sensing outcomes that made use of spectral data, and how specifically laboratory-based data has been used to help bridge the gap between the two techniques, as well as the use of photometry providing color indices as a means of measurement. The different astronomical photometric measuring systems were detailed and compared. Due to the focus on spectral measurements of resident space objects, the different methods that have been undertaken within literature to unmix spectra with the intent to help distinguish the true spectra of a component have been discussed, including traditional and linear methods, hyperspectral unmixing, and machine learning techniques.

An overview of all space-related material spectral measurements acquired for this work has been presented in Chapter 4. This includes the many materials measured in their pristine conditions for base-line signature representation, as well as spectra obtained on materials during GEO space simulated weathering to observe optical behavioral changes. A description of the respective laboratory settings where measurements were conducted was presented, as well as the overall procedure for taking measurements in both locations. Measurements focused on material spectra as well as calculating color indices from their given spectra when relevant. Results were presented and discussed accordingly in Chapter 5.

The overarching objective for analysis provided in this work stems from the aim to better distinguish materials per classification via optical means. This goal was motivated by the idea that materials belonging to different classifications exhibit different properties, particularly when taking an interest in material density. Material density is one factor used to assess and predict the magnitude of damage from potential orbital debris objects. Polymers are generally softer materials than metals, ceramics, and most composites, therefore this intelligence can be advantageous in

efficiently deducing material threat when traveling at elevated velocity in orbit if materials can be separated by their intrinsic properties. Because polymers are distinct in their reflectance signatures, exhibiting a greater amount of absorption features related to organics within their chemistry when compared to materials of other categories, their spectral signature can be utilized to distinguish themselves which can in turn aid in the efficiency of material characterization. Hence, material optical measurements were acquired and transformed into color index to possibly identify trends from a material classification standpoint. Color index was calculated since observations often make use of these measurements as an indicator to characterize objects remotely, though this was applied only to laboratory-based measurements in our analysis. To determine color index from material spectra, many defined astronomical filter passbands were used in combinations with each other, and further, passbands of various narrow wavelength range were selected with intent to assess if objects could be better discriminated by material type. It was found that with the plotting of certain indices against each other, a desired degree of separability could be obtained between certain materials. For example, the silicon and germanium solar cells resulted in color index isolation from all other materials both as individual materials, and both together as classes of solar cells, depending upon which filter passbands were used for analysis. The polyimide film also often resulted in clear separation from all other materials, which can be useful information since this material is a most frequently used polymer in space design.

6.2. CONCLUSIONS

It has been well established throughout literature and studies, including in this work, that optical measurements serve as a viable tool to help classify objects remotely through analysis of their spectral features. Remote observations make use of assigning objects by color index, a value that can be determined from the reflectance signature of a given material. From the multitude of

astronomical filter measuring systems, certain filters with respective passbands can be intentionally selected to better distinguish specific materials or material groupings. These measuring tools can provide enhanced data when utilizing passband combinations that fall in regions throughout both visible and infrared regions of the spectrum. Though location and magnitude of absorption features within material reflectance spectra can be used for obvious determination of materials possessing organics within their chemistry versus those without, it was explored how these characteristics can translate into color value for an alternate method of using optical measurements to characterize materials.

The comparison of uses for classic, modern, and theoretical filter passbands to calculate material color indices were evaluated. Through comparisons, conclusions drawn suggest greater effectivity in distinguishability for the germanium solar cell and polyimide materials using the variable/theoretical passbands proposed in Section 5.2.4. Though the silicon solar cell material still demonstrated better isolation/separation from other materials in plots using the traditional astronomical Z, Y, and H filter passbands.

6.3. Future Work

Because the taxonomy approach conducted in this work was an initial step toward assessing the ability to better categorize materials using laboratory-based data, there is much work that can be carried out in the future to advance strategies involved in material characterization for increased space situational awareness. It would be of great benefit if polymer-based materials could be sorted from other materials of greater density, regardless of whether spectra or color are being used for assessment. The ability to do this can be enhanced if incorporating the use of machine learning techniques. Applying machine learning to a large set of data housed in spectral libraries can allow for certain spectral features to be immediately associated with material information. If machine

learning can be used to determine likelihood of material classification from spectral data, and provide an estimate of material density, this can support the performance of risk assessment for certain materials being measured, as well a deliver a service that can be used to better evaluate material spectra, regardless of origin.

Machine learning is being utilized for more autonomous pattern matching to associate data [213, 39]. For the future, it would be valuable to incorporate machine learning techniques within spectral libraries for greater efficiency. If a large enough source of material data that represents all classes of materials and includes all potential spectral features arises in material spectra and is applied to machine learning , then a system can be developed where input data, regardless of origin knowledge, can produce output information for immediate deduction of material properties, such as density, that can be used to assess potential risks associated with a material if it is a contributor to the orbital debris environment, in addition to general specifications of a given article that can be used for comprehensive understanding.

In addition, spectral libraries may consider having the capability to generate color index plots for observational purposes. In doing so, collecting material measurements at various phase angle and rotation configurations would provide a comprehensive, data-driven model for remote observations. Though there is more to consider when using color indices for a method of characterization rather than using reflectance spectroscopic methods, it may provide some assistance in further bridging the gap between laboratory-based measurements and remote observations.

To bridge the gap between laboratory-based measurements and remote observations, if spectral libraries can then generate color indices autonomously from their spectral input, this can offer some degree of guidance for color associated with common spacecraft materials. The aim to

better characterize resident space objects remotely is an endeavor that is continuously sought to advance and methods that can be utilized to address this objective are worthy of investigation.

References

[1] R. A. Williamson, *The Fair and Responsible Use of Space: An International Perspective*, Springer-Verlag/Wien, 2010.

[2] L. Nardon, "Space Situational Awareness and International Policy," *Institut Francais des Relations Internationales*, 2007.

[3] D. H. Rumsfeld, "Report of the Commission to Assess the United States National Security Space Management and Organization," 2001.

[4] G. L. W. Lord, "Space Superiority," *High Frontier: The Journal for Space and Missile Professionals,* vol. 1, no. 3, pp. 3-4, 2005.

[5] H. M. Cowardin, "Characterization of Orbital Debris over Optical Wavelengths via Laboratory Measurements," dissertation, Houston, TX, 2010.

[6] Y. Tadjdeh, "U.S. Strengthening Space Domain Awareness," *National Defense,* 30 July 2021.

[7] Orbital Debris Program Office , "Fifty Years Ago," *Orbital Debris Quarterly News,* vol. 17, no. 3, p. 3, July 2013.

[8] NASA Orbital Debris Program Office, "Photo Gallery," [Online]. Available: https://orbitaldebris.jsc.nasa.gov/photo-gallery/. [Accessed 06 July 2022].

[9] B. Chertok, *Rockets and People Volume IV: The Moon Race*, vol. 4, Washington, DC: NASA, 2011.

[10] C. T. G. Smith, M. Delkowki, J. V. Anguita, D. C. Cox, C. Haas and S. R. P. Silva, "Complete Atomic Oxygen and UV Protection for Polymer and Composite Materials in a Low Earth Orbit," *ACS Applied Materials & Interfaces ,* vol. 13, no. 5, pp. 6670-6677, 2021.

[11] R. Zhai, "Atomic Oxygen Environment Analysis for Spacecraft in Low Earth Orbit," *43rd COSPAR Scientific Assembly,* vol. 43, p. 739, 2021.

[12] D. P. Engelhart, E. A. Plis, D. Ferguson, W. R. Johnston, R. Cooper and R. C. Hoffmann, "Space Plasma Interactions with Spacecraft Materials," *Plasma Science and Technology - Basic Fundamentals and Modern Applications,* November 2018.

[13] H.-S. Choi, J. Lee, K.-S. Cho, Y.-S. Kwak, I.-H. Cho, Y.-D. Park, Y.-H. Kim, D. N. Baker, G. D. Reeves and D.-K. Lee, "Analysis of GEO spacecraft anomalies: Space weather relationships," *Space Weather: The International Journal of Research and Applications,* vol. 9, no. 6, 2011.

[14] E. A. Plis, D. P. Engelhart, R. Cooper, W. R. Johnston, D. Ferguson and R. Hoffmann, "Review of Radiation-Induced Effects in Polyimide," *Applied Sciences,* vol. 9, no. 10, 1999.

[15] D. J. Kessler and B. G. Cour-Palais, "Collision Frequency of Artificial Satellites: The Creation of a Debris Belt," *Journal of Geophysical Researcy,* vol. 83, no. A6, 1 June 1978.

[16] P. Anz-Meador, "Root Cause Classification of Breakup Events 1961-2018," in *First International Orbital Debris Conference*, Houston, TX, 2019.

[17] J.-C. Liou, "Collision activities in the future orbital debris environment," *Advances in Space Research,* vol. 38, no. 9, pp. 2102-2106, 2006.

[18] V. V. Adushkin, O. Y. Aksenov, S. S. Veniaminov, S. I. Kozlov and V. V. Tyurenkova, "The small orbital debris population and its impact on space activities and ecological safety," *Acta Astronautica,* vol. 176, pp. 591-597, November 2020.

[19] Orbital Debris Program Office , "'Large' Solid Rocket Motor Particle Impact on Shuttle Window," *Orbital Debris Quarterly News,* vol. 2, no. 2, p. 3, April-June 1997.

[20] S. G. Love and D. E. Brownlee, "A Direct Measurement of the Terrestrial Mass Accretion Rate of Cosmic Dust," *Science,* vol. 262, pp. 550-551, 22 October 1993.

[21] J. L. Hyde, E. L. Christiansen, D. M. Lear, K. Nagy and E. L. Berger, "Surveys of Returned ISS Hardware for MMOD Impacts," in *Proc. 7th European Conference on Space Debris*, Darmstadt, Germany, 2017.

[22] A. V. Moorhead, W. J. Cooke and M. D. Campbell-Brown, "Meteor Shower Forecasting for Spacecraft Operations," in *Proc. 7th European Conference on Space Debris*, Darmstadt, Germany, 2017.

[23] A. Manis, M. Matney, P. Anz-Meador and H. Cowardin, "The Updated GEO Population for ORDEM 3.1," in *1st International Orbital Debris Conference*, Houston, Texas, 2019.

[24] D. J. Kessler, J. Zhang, M. J. Matney and et al., "A Computer-Based Orbital Debris Environment Model for Spacecraft Design and Observation in Low Earth Orbit," NASA TM-104825, 1996.

[25] J.-C. Liou, M. Matney, P. Anz-Meador and et al., "The New NASA Orbital Debris Engineering Model ORDEM2000," technical report, NASA/TP-2002-210780, 2002.

[26] E. G. Stansbery, M. Matney, P. H. Krisko and et al., "NASA Orbital Debris Engineering Model ORDEM 3.0 - Verification and Validation," technical report, NASA/TB-2015-218592, 2015.

[27] M. Matney, A. Manis, P. Anz-Meador, D. Gates, J. Seago, A. Vavrin and Y.-L. Xu, "The NASA Orbital Debris Engineering Model 3.1: Development, Verification, and Validation," in *1st International Orbital Debris Conference*, Houston, Texas, 2019.

[28] A. Horstmann, H. Krag and E. Stoll, "Providing Flux Uncertainties in ESA-MASTER: The Accuracy of the 1cm Population," in *1st International Orbital Debris Conference*, Houston, Texas, 2019.

[29] A. Horstmann, A. Manis, V. Braun and et al., "Flux Comparison of MASTER-8 and ORDEM 3.1 Modelled Space Debris Population," in *Proc. 8th European Conference on Space Debris (virtual)*, Darmstadt, Germany, 2021.

[30] R. Nail and C. Fernando, "'Lucky strike': International Space Station's robotic arm survives after being hit by space junk," *USA Today,* 2 June 2021.

[31] D. Chow, "Space junk damages International Space Station's robotic arm," *NBC News,* 1 June 2021.

[32] C. Pardini and L. Anselmo, "Physical properties and long-term evolution of the debris clouds produced by two catastrophic collisions in Earth orbit," *Advances in Space Research,* vol. 48, no. 3, pp. 557-569, 2011.

[33] J.-C. Liou, "Update on Three Major Debris Clouds," *Orbital Debris Quarterly News,* vol. 14, no. 2, April 2010.

[34] Orbital Debris Program Office, "Breakup Events in 2020," *Orbital Debris Quarterly News,* vol. 25, no. 1, February 2021.

[35] J. Murray, R. Miller, M. Matney, P. Anz-Meador and T. Kennedy, "Recent Results from the Goldstone Orbital Debris Radar: 2016-2017," in *First International Orbital Debris Conference*, Houston, TX, 2019.

[36] V. Ruch, R. Serra, P. Omaly and J. C. Dolado Perez, "Decoupled analysis of the effect of past and future space activity on the orbital environment," in *8th European Conference on Space Debris*, Darmstadt, Germany, 2021.

[37] J. Reyes and D. Cone, "Characterization of Aerospace Materials Related to Orbital Debris using Reflectance Spectroscpoy," in *International Association for the Advancement of Space Safety (IAASS)*, El Segundo, California, 2019.

[38] H. Cowardin, P. Anz-Meador and J. A. Reyes, "Characterizing GEO Titan IIIC Transtage Fragmentations using Ground-based and Telescopic Measurements," in *Advanced Maui Optical and Space Surveillance Technologies Conference (AMOS)*, Maui, Hawaii, 2017.

[39] J. A. Reyes and H. Cowardin, "Spectral characterization of spacecraft materials used in hypervelocity impact testing," Proc. *SPIE 11727, Algorithms, Technologies, and Applications for Multispectral and Hyperspectral Imaging XXVII*, 117271G, 12 April 2021; https://doi.org/10.1117/12.2589299.

[40] A. M. Abd El-Hameed and Y. A. Abdel-Aziz, "Aluminum Alloys in Space Applications: A Short Report," *Journal of Advanced Research in Applied Sciences and Engineering Technology,* vol. 22, no. 1, 2021.

[41] A. M. Abd El-Hameed, Y. A. Abdez-Aziz and F. S. El-Tokhy, "Anodic Coating Characteristics of Different Aluminum Alloys for Spacecraft Materials Applications," *Materials Science and Applications,* vol. 8, 2017.

[42] ASM International, *ASM Handbook Volume 2: Properties and Selection: Nonferrous Alloys and Special-Purpose Materials*, vol. 2, ASM International, 1990.

[43] H. E. Boyer and T. L. Gall, *Metals Handbook*, Materials Park, OH: Americal Sociey for Metals, 1985.

[44] D. C. Ferguson, B. V. Vayner, J. T. Galofaro and et al., "NASA GRC and MSFC Space Plasma Arc Testing Procedures," *IEEE Transactions on Plasma Science,* vol. 34, no. 5, 2006.

[45] Y. A. Abdel-Aziz, A. M. Abd El-Hameed, F. S. El-Tokhy and et al., "Ground-Based Simulation for the Effects of Space Plasma on Spacecraft," *Advnaces in Space Research ,* vol. 51, no. 1, pp. 133-142, 2013.

[46] A. Ampatzoglou and V. Kostopoulos, "Design, Analysis, Optimization, Manufacturing, and Testing of a 2U Cubesat," *International Journal of Aerospace Engineering,* vol. 2018, Article ID 9724263, 15 pages, 2018. https://doi.org/10.1155/2018/9724263.

[47] S. Rawal, J. Brantley and N. Karabudak, "Addititve Manufacturing of Ti-6Al-4V Alloy Components for Spacecraft Applications," *2013 6th International Conference on Recent Advances in Space Technologies (RAST)*, 2013, pp. 5-11, doi: 10.1109/RAST.2013.6581260.

[48] P. I. Pradeep, A. Akhilesh, V. Anil Kumar and et al., "Characterization of Titanium Alloy Ti6Al4V-ELI Components made by Laser Powder Bed Fusion Route for Space Applications," *Transactions of the Indian National Academy of Engineering,* 2021.

[49] J. L. Buckner, S. W. Stafford and D. M. Cone, "Microstructural characterization of Ti-6Al-4V X-links from the Space Shuttle," *Materials Characterization,* vol. 131, pp. 261-265, 2017. https://doi.org/10.1016/j.matchar.2017.07.010.

[50] DuPont, "*DuPont Kapton® Summary of Properties*," report, DuPont, 2017.

[51] DuPont, "*DuPont Kapton® HN Polyimide Film*," report, DuPont, 2019.

[52] A. Mazzinghi, M. Sabbadini and A. Freni, "Enhanced RF Behavior Multi-Layer Thermal Insulation," *Nature Scientific Reports,* vol. 8, 91, 2018. https://doi.org/10.1038/s41598-017-18337-3.

[53] R. Yokota, "Recent Trends and Space Applications of Polyimides," *Journal of Photopolymer Science and Technology,* vol. 12, no. 2, pp. 209-216, 1999.

[54] L. Narici, M. Casolino, L. Di Fino and et al., "Performances of Kevlar and Polyethylene as radiation shielding on-board the International Space Station in high latitude radiation environment," *Nature Scientific Reports,* 2017.

[55] H. Bansemir and O. Haider, "Fibre composite structures for space applications - recent and future developments," *Cryogenics,* vol. 38, no. 1, 1997.

[56] M. De Cesare, A. Di Leva, A. Del Vecchio and et al., "A novel recession rate physics methodology for space applications at CIRCA by means of CIRCE radioactive beam tracers," *Journal of Physics D: Applied Physics,* vol. 51, 2018.

[57] A. Fedele, R. Gardi and G. Pezzella, "Aerothermodynamics and thermal design for on-ground and in-flight testing of a deployable heat shield capsule," *CEAS Space Journal,* 2020.

[58] G. A. Haynes, "Effect of radiation on cerium-doped solar-cell cover glass," technical report, NASA, 1970.

[59] G. R. Devi and K. R. Rao, "Carbon-Carbon Composites - An Overview," *Defence Science Journal,* vol. 43, no. 4, p. 369, 1993.

[60] TORAY, "'Toray' T1000G Intermediate Modulus Carbon Fiber," report, TORAY, 2018.

[61] TORAY, "'Toray' Aerospace Prepreg Selector Guide," report, TORAY, 2017.

[62] A. Bulletti, L. Capineri, M. Materassi and et al., "Surface Resistivity Characterization of New Printed Circuit Board Materials for Use in Spacecraft Electronics," *IEEE Transactions on Electronics Packaging Manufacturing,* vol. 30, no. 2, pp. 115-122, 2007.

[63] A. R. Frederickson, E. G. Mullen, K. J. Kerns and et al., "The CRESS IDM Spacecraft Experiment for Insulator Discharge Pulses," *IEEE Transactions on Nuclear Science,* vol. 40, no. 2, 1993.

[64] MatWeb, "Electro-Isola G-Etronax EP FR4 Epoxy, Glass Fabric Reinforcement, Light Yellow, Sheets," MatWeb, LLC., 1996-2021. [Online]. Available: http://www.matweb.com/search/DataSheet.aspx?MatGUID=3c5f252f235844fb9ffec6d1856ba0e3. [Accessed 28 February 2021].

[65] MatWeb, "Rogers Arlon CuClad 217 PTFE/Woven Fiberglass Laminate Microwave Printed Circuit Board Substrate," MatWeb, LLC., 1996-2021. [Online]. Available:

http://www.matweb.com/search/DataSheet.aspx?MatGUID=952559b637a940658f6ab71767504fdc. [Accessed 28 February 2021].

[66] J. Frith, P. Anz-Meador, H. Cowardin and et al., "An Analysis of 20 Years of Space Weathering Effects on the Boeing 376 Spacecraft," in *Advanced Maui Optical and Space Surveillance,* Maui, Hawaii, 2015.

[67] R. R. King, D. C. Law, K. M. Edmondson and et al., "40% efficient metamorphic GaInP/GaInAs/Ge multijunction solar cells," *Applied Physics Letter,* vol. 90, no. 18, 2007.

[68] A. Hadj Dida and M. Bekhti, "Study, Modeling and Simulation of the Electrical Characteristic of Space Satellite Solar Cells," in *6th International conference on Renewable Energy Research Applications*, San Diego, California, 2017.

[69] O. Uyanna and H. Najafi, "Thermal protection systems for space vehicles: A review on technology development, current challenges and future prospects," *Acta Astronautica,* vol. 176, pp. 341-356, 2020.

[70] F. S. Milos and Y.-K. Chen, "Ablation and Thermal Response Property Model Validation for Phenolic Impregnated Carbon Ablator," *Journal of Spacecraft and Rockets,* vol. 47, no. 5, 2010.

[71] V. Carandente, R. Scigliano, V. De Simone and et al., "A Finite Element approach for the design of innovative ablative materials for space applications," in *6th European Conference for Aeronautics and Space Sciences (EUCASS)*, Krakow, Poland, 2015.

[72] H. K. Tran, C. E. Johnson, D. J. Rasky and et al., "Silicone impregnated reusable ceramic ablators for Mars follow-on missions," *31st Thermophysics Conference*, *American Institute of Aeronautics and Astronautics, Inc.,* New Orleans, LA, June 1996.

[73] J. R. Gaier, D. L. Waters, S. Baldwin and et al., "Degradation of Beta Cloth Covering for a Battery Orbital Replacement Unit in Low Earth Orbit," in *SPACE Conferences and Exposition*, Long Beach, California, 2016.

[74] R. R. Kamenetzky and M. M. Finckenor, "Comparison of Observed Beta Cloth Interactions With Simulated and Actual Space Environment," NASA, NASA/TM-1999-209575, 1999.

[75] T. Schildknecht, R. Musci, M. Ploner and et al., "Optical observations of space debris in GEO and highly-eccentric orbits," *Advances in Space Research,* vol. 34, no. 5, pp. 901-911, 2004.

[76] C. Früh and M. K. Jah, "Coupled orbit-attitude motion of high area-to-mass ratio (HAMR) objects including efficient self-shadowing," *Acta Astronautica,* vol. 95, pp. 227-241, 2014.

[77] D. G. Gilmore, *Spacecraft Thermal Control Handbook Volume 1: Fundamental Technologies*, 2nd Edition ed., vol. I, El Segundo, California: The Aerospace Corporation, 2002.

[78] M. M. Finckenor and D. Dooling, "Multilayer Insulation Material Guidelines," NASA, NASA/TP-1999-209263, 1999.

[79] A. Kumar and B. R., "A Review on Design Features of the Falcon-9 Space Launch Vehicle," *International Research Journal of Modernization in Engineering Technology and Science,* vol. 3, no. 9, 2021.

[80] K. Jorgensen-Abercromby, M. Guyote and J. Okada, "Inertial Upper Stage Surface Property Study," in *Proc. 4th European Conference on Space Debris*, Darmstadt, Germany, 2005.

[81] D. Sousek, "Orbital Simulation of the Titan III Transtage Spacecraft," *Proceedings of the IES,* pp. 561-567, 1996.

[82] J. A. Reyes, B. G. Miller, E. A. Plis and et al., "Understanding optical changes in on-orbit spacecraft materials," in *SPIE Proceedings Volume 11101, Material Technologies and Applications to Optics, Structures, Components, and Sub-Systems IV;*, San Diego, California, 2019.

[83] A. Jaworske, "Thermal Cycling of Thermal Control Paints on Carbon-Carbon and Carbon-Polyimide Composites," in *3rd International Energy Conversion Engineering Conference*, San Francisco, CA, 2005.

[84] C. I. Calle, C. R. Buhler, M. D. Hogue and et al., "Development of a dust mitigation technology for thermal radiators for lunar exploration," in *IEEE Aerospace Conference*, Big Sky, MT, 2010.

[85] M. Choi, "Thermal vacuum/balance test results of swift BAT with loop heat pipe thermal system," in *2nd International Energy Conversion Engineering Conference*, Providence, RI, 2004.

[86] M. M. Finckenor, J. L. Golden and M. Kravchenko, "Analysis of International Space Station Vehicle Materials Exposed on Materials International Space Station Experiment from 2001 to 2011," NASA, NASA/TP-2013-217498, 2013.

[87] R. Cooper and R. Hoffmann, "Jumbo Space Environment Simulation and Spacecraft Charging Chamber Characterization," Air Force Technical Report AD1000521, 2015.

[88] J. A. Reyes, K. W. Fulford, E. A. Plis and et al., "Spectroscopic behavior of various materials in a GEO simulated environment," *Acta Astronautica,* vol. 189, pp. 576-583, December 2021.

[89] I. Levchenko, K. Bazaka, T. Belmonte and et al., "Advanced Materials for Next-Generation Spacecraft," *Advanced Materials,* 1802201, 2018. doi:10.1002/adma.201802201.

[90] H. M. Cowardin, J. M. Hostetler, J. I. Murray, J. A. Reyes and C. L. Cruz, "Optical Characterization of DebriSat Fragments in Support of Orbital Debris Environmental Models," *Journal of the Astronautical Sciences,* vol. 68, 1186–1205 (2021). https://doi.org/10.1007/s40295-021-00278-9.

[91] M. Werremeyer, "Design of Sub-systems for a Representative Modern LEO Satellite," dissertation, University of Florida, 2013.

[92] S. Clark, "Design of a Representative LEO Satellite and Hypervelocity Impact Test to Improve the NASA Standard Brekup Model," 2013.

[93] E. Ausay, A. Cornejo, A. Horn and et al., "A Comparison of the SOCIT and DebriSat Experiments," in *European Conference on Space Debris*, Darmstadt, Germany, 2017.

[94] H. Cowardin, P. Anz-Meador, J. Murray and et al., "Updates to the DebriSat Project in Support of Improving Breakup Models and Orbital Debris Risk Assessments," in *Hypervelocity Impact Symposium*, Destin, Florida, 2019.

[95] J. Opiela, "A Study of the Material Density Distribution of Space Debris," *Advances in Space Research,* vol. 47, no. 7, pp. 1058-1064, 2009.

[96] R. Madler, K. Jorgensen, R. D. Culp and D. Spencer, "Estimating the Area of Artificial Space Debris," in *2nd European Conference on Space Debris*, Darmstadt, Germany, 1997.

[97] H. M. Rodriguez, K. J. Abercromby, K. S. Jarvis and et al., "Using Light Curves to Characterize Size and Shape of Pseudo-Debris," *Advanced Maui Optical and Space Surveillance Technologies conference*, Maui, Hawaii, 2006.

[98] P. H. Krisko, M. Horstman and M. L. Fudge, "SOCIT4 collisional-breakup test data analysis: With shape and materials characterization," *Advances in Space Research,* vol. 41, pp. 1138-1146, 2008.

[99] R. L. Werneth, "Lessons learned from Hubble Space Telescope extra vehicular activity supportability," in *AIP Conference Proceedings 552*, 2001.

[100] Orbital Debris Program Office, "Image Survey of the Hubble Space Telescope," *Orbital Debris Quarterly News,* vol. III, no. 4, pp. 1-2, October 1998.

[101] Lockheed Martin, *Hubble Space Telescope Serviceing Mission 3A Media Reference Guide*, report, Lockheed Martin, 1999.

[102] E. A. Taylor, N. R. G. Shrine, N. McBride and et al., "Impacts on HST and Eureca solar arrays compared with LDEF using a new glass-to-aluminum conversion," *Advances in Space Research ,* vol. 23, no. 1, pp. 83-87, 1999.

[103] G. Graham, N. McBride, A. T. Kearsley and et al., "The Chemistry of Micrometeoroid and Space Debris Remnants Captures on Hubble Space Telescope Solar Cells," *International Journal of Impact Engineering,* vol. 26, pp. 263-274, 2001.

[104] Orbital Debris Program Office, "SEM Analysis Results of Returned ISS PMA-2 Cover," *Orbital Debris Quarterly News,* vol. 22, no. 1, February 2018.

[105] R. P. Bernhard, C. Durin and M. E. Zolensky, "Scanning electron microscope/energy dispersive x ray analysis of impact residues in LDEF tray clamps," in *NASA. Langley Research Center, LDEF: 69 Months in Space. Second Post-Retrieval Symposium, Part 2*, 1993.

[106] R. P. Bernhard, T. H. See and F. Hoerz, "Projectile compositions and modal frequencies on the chemistry of micrometeoroids LDEF experiment," in *In NASA. Langley Research Center, LDEF: 69 Months in Space. Second Post-Retrieval Symposium, Part 2*, 1993.

[107] J. Murray, R. Miller, M. Matney and T. Kennedy, "Orbital Debris Radar Measurements from the Haystack Ultra-wideband Satellite Imaging Radar (HUSIR): 2014-2017," in *1st International Orbital Debris Conference*, Houston, Texas, 2019.

[108] J. V. Eshbaugh, J. R. L. Morrison, E. Weber Hoen, T. C. Hiett and G. R. Benitz, "HUSIR Signal Processing," *Lincoln Laboratory Journal,* vol. 21, no. 1, pp. 115-134, 2014.

[109] R. Miller, J. Murray and T. Kennedy, "Goldstone Radar Measurements of the Orbital Debris Environment: 2018," *Orbital Debris Program Office,* May 2021.

[110] Orbital Debris Program Office, "Projected GEO Survey Capabilities of the Meter Class Eugene Stansbery Orbital Debris Telescope," *Orbital Debris Quarterly News,* vol. 21, no. 4, 2017.

[111] J. Šilha, "Small telescopes and their application in space debris research and space surveillance tracking," *Contributions of the Astronomical Observatory Skalnaté Pleso,* vol. 49, no. 2, pp. 307-319, 2019.

[112] M. Fukugita, T. Ichikawa and J. E. Gunn, "The Sloan Digital Sky Survey Photometric System," *The Astronomical Journal,* vol. 11, no. 4, 1996.

[113] NASA ODPO, "Optical Measurements," [Online]. Available: https://orbitaldebris.jsc.nasa.gov/measurements/optical.html. [Accessed 31 March 2022].

[114] P. Seitzer, S. M. Lederer, E. S. Barker and et al., "A Search for Optically Faint GEO Debris," in *Advanced Maui Optical and Space Surveillance Technologies Conference (AMOS)*, Maui, Hawaii, 2011.

[115] S. M. Lederer, A. Vavrin, H. M. Cowardin and et al., "Integrating Orbital Debris Measurements and Modeling – How Observations and Laboratory Data are used to Help Make Space Operations Safer," in *Advanced Maui Optical and Space Surveillance Technologies Conference (AMOS)*, Maui, Hawaii, 2018.

[116] S. M. Lederer, B. Buckalew, P. Hickson and H. Cowardin, "NASA's Orbital Debris Optical Program: ES-MCAT Updated and Upgraded," in *Advanced Maui Optical and Space Surveillance Technologies Conference (AMOS)*, Maui, Hawaii, 2019.

[117] R. Sridharan and A. F. Pensa, "U.S. Space Surveillance Network Capabilities," in *SPIE Conference on Characteristics and Consequences of Space Debris and Near-Earth Objects*, San Diego, Califronia, 1998.

[118] T. A. F. A. Sgobba, "Chapter 8 - Orbital Operatons Safety," in *Safety Design for Space Operations*, Butterworth-Heinemann, 2013, pp. 411-602.

[119] K. Markus, L. Moroz, G. Arnold and et al., "Reflectance spectra of synthetic Fe-free ortho- and clinoenstatites in the UV/VIS/ IR and implications for remote sensing detection of Fe-free pyroxenes on planetary surfaces," *Planetary and Space Science,* vol. 159, pp. 43-55, 2018.

[120] A. Pisello, F. P. Vetere, M. Bisolfati and et al., "Retrieving magma composition from TIR spectra: implications for terrestrial planets investigations," *Nature Scientific Reports,* vol. 9, 15200 (2019). https://doi.org/10.1038/s41598-019-51543-9.

[121] J. Benkhoff, J. van Casteren, H. Hayakawa and et al., "BepiColombo—Comprehensive Exploration of Mercury: Mission overview and science goals," *Planetary and Space Science,* vol. 28, no. 1-2, pp. 2-20, 2009.

[122] R. Prost, "The Influence of the Christiansen Effect on I.R. Spectra of Powders," *Clays and Clay Minerals,* vol. 21, pp. 363-368, 1973.

[123] H. R. Carlon, "Christiansen effect in IR spectra of soil-derived atmospheric dusts," *Applied Optics,* vol. 18, no. 21, 1979.

[124] A. Maturilli, J. Helbert and G. Arnold, "The newly improved set-up at the Planetary Spectroscopy Laboratory (PSL)," Proc. SPIE 11128, Infrared Remote Sensing and Instrumentation XXVII, 111280T (9 September 2019). https://doi.org/10.1117/12.2529266.

[125] A. Maturilli, J. Helbert and L. Moroz, "The Berlin emissivity database (BED)," *Planetary and Space Science,* vol. 56, no. 3-4, pp. 420-425, 2008.

[126] A. Maturilli, J. Helbert, J. M. St. John and et al., "Komatiites as Mercury surface analogues: Spectral measurements at PEL," *Earth and Planetary Science Letters,* vol. 398, pp. 58-65, 2014.

[127] A. Maturilli, J. Helbert, A. Witzke and L. Moroz, "Emissivity measurements of analogue materials for the interpretation of data from PFS on Mars Express and MERTIS on Bepi-Colombo," *Planetary and Space Science 54,* pp. 1057-1064, 2006.

[128] E. A. Cloutis, V. B. Pietrasz, C. Kiddell and et al., "Spectral reflectance "deconstruction"of the Murchison CM2 carbonaceous chondrite and implications for spectroscopic investigations of dark asteroids," *Icarus,* vol. 305, p. 203-244, 2018.

[129] Analytical Spectral Devices, Inc. (ASD), "Technical Guide," Boulder, Colorado, 1999.

[130] K. Kitazato, R. E. Milliken, T. Iwata and et al., "The surface composition of asteroid 162173 Ryugu from Hayabusa2 near-infrared spectroscopy," *Science,* vol. 364, no. 6437, 2019.

[131] O. Poch, I. Istiqomah, E. Quirico and et al., "Ammonium salts are a reservoir of nitrogen on a cometary nucleus and possibly on some asteroids," *Science 367,* vol. 367, no. 6483, 2020.

[132] M. I. Blecka, F. Capaccioni, G. Filacchione and et al., "Searching for the spectral features of minerals on the surface and in the dust of the comet 67P/Churyumov- Gerasimenko in NIR spectral range of VIRTIS-M data," *European Planetary Science Congress,* Nantes, France, 2015.

[133] P. Seitzer, S. M. Lederer, H. Cowardin and et al., "Visible Light Spectroscopy of GEO Debris," in *Advanced Maui Optical and Space Surveillance Technologies Conference (AMOS)*, Maui, Hawaii, 2012.

[134] K. Jorgensen, "Using Reflectance Spectroscopy to Determine Material Type of Orbital Debris," dissertation, University of Colorado, 2000.

[135] K. Abercromby, P. Abell and E. Barker, "Reflectance Spectra Comparison of Orbital Debris, Intact Spacecraft, and Intact Rocket Bodies in the GEO Regime," in *Proceedings of the Fifth European Conference on Space Debris*, Darmstadt, Germany, 2009.

[136] D. Bedard and G. A. Wade, "Time-resolved visible/near-infrared spectrometric observations of the Galaxy 11 geostationary satellite," *Advances in Space Research,* vol. 59, no. 1, 2016.

[137] A. Vananti, T. Schildknecht and H. Krag, "Reflectance Spectroscopy Characterization of Space Debris," *Advances in Space Research,* vol. 59, no. 10, p. 2488-2500, 2017.

[138] K. Jorgensen, J. Africano, K. Hamada and et al., "Physical properties of orbital debris from spectroscopic observations," *Advances in Space Research ,* pp. 1021-1025, 2004.

[139] J. T. Rayner, D. W. Toomey, P. M. Onaka, A. J. Denault, W. E. Stahlberger, W. D. Vaca, M. C. Cushing and S. Wang, "SpeX: A medium-resolution 0.8-5.5 micron spectrograph and imager for the NASA Infrared Telescope Facility," *Publications of the Astronomical Society of the Pacific,* pp. 362-382, 2003.

[140] K. Jorgensen, J. Okada, L. Bradford and et al., "Obtaining Material Type of Orbiting Objects through Reflectance Spectroscopy Measurements," in *Advanced Maui Optical and Space Surveillance Technologies Conference (AMOS)*, Maui, Hawaii, 2003.

[141] M. Bengtson, J. Maxwell, R. Hoffmann and et al., "Optical Characterization of Commonly Used Thermal Control Paints in a Simulated GEO Environment," in *Advanced Maui Optical and Space Surveillance Technologies Conference (AMOS)*, Maui, Hawaii, 2018.

[142] D. P. Engelhart, R. Cooper, H. Cowardin and et al., "Space Weathering Experiments on Spacecraft Materials," in *Advanced Maui Optical and Space Surveillance Technologies Conference (AMOS)*, Maui, Hawaii, 2017.

[143] E. Plis, K. Fulford, D. Engelhart and et al., "Space weathering of solar array coverglasses," Proc. *SPIE 11755, Sensors and Systems for Space Applications XIV*, 117550Q (12 April 2021); https://doi.org/10.1117/12.2585306.

[144] P. P. Jenkins, R. J. Walters and L. C. Creer, "In-Flight Performance of III-V Multi-junction Solar Cells from the Forward Technology Solar Cell Experiment," *2008 33rd IEEE Photovoltaic Specialists Conference*, 2008, pp. 1-6, doi: 10.1109/PVSC.2008.4922859.

[145] J. R. Dennison, J. Prebola, A. Evans and et al., "Comparison of Flight and Ground Tests of Environmental Degradation of MISSE-6 SUSpECS Materials," in *Proceedings of the 11th Spacecraft Charging Technology Conference*, Albuquerque, NM, 2010.

[146] S. W. Samwel, "Low Earth Orbit Atomic Oxygen Erosion Effect on Spacecraft Materials," *Space Research Journal,* 7: 1-13, 2014. doi: 10.3923/srj.2014.1.13.

[147] B. A. Banks, S. K. Miller and K. K. de Groh, "Low Earth Orbital Atomic Oxygen Interactions with Materials," in *2nd International Energy Conversion Engineering Conference*, Providence, Rhode Island, 2004.

[148] D. Dooling and M. M. Finckenor, "Material Selection Guidelines to Limit Atomic Oxygen Effects on Spacecraft Surfaces," technical report, NASA, NASA/TP-1999-209260, 1999.

[149] M. R. Reddy, "Review Effect of low earth orbit atomic oxygen on spacecraft materials," *Journal of Materials Science,* pp. 281-307, 1995.

[150] H. D. Burns, A. F. Whitaker and R. C. Linton, "Atomic Oxygen Resistant Protective Coatings for the Hubble Space Telescope Solar Array in Low Earth Orbit," *Surface and Coatings Technology,* pp. 627-636, 1989.

[151] N. J. Ianno, D. W. Thompson, S. Sharma and et al., "Atomic Oxygen Induced Degredation of MGF2 Anti-reflective Coatings," *2008 33rd IEEE Photovoltaic Specialists Conference*, 2008, pp. 1-5, doi: 10.1109/PVSC.2008.4922702.

[152] M. J. Berger, J. S. Coursey and M. A. Zucker, "ESTAR, PSTAR, and ASTAR: Computer Programs for Calculating Stopping-Power and Range Tables for Electrons, Protons, and Helium Ions (version 1.21)," 1999. http://physics.nist.gov/Star, [online], http://physics.nist.gov/Star (Accessed August 1, 2022).

[153] R. Mishra, S. P. Tripathy, D. Sinha and et al., "Optical and electrical properties of some electron and proton irradiated polymers," *Nuclear Instruments and Methods in Physics Reserach Section B: Beam Interactions with Materials and Atoms,* vol. 168, no. 1, pp. 59-64, 2000.

[154] T. Steckenreiter, E. Balanzat, H. Fuess and C. Trautmann, "Chemical modifications of PET induced by swift heavy ions," *Nuclear Instruments and Methods in Physics Research Section B: Beam Interactions with Materials and Atoms,* vol. 131, no. 1-4, 1997.

[155] D. A. Jaworske and S. E. Kline, "Review of end-of-life thermal control coating performance," NASA, NASA/TM-2008-215173, 2008.

[156] J. M. Bioucas-Dias, A. Plaza, G. Camps-Valls, P. Scheunders, N. Nasrabadi and J. Chanussot, "Hyperspectral Remote Sensing Data Analysis and Future Challenges," *IEEE Geoscience and Remote Sensing Magazine,* vol. 1, no. 2, pp. 6-36, June 2013, doi: 10.1109/MGRS.2013.2244672.

[157] J. Yi and M. Velez-Reyes, "Simplified simulation of unresolved objects in hyperspectral remote sensing for space situational awareness," Proc. *SPIE 11392, Algorithms, Technologies, and Applications for Multispectral and Hyperspectral Imagery XXVI*, 113921F (12 June 2020); https://doi.org/10.1117/12.2560127.

[158] J. Murray-Krezan and W. Wing, "Uncertainty analysis for characterization small GEO belt debris population," *Optical Engineering* 58(4), 041608 (24 January 2019). https://doi.org/10.1117/1.OE.58.4.041608.

[159] H. Cowardin, K. Abercromby, E. Barker and et al., "An Assessment of GEO Orbital Debris Photometric Properties Derived from Laboratory-Based Measurements," in *Advanced Maui Optical and Space Surveillance Technologies Conference (AMOS)*, Maui, Hawaii, 2009.

[160] J. Moore, "Photometric Observations of the Second Soviet Satellite," *Publications of the Astronomical Society of the Pacific,* vol. 71, no. 419, pp. 163-165, 1959.

[161] P. P. Sukhov and K. P. Sukhov, "On Some Problems of Photometric Identification of Geostationary Satellites," *Kinematics and Physics of Celestial Bodies,* vol. 31, no. 6, pp. 314-318, 2015.

[162] J. M. Sorvari, "Photometry of Artificial Satellites Application to the Ground Electro-optical Deep Space Surveillance (GEODSS) Program," technical report, Massachusetts Inst of Tech Lexington Lincoln Laboratory, ADA078675, 1979.

[163] A. Murtazov, "Physical simulation of space objects' spectral characteristics for solving the reverse problem of their photometry," *American Journal of Modern Physics,* vol. II, no. 6, pp. 282-286, 2013.

[164] E. C. Pearce, H. A. Ford, T. Schildknecht and et al., "Rapid Characterization of Geosynchronous Space Debris with 5-color Near-IR Photometry," in *Proceedings of the Advanced Maui Optical and Space Surveillance (AMOS) Technologies Conference*, Maui, Hawaii, 2017.

[165] T. E. Payne, S. A. Gregory, D. J. Sanchez and et al., "Color Photometry of Geosynchronous Satellites Using the SILC Filters," Proc. *SPIE 4490, Multifrequency Electronic/Photonic Devices and Systems for Dual-Use Applications*, (27 December 2001); https://doi.org/10.1117/12.455426.

[166] J. Frith, B. Gibson, R. Knox and K. Kuluhiwa, "Simultaneous Single Site Color Photometry of LEO Satellites," in *Proceedings of the Advanced Maui Optical and Space Surveillance Technologies Conference*, Maui, Hawaii, 2008.

[167] H. L. Johnson, R. I. Mitchell, B. Iriarte and et al., "UBVRIJKL Photometry of the Bright Stars," *Communications of the Lunar and Planetary Laboratory,* vol. 4, no. 1, pp. 99-110, 1966.

[168] A. W. J. Cousins, "VRI photometry of southern stars," *South African Astron. Obs. Circ.,* 1980.

[169] M. S. Bessell, "VRI Photometry: An Addendum," *Publications of the Astronomical Society of the Pacific,* 1983.

[170] C. Rodgers, R. Canterna, J. A. Smith and et al., " Improved u'g'r'i'z' to UBVRCIC Transformation Equations for Main-Sequence Stars," *The Astronomical Journal,* pp. 989-993, 2006.

[171] P. Seitzer, H. M. Cowardin, E. Barker and et al., "Photometric Studies of GEO Debris," in *Advanced Maui Optical and Space Surveillance Technologies Conference (AMOS)*, Maui, Hawaii, 2009.

[172] S. M. Lederer, P. Seitzer, H. M. Cowardin and et al., "Preliminary Characterization of IDCSP Spacecrafts through a Multi-Analytical Approach," 2012.

[173] A. Lawrence, S. Warren, O. Almaini and e. al., "The UKIRT Infrared Deep Sky Survey (UKIDSS)," *Monthly Notices of the Royal Astonomical Society,* vol. 379, no. 4, 2007.

[174] J. Frith, P. Anz-Meador, H. Cowardin and et al., "Near-infrared color vs launch date: an analysis of 20 years of space weathering effects on the Boeing 376 spacecraft," in *Proceedings of the Advanced Maui Optical and Space Surveillance Technologies Conference*, Maui, Hawaii, 2015.

[175] K. Abercromby, B. Buckalew, P. Abell and H. Cowardin, "Infrared Telescope Facility's Spectrograph Observations of Human-Made Space Objects," in *Advanced Maui Optical and Space Surveillance Technologies Conference (AMOS)*, Maui, Hawaii, 2015.

[176] M. Q. Alkhatib and M. Velez-Reyes, "Improved Spatial-Spectral Superpixel Hyperspectral Unmixing," *Remote Sensing,* 2019, 11(20), 2374; https://doi.org/10.3390/rs11202374.

[177] B. Aryal, S. M. Escarzaga, S. A. Vargas Zesati, M. Velez-Reyes, O. Fuentes and C. Tweedie, "Semi-Automated Semantic Segmentation of Arctic Shorelines Using Very High-Resolution Airborne Imagery, Spectral Indices and Weakly Supervised Machine Learning Approaches," in *Remote Sensing*, 2021, 13(22), 4572; https://doi.org/10.3390/rs13224572.

[178] M. Burke, C. Dawson, C. S. Allen and et al., "Reflective spectroscopy investigations of clothing items to support law enforcement, search and rescue, and war crime investigations," *Forensic Science International,* vol. 304, November 2019.

[179] J. Yi, M. Velez-Reyes and H. Erives, "Studying the Potential of Hyperspectral Unmixing for Extracting Composition of Unresolved Space Objects using Simulation Models," in *Advanced Maui Optical and Space Surveillance Technologies Conference (AMOS)*, 2021.

[180] A. B. Chaudhary, T. Payne, S. Gregory and P. Dao, "Fingerprinting of Non-resolved Three-axis Stabilized Space Objects Using a Two-Facet Analytical Model," technical report, Air Force Research Laboratory, 2011.

[181] P. Dao, P. McNicholl and A. Dentamaro, "Unmixing Space Object's Moderate Resolution Spectra," in *Advanced Maui Optical and Space Surveillance Technologies Conference (AMOS)*, Maui, Hawaii, 2013.

[182] K. J. Abercromby, J. Rapp, D. Bedard and et al., "Comparisons of a Constrained Least Squares Model versus Human-in-the-loop for Spectral Unmixing to Determine Material Type of GEO Debris1," in *Sixth European Conference on Space Debris*, 2013.

[183] M. Velez-Reyes and J. Yi, "Hyperspectral Unmixing for Remote Sensing of Unresolved Objects," in *Advanced Maui Optical and Space Surveillance Technologies Conference (AMOS)*, Maui, Hawaii, 2020.

[184] K. DeWitt, "Machine learning for better trace chemical detection," in *Proc. SPIE 10986, Algorithms, Technologies, and Applications for Multispectral and Hyperspectral Imagery XXV*, Baltimore, Maryland, 2019.

[185] F. Kokaly, R. N. Clark, G. A. Swayze and et al., "USGS Spectral Library Version 7: U.S. Geological Survey Data Series," 61 p., 2017, https://doi.org/10.3133/ds1035.

[186] S. K. Meerdink, S. J. Hook, D. A. Roberts and E. A. Abbott, "The ECOSTRESS Spectral Library Version 1.0," *Remote Sensing of Environment,* vol. 230, September 2019.

[187] A. M. Baldridge, S. J. Hook, C. I. Grove and G. Rivera, "The ASTER spectral library version 2.0," *Remote Sensing of Environment,* vol. 113, no. 4, pp. 711-715, 2009.

[188] NASA Orbital Debris Program Office, "NASA JSC Spacecraft Materials Spectral Database," digitial database, NASA Johnson Space Center, Houston, 2019.

[189] Spectral Evolution, "Full Range Spectroradiometers UV-VIS-NIR-SWIR," manual, Spectral Evolution, Haverhill, MA.

[190] J. Frith, J. Reyes, H. Cowardin and et al., "Infrared Studies of the Reflective Properties of Solar Cells of the HS376 Spacecraft," technical report, NASA, JSC-CN-37428, 2016.

[191] F. Campbell, Elements of metallurgy and engineering alloys, Materials Park, Ohio: ASM International, 2008, pp. 321-322.

[192] R. N. Clark, "Chapter 1: Spectroscopy of Rocks and Minerals, and Principles of Spectroscopy," *Manual of Remote Sensing,* vol. III, 1999.

[193] J. F. Mustard, "Chemical analysis of actinolite from reflectance spectra," *American Mineralogist,* vol. 77, pp. 345-358, 1992.

[194] G. G. Sward, "Paint Testing Manual Physical and Chemical Examination of Paints, Varnishes, Lacquers, and Colors Thirteenth Edition," American Society for Testing and Materials, 1972.

[195] D. E. Packham, Handbook of Adhesion Second Edition, 2nd Edition ed., West Sussex: John Wiley & Sons Ltd., 2005, pp. 308-309.

[196] P. J. Curran, "Remote Sensing of Foliar Chemistry," *Remote Sensing of Environment,* vol. 30, no. 3, pp. 271-278, 1989.

[197] W. W. Coblentz, "The Reflecting Power of Various Metals," *Bulletin of the Bureau of Standards,* vol. 7, no. 2, pp. 213-215, 1910.

[198] J. Mao and F. Bierlein, "Mineral Deposit Research: Meeting the Global Challenge," in *Proc. 8th Biennial SGA Meeting*, Beijing, China, 2005.

[199] S. J. Koester, "Germanium-on-SOI Infrared Detectors for Integrated Photonic Applications," *IEEE Journal of Selected Topics in Quantum Electronics,* vol. 12, no. 6, pp. 1489-1492, 2006.

[200] J. Hatch, Aluminum - Properties and Physical Metallurgy, Materials Park, OH: ASM International.

[201] E. A. Cloutis, "Spectral Reflectance Properties of Hydrocarbons: Remote-Sensing Implications," *Science,* vol. 245, no. 4914, pp. 165-168, 1989.

[202] M. Altmann, S. Bouquillon, F. Taris and e. al, "GBOT: ground based optical tracking of the Gaia satellite," in *Proc. SPIE 9149, Observatory Operations: Strategies, Processes, and Systems V*, 2014.

[203] A. Buzzoni, G. Altavilla and S. Calleti, "Optical tracking of deep-space spacecraft in Halo L2 orbits and beyond: The Gaia mission as a pilot case," *Advances in Space Research,* vol. 57, no. 7, pp. 1515-1527, 2016.

[204] J. Brum, C. Schlegel, C. Chappell and et al., "Reflective spectra of gasoline, diesel, and jet fuel A on sand substrates under ambient and cold conditions: Implications for detection using hyperspectral remote sensing and development of age estimation models," *Environmental Earth Sciences,* vol. 79, 2020.

[205] C. Wang, Q. Chen, M. Hussain and et al., "Application of Principal Component Analysis to Classify Textile Fibers Based on UV-Vis Diffuse Reflectance Spectroscopy," *Journal of Applied Spectroscopy,* vol. 84, no. 3, 2017.

[206] S. Hotthaus, T. E. L. Smith, M. J. Wooster and C. S. B. Grimmond, "Derivation of an urban materials spectral library through emittance and reflectance spectroscopy," *ISPRS Journal of Photogrammetry and Remote Sensing,* vol. 94, pp. 194-212, August 2014.

[207] H. Cowardin, P. Seitzer, A. K., E. Barker and T. Schildknecht, "Characterization of Orbital Debris Photometric Properties Derived from Laboratory-Based Measurements," in *Proc. Advanced Maui Optical and Space Surveillance Technologies Conference (AMOS)*, Maui, Hawaii, 2010.

[208] P.-E. Danielsson, "Euclidean Distance Mapping," *Computer Graphics and Image Processing,* vol. 14, no. 3, pp. 227-248, 1980.

[209] P. C. Hewett, S. J. Warren, S. K. Leggett and S. T. Hodgkin, "The UKIRT Infrared Deep Sky Survey ZY JHK photometric system: passbands and synthetic colours," *Monthly Notices of the Royal Astronomical Society,* vol. 367, no. 2, pp. 454-468, 2006.

[210] X. Fan, M. A. Strauss, D. P. Schneider and e. al., "A Survey of z > 5.7 Quasars in the SLOAN Digital Sky Survey. II. Discovery of the Three Additional Quasart at z > 6," *The Astronomical Journal,* vol. 125, no. 4, 2003.

[211] R. R. Nidamanuri and A. M. Ramiya, "Spectral identification of materials by reflectance spectral library search," *Geocarto International,* vol. 29, no. 6, pp. 609-624, 2014.

[212] J. B. Percival, S. A. Bosman, E. G. Potter and et al., "Customized Spectral Libraries for Effective Mineral Exploration: Mining National Mineral Collections," *Clays and Clay Minerals,* vol. 66, no. 3, pp. 297-314, 2018.

[213] I. Marques, M. Grana, S. M. Sanchez, M. Q. Alkhatib and M. Velez-Reyes, "Person detection in hyperspectral images via skin segmentation using an active learning approach," Proc. SPIE 9472, Algorithms and Technologies for Multispectral, Hyperspectral, and Ultraspectral Imagery XXI, 947207 (21 May 2015); https://doi.org/10.1117/12.2179333.

[214] P. Anz-Meador, J. N. Opiela, D. Shoots and J.-C. Liou, "History of On-Orbit Satellite Fragmentations 15th Edition," technical report, NASA, JSC-E-DAA-TN62909, Houston, TX, 2018.

[215] R. A. Williamson, The Fair and Responsible Use of Space: An International Perspective, Springer-Verlag/Wien, 2010.

[216] *Orbital Debris Quarterly News,* vol. 25, no. 1, February 2021.

Bibliography

E. Hecht, *Optics 5th Edition*. Harlow, England: Pearson, 2017.

M. Bessell, G. Bloxham, "Chapter 3: Astronomical Filters," in *The WSPC Handbook of Astronomical Instrumentation Volume 2: UV, Optical & IR Instrumentation: Part 1*, A. M. Moore and D. N. Burrows, Eds. 2021, pp. 55-69.

S. T. Hodgkin, M. J. Irwin, P. C. Hewett, S. J. Warren, "The UKIRT wide field camera ZYJHK photometric system: calibration from 2MASS," *Monthly Notices of the Royal Astronomical Society*, vol. 349, no. 2, 2009.

A. Lawrence, S. J. Warren, O. Almaini, et al., "The UKIRT Infrared Deep Sky Survey (UKIDSS)," *Monthly Notices of the Royal Astronomical Society*, vol. 379, no. 4, 2007.

B. Mahltig, Y. Kyosev, *Inorganic and Composite Fibers: Production, Properties, and Applications*, Elsevier Ltd., 2018.

T. D. Burchell, *Carbon Materials for Advanced Technologies*, Elsevier Science Ltd, 1999.

C. G. Goetzel, J. B. Rittenhouse, J. B. Singletary, *Space Materials Handbook*, Lockheed Missiles and Space Company, 1965.

D. N. Baker, P. J. Erickson, J. F. Fennell, et al. “Space Weather Effects in the Earth’s Radiation Belts,” *Space Science Reviews*, 2018.

R. J. Zomer, A. Trabucco, S. L. Ustin, “Building spectral libraries for wetlands land cover classification and hyperspectral remote sensing,” *Journal of Environmental Management*, pp. 2170-2177, 2009.

S. Kotthous, T. E. L. Smith, M. J. Wooster, C. S. B. Grimmond, “Derivation of an urban materials spectral library through emittance and reflectance spectroscopy,” *ISPRS Journal of Photogrammetry and Remote Sensing*, pp. 194-212, 2016.

M. Burke, J. Rakovan, M. P. S. Krekeler, “A study by electron microscopy of gold and associated minerals from Round Mountain, Nevada,” *Ore Geology Review*, pp. 708-717, 2017.

M. Barnes, C. L. McLeod, C. Chappell, et al. “Characterizing the geogenic background of the Midwest: a detailed mineralogical and geochemical investigation of a glacial till in southwestern Ohio”, *Environmental Earth Sciences*, 2020.

Appendix

A.1. Spectral Signatures of Spacecraft Materials

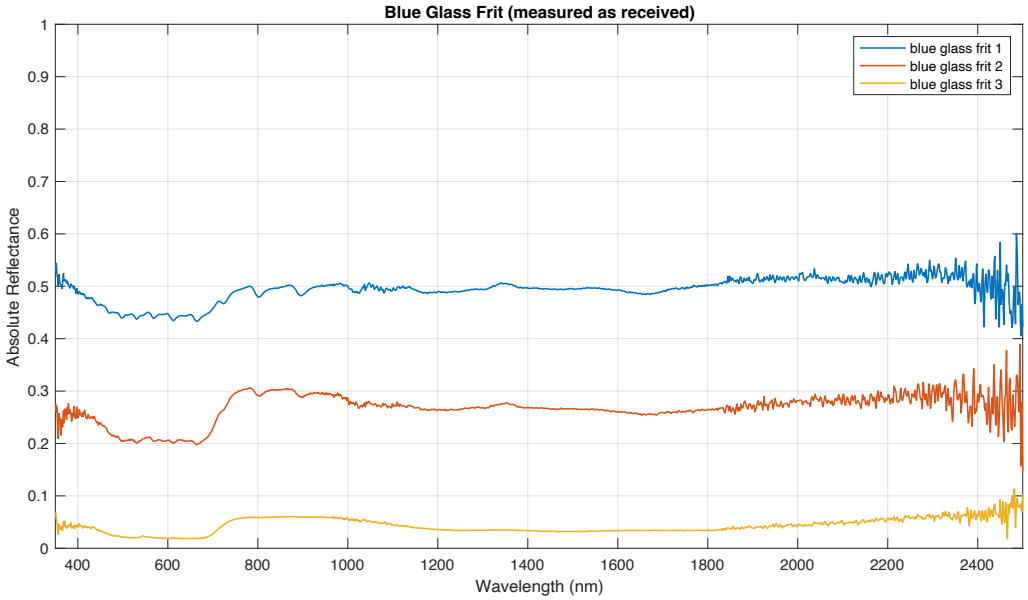

Figure A. 1: Reflectance spectra of blue glass frit material in its received condition. Three measurement reading results are included. *Credit: NASA*

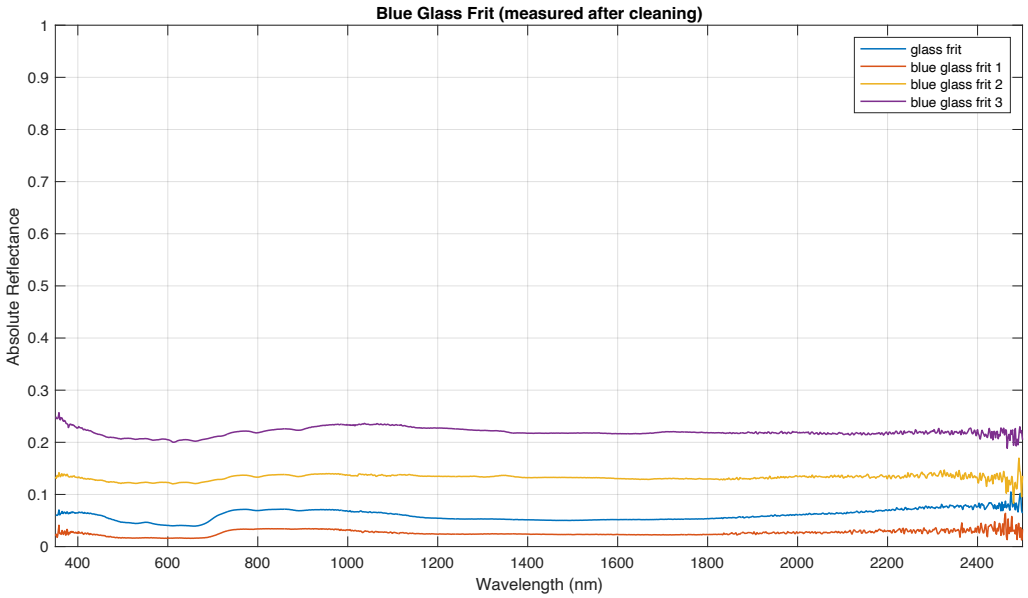

Figure A. 2: Reflectance spectra of glass frit material after being cleaned for debris or impurity removal. Four measurement reading results are included. *Credit: NASA*

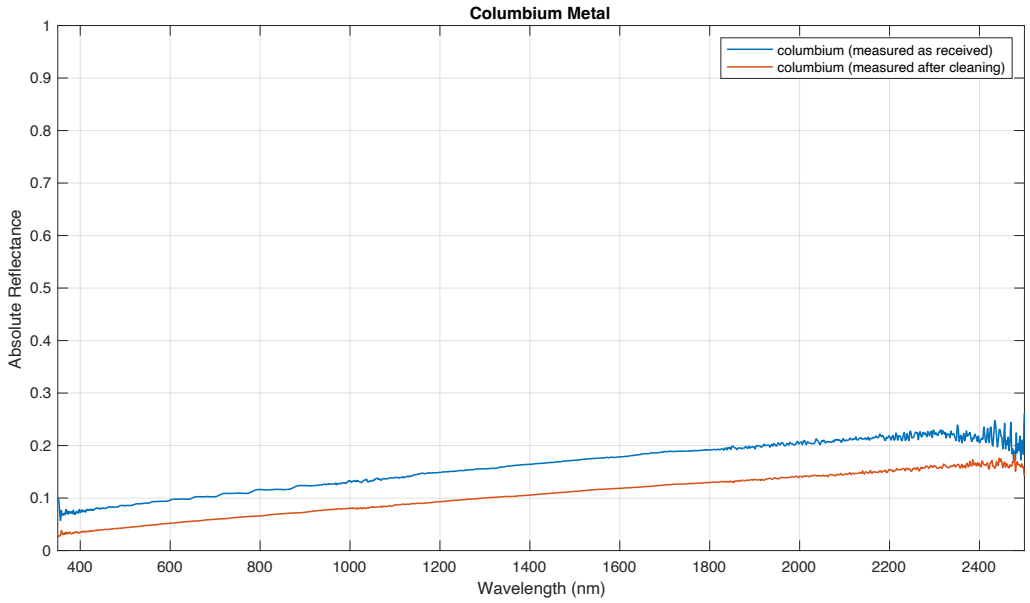

Figure A. 3: Reflectance spectra of columbium metal material in both as received and after cleaning of debris/impurities conditions. *Credit: NASA*

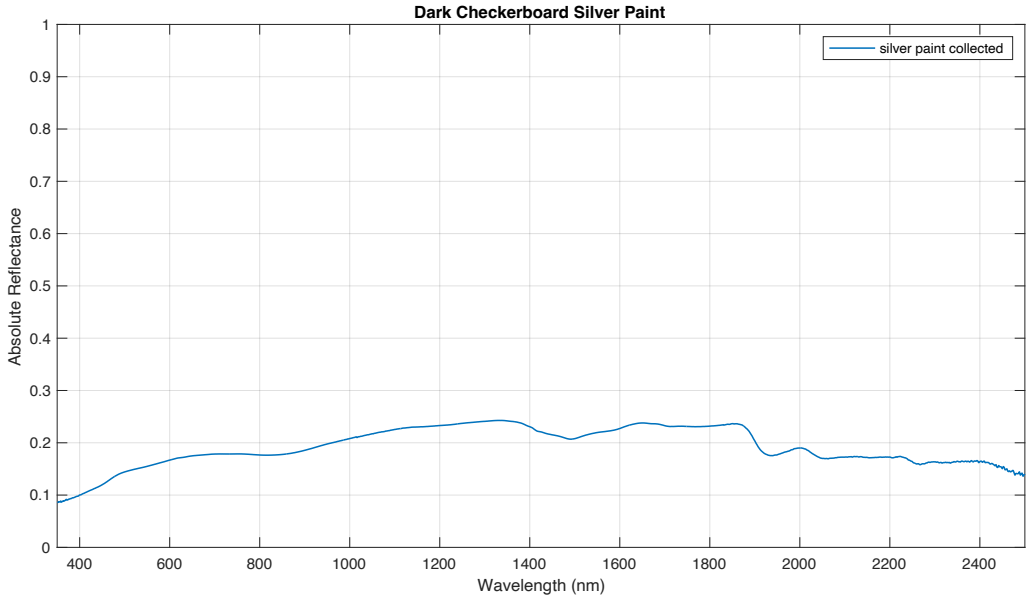

Figure A. 4: Reflectance spectra of dark checkerboard regions on the Titan IIIC Transtage mockup rocket body silver paint material sample collected. *Credit: NASA*

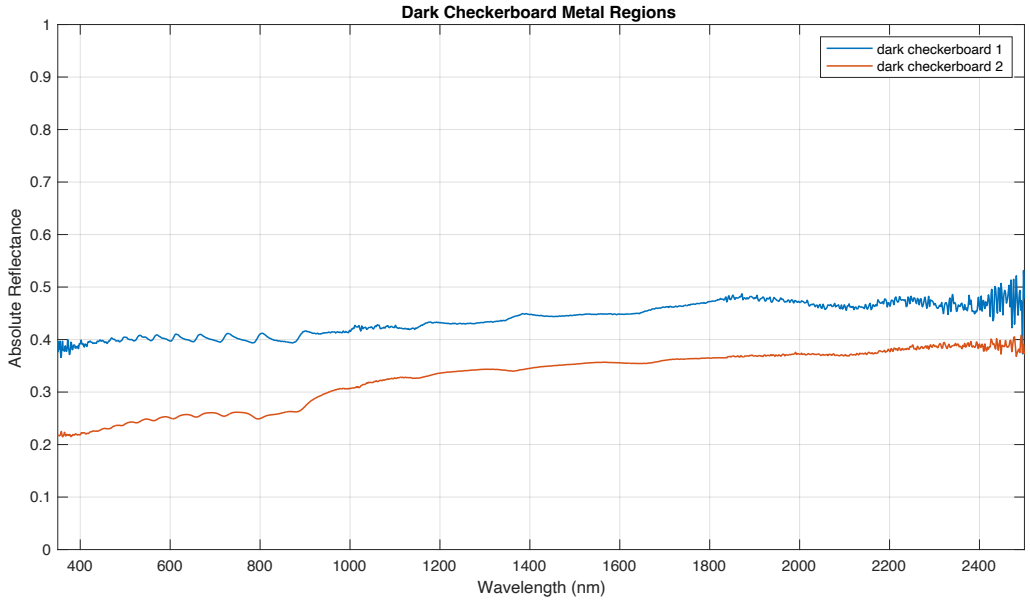

Figure A. 5: Reflectance spectra of dark checkerboard metal regions on the Titan IIIC Transtage mockup rocket body. *Credit: NASA*

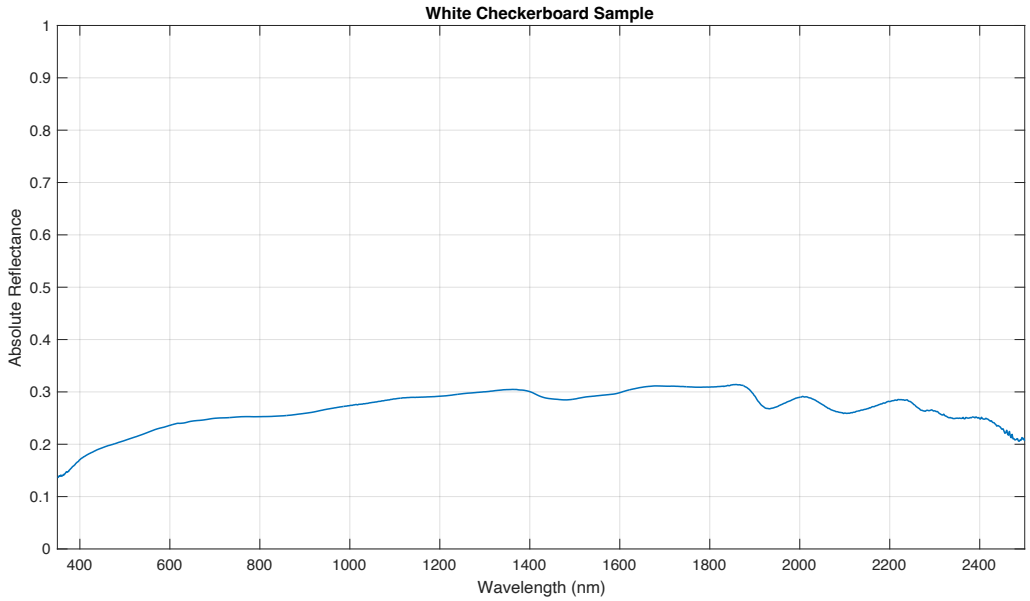

Figure A. 6: Reflectance spectra of white checkerboard regions on the Titan IIIC Transtage mockup rocket body paint material sample collected. *Credit: NASA*

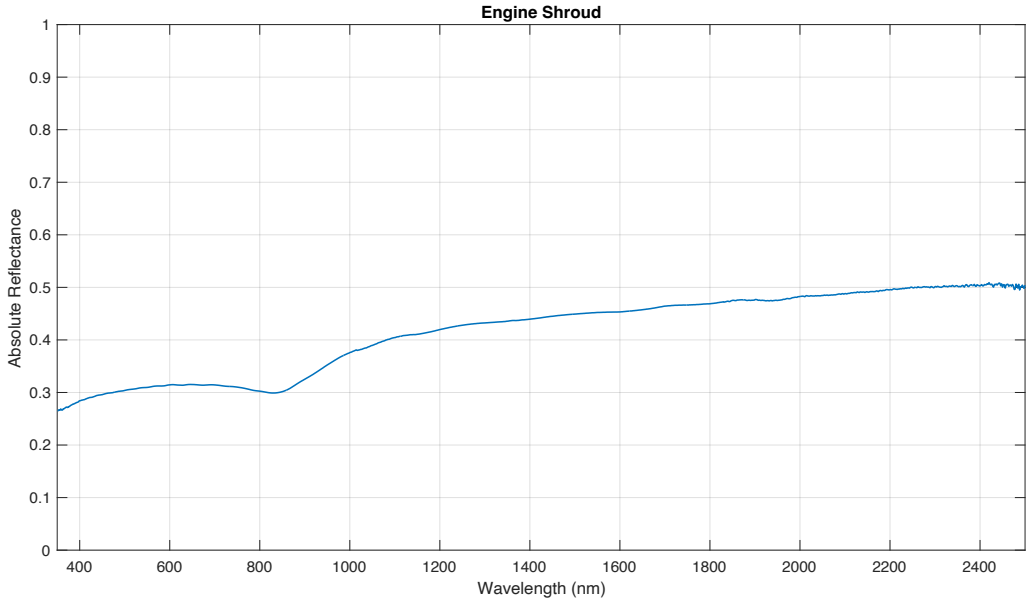

Figure A. 7: Reflectance spectra of the engine shroud regions on the Titan IIIC Transtage mockup rocket body. *Credit: NASA*

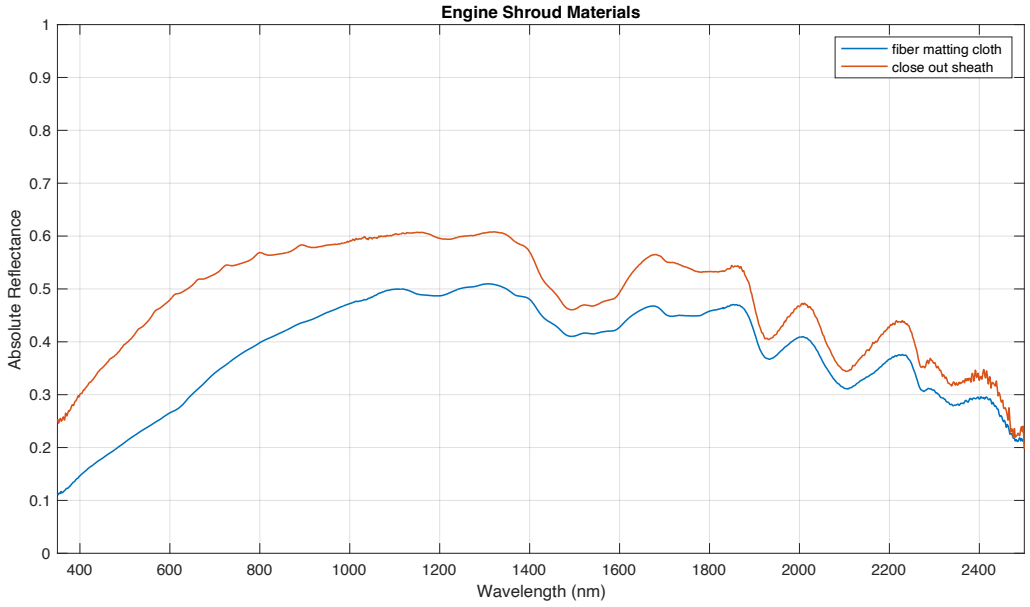

Figure A. 8: Reflectance spectra of the engine shroud material regions on the Titan IIIC Transtage mockup rocket body for fiber matting cloth and close-out sheath materials. *Credit: NASA*

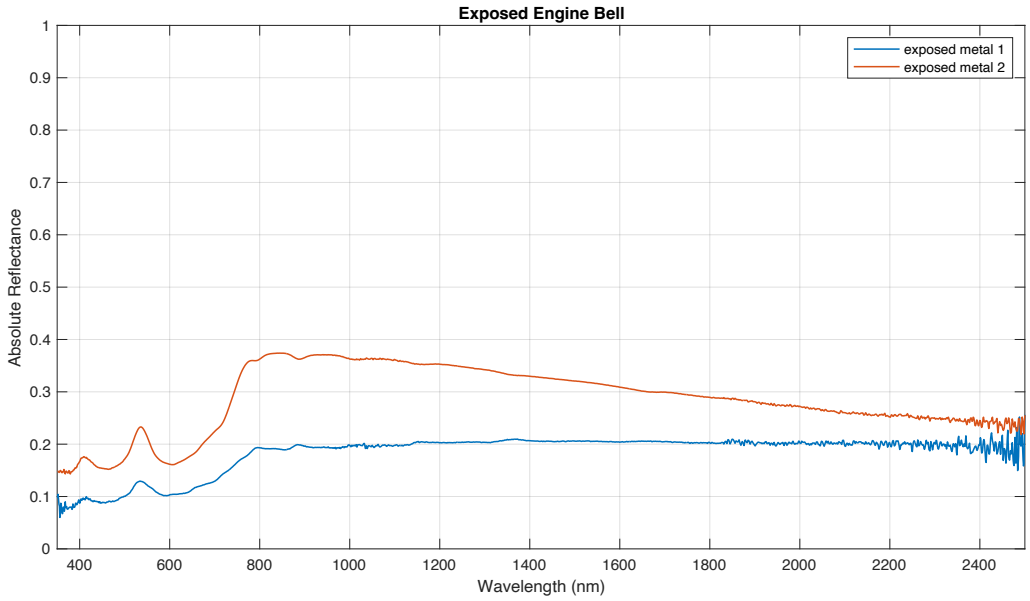

Figure A. 9: Reflectance spectra of the exposed engine bell regions on the Titan IIIC Transtage mockup rocket body. Two measurement reading results are included. *Credit: NASA*

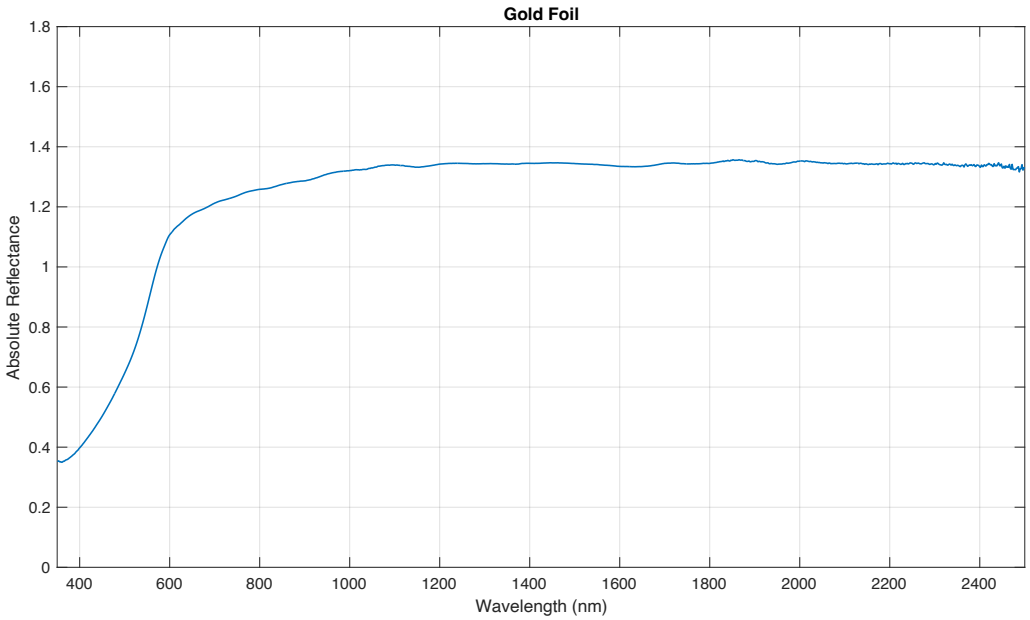

Figure A. 10: Reflectance spectra of dark checkerboard regions on the Titan IIIC Transtage mockup rocket body silver paint material sample collected. *Credit: NASA*

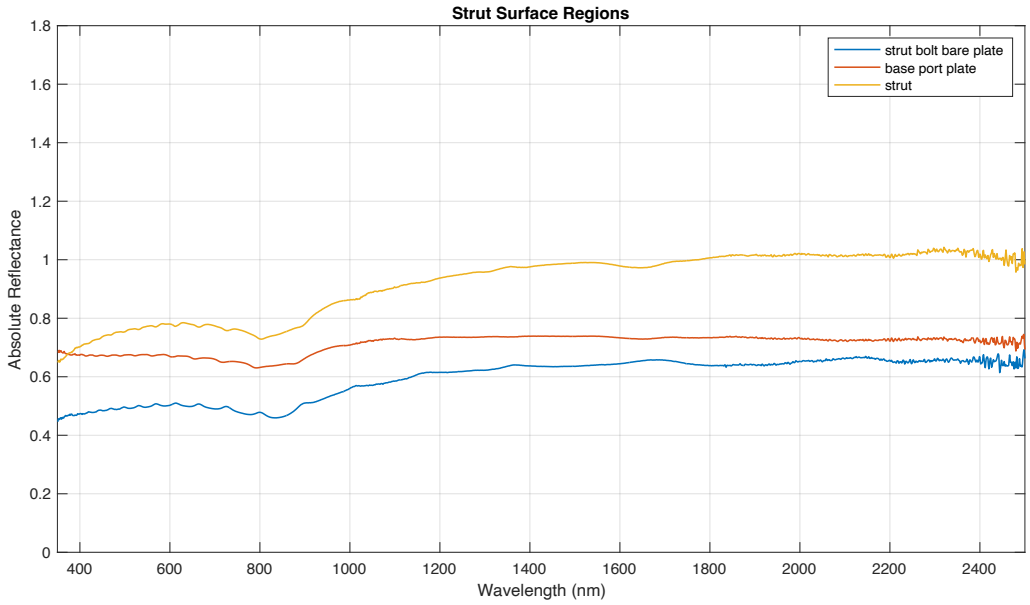

Figure A. 11: Reflectance spectra of the strut surface regions on the Titan IIIC Transtage mockup rocket body strut bolt bare plate, base port plate, and strut materials. *Credit: NASA*

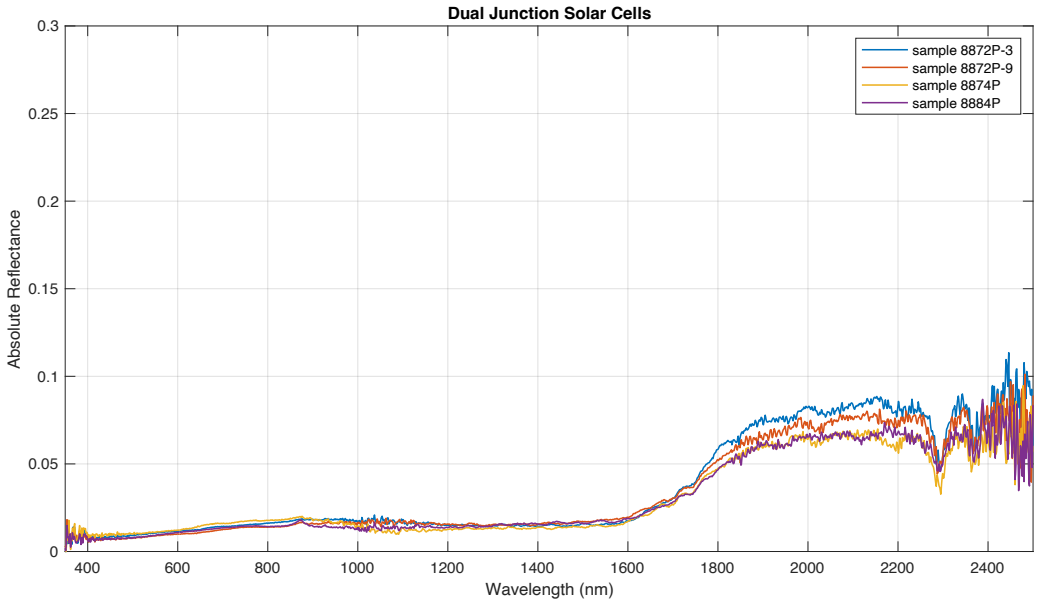

Figure A. 12: Reflectance spectra for several samples of dual junction solar cells. *Credit: NASA*

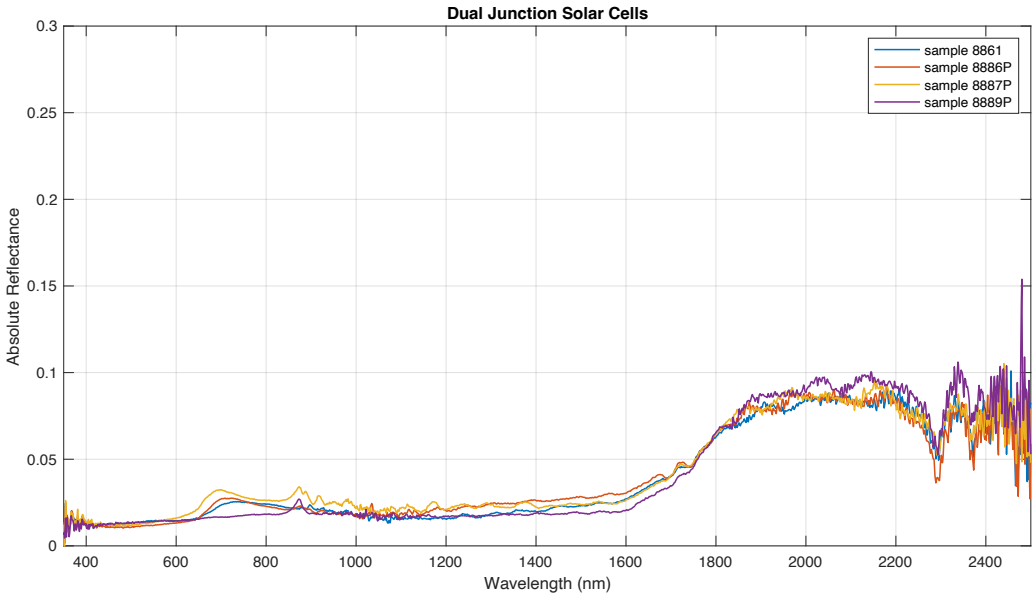

Figure A. 13: Reflectance spectra for several samples of dual junction solar cells. *Credit: NASA*

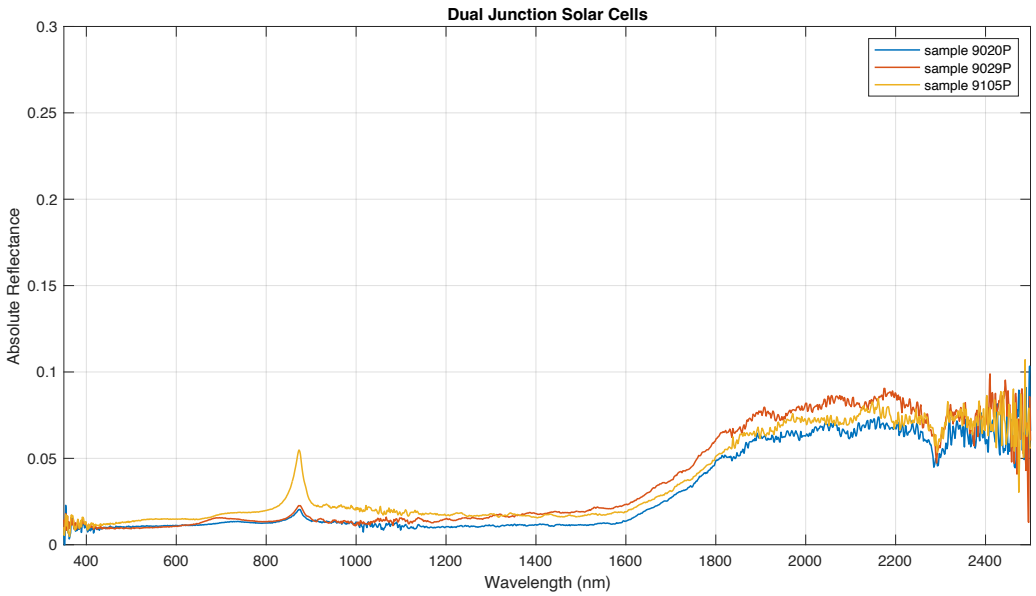

Figure A. 14: Reflectance spectra for several samples of dual junction solar cells. *Credit: NASA*

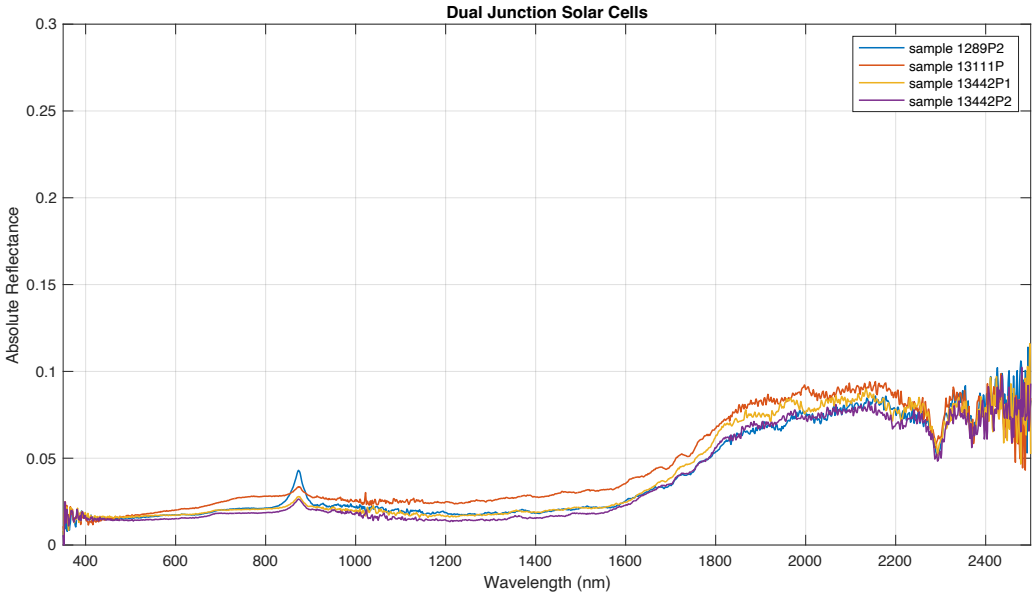

Figure A. 15: Reflectance spectra for several samples of dual junction solar cells. *Credit: NASA*

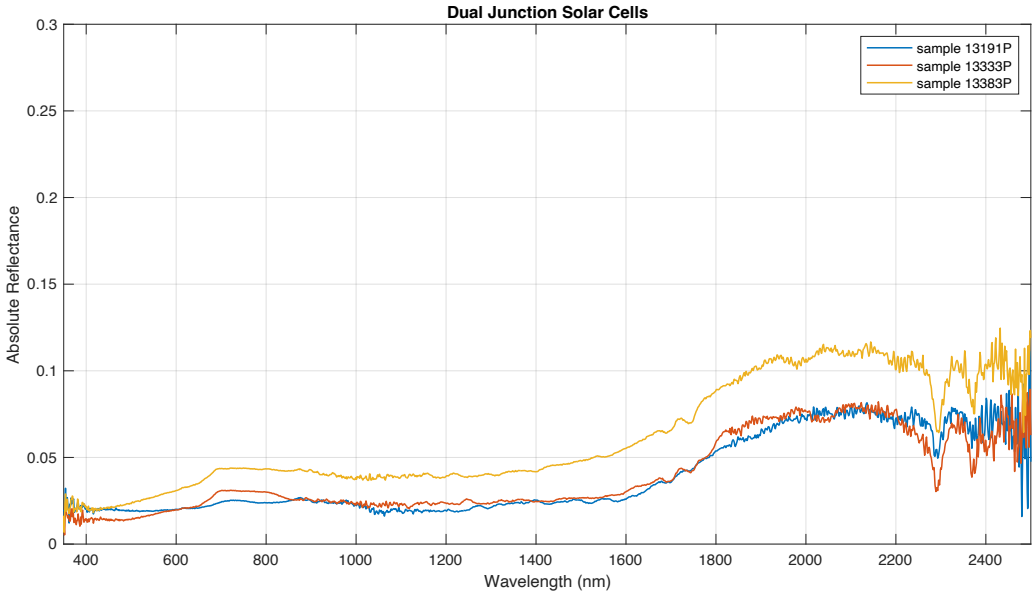

Figure A. 16: Reflectance spectra for several samples of dual junction solar cells. *Credit: NASA*

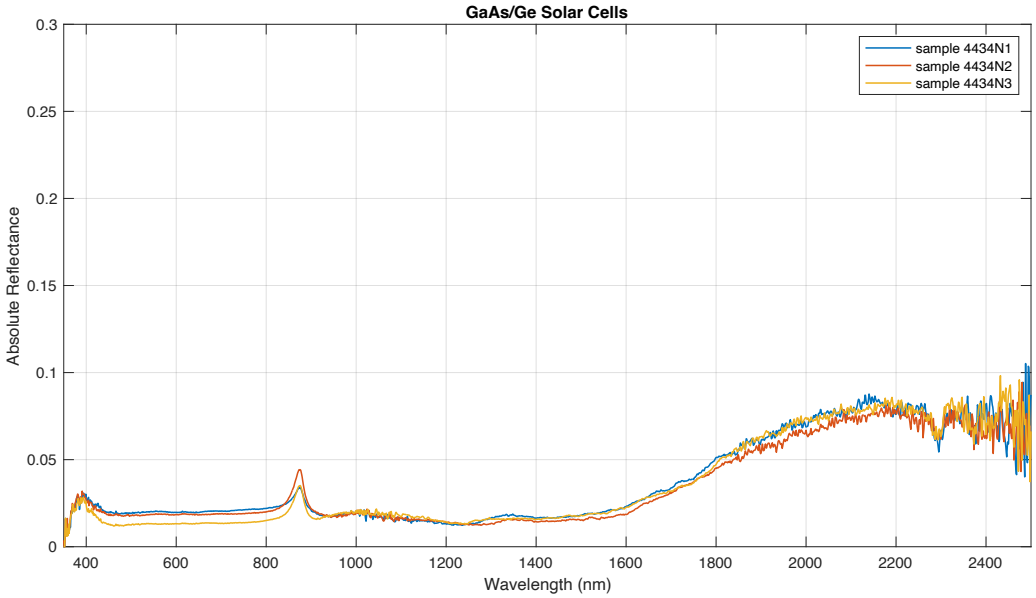

Figure A. 17: Reflectance spectra for several samples of GaAs/Ge solar cells. *Credit: NASA*

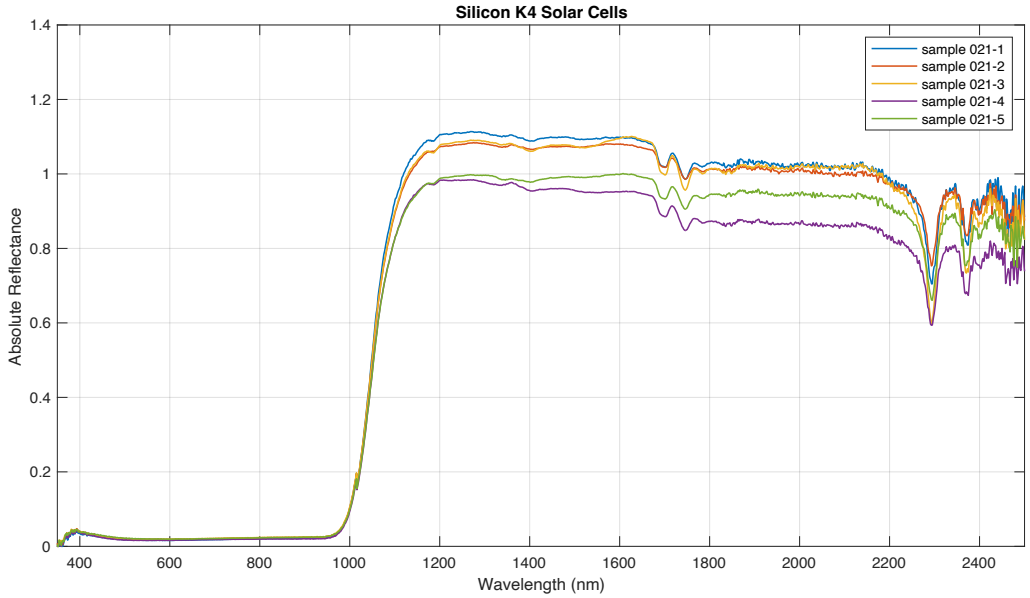

Figure A. 18: Reflectance spectra for several samples of silicon based solar cells. *Credit: NASA*

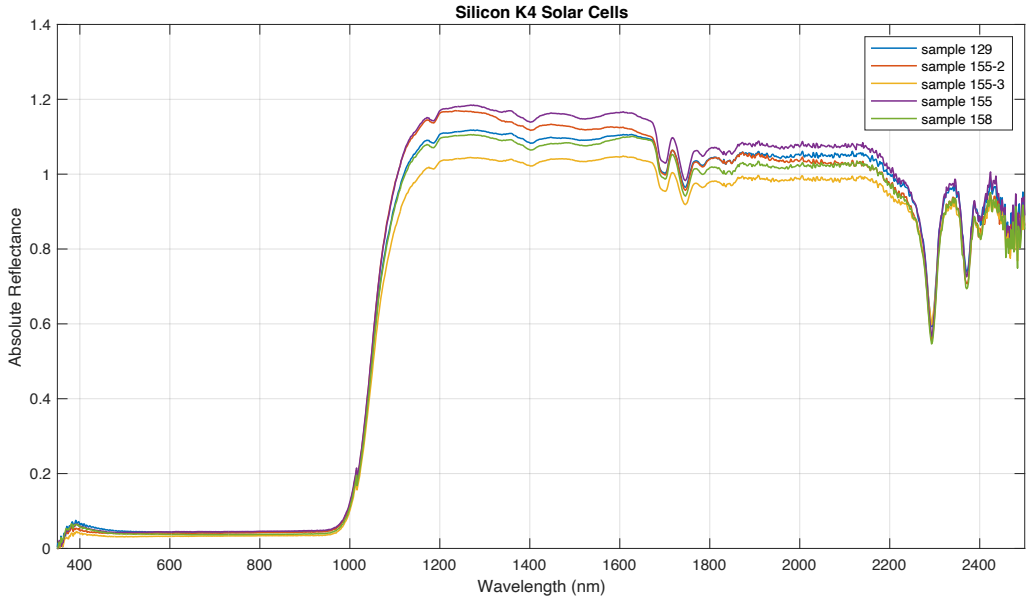

Figure A. 19: Reflectance spectra for several samples of silicon based solar cells. *Credit: NASA*

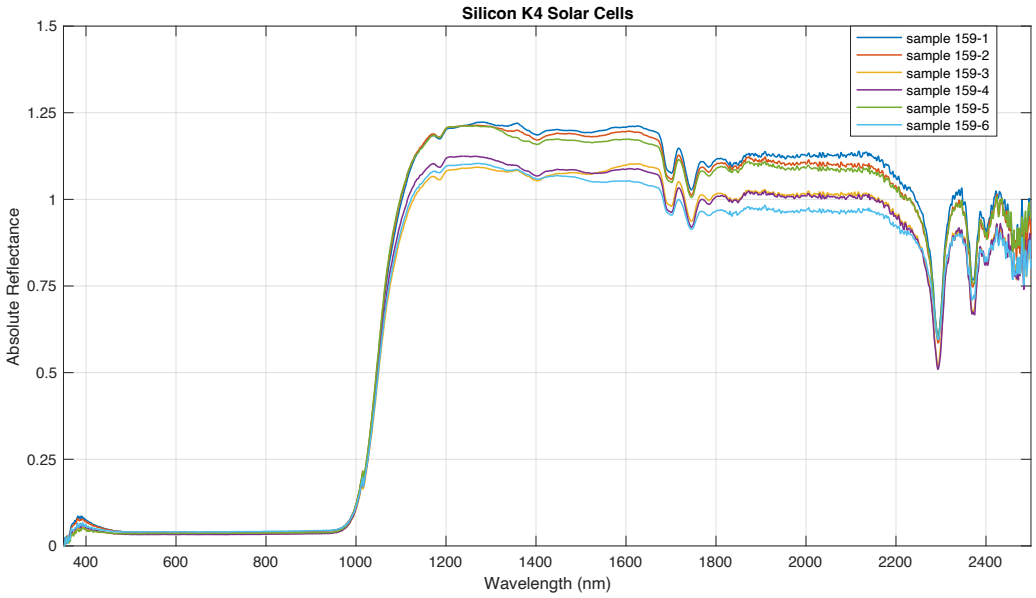

Figure A. 20: Reflectance spectra for several samples of silicon based solar cells. *Credit: NASA*

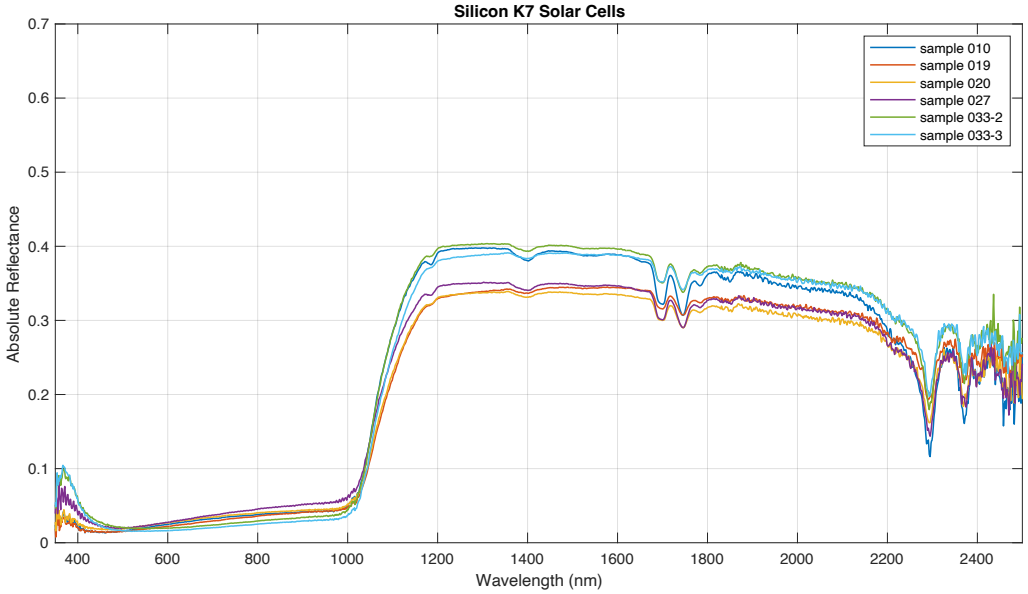

Figure A. 21: Reflectance spectra for several samples of silicon based solar cells. *Credit: NASA*

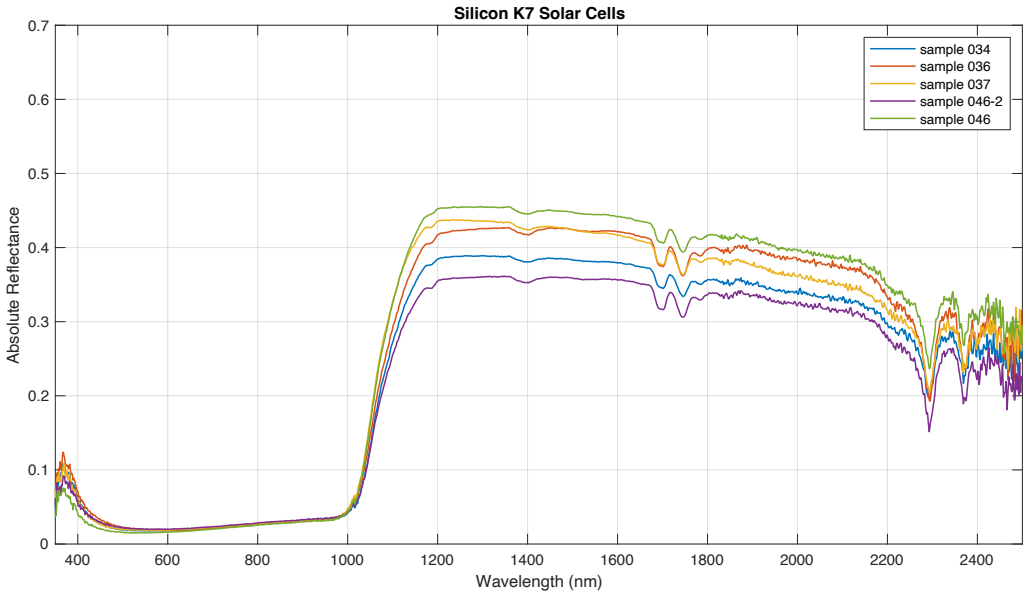

Figure A. 22: Reflectance spectra for several samples of silicon based solar cells. *Credit: NASA*

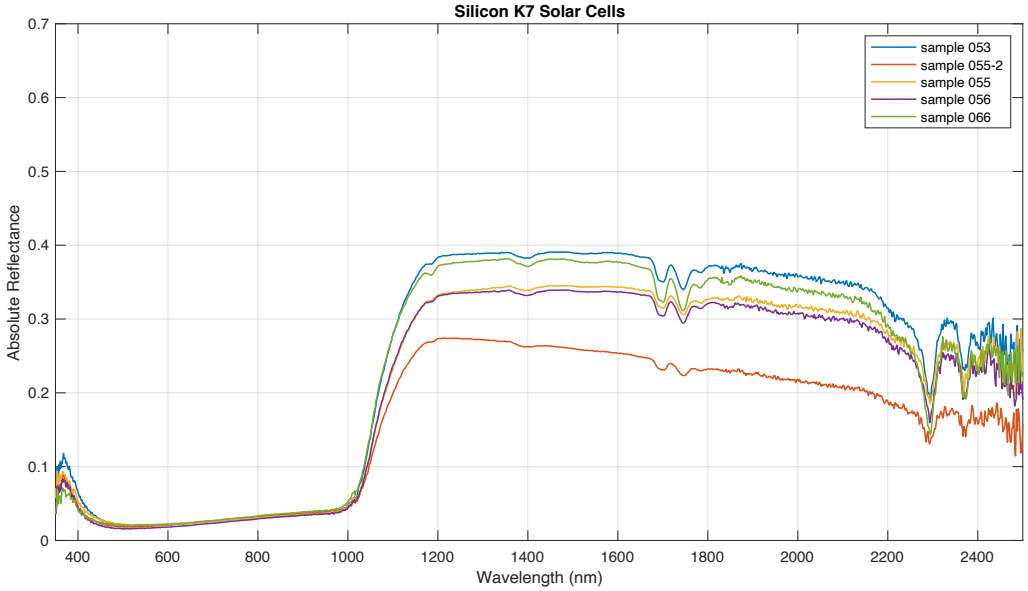

Figure A. 23: Reflectance spectra for several samples of silicon based solar cells. *Credit: NASA*

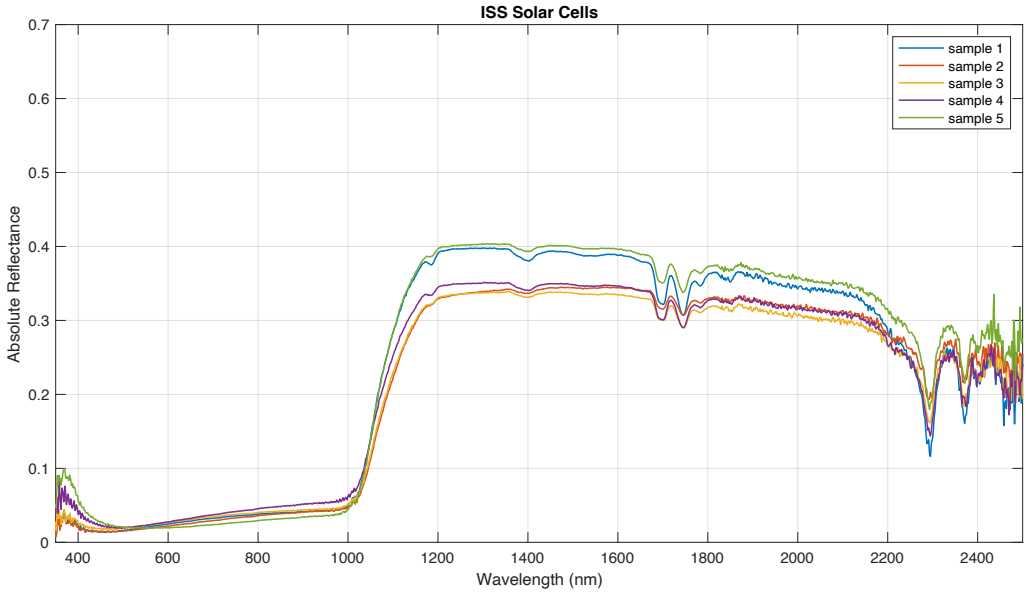

Figure A. 24: Reflectance spectra for several samples of ISS solar cells. *Credit: NASA*

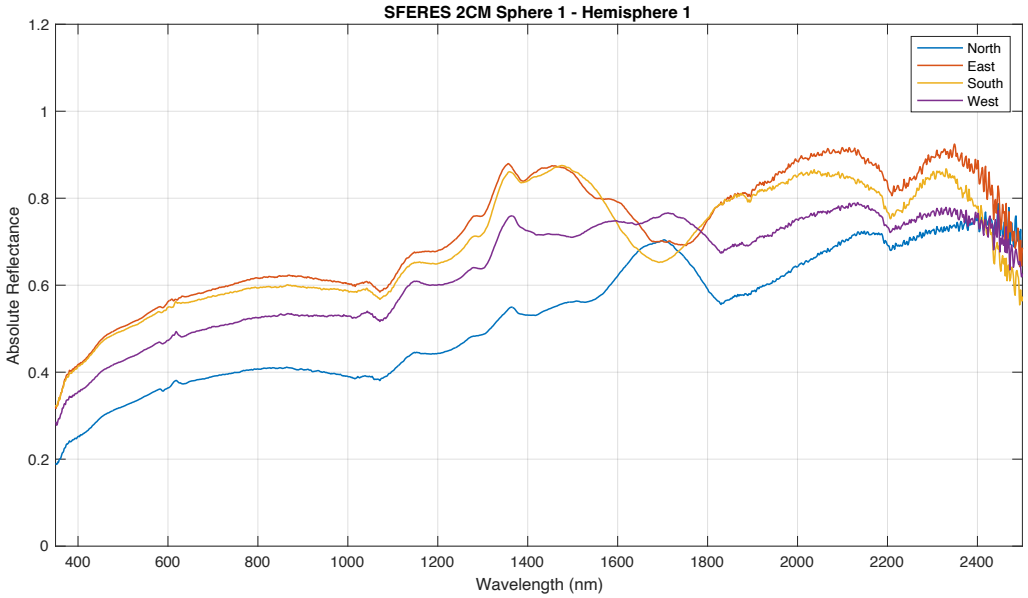

Figure A. 25: Reflectance spectra of north, east, south, and west coordinate measurement readings on a 2 cm-diameter metallic sphere sample. *Credit: NASA*

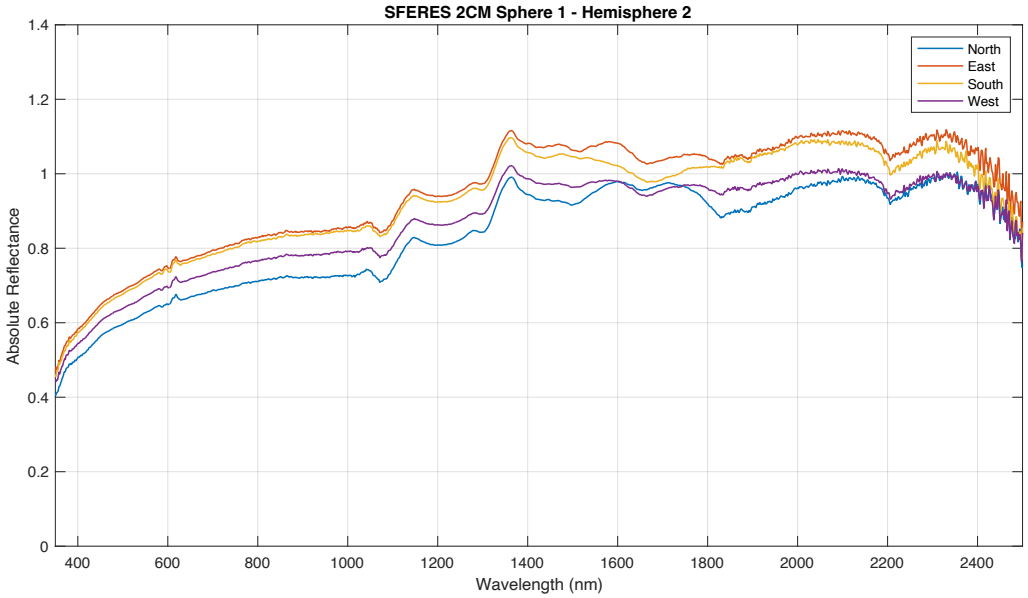

Figure A. 26: Reflectance spectra of north, east, south, and west coordinate measurement readings on a 2 cm-diameter metallic sphere sample. *Credit: NASA*

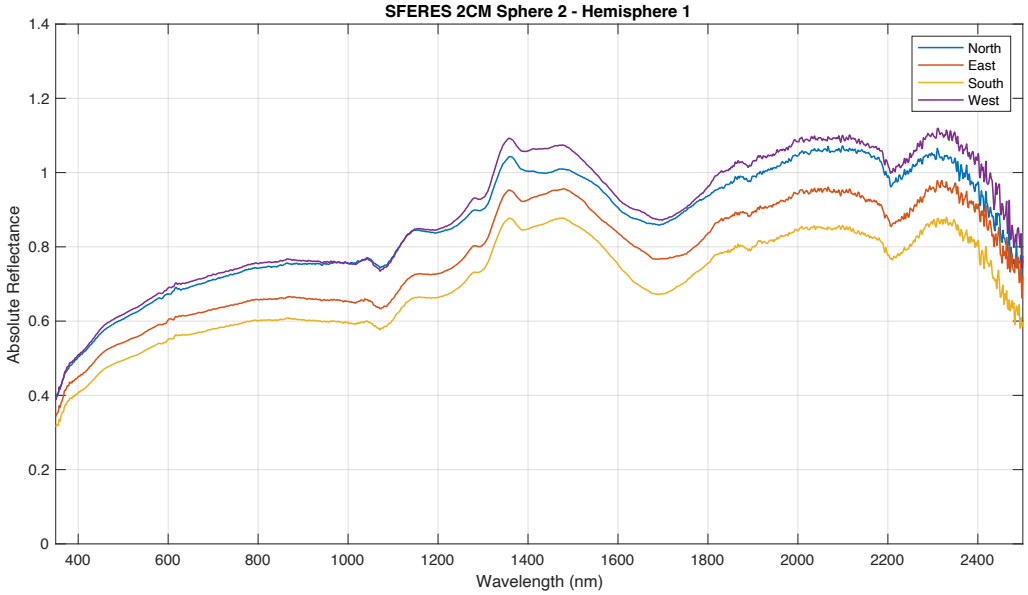

Figure A. 27: Reflectance spectra of north, east, south, and west coordinate measurement readings on a 2 cm-diameter metallic sphere sample. *Credit: NASA*

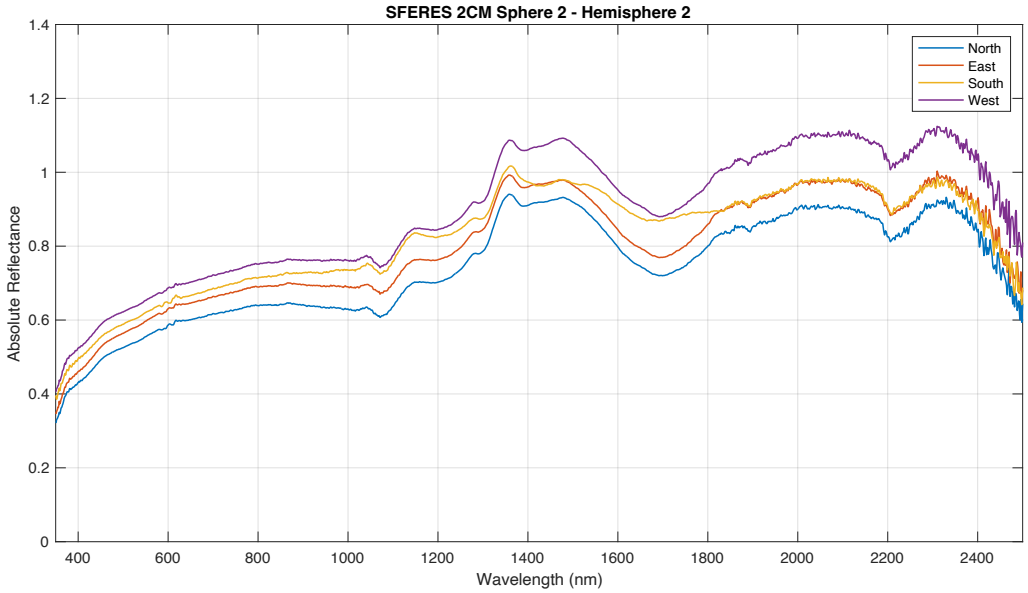

Figure A. 28: Reflectance spectra of north, east, south, and west coordinate measurement readings on a 2 cm-diameter metallic sphere sample. *Credit: NASA*

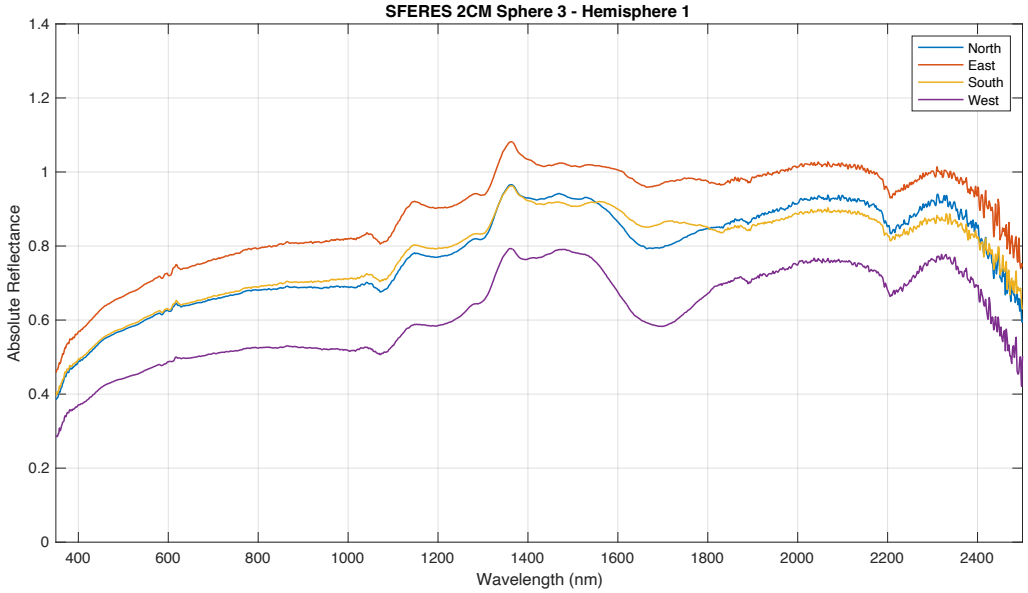

Figure A. 29: Reflectance spectra of north, east, south, and west coordinate measurement readings on a 2 cm-diameter metallic sphere sample. *Credit: NASA*

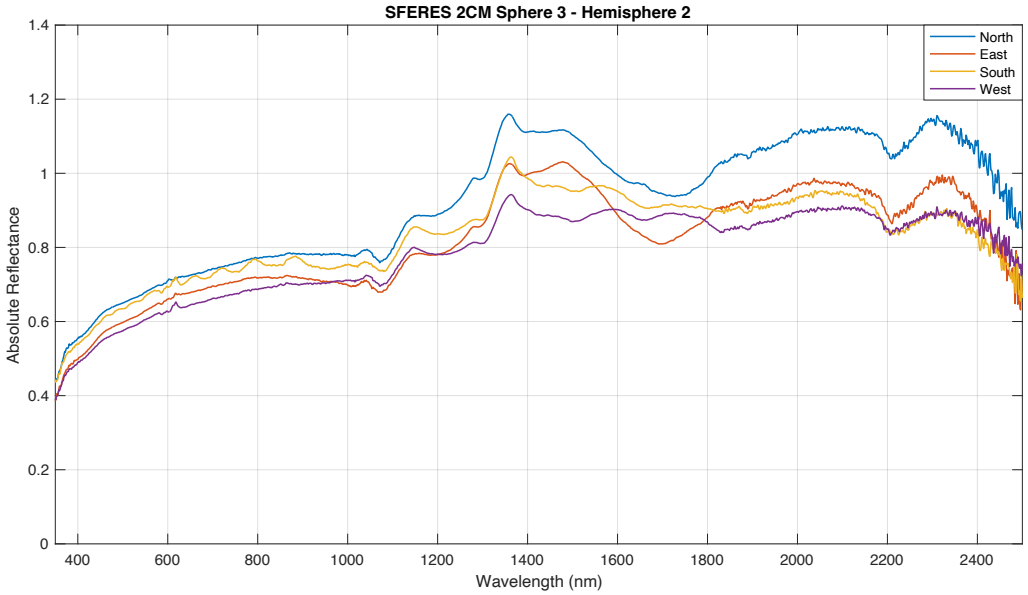

Figure A. 30: Reflectance spectra of north, east, south, and west coordinate measurement readings on a 2 cm-diameter metallic sphere sample. *Credit: NASA*

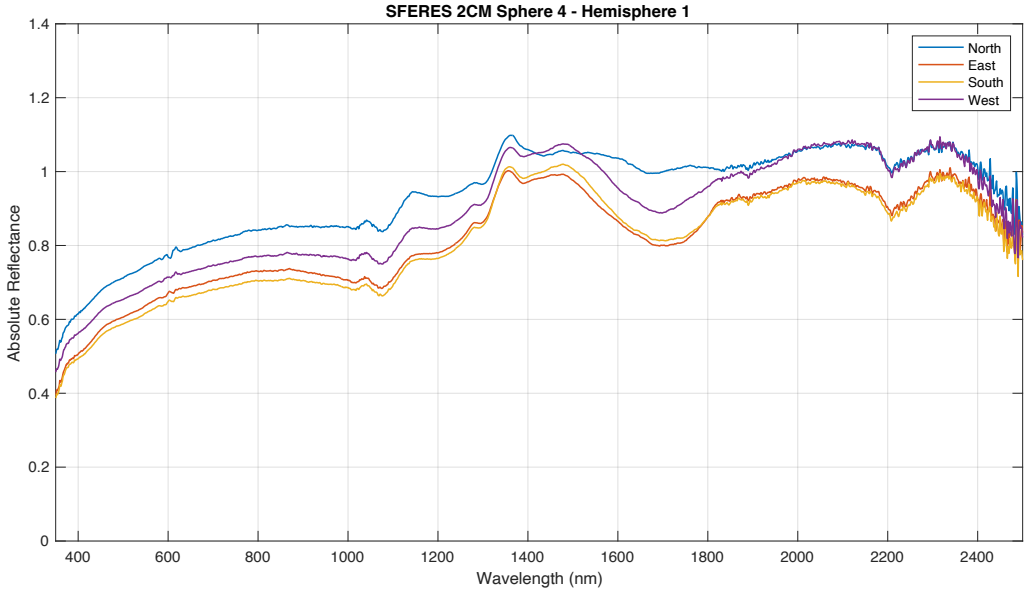

Figure A. 31: Reflectance spectra of north, east, south, and west coordinate measurement readings on a 2 cm-diameter metallic sphere sample. *Credit: NASA*

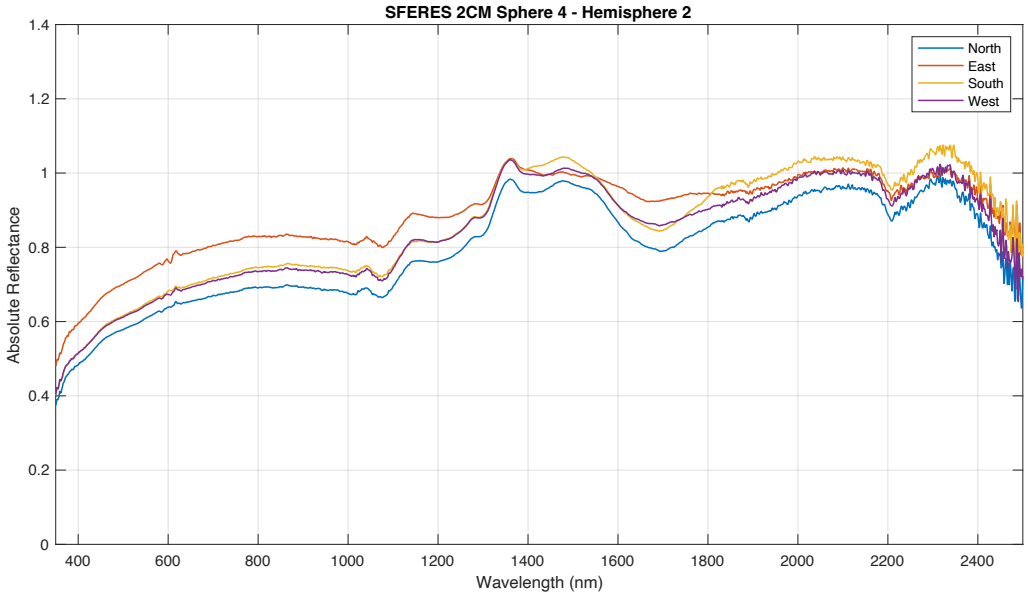

Figure A. 32: Reflectance spectra of north, east, south, and west coordinate measurement readings on a 2 cm-diameter metallic sphere sample. *Credit: NASA*

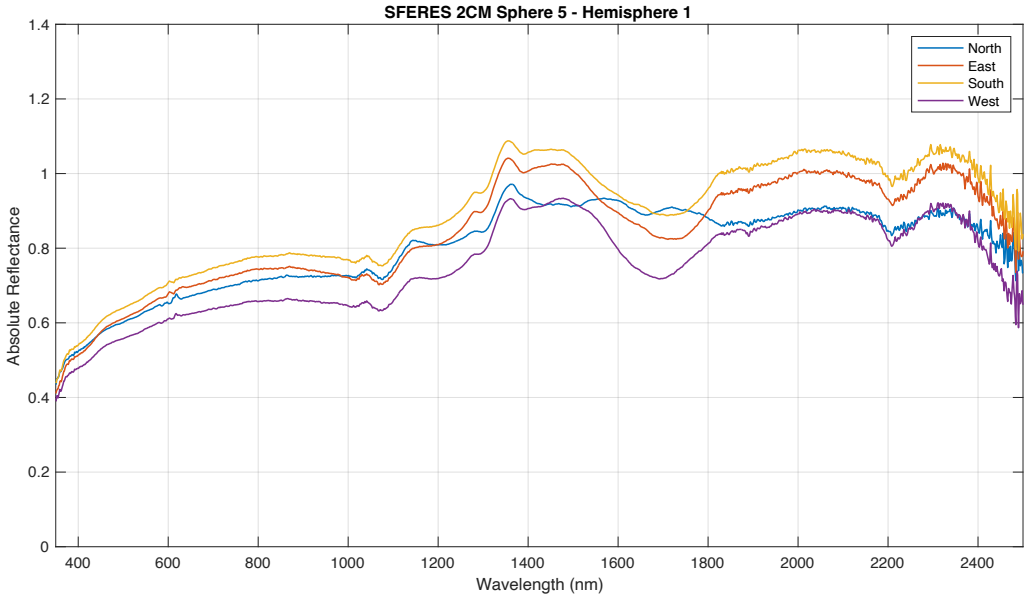

Figure A. 33: Reflectance spectra of north, east, south, and west coordinate measurement readings on a 2 cm-diameter metallic sphere sample. *Credit: NASA*

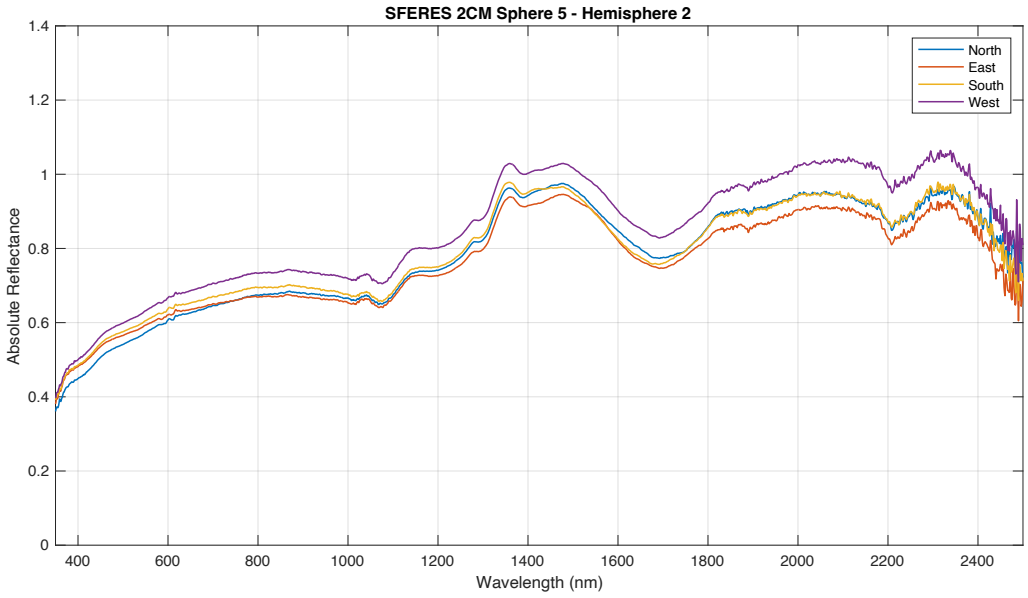

Figure A. 34: Reflectance spectra of north, east, south, and west coordinate measurement readings on a 2 cm-diameter metallic sphere sample. *Credit: NASA*

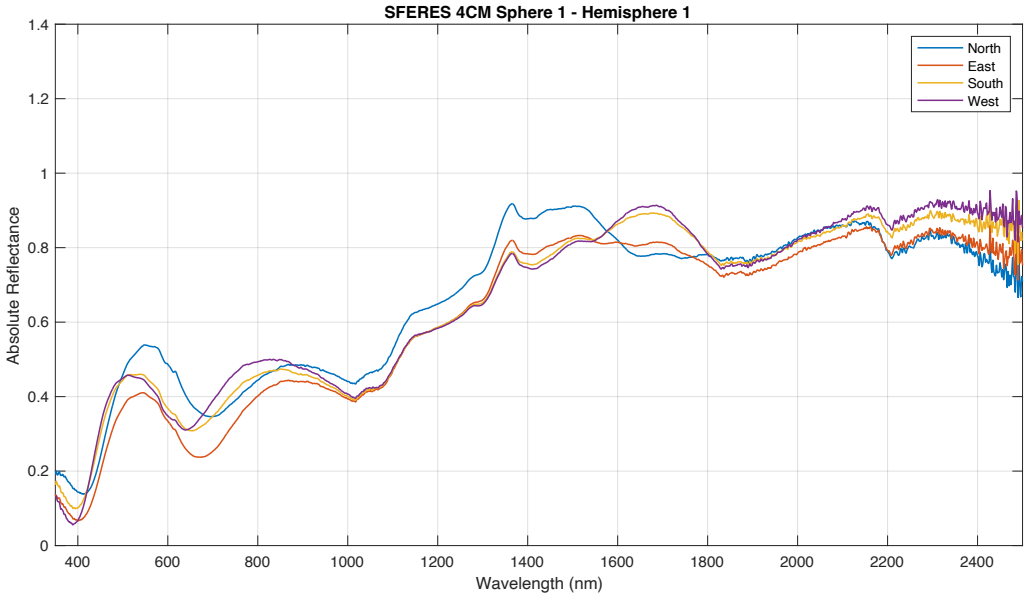

Figure A. 35: Reflectance spectra of north, east, south, and west coordinate measurement readings on a 4 cm-diameter metallic sphere sample with electrodeposited zinc plating (5.08E-4 cm thick) with yellow chromate coating. *Credit: NASA*

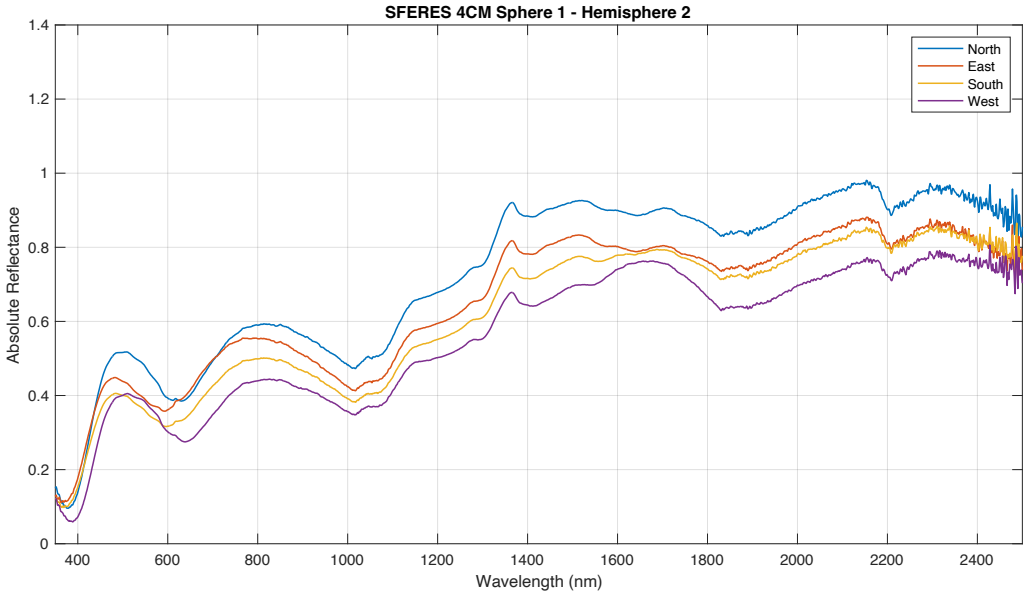

Figure A. 36: Reflectance spectra of north, east, south, and west coordinate measurement readings on a 4 cm-diameter metallic sphere sample with electrodeposited zinc plating (5.08E-4 cm thick) with yellow chromate coating. *Credit: NASA*

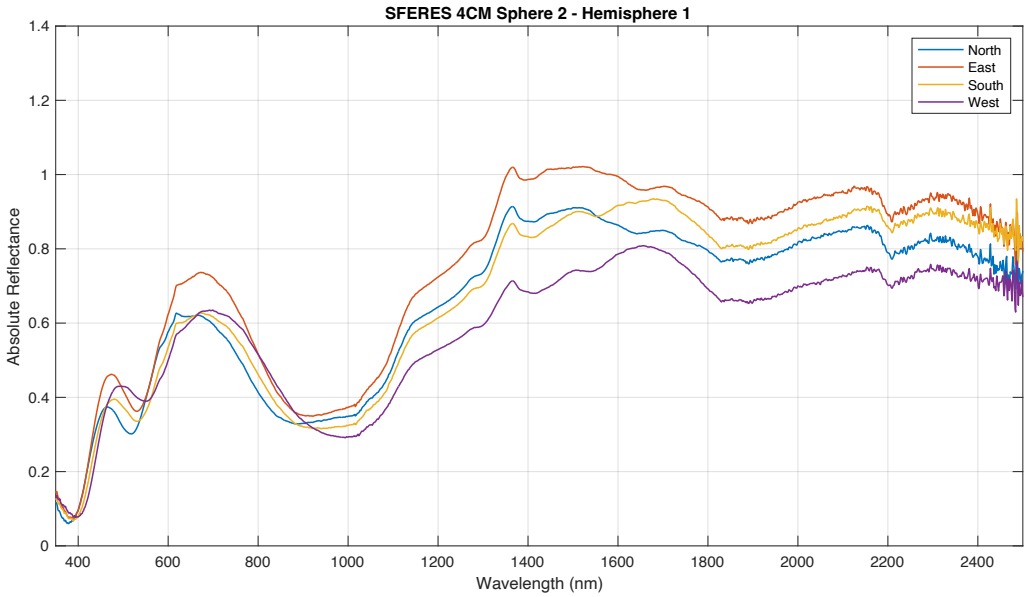

Figure A. 37: Reflectance spectra of north, east, south, and west coordinate measurement readings on a 4 cm-diameter metallic sphere sample with electrodeposited zinc plating (5.08E-4 cm thick) with yellow chromate coating. *Credit: NASA*

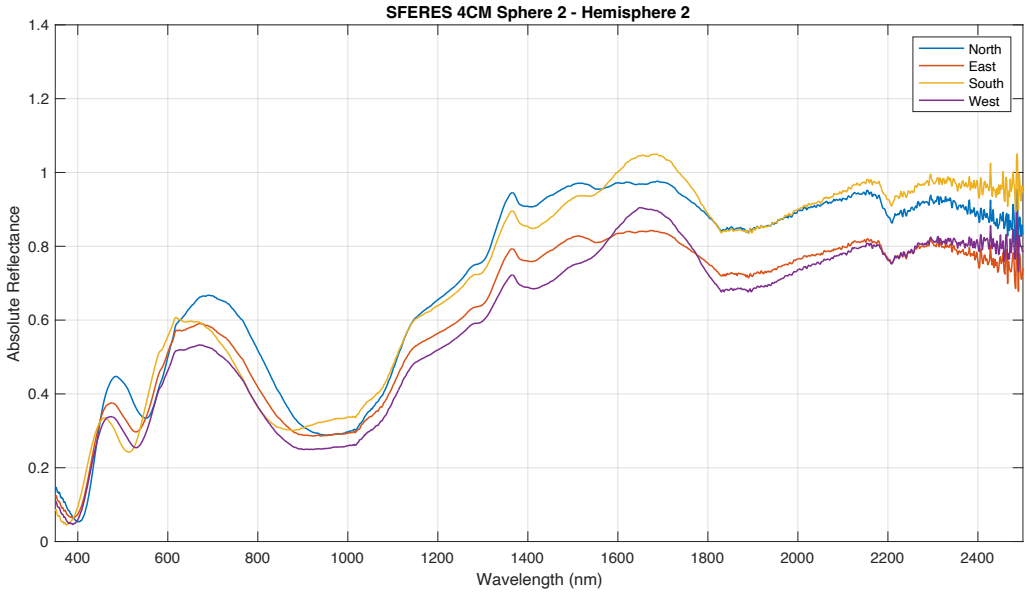

Figure A. 38: Reflectance spectra of north, east, south, and west coordinate measurement readings on a 4 cm-diameter metallic sphere sample with electrodeposited zinc plating (5.08E-4 cm thick) with yellow chromate coating. *Credit: NASA*

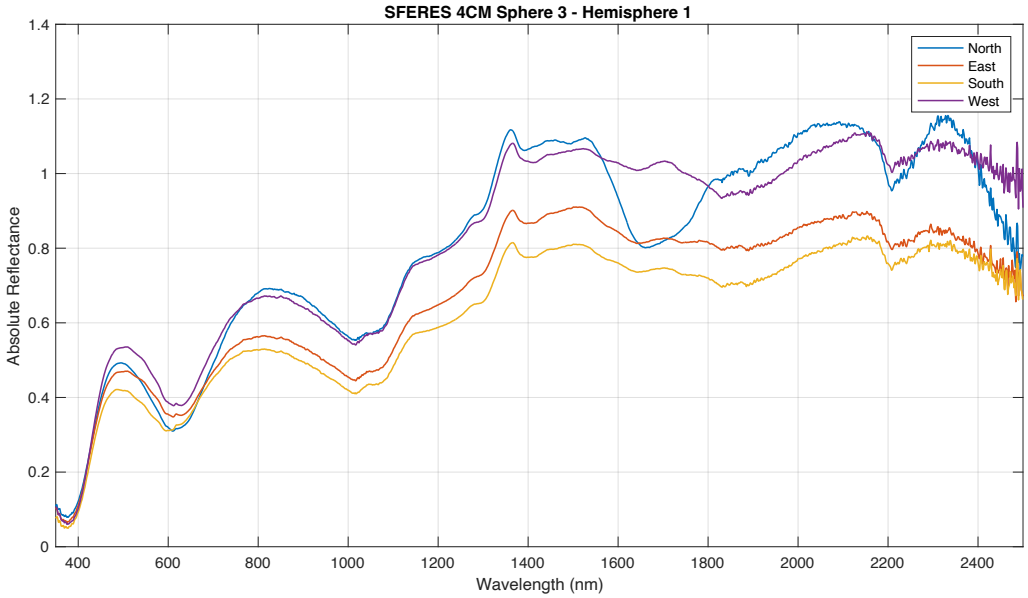

Figure A. 39: Reflectance spectra of north, east, south, and west coordinate measurement readings on a 4 cm-diameter metallic sphere sample with electrodeposited zinc plating (5.08E-4 cm thick) with yellow chromate coating. *Credit: NASA*

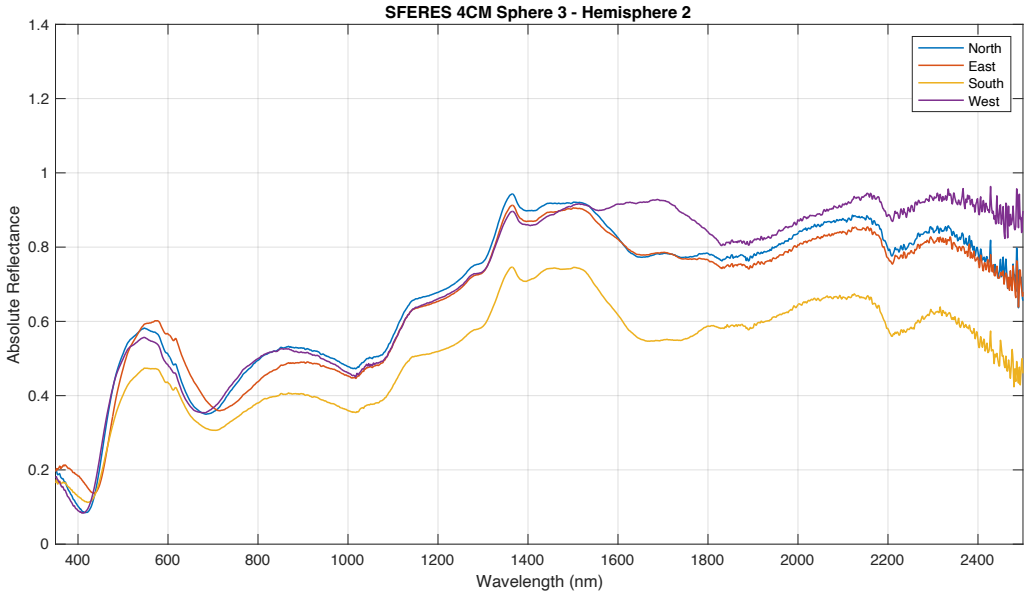

Figure A. 40: Reflectance spectra of north, east, south, and west coordinate measurement readings on a 4 cm-diameter metallic sphere sample with electrodeposited zinc plating (5.08E-4 cm thick) with yellow chromate coating. *Credit: NASA*

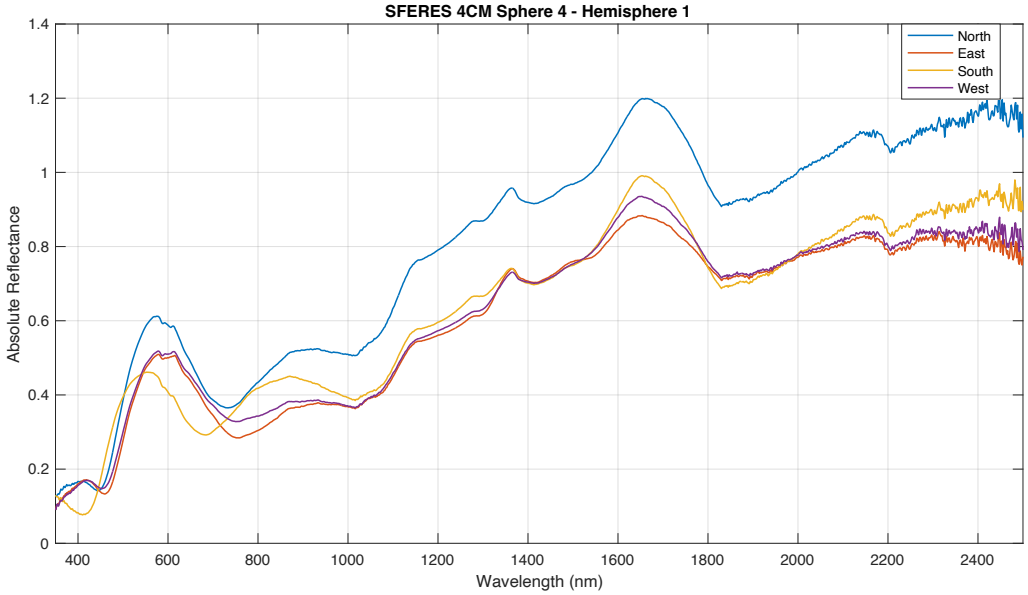

Figure A. 41: Reflectance spectra of north, east, south, and west coordinate measurement readings on a 4 cm-diameter metallic sphere sample with electrodeposited zinc plating (5.08E-4 cm thick) with yellow chromate coating. *Credit: NASA*

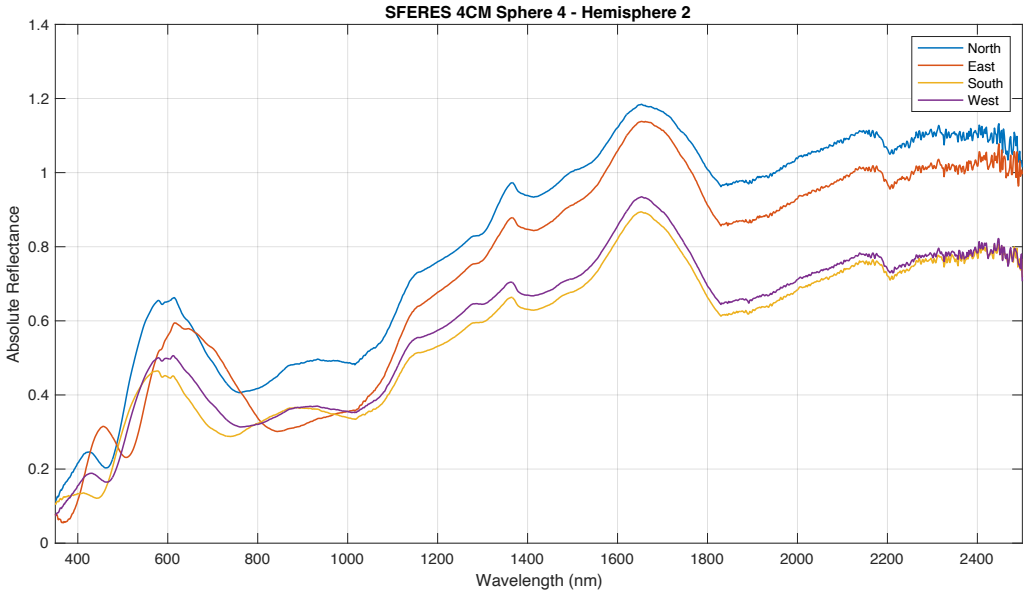

Figure A. 42: Reflectance spectra of north, east, south, and west coordinate measurement readings on a 4 cm-diameter metallic sphere sample with electrodeposited zinc plating (5.08E-4 cm thick) with yellow chromate coating. *Credit: NASA*

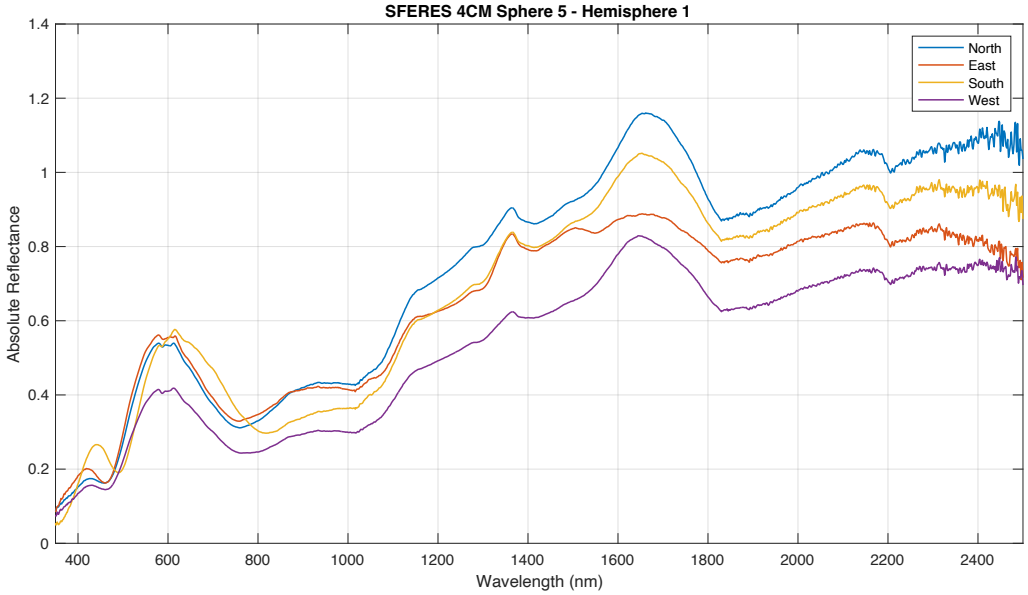

Figure A. 43: Reflectance spectra of north, east, south, and west coordinate measurement readings on a 4 cm-diameter metallic sphere sample with electrodeposited zinc plating (5.08E-4 cm thick) with yellow chromate coating. *Credit: NASA*

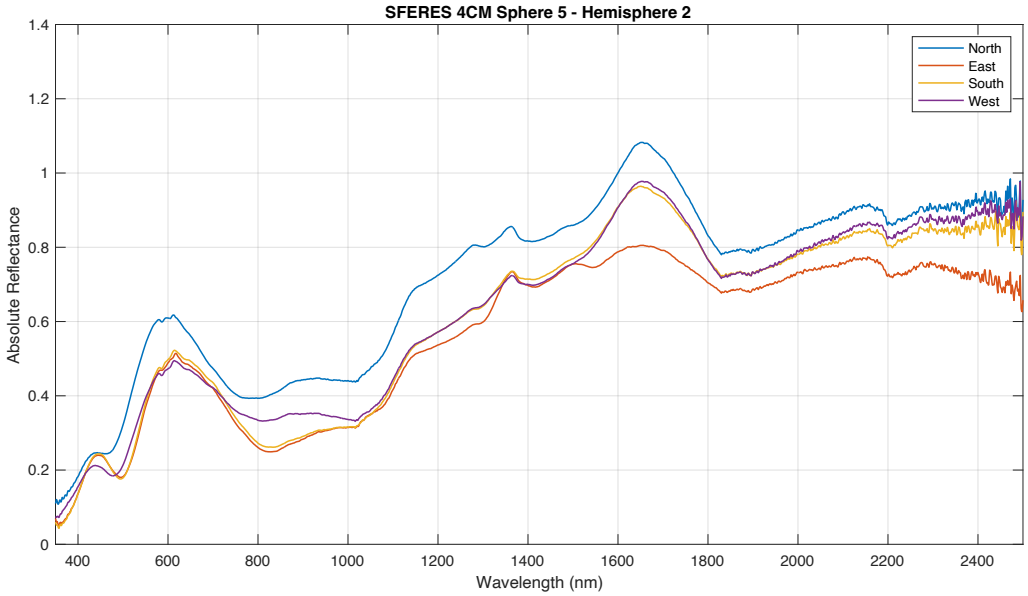

Figure A. 44: Reflectance spectra of north, east, south, and west coordinate measurement readings on a 4 cm-diameter metallic sphere sample with electrodeposited zinc plating (5.08E-4 cm thick) with yellow chromate coating. *Credit: NASA*

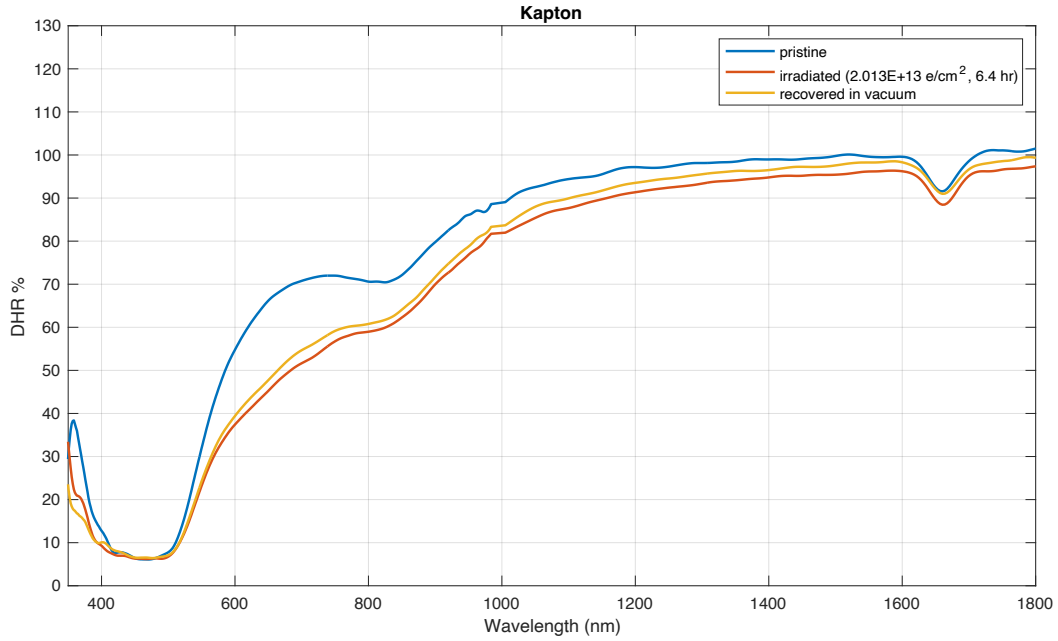

Figure A. 45: Reflectance spectra of polyimide film (Kapton) in pristine, irradiated (2.013E+13 e/cm^2), and recovered in vacuum, conditions. *Credit: NASA*

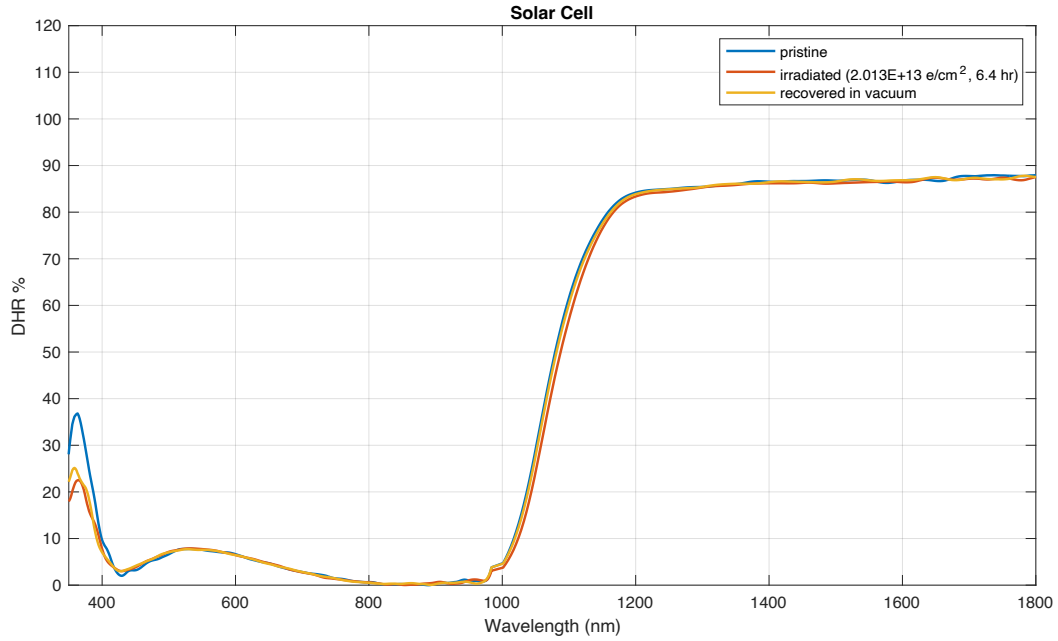

Figure A. 46: Reflectance spectra of a solar cell sample in pristine, irradiated (2.013E+13 e/cm^2), and recovered in vacuum, conditions. *Credit: NASA*

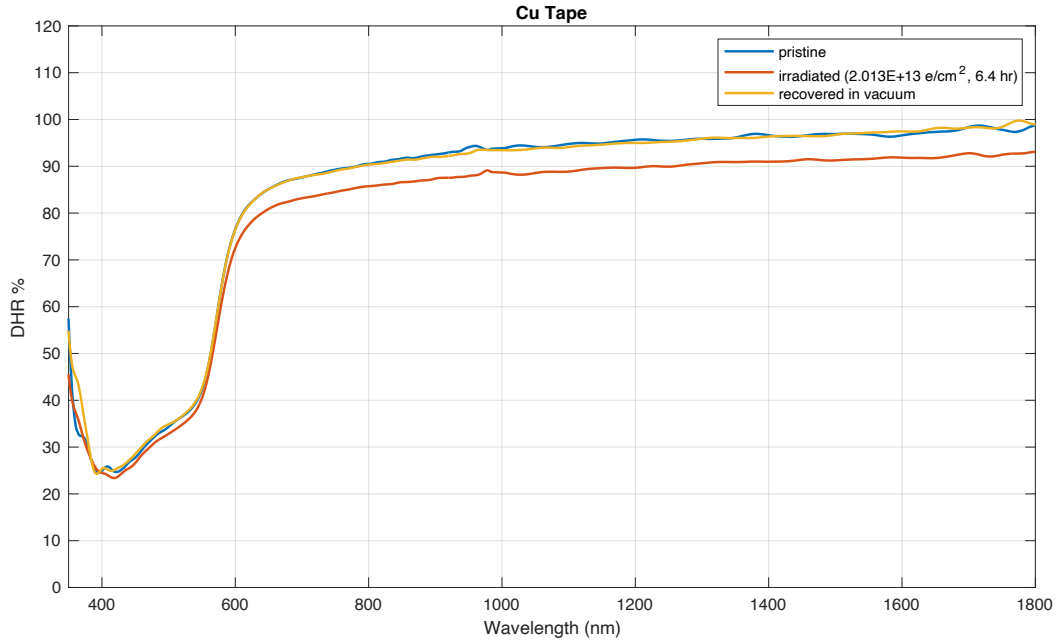

Figure A. 47: Reflectance spectra of copper tape (metal side) in pristine, irradiated (2.013E+13 e/cm^2), and recovered in vacuum, conditions. *Credit: NASA*

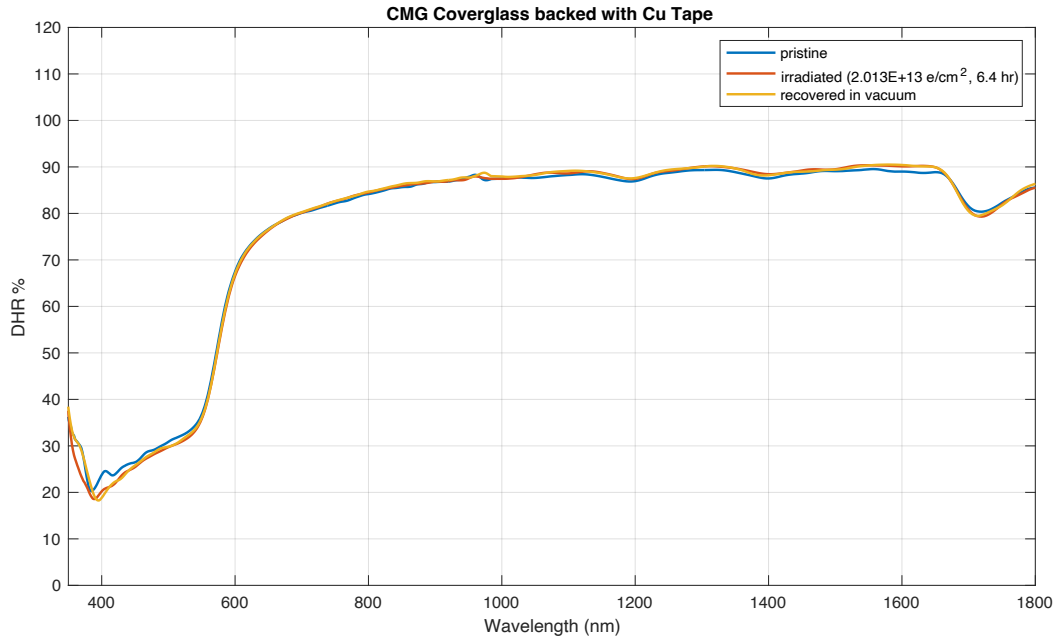

Figure A. 48: Reflectance spectra of coverglass backed with Cu tape in pristine, irradiated (2.013E+13 e/cm^2), and recovered in vacuum, conditions. *Credit: NASA*

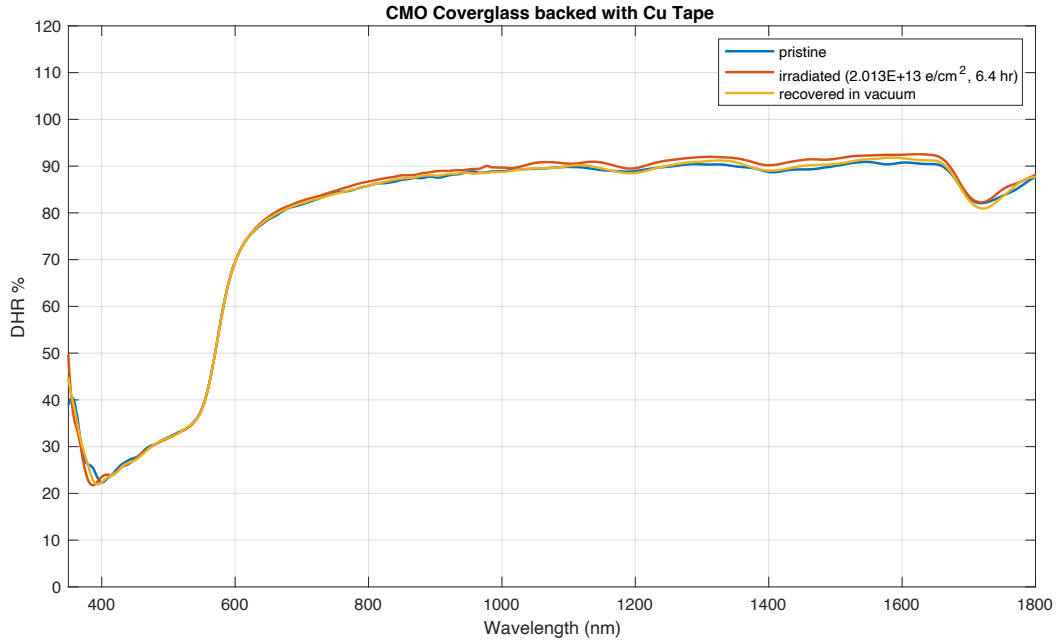

Figure A. 49: Reflectance spectra of coverglass backed with Cu tape in pristine, irradiated (2.013E+13 e/cm^2), and recovered in vacuum, conditions. *Credit: NASA*

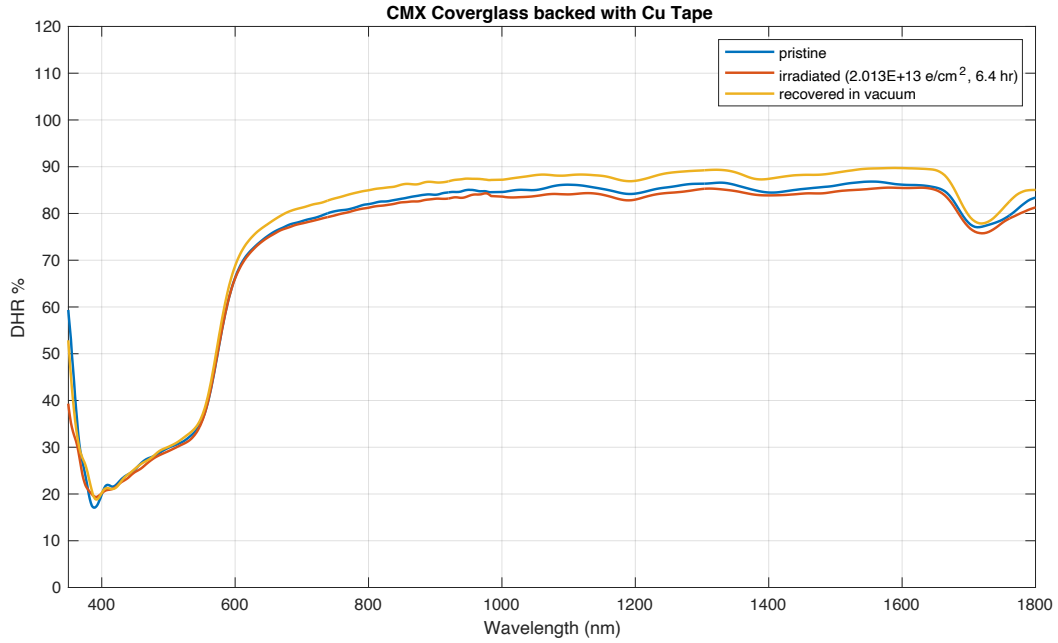

Figure A. 50: Reflectance spectra of coverglass backed with Cu tape in pristine, irradiated (2.013E+13 e/cm^2), and recovered in vacuum, conditions. *Credit: NASA*

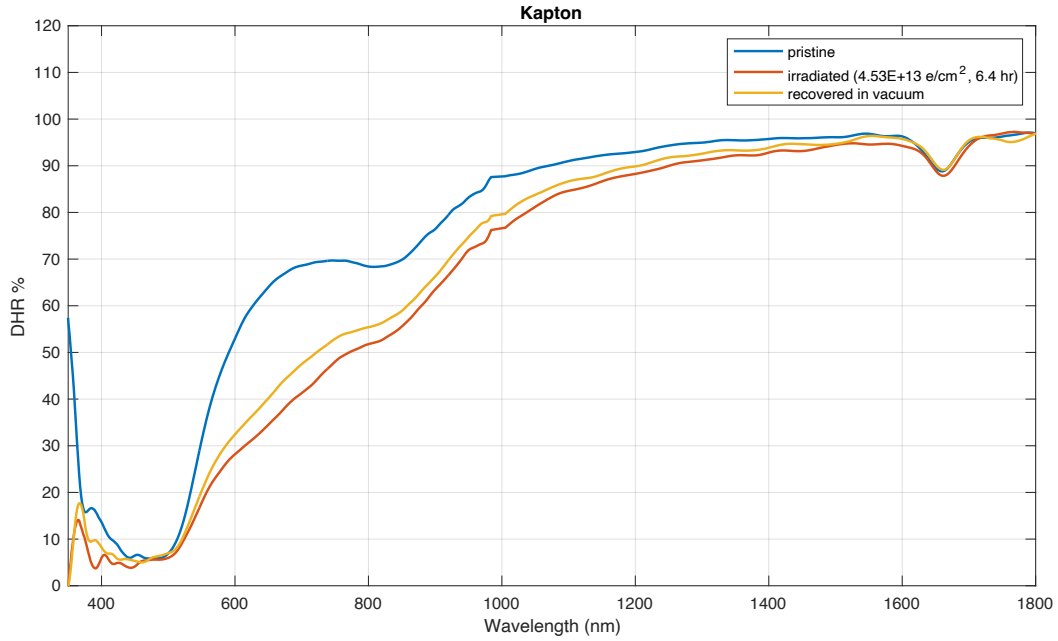

Figure A. 51: Reflectance spectra of polyimide (Kapton) material in pristine, irradiated (4.53E+13 e/cm^2), and recovered in vacuum, conditions. *Credit: NASA*

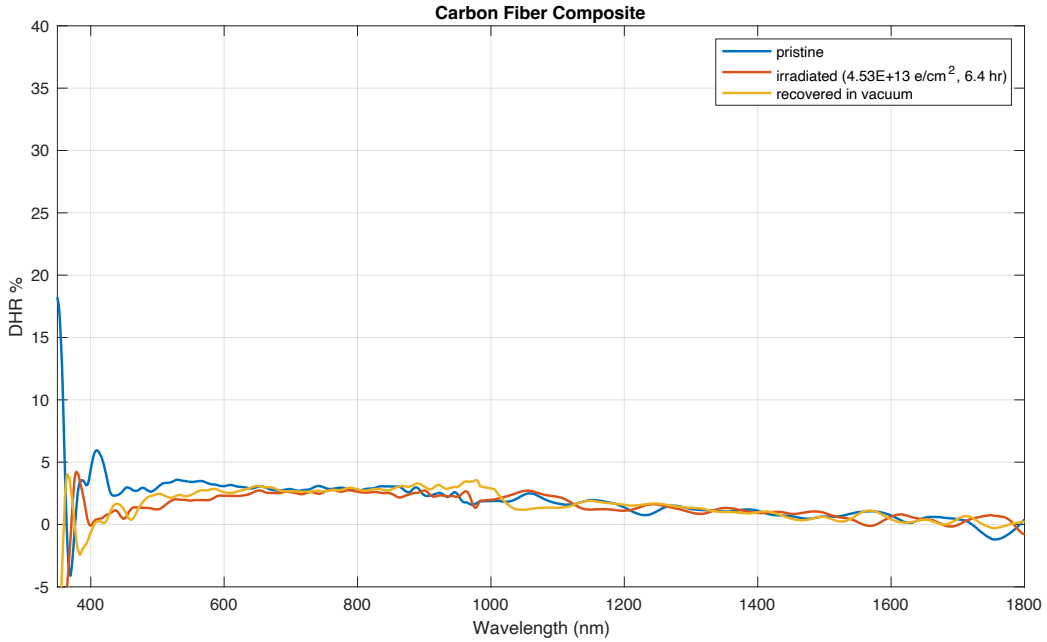

Figure A. 52: Reflectance spectra of carbon fiber composite material in pristine, irradiated (4.53E+13 e/cm^2), and recovered in vacuum, conditions. *Credit: NASA*

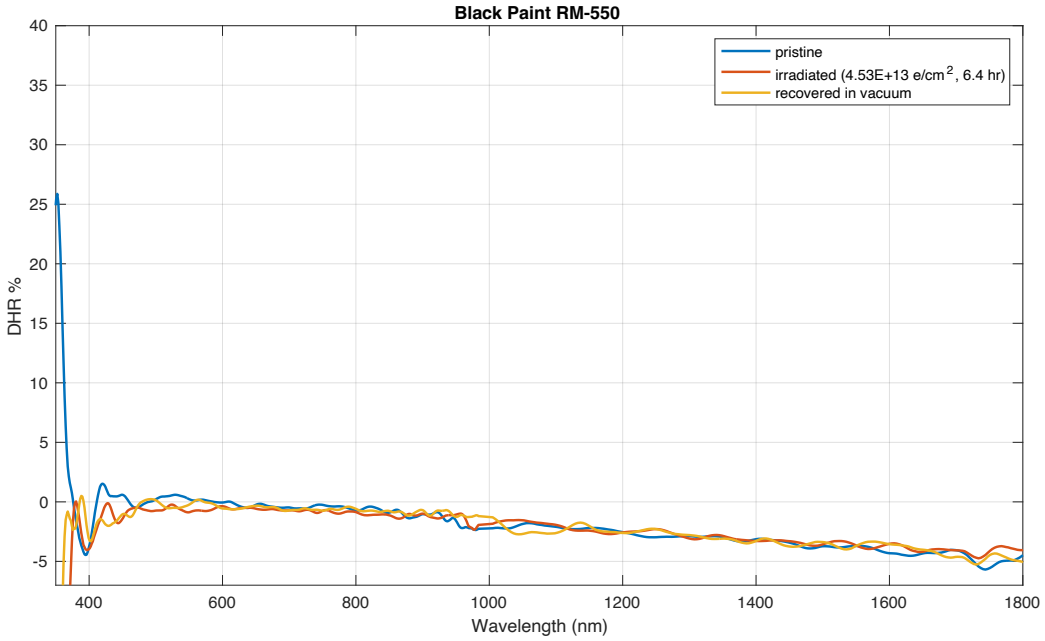

Figure A. 53: Reflectance spectra of black paint in pristine, irradiated (4.53E+13 e/cm^2), and recovered in vacuum, conditions. *Credit: NASA*

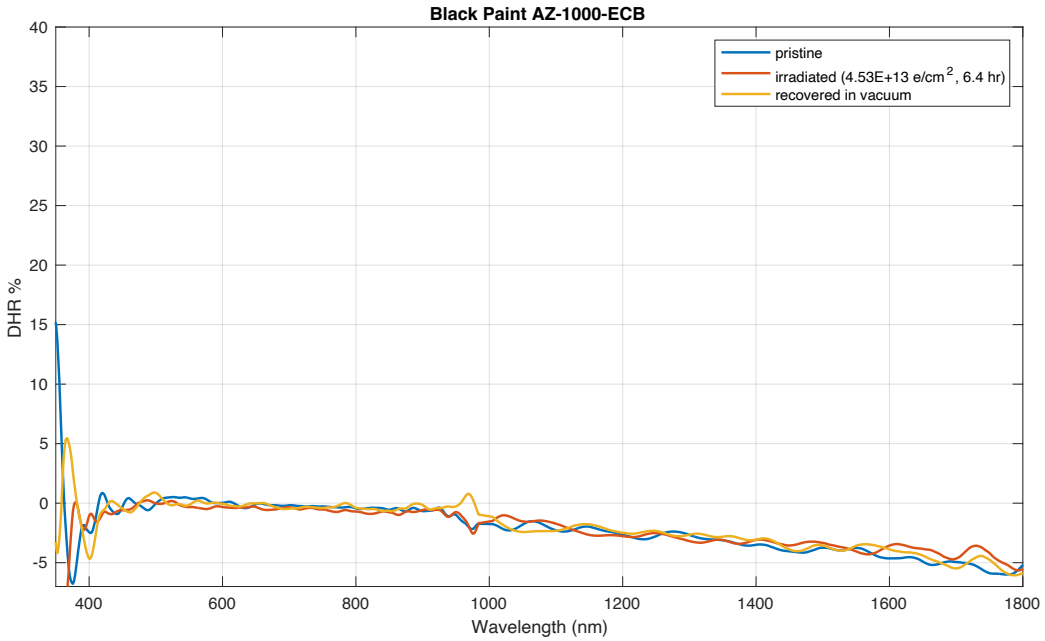

Figure A. 54: Reflectance spectra of black paint in pristine, irradiated (4.53E+13 e/cm^2), and recovered in vacuum, conditions. *Credit: NASA*

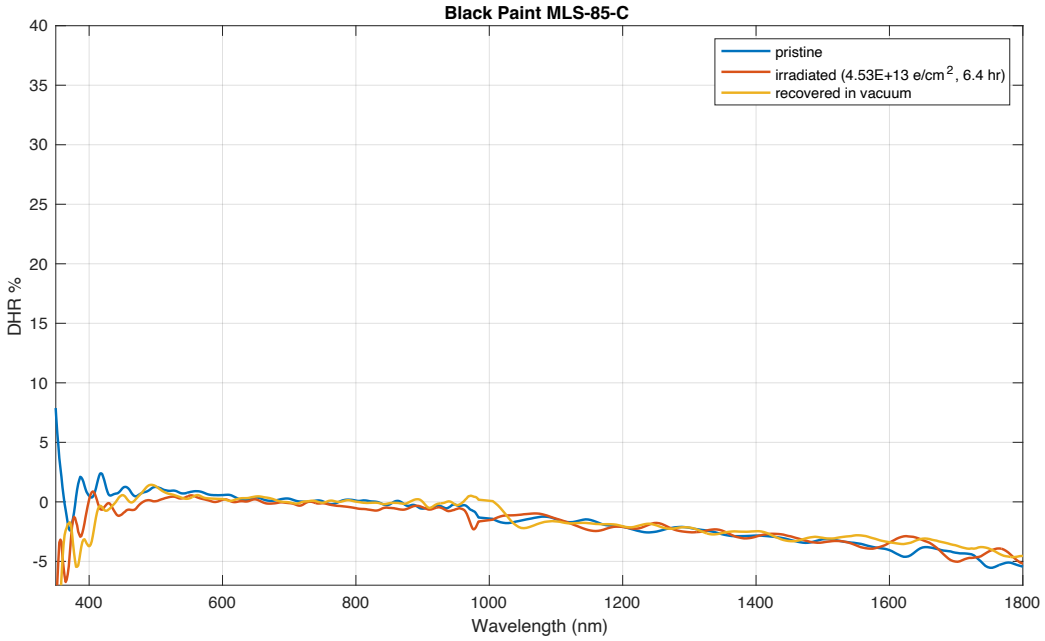

Figure A. 55: Reflectance spectra of black paint in pristine, irradiated (4.53E+13 e/cm^2), and recovered in vacuum, conditions. *Credit: NASA*

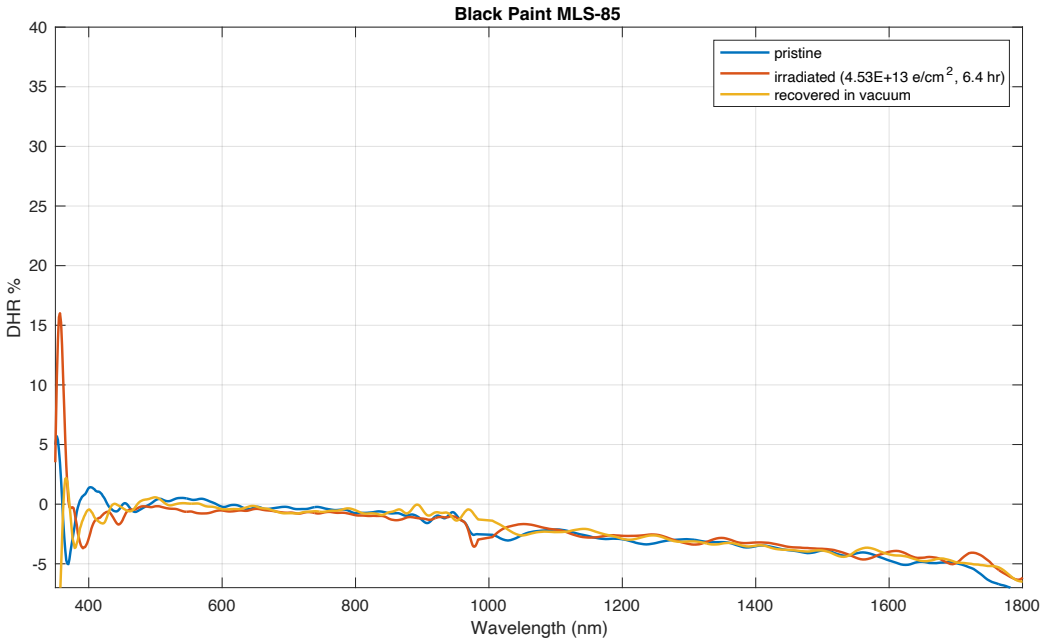

Figure A. 56: Reflectance spectra of black paint in pristine, irradiated (4.53E+13 e/cm^2), and recovered in vacuum, conditions. *Credit: NASA*

A.2. COLOR-COLOR DIAGRAMS

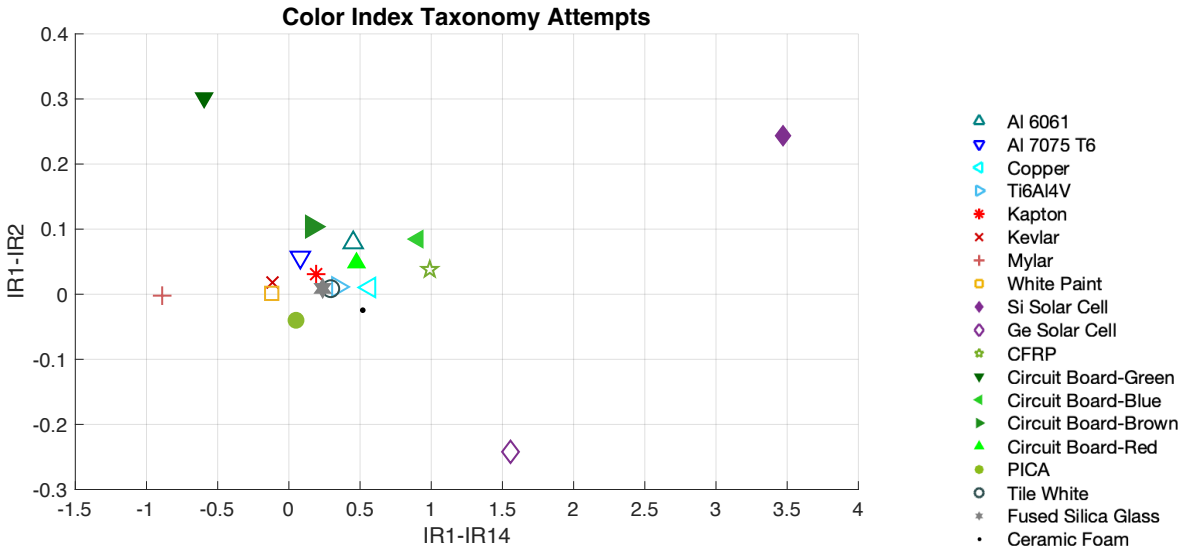

Figure A. 57: Color-color diagrams for IR1-IR2 versus IR1-IR14 color indices according to their respective filter passbands listed in Table 5.2. *Credit: NASA*

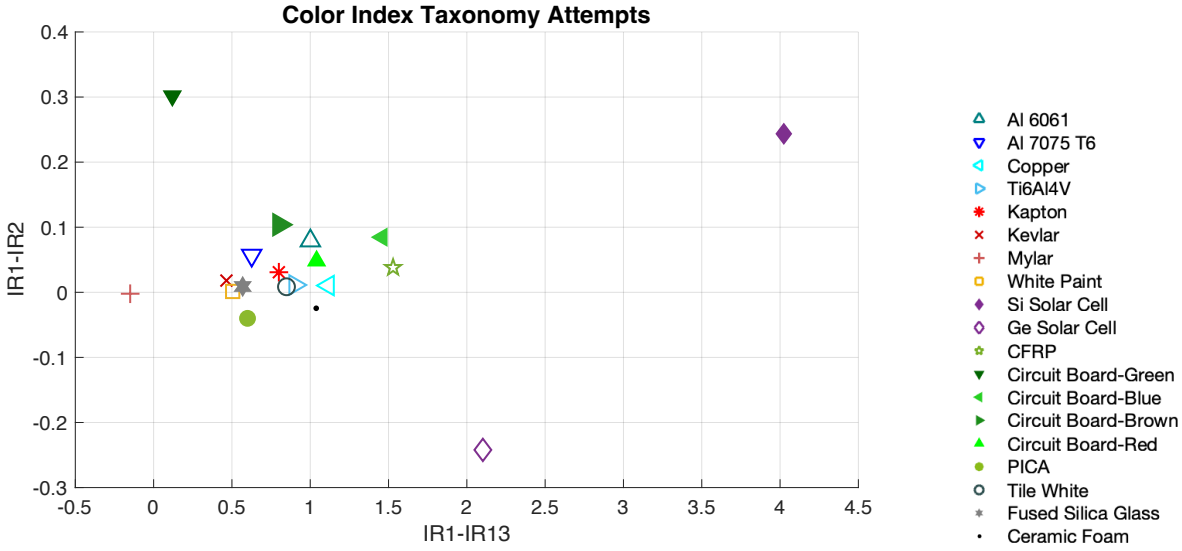

Figure A. 58: Color-color diagrams for IR1-IR2 versus IR1-IR13 color indices according to their respective filter passbands listed in Table 5.2. *Credit: NASA*

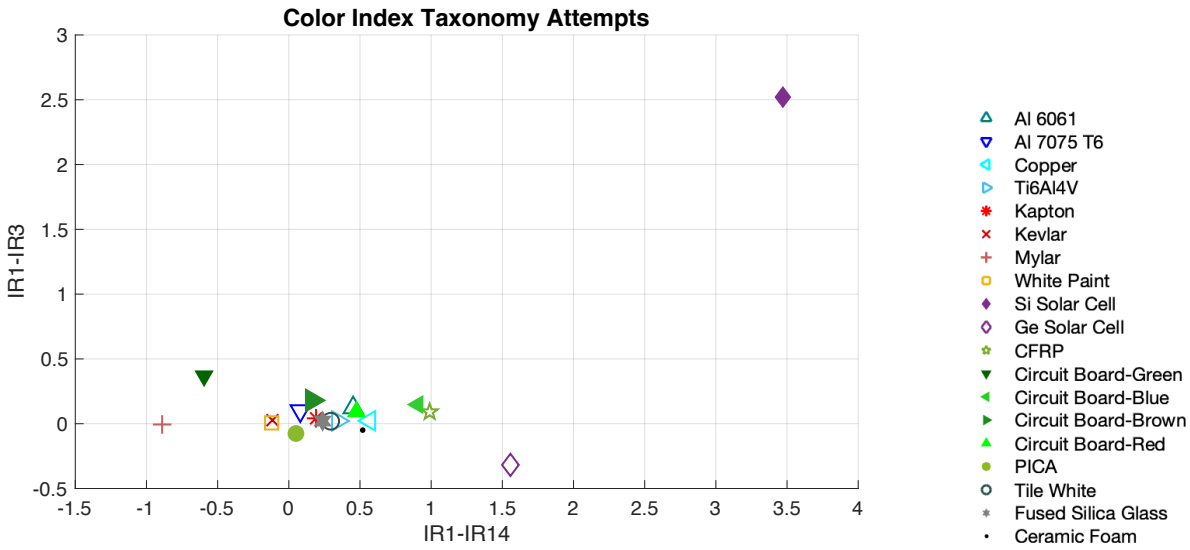

Figure A. 59: Color-color diagrams for IR1-IR3 versus IR1-IR14 color indices according to their respective filter passbands listed in Table 5.2. *Credit: NASA*

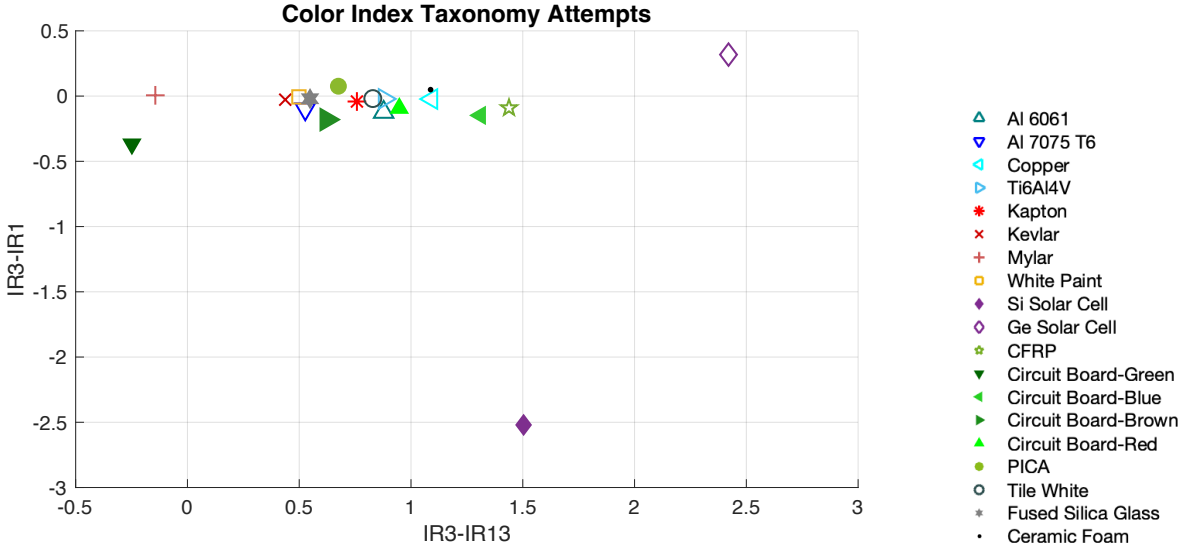

Figure A. 60: Color-color diagrams for IR3-IR1 versus IR3-IR13 color indices according to their respective filter passbands listed in Table 5.2. *Credit: NASA*

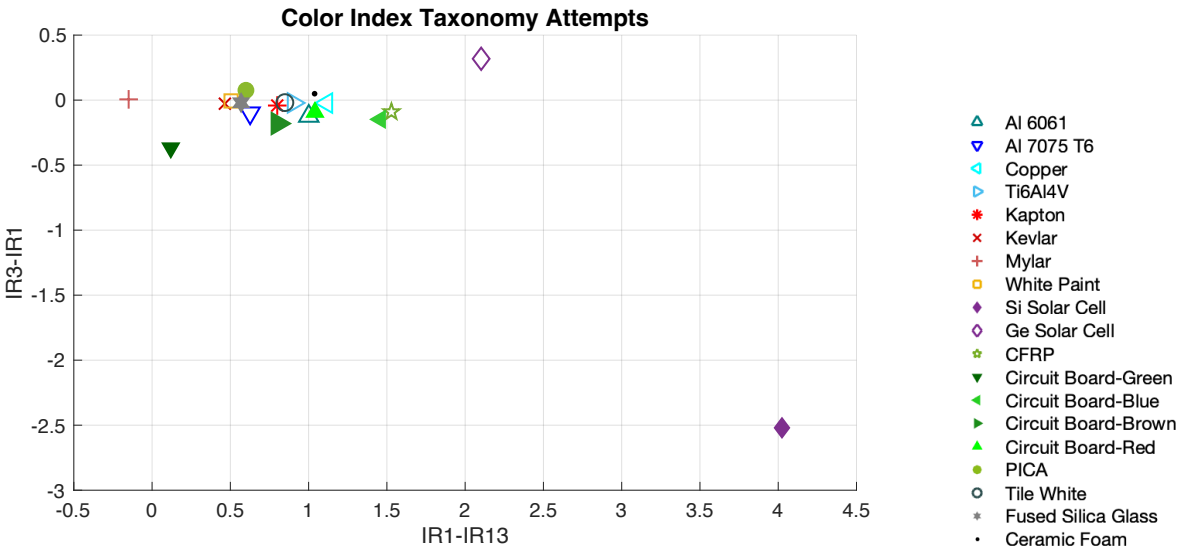

Figure A. 61: Color-color diagrams for IR3-IR1 versus IR1-IR13 color indices according to their respective filter passbands listed in Table 5.2. *Credit: NASA*

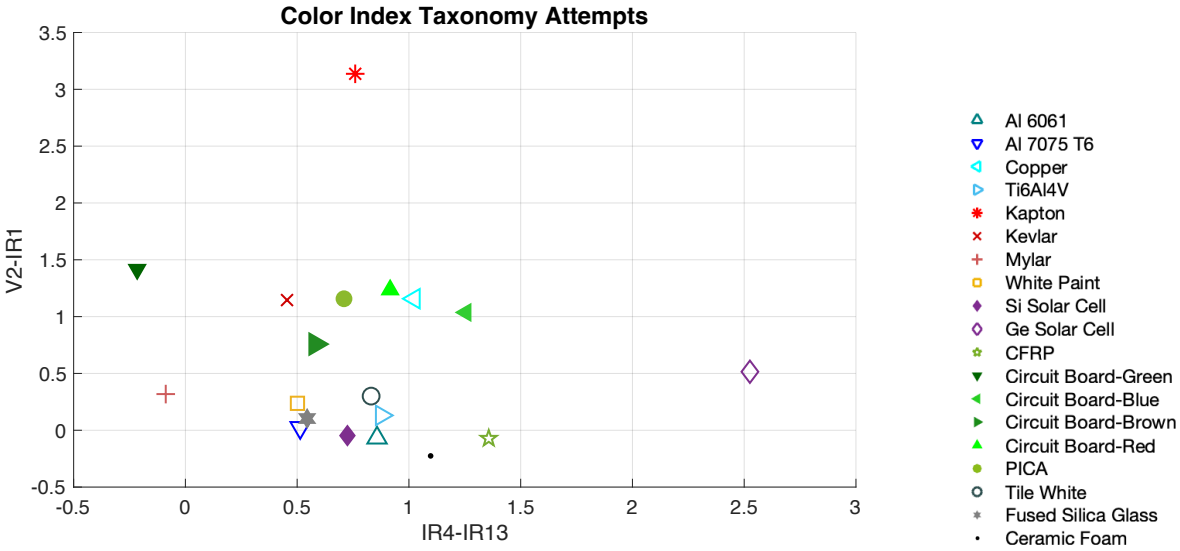

Figure A. 62: Color-color diagrams for V2-IR1 versus IR4-IR13 color indices according to their respective filter passbands listed in Table 5.2. *Credit: NASA*

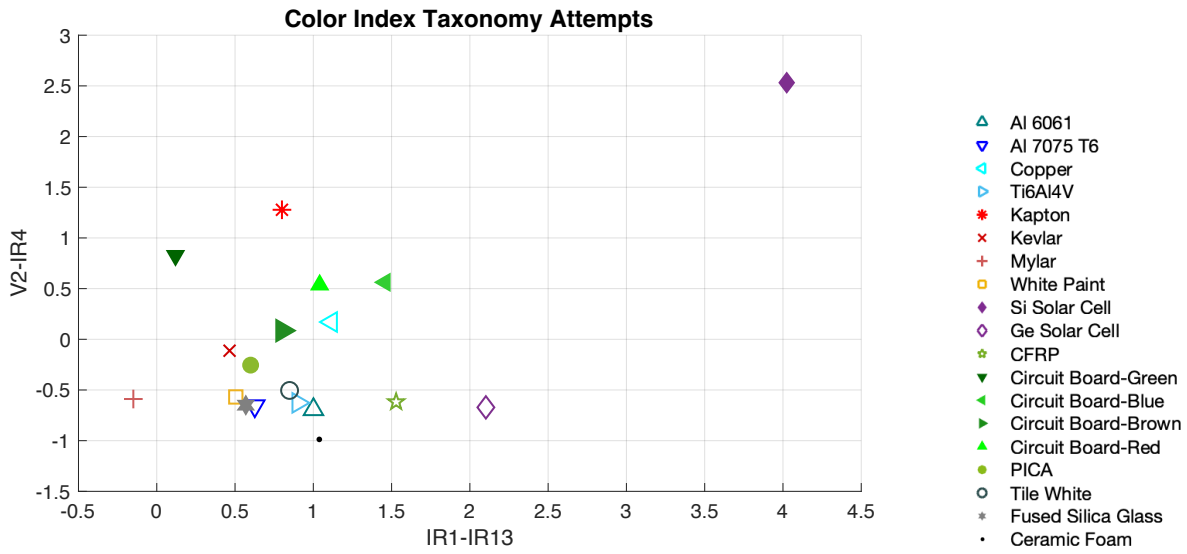

Figure A. 63: Color-color diagrams for V2-IR4 versus IR1-IR13 color indices according to their respective filter passbands listed in Table 5.2. *Credit: NASA*

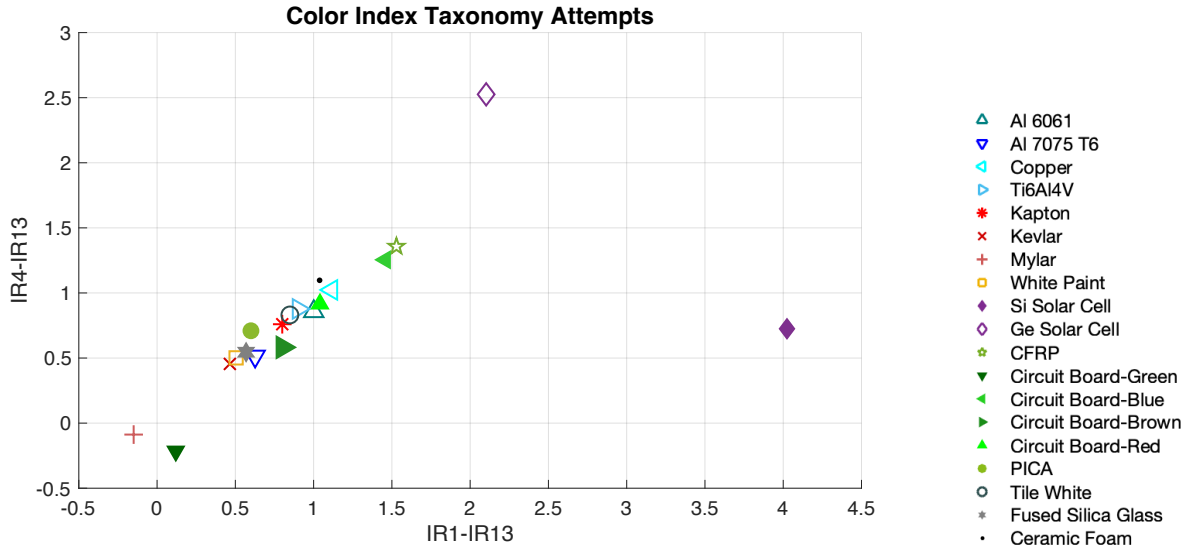

Figure A. 64: Color-color diagrams for IR4-IR13 versus IR1-IR13 color indices according to their respective filter passbands listed in Table 5.2. *Credit: NASA*

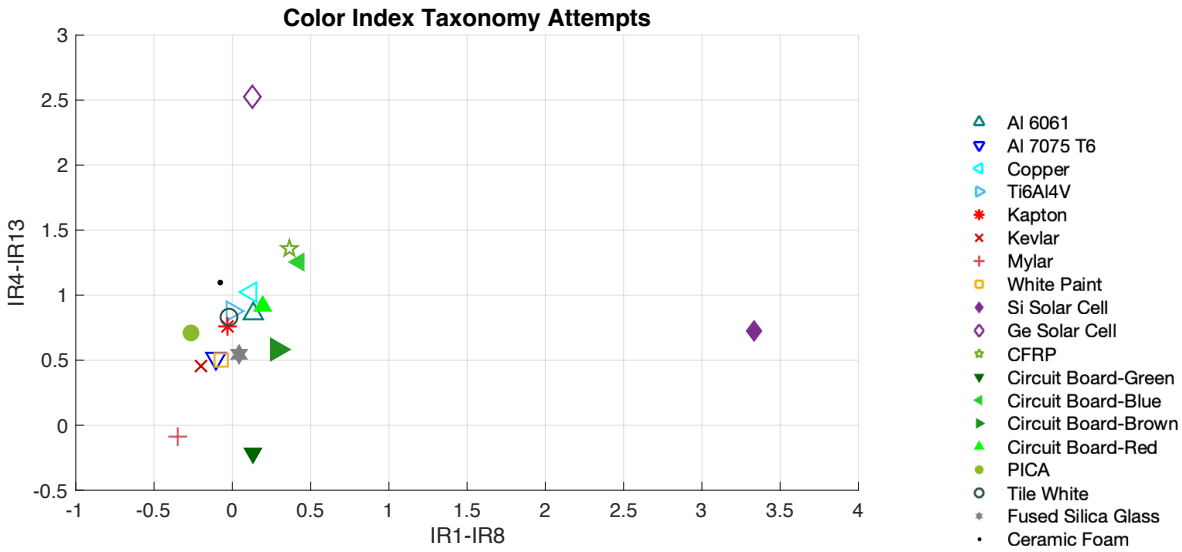

Figure A. 65: Color-color diagrams for IR4-IR13 versus IR1-IR8 color indices according to their respective filter passbands listed in Table 5.2. *Credit: NASA*

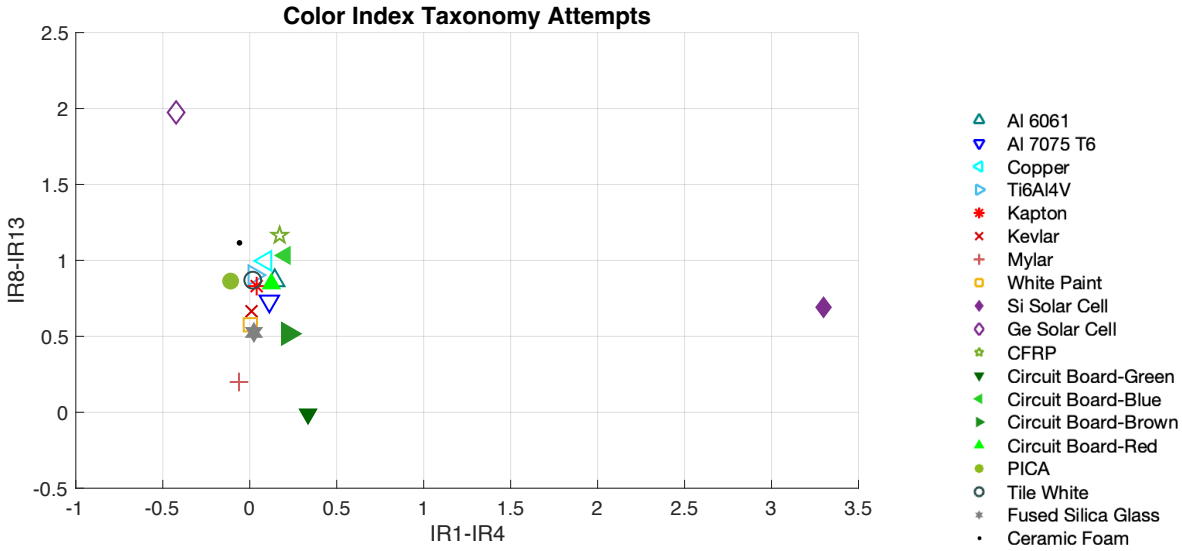

Figure A. 66: Color-color diagrams for IR8-IR13 versus IR1-IR4 color indices according to their respective filter passbands listed in Table 5.2. *Credit: NASA*

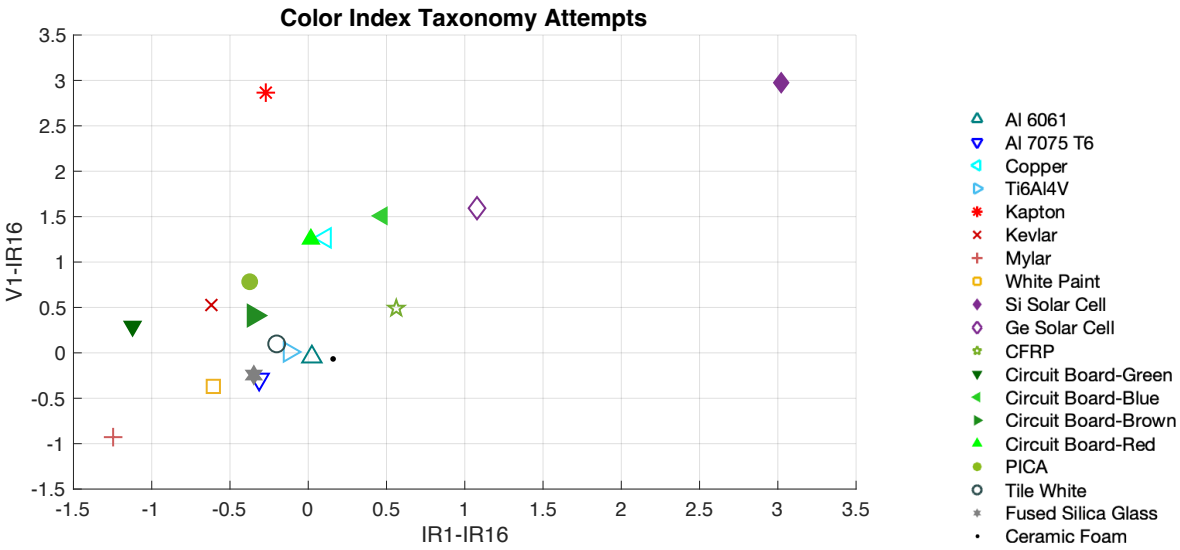

Figure A. 67: Color-color diagrams for V1-IR16 versus IR1-IR16 color indices according to their respective filter passbands listed in Table 5.2. *Credit: NASA*

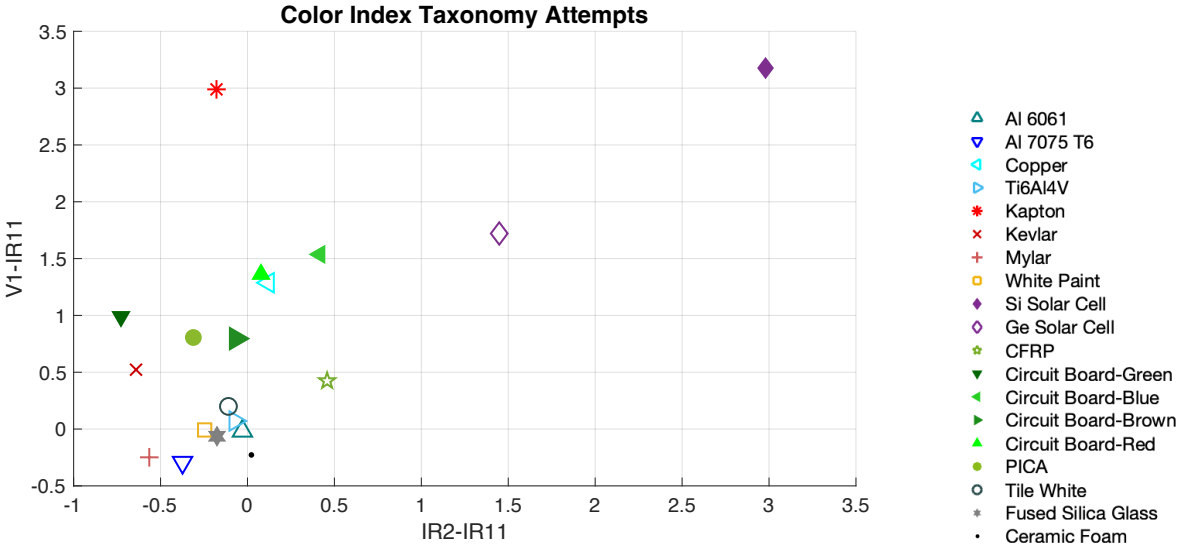

Figure A. 68: Color-color diagrams for V1-IR11 versus IR2-IR11 color indices according to their respective filter passbands listed in Table 5.2. *Credit: NASA*

Figure A. 69: Color-color diagrams for V1-V3 versus V1-IR2 color indices according to their respective filter passbands listed in Table 5.2. *Credit: NASA*

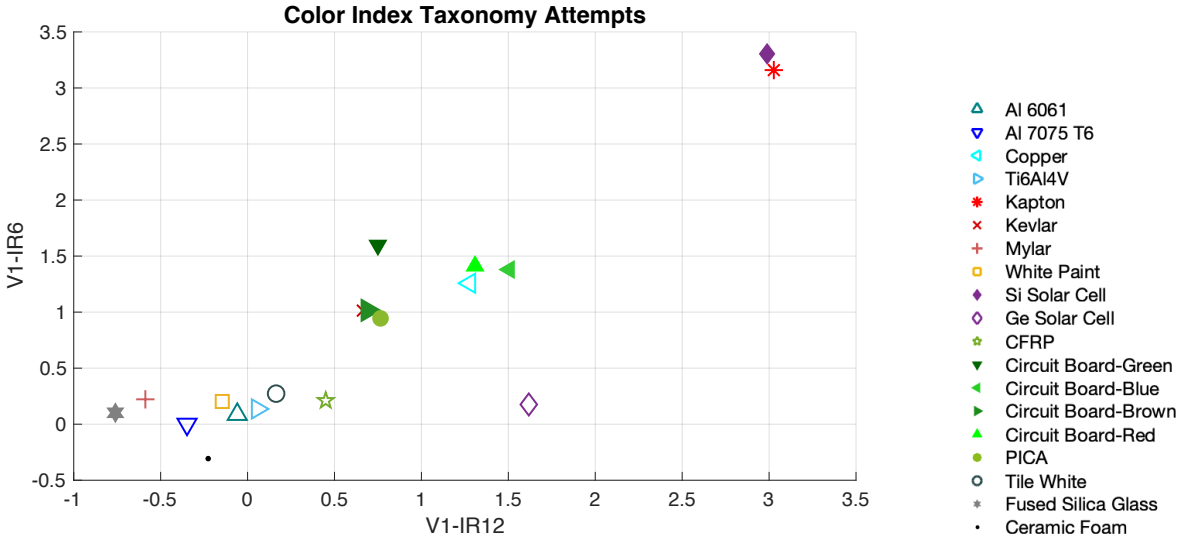

Figure A. 70: Color-color diagrams for V1-IR6 versus V1-IR12 color indices according to their respective filter passbands listed in Table 5.2. *Credit: NASA*

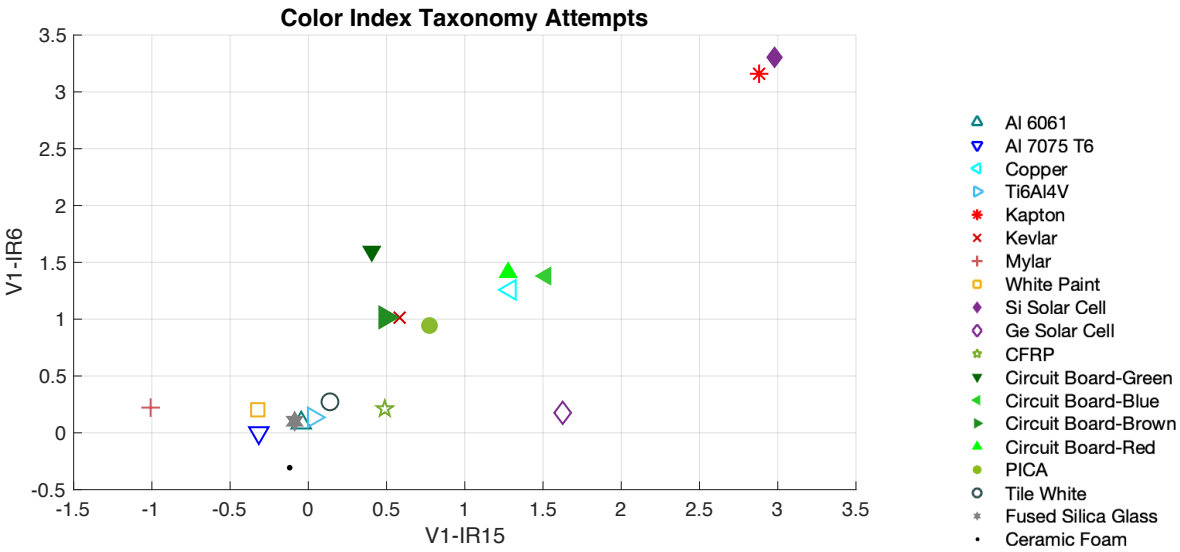

Figure A. 71: Color-color diagrams for V1-IR6 versus V1-IR15 color indices according to their respective filter passbands listed in Table 5.2. *Credit: NASA*

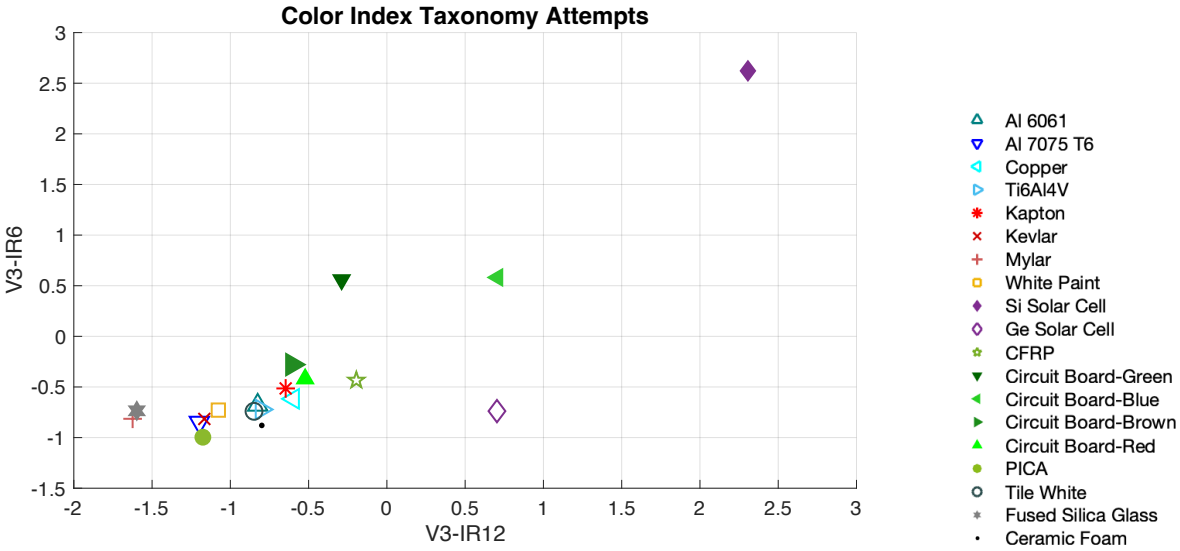

Figure A. 72: Color-color diagrams for V3-IR6 versus V3-IR12 color indices according to their respective filter passbands listed in Table 5.2. *Credit: NASA*

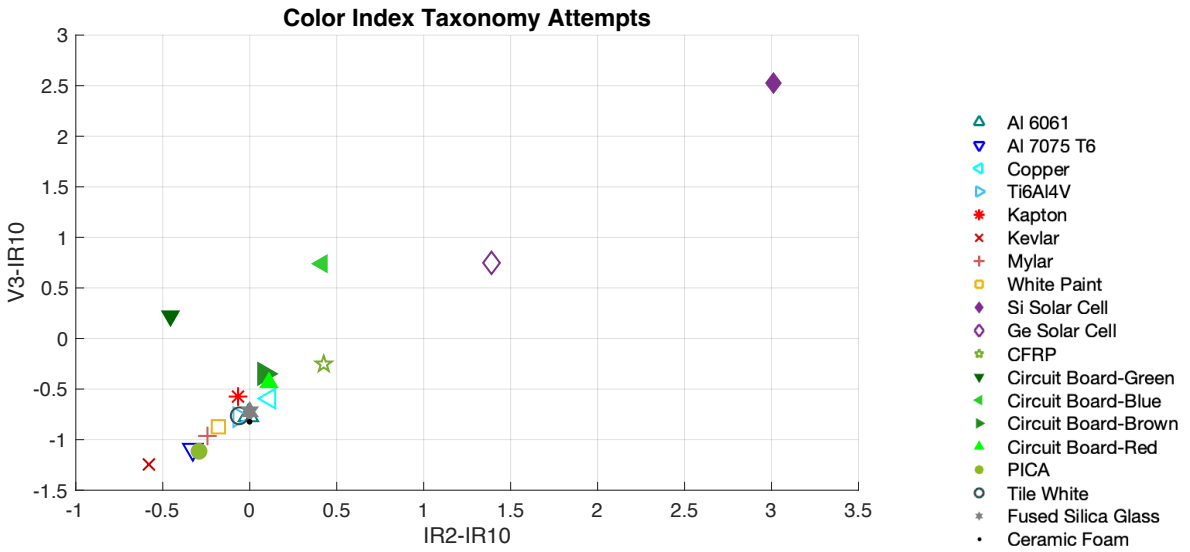

Figure A. 73: Color-color diagrams for V3-IR10 versus IR2-IR10 color indices according to their respective filter passbands listed in Table 5.2. *Credit: NASA*

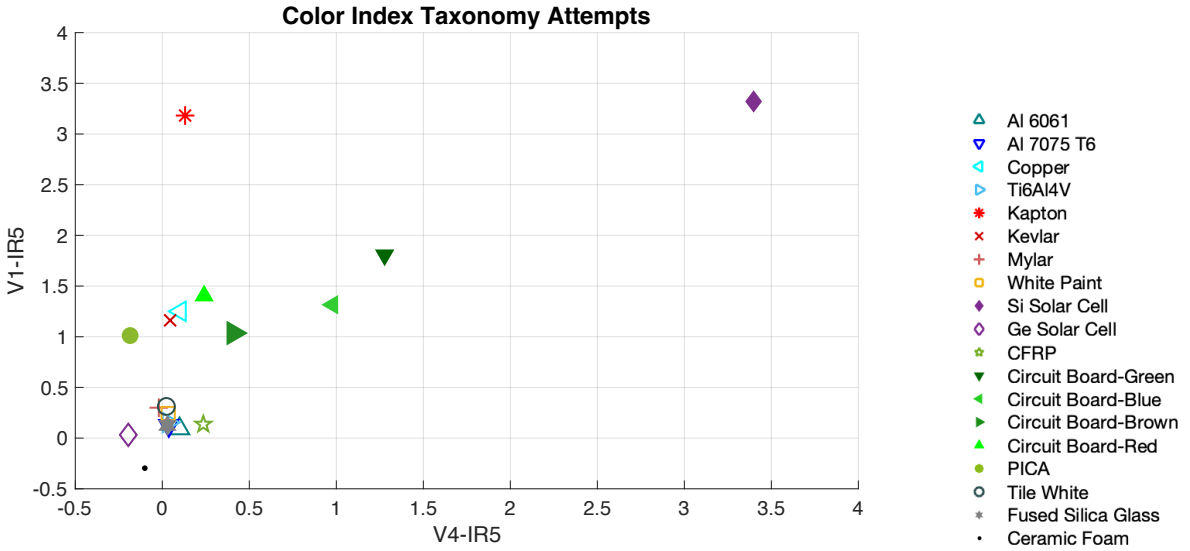

Figure A. 74: Color-color diagrams for V1-IR5 versus V4-IR5 color indices according to their respective filter passbands listed in Table 5.2. *Credit: NASA*

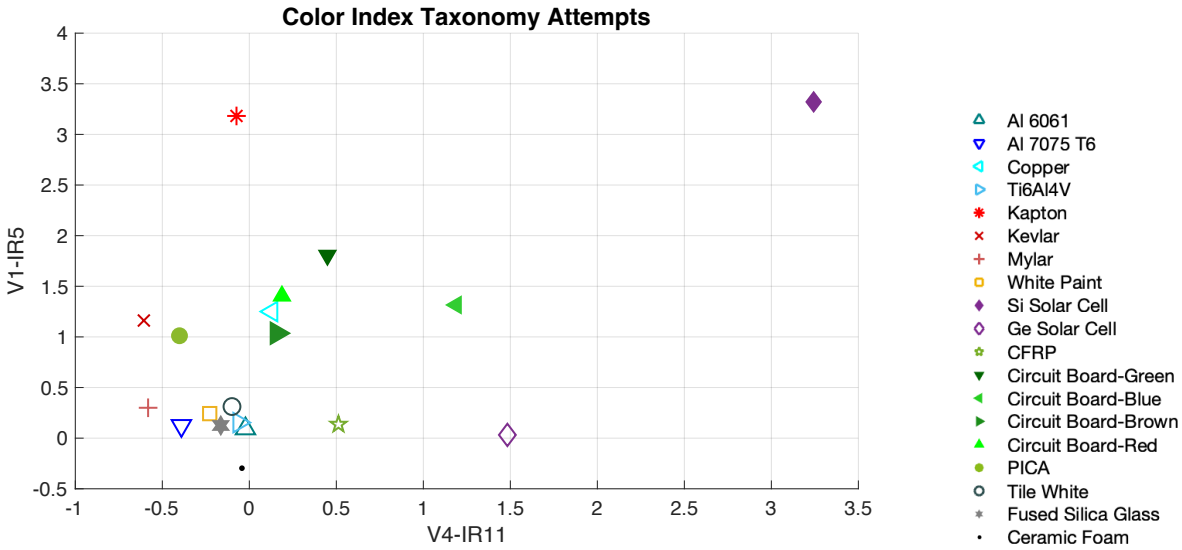

Figure A. 75: Color-color diagrams for V1-IR5 versus V4-IR11 color indices according to their respective filter passbands listed in Table 5.2. *Credit: NASA*

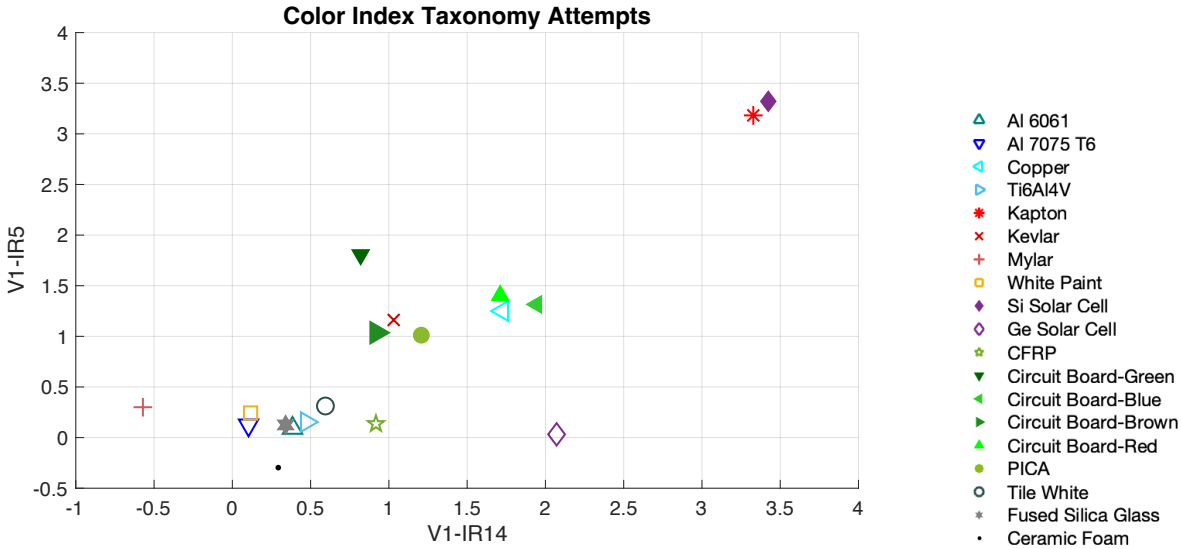

Figure A. 76: Color-color diagrams for V1-IR5 versus V1-IR14 color indices according to their respective filter passbands listed in Table 5.2. *Credit: NASA*

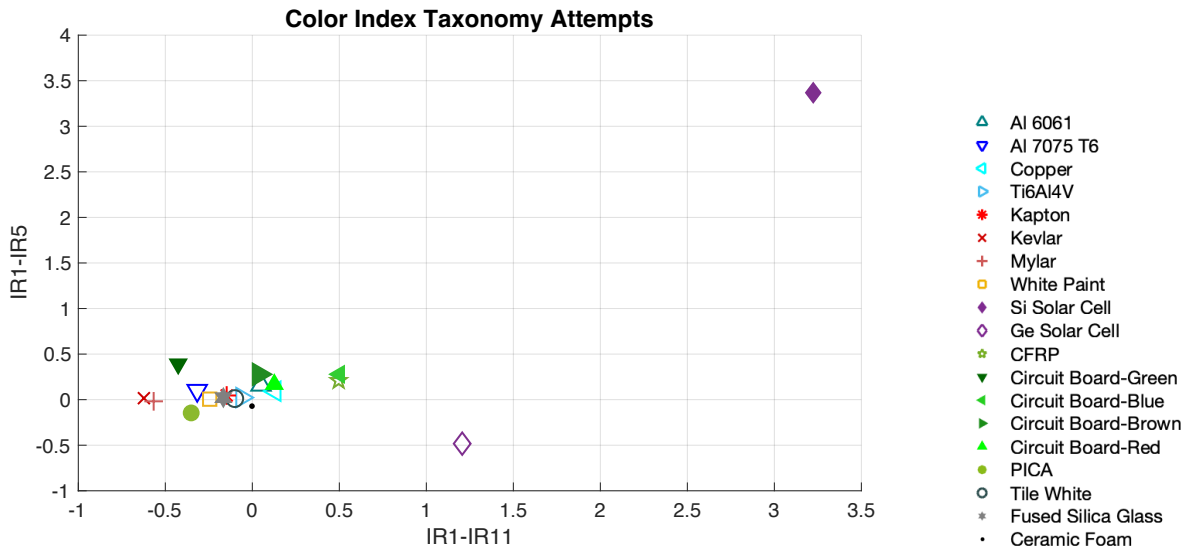

Figure A. 77: Color-color diagrams for IR1-IR5 versus IR1-IR11 color indices according to their respective filter passbands listed in Table 5.2. *Credit: NASA*

A.3. COLOR INDEX VALUES

Table A. 1: Materials and respective nomenclature for DebriSat material data used to calculate indices and generate color-color diagrams for Tables A.2-A.5.

Nomenclature	Material	Nomenclature	Material
M1	UTJ Solar Cell	M8	Composite: gold shimmer
M2	Red painted Aluminum 6061	M9	Composite: Black COPV
M3	Magenta painted Aluminum 6061	M10	Circuit Board - Red
M4	Gold painted Aluminum 6061	M11	Circuit Board – Green
M5	Blue painted Aluminum 6061	M12	Circuit Board – Brown
M6	Black painted Aluminum 6061	M13	Circuit Board – Blue
M7	Anodized/unpainted Aluminum 6061		

Table A. 2: Color index values of materials calculated from reflectance spectra in Figures 4.11-4.13 for materials used in DebriSat analysis.

Color Index	M1	M2	M3	M4	M5	M6	M7	M8	M9	M10	M11	M12	M13
r'-i'	0.171	0.539	0.357	0.087	1.373	1.981	0.045	0.190	0.153	0.511	0.883	0.391	1.070
g'-i'	0.062	2.243	1.468	1.203	0.756	1.986	-0.116	0.001	-0.143	1.093	0.520	0.503	0.492
r'-z'	0.863	1.486	1.290	0.994	2.275	3.265	1.081	0.985	0.943	1.340	2.559	1.327	2.343
i'-z'	0.693	0.948	0.933	0.907	0.902	1.284	1.036	0.795	0.790	0.830	1.676	0.936	1.273
g'-r'	-0.109	1.705	1.110	1.115	-0.617	0.005	-0.161	-0.189	-0.296	0.583	-0.363	0.111	-0.577

A.4. DISTANCE MATRICES

Table A. 3: Matrix for distances between indices for all DebriSat materials for the r'-i' versus g'-i' color-color diagram.

	M1	M2	M3	M4	M5	M6	M7	M8	M9	M10	M11	M12	M13
M1	0.000	2.212	1.419	1.144	1.388	2.642	0.218	0.064	0.206	1.086	0.847	0.493	0.997
M2	2.212	0.000	0.796	1.134	1.706	1.465	2.411	2.269	2.418	1.150	1.757	1.747	1.830
M3	1.419	0.796	0.000	0.379	1.240	1.705	1.615	1.477	1.624	0.405	1.084	0.966	1.208
M4	1.144	1.134	0.379	0.000	1.361	2.050	1.319	1.206	1.348	0.437	1.049	0.763	1.212
M5	1.388	1.706	1.240	1.361	0.000	1.373	1.589	1.403	1.516	0.926	0.543	1.014	0.402
M6	2.642	1.465	1.705	2.050	1.373	0.000	2.858	2.674	2.807	1.720	1.832	2.175	1.750
M7	0.218	2.411	1.615	1.319	1.589	2.858	0.000	0.186	0.112	1.296	1.053	0.709	1.192
M8	0.064	2.269	1.477	1.206	1.403	2.674	0.186	0.000	0.149	1.139	0.866	0.541	1.008
M9	0.206	2.418	1.624	1.348	1.516	2.807	0.112	0.149	0.000	1.287	0.987	0.689	1.116
M10	1.086	1.150	0.405	0.437	0.926	1.720	1.296	1.139	1.287	0.000	0.684	0.603	0.821
M11	0.847	1.757	1.084	1.049	0.543	1.832	1.053	0.866	0.987	0.684	0.000	0.492	0.188
M12	0.493	1.747	0.966	0.763	1.014	2.175	0.709	0.541	0.689	0.603	0.492	0.000	0.679
M13	0.997	1.830	1.208	1.212	0.402	1.750	1.192	1.008	1.116	0.821	0.188	0.679	0.000

Table A. 4: Matrix for distances between indices for all DebriSat materials for the r'-i' versus g'-r' color-color diagram.

	M1	M2	M3	M4	M5	M6	M7	M8	M9	M10	M11	M12	M13
M1	0.000	1.851	1.234	1.227	1.305	1.814	0.136	0.082	0.188	0.771	0.757	0.312	1.014
M2	1.851	0.000	0.621	0.742	2.467	2.229	1.930	1.925	2.038	1.122	2.096	1.600	2.343
M3	1.234	0.621	0.000	0.270	2.004	1.964	1.309	1.310	1.422	0.549	1.565	1.000	1.832
M4	1.227	0.742	0.270	0.000	2.158	2.195	1.277	1.308	1.413	0.680	1.679	1.049	1.957
M5	1.305	2.467	2.004	2.158	0.000	0.870	1.405	1.258	1.262	1.478	0.552	1.223	0.306
M6	1.814	2.229	1.964	2.195	0.870	0.000	1.944	1.802	1.853	1.580	1.158	1.593	1.082
M7	0.136	1.930	1.309	1.277	1.405	1.944	0.000	0.148	0.174	0.877	0.863	0.441	1.107
M8	0.082	1.925	1.310	1.308	1.258	1.802	0.148	0.000	0.114	0.836	0.715	0.362	0.962
M9	0.188	2.038	1.422	1.413	1.262	1.853	0.174	0.114	0.000	0.949	0.734	0.472	0.959
M10	0.771	1.122	0.549	0.680	1.478	1.580	0.877	0.836	0.949	0.000	1.017	0.486	1.288
M11	0.757	2.096	1.565	1.679	0.552	1.158	0.863	0.715	0.734	1.017	0.000	0.684	0.284
M12	0.312	1.600	1.000	1.049	1.223	1.593	0.441	0.362	0.472	0.486	0.684	0.000	0.967
M13	1.014	2.343	1.832	1.957	0.306	1.082	1.107	0.962	0.959	1.288	0.284	0.967	0.000

Table A. 5: Matrix for distance values between indices for all DebriSat materials for the r'-i' versus r'-z' color-color diagram.

	M1	M2	M3	M4	M5	M6	M7	M8	M9	M10	M11	M12	M13
M1	0.000	0.724	0.466	0.155	1.854	3.008	0.252	0.123	0.082	0.586	1.840	0.513	1.731
M2	0.724	0.000	0.267	0.668	1.148	2.290	0.639	0.611	0.666	0.149	1.127	0.217	1.008
M3	0.466	0.267	0.000	0.401	1.414	2.557	0.376	0.348	0.403	0.161	1.374	0.050	1.271
M4	0.155	0.668	0.401	0.000	1.815	2.957	0.097	0.103	0.083	0.547	1.756	0.451	1.669
M5	1.854	1.148	1.414	1.815	0.000	1.162	1.786	1.750	1.806	1.272	0.566	1.365	0.311
M6	3.008	2.290	2.557	2.957	1.162	0.000	2.919	2.900	2.955	2.422	1.305	2.507	1.297
M7	0.252	0.639	0.376	0.097	1.786	2.919	0.000	0.174	0.175	0.533	1.700	0.425	1.626
M8	0.123	0.611	0.348	0.103	1.750	2.900	0.174	0.000	0.056	0.479	1.720	0.397	1.618
M9	0.082	0.666	0.403	0.083	1.806	2.955	0.175	0.056	0.000	0.534	1.773	0.452	1.673
M10	0.586	0.149	0.161	0.547	1.272	2.422	0.533	0.479	0.534	0.000	1.275	0.120	1.148
M11	1.840	1.127	1.374	1.756	0.566	1.305	1.700	1.720	1.773	1.275	0.000	1.327	0.286
M12	0.513	0.217	0.050	0.451	1.365	2.507	0.425	0.397	0.452	0.120	1.327	0.000	1.222
M13	1.731	1.008	1.271	1.669	0.311	1.297	1.626	1.618	1.673	1.148	0.286	1.222	0.000

Table A. 6: Materials and respective nomenclature for material data used to calculate indices and generate color-color diagrams for Tables A.7-A.25.

Nomenclature	Material	Nomenclature	Material
M1	Al 6061	M11	CFRP
M2	Al 7075-T6	M12	Circuit Board – Green
M3	Copper	M13	Circuit Board – Blue
M4	Ti6Al4V	M14	Circuit Board – Brown
M5	Polyimide (Kapton®)	M15	Circuit Board – Red
M6	Kevlar	M16	PICA
M7	Mylar	M17	Tile White
M8	White Paint	M18	Fused Silica Glass
M9	Si Solar Cell	M19	Ceramic Foam
M10	Ge Solar Cell	M20	Spectralon®

Table A. 7: Magnitude values of materials for each respective filter passband calculated from reflectance spectra in Figure 5.3 for materials used in taxonomy analysis.

FILTER / PASS-BAND	M1	M2	M3	M4	M5	M6	M7	M8	M9	M10	M11	M12	M13	M14	M15	M16	M17	M18	M19	M20
g'	-5.34	-4.70	-4.01	-4.11	-2.40	-4.51	-5.14	-4.83	-1.81	-0.91	-3.31	-2.33	-3.77	-2.82	-3.74	-2.77	-4.70	-5.44	-1.95	-5.37
r'	-5.16	-4.58	-4.71	-3.97	-4.59	-4.97	-5.08	-4.72	-1.58	-0.77	-3.01	-1.97	-3.20	-2.93	-4.33	-3.40	-4.68	-5.29	-1.62	-5.15
i'	-5.24	-4.68	-4.97	-4.15	-5.17	-5.23	-5.32	-4.94	-1.71	-1.10	-3.17	-2.85	-4.27	-3.32	-4.84	-3.58	-4.89	-5.45	-1.71	-5.30
z'	-5.99	-5.42	-5.71	-4.89	-5.98	-5.99	-6.03	-5.68	-4.04	-1.91	-3.96	-4.53	-5.54	-4.26	-5.67	-4.22	-5.63	-6.19	-2.38	-6.02
B	-5.96	-5.33	-4.73	-4.73	-3.83	-5.13	-5.63	-5.31	-2.52	-1.57	-3.94	-2.87	-4.23	-3.44	-4.37	-3.47	-5.32	-6.06	-2.59	-6.00
V	-6.00	-5.40	-5.28	-4.80	-4.95	-5.68	-5.90	-5.55	-2.41	-1.59	-3.89	-2.97	-4.24	-3.69	-4.91	-4.03	-5.47	-6.12	-2.51	-6.00
R	-6.71	-6.15	-6.40	-5.60	-6.56	-6.67	-6.74	-6.38	-3.76	-2.56	-4.64	-4.73	-5.84	-4.81	-6.25	-4.99	-6.33	-6.90	-3.15	-6.75
I	-6.47	-5.90	-6.19	-5.37	-6.43	-6.46	-6.52	-6.16	-4.26	-2.36	-4.42	-4.77	-5.86	-4.68	-6.12	-4.74	-6.11	-6.67	-2.88	-6.51
Z	-4.81	-4.24	-4.58	-3.75	-4.84	-4.85	-4.91	-4.56	-1.35	-0.97	-2.79	-3.29	-4.36	-3.06	-4.51	-3.13	-4.50	-5.06	-1.27	-4.89
Y	-5.04	-4.46	-4.73	-3.91	-5.00	-5.01	-5.04	-4.70	-3.60	-0.80	-3.00	-3.61	-4.60	-3.32	-4.71	-3.21	-4.65	-5.21	-1.37	-5.03
J	-5.56	-4.95	-5.28	-4.39	-5.48	-5.48	-5.50	-5.17	-5.31	-1.10	-3.61	-4.11	-5.21	-3.91	-5.27	-3.61	-5.12	-5.69	-1.82	-5.51
H	-6.19	-5.40	-5.95	-5.02	-6.10	-5.95	-5.97	-5.75	-5.92	-2.37	-4.41	-4.56	-6.02	-4.60	-5.96	-4.15	-5.75	-6.37	-2.48	-6.16
K	-6.29	-5.36	-6.17	-5.15	-6.16	-5.76	-5.67	-5.69	-5.93	-3.57	-4.76	-4.03	-6.27	-4.46	-6.05	-4.25	-5.86	-6.24	-2.76	-6.32
V1	-4.97	-4.32	-3.53	-3.73	-1.80	-3.82	-4.71	-4.43	-1.49	-0.55	-2.97	-1.81	-3.40	-2.38	-3.37	-2.10	-4.31	-5.07	-1.62	-5.01
V2	-5.74	-5.12	-4.61	-4.52	-3.70	-5.08	-5.55	-5.24	-2.21	-1.32	-3.69	-2.74	-4.08	-3.27	-4.19	-3.40	-5.13	-5.84	-2.32	-5.76
V3	-5.74	-5.17	-5.41	-4.59	-5.48	-5.64	-5.74	-5.36	-2.17	-1.47	-3.61	-2.85	-4.20	-3.67	-5.20	-4.04	-5.32	-5.90	-2.19	-5.76
V4	-4.96	-4.41	-4.68	-3.85	-4.85	-4.93	-5.03	-4.64	-1.41	-0.78	-2.87	-2.34	-3.74	-3.00	-4.53	-3.30	-4.60	-5.16	-1.43	-5.01
IR1	-4.90	-4.35	-4.69	-3.86	-4.94	-4.96	-5.03	-4.67	-1.44	-1.07	-2.90	-3.23	-4.44	-3.13	-4.60	-3.26	-4.61	-5.17	-1.40	-5.01
IR2	-4.98	-4.40	-4.70	-3.88	-4.97	-4.98	-5.02	-4.67	-1.69	-0.83	-2.94	-3.53	-4.52	-3.24	-4.65	-3.22	-4.62	-5.18	-1.37	-5.01
IR3	-5.02	-4.45	-4.71	-3.89	-4.98	-4.99	-5.02	-4.67	-3.96	-0.75	-2.99	-3.60	-4.58	-3.31	-4.70	-3.18	-4.63	-5.19	-1.35	-5.01
IR4	-5.05	-4.46	-4.78	-3.89	-4.98	-4.97	-4.96	-4.67	-4.74	-0.65	-3.07	-3.57	-4.64	-3.36	-4.73	-3.15	-4.63	-5.19	-1.34	-5.01
IR5	-5.06	-4.45	-4.78	-3.89	-4.99	-4.98	-5.01	-4.67	-4.81	-0.59	-3.11	-3.62	-4.71	-3.41	-4.77	-3.11	-4.62	-5.19	-1.32	-5.01
IR6	-5.06	-4.32	-4.79	-3.87	-4.96	-4.83	-4.93	-4.63	-4.79	-0.73	-3.18	-3.41	-4.78	-3.39	-4.78	-3.05	-4.58	-5.17	-1.31	-5.01
IR7	-5.05	-4.29	-4.80	-3.87	-4.97	-4.79	-4.97	-4.64	-4.79	-0.85	-3.23	-3.56	-4.84	-3.49	-4.82	-3.02	-4.59	-5.21	-1.32	-5.01
IR8	-5.04	-4.24	-4.81	-3.86	-4.91	-4.76	-4.68	-4.60	-4.78	-1.20	-3.26	-3.36	-4.86	-3.42	-4.80	-2.99	-4.59	-5.21	-1.32	-5.01
IR9	-5.73	-4.85	-5.51	-4.57	-5.66	-5.46	-5.55	-5.28	-5.47	-2.81	-4.05	-4.07	-5.68	-4.17	-5.54	-3.68	-5.30	-5.96	-2.08	-5.75
IR10	-4.97	-4.08	-4.81	-3.81	-4.90	-4.40	-4.78	-4.49	-4.70	-2.22	-3.36	-3.08	-4.94	-3.32	-4.76	-2.93	-4.56	-5.18	-1.37	-4.97
IR11	-4.95	-4.03	-4.82	-3.80	-4.79	-4.34	-4.46	-4.42	-4.67	-2.27	-3.39	-2.80	-4.94	-3.17	-4.73	-2.91	-4.51	-5.00	-1.39	-4.96
IR12	-4.91	-3.98	-4.81	-3.79	-4.83	-4.48	-4.12	-4.29	-4.48	-2.17	-3.42	-2.56	-4.90	-3.07	-4.67	-2.87	-4.48	-4.31	-1.40	-4.98
IR13	-5.90	-4.97	-5.80	-4.77	-5.74	-5.43	-4.88	-5.17	-5.47	-3.17	-4.43	-3.35	-5.89	-3.94	-5.64	-3.86	-5.46	-5.74	-2.43	-5.96
IR14	-5.35	-4.43	-5.26	-4.21	-5.13	-4.85	-4.14	-4.55	-4.91	-2.63	-3.89	-2.63	-5.34	-3.30	-5.08	-3.31	-4.91	-5.41	-1.92	-5.40
IR15	-4.92	-4.01	-4.82	-3.77	-4.68	-4.40	-3.70	-4.11	-4.47	-2.18	-3.46	-2.22	-4.92	-2.87	-4.64	-2.88	-4.45	-4.98	-1.50	-4.96
IR16	-4.92	-4.03	-4.80	-3.74	-4.67	-4.34	-3.78	-4.06	-4.46	-2.15	-3.46	-2.11	-4.91	-2.79	-4.62	-2.88	-4.41	-4.82	-1.55	-4.95

Table A. 8: Matrix for distance values between indices for all materials used in color index analysis taxonomy attempts for the r'-i' versus g'-i' color-color diagram.

	M1	M2	M3	M4	M5	M6	M7	M8	M9	M10	M11	M12	M13	M14	M15	M16	M17	M18	M19	M20
M1	0.000	0.084	1.078	0.170	2.915	0.845	0.323	0.249	0.045	0.382	0.085	1.017	1.155	0.680	1.271	0.919	0.322	0.147	0.142	0.079
M2	0.084	0.000	0.994	0.093	2.831	0.761	0.242	0.170	0.084	0.307	0.132	0.950	1.094	0.598	1.187	0.836	0.240	0.074	0.223	0.066
M3	1.078	0.994	0.000	0.926	1.838	0.237	0.783	0.857	1.072	0.771	1.109	0.763	0.935	0.476	0.284	0.168	0.773	0.949	1.216	1.033
M4	0.170	0.093	0.926	0.000	2.762	0.691	0.154	0.079	0.150	0.214	0.183	0.857	1.004	0.512	1.107	0.773	0.157	0.023	0.295	0.108
M5	2.915	2.831	1.838	2.762	0.000	2.071	2.615	2.690	2.908	2.591	2.944	2.270	2.329	2.275	1.678	1.998	2.606	2.785	3.053	2.869
M6	0.845	0.761	0.237	0.691	2.071	0.000	0.547	0.621	0.837	0.536	0.874	0.658	0.844	0.258	0.448	0.116	0.536	0.713	0.982	0.798
M7	0.323	0.242	0.783	0.154	2.615	0.547	0.000	0.077	0.304	0.083	0.333	0.727	0.886	0.358	0.955	0.637	0.026	0.178	0.448	0.261
M8	0.249	0.170	0.857	0.079	2.690	0.621	0.077	0.000	0.227	0.137	0.256	0.784	0.936	0.434	1.031	0.708	0.085	0.102	0.372	0.184
M9	0.045	0.084	1.072	0.150	2.908	0.837	0.304	0.227	0.000	0.356	0.050	0.982	1.117	0.661	1.257	0.916	0.306	0.126	0.146	0.044
M10	0.382	0.307	0.771	0.214	2.591	0.536	0.083	0.137	0.356	0.000	0.376	0.649	0.804	0.318	0.921	0.636	0.105	0.236	0.496	0.312
M11	0.085	0.132	1.109	0.183	2.944	0.874	0.333	0.256	0.050	0.376	0.000	0.987	1.116	0.689	1.287	0.956	0.339	0.160	0.120	0.077
M12	1.017	0.950	0.763	0.857	2.270	0.658	0.727	0.784	0.982	0.649	0.987	0.000	0.188	0.492	0.684	0.760	0.743	0.876	1.103	0.939
M13	1.155	1.094	0.935	1.004	2.329	0.844	0.886	0.936	1.117	0.804	1.116	0.188	0.000	0.679	0.821	0.944	0.904	1.021	1.228	1.076
M14	0.680	0.598	0.476	0.512	2.275	0.258	0.358	0.434	0.661	0.318	0.689	0.492	0.679	0.000	0.603	0.373	0.358	0.536	0.806	0.618
M15	1.271	1.187	0.284	1.107	1.678	0.448	0.955	1.031	1.257	0.921	1.287	0.684	0.821	0.603	0.000	0.433	0.950	1.131	1.402	1.215
M16	0.919	0.836	0.168	0.773	1.998	0.116	0.637	0.708	0.916	0.636	0.956	0.760	0.944	0.373	0.433	0.000	0.624	0.796	1.059	0.879
M17	0.322	0.240	0.773	0.157	2.606	0.536	0.026	0.085	0.306	0.105	0.339	0.743	0.904	0.358	0.950	0.624	0.000	0.180	0.452	0.265
M18	0.147	0.074	0.949	0.023	2.785	0.713	0.178	0.102	0.126	0.236	0.160	0.876	1.021	0.536	1.131	0.796	0.180	0.000	0.272	0.085
M19	0.142	0.223	1.216	0.295	3.053	0.982	0.448	0.372	0.146	0.496	0.120	1.103	1.228	0.806	1.402	1.059	0.452	0.272	0.000	0.188
M20	0.079	0.066	1.033	0.108	2.869	0.798	0.261	0.184	0.044	0.312	0.077	0.939	1.076	0.618	1.215	0.879	0.265	0.085	0.188	0.000

Table A. 9: Matrix for distance values between indices for all materials used in color index analysis taxonomy attempts for the V-R versus B-R color-color diagram.

	M1	M2	M3	M4	M5	M6	M7	M8	M9	M10	M11	M12	M13	M14	M15	M16	M17	M18	M19	M20
M1	0.000	0.070	0.995	0.141	2.170	0.826	0.380	0.335	0.798	0.344	0.063	1.512	1.234	0.740	1.284	0.806	0.299	0.113	0.206	0.031
M2	0.070	0.000	0.925	0.075	2.100	0.757	0.311	0.265	0.739	0.282	0.118	1.448	1.171	0.671	1.215	0.737	0.230	0.050	0.275	0.071
M3	0.995	0.925	0.000	0.857	1.175	0.185	0.617	0.661	0.487	0.693	1.032	0.667	0.494	0.292	0.308	0.213	0.699	0.886	1.201	0.989
M4	0.141	0.075	0.857	0.000	2.032	0.692	0.249	0.202	0.664	0.207	0.175	1.372	1.096	0.599	1.144	0.674	0.159	0.029	0.344	0.131
M5	2.170	2.100	1.175	2.032	0.000	1.350	1.792	1.836	1.515	1.857	2.206	0.891	1.121	1.443	0.896	1.374	1.873	2.061	2.375	2.163
M6	0.826	0.757	0.185	0.692	1.350	0.000	0.446	0.491	0.472	0.547	0.867	0.835	0.627	0.212	0.493	0.030	0.536	0.721	1.032	0.822
M7	0.380	0.311	0.617	0.249	1.792	0.446	0.000	0.047	0.529	0.182	0.423	1.179	0.915	0.384	0.913	0.426	0.105	0.277	0.586	0.378
M8	0.335	0.265	0.661	0.202	1.836	0.491	0.047	0.000	0.545	0.157	0.377	1.211	0.944	0.420	0.955	0.472	0.063	0.230	0.541	0.332
M9	0.798	0.739	0.487	0.664	1.515	0.472	0.529	0.545	0.000	0.457	0.806	0.735	0.450	0.266	0.638	0.486	0.536	0.689	0.979	0.777
M10	0.344	0.282	0.693	0.207	1.857	0.547	0.182	0.157	0.457	0.000	0.361	1.169	0.890	0.414	0.963	0.535	0.106	0.233	0.536	0.326
M11	0.063	0.118	1.032	0.175	2.206	0.867	0.423	0.377	0.806	0.361	0.000	1.529	1.249	0.768	1.316	0.849	0.333	0.147	0.175	0.047
M12	1.512	1.448	0.667	1.372	0.891	0.835	1.179	1.211	0.735	1.169	1.529	0.000	0.285	0.796	0.418	0.864	1.224	1.400	1.704	1.495
M13	1.234	1.171	0.494	1.096	1.121	0.627	0.915	0.944	0.450	0.890	1.249	0.285	0.000	0.540	0.378	0.655	0.952	1.122	1.423	1.216
M14	0.740	0.671	0.292	0.599	1.443	0.212	0.384	0.420	0.266	0.414	0.768	0.796	0.540	0.000	0.549	0.222	0.442	0.627	0.942	0.728
M15	1.284	1.215	0.308	1.144	0.896	0.493	0.913	0.955	0.638	0.963	1.316	0.418	0.378	0.549	0.000	0.521	0.986	1.173	1.488	1.275
M16	0.806	0.737	0.213	0.674	1.374	0.030	0.426	0.472	0.486	0.535	0.849	0.864	0.655	0.222	0.521	0.000	0.519	0.702	1.012	0.804
M17	0.299	0.230	0.699	0.159	1.873	0.536	0.105	0.063	0.536	0.106	0.333	1.224	0.952	0.442	0.986	0.519	0.000	0.188	0.503	0.290
M18	0.113	0.050	0.886	0.029	2.061	0.721	0.277	0.230	0.689	0.233	0.147	1.400	1.122	0.627	1.173	0.702	0.188	0.000	0.315	0.103
M19	0.206	0.275	1.201	0.344	2.375	1.032	0.586	0.541	0.979	0.536	0.175	1.704	1.423	0.942	1.488	1.012	0.503	0.315	0.000	0.213
M20	0.031	0.071	0.989	0.131	2.163	0.822	0.378	0.332	0.777	0.326	0.047	1.495	1.216	0.728	1.275	0.804	0.290	0.103	0.213	0.000

Table A. 10: Matrix for distance values between indices for all materials used in color index analysis taxonomy attempts for the z'-i' versus z'-H color-color diagram.

	M1	M2	M3	M4	M5	M6	M7	M8	M9	M10	M11	M12	M13	M14	M15	M16	M17	M18	M19	M20
M1	0.000	0.219	0.044	0.074	0.101	0.237	0.268	0.129	2.304	0.264	0.251	0.937	0.587	0.227	0.114	0.293	0.090	0.030	0.134	0.068
M2	0.219	0.000	0.259	0.146	0.157	0.032	0.050	0.090	2.481	0.483	0.470	0.945	0.731	0.408	0.319	0.104	0.130	0.194	0.132	0.160
M3	0.044	0.259	0.000	0.114	0.145	0.278	0.306	0.170	2.286	0.229	0.215	0.962	0.585	0.221	0.103	0.326	0.129	0.065	0.159	0.100
M4	0.074	0.146	0.114	0.000	0.072	0.165	0.194	0.056	2.366	0.338	0.325	0.940	0.635	0.285	0.182	0.222	0.016	0.048	0.079	0.026
M5	0.101	0.157	0.145	0.072	0.000	0.163	0.207	0.082	2.326	0.341	0.332	0.868	0.583	0.251	0.169	0.253	0.074	0.095	0.145	0.096
M6	0.237	0.032	0.278	0.165	0.163	0.000	0.053	0.109	2.478	0.497	0.486	0.920	0.725	0.412	0.330	0.121	0.150	0.213	0.162	0.183
M7	0.268	0.050	0.306	0.194	0.207	0.053	0.000	0.139	2.528	0.531	0.519	0.968	0.777	0.458	0.369	0.071	0.178	0.241	0.168	0.206
M8	0.129	0.090	0.170	0.056	0.082	0.109	0.139	0.000	2.406	0.393	0.380	0.933	0.665	0.327	0.231	0.175	0.041	0.105	0.080	0.075
M9	2.304	2.481	2.286	2.366	2.326	2.478	2.528	2.406	0.000	2.082	2.102	1.958	1.758	2.080	2.189	2.579	2.379	2.333	2.437	2.370
M10	0.264	0.483	0.229	0.338	0.341	0.497	0.531	0.393	2.082	0.000	0.022	0.965	0.464	0.176	0.174	0.555	0.354	0.292	0.388	0.329
M11	0.251	0.470	0.215	0.325	0.332	0.486	0.519	0.380	2.102	0.022	0.000	0.978	0.483	0.184	0.168	0.541	0.341	0.278	0.372	0.315
M12	0.937	0.945	0.962	0.940	0.868	0.920	0.968	0.933	1.958	0.965	0.978	0.000	0.597	0.800	0.883	1.038	0.941	0.950	1.010	0.963
M13	0.587	0.731	0.585	0.635	0.583	0.725	0.777	0.665	1.758	0.464	0.483	0.597	0.000	0.365	0.482	0.833	0.646	0.614	0.713	0.646
M14	0.227	0.408	0.221	0.285	0.251	0.412	0.458	0.327	2.080	0.176	0.184	0.800	0.365	0.000	0.117	0.501	0.299	0.255	0.359	0.290
M15	0.114	0.319	0.103	0.182	0.169	0.330	0.369	0.231	2.189	0.174	0.168	0.883	0.482	0.117	0.000	0.403	0.196	0.144	0.248	0.181
M16	0.293	0.104	0.326	0.222	0.253	0.121	0.071	0.175	2.579	0.555	0.541	1.038	0.833	0.501	0.403	0.000	0.207	0.264	0.171	0.227
M17	0.090	0.130	0.129	0.016	0.074	0.150	0.178	0.041	2.379	0.354	0.341	0.941	0.646	0.299	0.196	0.207	0.000	0.064	0.072	0.035
M18	0.030	0.194	0.065	0.048	0.095	0.213	0.241	0.105	2.333	0.292	0.278	0.950	0.614	0.255	0.144	0.264	0.064	0.000	0.104	0.038
M19	0.134	0.132	0.159	0.079	0.145	0.162	0.168	0.080	2.437	0.388	0.372	1.010	0.713	0.359	0.248	0.171	0.072	0.104	0.000	0.068
M20	0.068	0.160	0.100	0.026	0.096	0.183	0.206	0.075	2.370	0.329	0.315	0.963	0.646	0.290	0.181	0.227	0.035	0.038	0.068	0.000

Table A. 11: Matrix for distance values between indices for all materials used in color index analysis taxonomy attempts for the z'-i' versus H-K color-color diagram.

	M1	M2	M3	M4	M5	M6	M7	M8	M9	M10	M11	M12	M13	M14	M15	M16	M17	M18	M19	M20
M1	0.000	0.135	0.120	0.038	0.071	0.292	0.401	0.165	1.583	1.107	0.258	1.117	0.543	0.295	0.076	0.111	0.025	0.229	0.200	0.071
M2	0.135	0.000	0.252	0.170	0.122	0.161	0.266	0.034	1.602	1.241	0.393	1.066	0.615	0.226	0.165	0.155	0.153	0.095	0.320	0.196
M3	0.120	0.252	0.000	0.083	0.176	0.411	0.518	0.283	1.611	0.990	0.147	1.201	0.538	0.403	0.151	0.156	0.099	0.347	0.092	0.059
M4	0.038	0.170	0.083	0.000	0.105	0.328	0.436	0.201	1.598	1.072	0.225	1.148	0.547	0.331	0.096	0.106	0.017	0.264	0.161	0.034
M5	0.071	0.122	0.176	0.105	0.000	0.257	0.371	0.142	1.523	1.146	0.297	1.046	0.503	0.228	0.045	0.172	0.095	0.202	0.264	0.138
M6	0.292	0.161	0.411	0.328	0.257	0.000	0.116	0.128	1.588	1.399	0.548	0.977	0.684	0.187	0.301	0.308	0.312	0.067	0.481	0.356
M7	0.401	0.266	0.518	0.436	0.371	0.116	0.000	0.236	1.650	1.508	0.659	0.990	0.790	0.278	0.416	0.399	0.419	0.172	0.581	0.461
M8	0.165	0.034	0.283	0.201	0.142	0.128	0.236	0.000	1.592	1.272	0.423	1.042	0.621	0.203	0.186	0.188	0.184	0.064	0.353	0.228
M9	1.583	1.602	1.611	1.598	1.523	1.588	1.650	1.592	0.000	1.935	1.581	0.852	1.089	1.405	1.507	1.693	1.599	1.603	1.687	1.621
M10	1.107	1.241	0.990	1.072	1.146	1.399	1.508	1.272	1.935	0.000	0.851	1.939	1.054	1.343	1.106	1.124	1.089	1.336	0.936	1.047
M11	0.258	0.393	0.147	0.225	0.297	0.548	0.659	0.423	1.581	0.851	0.000	1.252	0.492	0.508	0.258	0.300	0.242	0.486	0.144	0.206
M12	1.117	1.066	1.201	1.148	1.046	0.977	0.990	1.042	0.852	1.939	1.252	0.000	0.885	0.840	1.055	1.206	1.140	1.021	1.293	1.180
M13	0.543	0.615	0.538	0.547	0.503	0.684	0.790	0.621	1.089	1.054	0.492	0.885	0.000	0.516	0.471	0.652	0.553	0.661	0.606	0.562
M14	0.295	0.226	0.403	0.331	0.228	0.187	0.278	0.203	1.405	1.343	0.508	0.840	0.516	0.000	0.255	0.369	0.320	0.199	0.491	0.365
M15	0.076	0.165	0.151	0.096	0.045	0.301	0.416	0.186	1.507	1.106	0.258	1.055	0.471	0.255	0.000	0.187	0.094	0.246	0.242	0.127
M16	0.111	0.155	0.156	0.106	0.172	0.308	0.399	0.188	1.693	1.124	0.300	1.206	0.652	0.369	0.187	0.000	0.098	0.241	0.188	0.103
M17	0.025	0.153	0.099	0.017	0.095	0.312	0.419	0.184	1.599	1.089	0.242	1.140	0.553	0.320	0.094	0.098	0.000	0.247	0.175	0.047
M18	0.229	0.095	0.347	0.264	0.202	0.067	0.172	0.064	1.603	1.336	0.486	1.021	0.661	0.199	0.246	0.241	0.247	0.000	0.414	0.291
M19	0.200	0.320	0.092	0.161	0.264	0.481	0.581	0.353	1.687	0.936	0.144	1.293	0.606	0.491	0.242	0.188	0.175	0.414	0.000	0.129
M20	0.071	0.196	0.059	0.034	0.138	0.356	0.461	0.228	1.621	1.047	0.206	1.180	0.562	0.365	0.127	0.103	0.047	0.291	0.129	0.000

Table A. 12: Matrix for distance values between indices for all materials used in color index analysis taxonomy attempts for the Z-Y versus Z-H color-color diagram.

	M1	M2	M3	M4	M5	M6	M7	M8	M9	M10	M11	M12	M13	M14	M15	M16	M17	M18	M19	M20
M1	0.000	0.230	0.075	0.146	0.145	0.295	0.341	0.209	3.779	0.404	0.230	0.142	0.275	0.155	0.071	0.392	0.159	0.111	0.226	0.149
M2	0.230	0.000	0.228	0.123	0.115	0.081	0.126	0.085	3.985	0.456	0.457	0.158	0.505	0.384	0.294	0.187	0.109	0.166	0.123	0.135
M3	0.075	0.228	0.000	0.114	0.118	0.276	0.318	0.179	3.827	0.330	0.241	0.193	0.295	0.191	0.085	0.361	0.129	0.068	0.184	0.109
M4	0.146	0.123	0.114	0.000	0.010	0.162	0.204	0.066	3.925	0.352	0.354	0.167	0.407	0.295	0.193	0.250	0.015	0.047	0.080	0.015
M5	0.145	0.115	0.118	0.010	0.000	0.158	0.201	0.064	3.924	0.362	0.357	0.158	0.409	0.296	0.195	0.248	0.014	0.052	0.084	0.025
M6	0.295	0.081	0.276	0.162	0.158	0.000	0.046	0.099	4.062	0.443	0.515	0.238	0.567	0.450	0.352	0.106	0.147	0.209	0.116	0.170
M7	0.341	0.126	0.318	0.204	0.201	0.046	0.000	0.139	4.109	0.456	0.558	0.283	0.610	0.495	0.396	0.062	0.189	0.251	0.146	0.210
M8	0.209	0.085	0.179	0.066	0.064	0.099	0.139	0.000	3.987	0.371	0.420	0.194	0.473	0.360	0.259	0.184	0.051	0.112	0.040	0.071
M9	3.779	3.985	3.827	3.925	3.924	4.062	4.109	3.987	0.000	3.998	3.605	3.830	3.545	3.635	3.742	4.166	3.938	3.886	4.004	3.927
M10	0.404	0.456	0.330	0.352	0.362	0.443	0.456	0.371	3.998	0.000	0.431	0.507	0.487	0.455	0.376	0.454	0.359	0.335	0.335	0.337
M11	0.230	0.457	0.241	0.354	0.357	0.515	0.558	0.420	3.605	0.431	0.000	0.360	0.060	0.097	0.164	0.602	0.369	0.308	0.423	0.350
M12	0.142	0.158	0.193	0.167	0.158	0.238	0.283	0.194	3.830	0.507	0.360	0.000	0.396	0.270	0.213	0.344	0.167	0.172	0.230	0.180
M13	0.275	0.505	0.295	0.407	0.409	0.567	0.610	0.473	3.545	0.487	0.060	0.396	0.000	0.126	0.214	0.656	0.422	0.362	0.479	0.404
M14	0.155	0.384	0.191	0.295	0.296	0.450	0.495	0.360	3.635	0.455	0.097	0.270	0.126	0.000	0.107	0.544	0.309	0.253	0.372	0.295
M15	0.071	0.294	0.085	0.193	0.195	0.352	0.396	0.259	3.742	0.376	0.164	0.213	0.214	0.107	0.000	0.442	0.208	0.149	0.267	0.191
M16	0.392	0.187	0.361	0.250	0.248	0.106	0.062	0.184	4.166	0.454	0.602	0.344	0.656	0.544	0.442	0.000	0.235	0.294	0.180	0.252
M17	0.159	0.109	0.129	0.015	0.014	0.147	0.189	0.051	3.938	0.359	0.369	0.167	0.422	0.309	0.208	0.235	0.000	0.062	0.070	0.026
M18	0.111	0.166	0.068	0.047	0.052	0.209	0.251	0.112	3.886	0.335	0.308	0.172	0.362	0.253	0.149	0.294	0.062	0.000	0.119	0.042
M19	0.226	0.123	0.184	0.080	0.084	0.116	0.146	0.040	4.004	0.335	0.423	0.230	0.479	0.372	0.267	0.180	0.070	0.119	0.000	0.078
M20	0.149	0.135	0.109	0.015	0.025	0.170	0.210	0.071	3.927	0.337	0.350	0.180	0.404	0.295	0.191	0.252	0.026	0.042	0.078	0.000

Table A. 13: Matrix for distance values between indices for all materials used in color index analysis taxonomy attempts for the z'-Y versus z'-H color-color diagram.

	M1	M2	M3	M4	M5	M6	M7	M8	M9	M10	M11	M12	M13	M14	M15	M16	M17	M18	M19	M20
M1	0.000	0.218	0.048	0.079	0.087	0.238	0.268	0.134	1.753	0.304	0.249	0.171	0.274	0.136	0.086	0.278	0.093	0.039	0.116	0.068
M2	0.218	0.000	0.259	0.147	0.137	0.029	0.056	0.093	1.965	0.500	0.467	0.065	0.492	0.354	0.303	0.075	0.132	0.195	0.124	0.162
M3	0.048	0.259	0.000	0.114	0.123	0.277	0.306	0.170	1.722	0.256	0.208	0.216	0.235	0.103	0.047	0.314	0.129	0.065	0.146	0.099
M4	0.079	0.147	0.114	0.000	0.010	0.164	0.192	0.056	1.831	0.356	0.322	0.114	0.348	0.213	0.159	0.201	0.015	0.048	0.038	0.016
M5	0.087	0.137	0.123	0.010	0.000	0.154	0.182	0.047	1.840	0.366	0.332	0.104	0.358	0.222	0.169	0.192	0.006	0.058	0.033	0.026
M6	0.238	0.029	0.277	0.164	0.154	0.000	0.030	0.108	1.988	0.512	0.485	0.093	0.511	0.375	0.322	0.047	0.148	0.212	0.136	0.178
M7	0.268	0.056	0.306	0.192	0.182	0.030	0.000	0.136	2.018	0.536	0.514	0.121	0.540	0.404	0.351	0.022	0.177	0.240	0.162	0.206
M8	0.134	0.093	0.170	0.056	0.047	0.108	0.136	0.000	1.887	0.407	0.378	0.078	0.405	0.269	0.216	0.145	0.041	0.105	0.032	0.071
M9	1.753	1.965	1.722	1.831	1.840	1.988	2.018	1.887	0.000	1.570	1.520	1.905	1.491	1.619	1.675	2.031	1.846	1.785	1.867	1.819
M10	0.304	0.500	0.256	0.356	0.366	0.512	0.536	0.407	1.570	0.000	0.153	0.468	0.169	0.215	0.230	0.539	0.370	0.311	0.377	0.340
M11	0.249	0.467	0.208	0.322	0.332	0.485	0.514	0.378	1.520	0.153	0.000	0.418	0.029	0.115	0.163	0.523	0.337	0.274	0.354	0.308
M12	0.171	0.065	0.216	0.114	0.104	0.093	0.121	0.078	1.905	0.468	0.418	0.000	0.442	0.304	0.256	0.140	0.100	0.156	0.107	0.129
M13	0.274	0.492	0.235	0.348	0.358	0.511	0.540	0.405	1.491	0.169	0.029	0.442	0.000	0.138	0.189	0.549	0.363	0.300	0.381	0.334
M14	0.136	0.354	0.103	0.213	0.222	0.375	0.404	0.269	1.619	0.215	0.115	0.304	0.138	0.000	0.056	0.414	0.228	0.166	0.248	0.200
M15	0.086	0.303	0.047	0.159	0.169	0.322	0.351	0.216	1.675	0.230	0.163	0.256	0.189	0.056	0.000	0.361	0.175	0.112	0.193	0.146
M16	0.278	0.075	0.314	0.201	0.192	0.047	0.022	0.145	2.031	0.539	0.523	0.140	0.549	0.414	0.361	0.000	0.186	0.249	0.169	0.215
M17	0.093	0.132	0.129	0.015	0.006	0.148	0.177	0.041	1.846	0.370	0.337	0.100	0.363	0.228	0.175	0.186	0.000	0.064	0.028	0.031
M18	0.039	0.195	0.065	0.048	0.058	0.212	0.240	0.105	1.785	0.311	0.274	0.156	0.300	0.166	0.112	0.249	0.064	0.000	0.082	0.034
M19	0.116	0.124	0.146	0.038	0.033	0.136	0.162	0.032	1.867	0.377	0.354	0.107	0.381	0.248	0.193	0.169	0.028	0.082	0.000	0.048
M20	0.068	0.162	0.099	0.016	0.026	0.178	0.206	0.071	1.819	0.340	0.308	0.129	0.334	0.200	0.146	0.215	0.031	0.034	0.048	0.000

Table A. 14: Matrix for distance values between indices for all materials used in color index analysis taxonomy attempts for the I-Y versus B-I color-color diagram.

	M1	M2	M3	M4	M5	M6	M7	M8	M9	M10	M11	M12	M13	M14	M15	M16	M17	M18	M19	M20
M1	0.000	0.069	0.955	0.138	2.104	0.827	0.394	0.347	1.453	0.320	0.025	1.420	1.139	0.740	1.244	0.774	0.292	0.111	0.231	0.046
M2	0.069	0.000	0.887	0.069	2.037	0.760	0.325	0.278	1.405	0.252	0.095	1.357	1.075	0.675	1.177	0.705	0.223	0.042	0.291	0.073
M3	0.955	0.887	0.000	0.820	1.150	0.127	0.564	0.609	0.850	0.675	0.980	0.531	0.258	0.241	0.293	0.199	0.664	0.849	1.171	0.953
M4	0.138	0.069	0.820	0.000	1.970	0.693	0.257	0.211	1.360	0.186	0.164	1.295	1.012	0.611	1.110	0.637	0.156	0.029	0.354	0.133
M5	2.104	2.037	1.150	1.970	0.000	1.277	1.715	1.759	1.171	1.821	2.129	0.760	0.991	1.370	0.861	1.340	1.815	1.999	2.321	2.103
M6	0.827	0.760	0.127	0.693	1.277	0.000	0.437	0.482	0.896	0.550	0.853	0.639	0.354	0.136	0.419	0.092	0.537	0.722	1.045	0.826
M7	0.394	0.325	0.564	0.257	1.715	0.437	0.000	0.048	1.178	0.133	0.419	1.054	0.767	0.368	0.856	0.380	0.102	0.286	0.607	0.389
M8	0.347	0.278	0.609	0.211	1.759	0.482	0.048	0.000	1.200	0.116	0.372	1.092	0.807	0.407	0.900	0.427	0.055	0.240	0.563	0.344
M9	1.453	1.405	0.850	1.360	1.171	0.896	1.178	1.200	0.000	1.310	1.471	0.533	0.621	0.856	0.757	0.986	1.238	1.384	1.680	1.476
M10	0.320	0.252	0.675	0.186	1.821	0.550	0.133	0.116	1.310	0.000	0.344	1.178	0.891	0.496	0.968	0.481	0.105	0.210	0.507	0.301
M11	0.025	0.095	0.980	0.164	2.129	0.853	0.419	0.372	1.471	0.344	0.000	1.443	1.163	0.764	1.269	0.799	0.317	0.136	0.210	0.057
M12	1.420	1.357	0.531	1.295	0.760	0.639	1.054	1.092	0.533	1.178	1.443	0.000	0.287	0.686	0.292	0.725	1.145	1.324	1.648	1.428
M13	1.139	1.075	0.258	1.012	0.991	0.354	0.767	0.807	0.621	0.891	1.163	0.287	0.000	0.401	0.185	0.443	0.860	1.041	1.365	1.145
M14	0.740	0.675	0.241	0.611	1.370	0.136	0.368	0.407	0.856	0.496	0.764	0.686	0.401	0.000	0.511	0.175	0.459	0.640	0.965	0.745
M15	1.244	1.177	0.293	1.110	0.861	0.419	0.856	0.900	0.757	0.968	1.269	0.292	0.185	0.511	0.000	0.490	0.955	1.139	1.463	1.244
M16	0.774	0.705	0.199	0.637	1.340	0.092	0.380	0.427	0.986	0.481	0.799	0.725	0.443	0.175	0.490	0.000	0.482	0.665	0.984	0.768
M17	0.292	0.223	0.664	0.156	1.815	0.537	0.102	0.055	1.238	0.105	0.317	1.145	0.860	0.459	0.955	0.482	0.000	0.185	0.508	0.289
M18	0.111	0.042	0.849	0.029	1.999	0.722	0.286	0.240	1.384	0.210	0.136	1.324	1.041	0.640	1.139	0.665	0.185	0.000	0.325	0.104
M19	0.231	0.291	1.171	0.354	2.321	1.045	0.607	0.563	1.680	0.507	0.210	1.648	1.365	0.965	1.463	0.984	0.508	0.325	0.000	0.220
M20	0.046	0.073	0.953	0.133	2.103	0.826	0.389	0.344	1.476	0.301	0.057	1.428	1.145	0.745	1.244	0.768	0.289	0.104	0.220	0.000

Table A. 15: Matrix for distance values between indices for all materials used in color index analysis taxonomy attempts for the i'-z' versus g'-i' color-color diagram.

	M1	M2	M3	M4	M5	M6	M7	M8	M9	M10	M11	M12	M13	M14	M15	M16	M17	M18	M19	M20
M1	0.000	0.083	1.062	0.141	2.872	0.826	0.282	0.206	1.580	0.299	0.056	1.112	0.789	0.631	1.197	0.920	0.291	0.119	0.166	0.049
M2	0.083	0.000	0.982	0.060	2.792	0.745	0.199	0.126	1.604	0.227	0.136	1.088	0.746	0.562	1.119	0.838	0.210	0.037	0.232	0.048
M3	1.062	0.982	0.000	0.922	1.811	0.238	0.784	0.856	1.919	0.772	1.105	1.038	0.712	0.499	0.162	0.176	0.772	0.944	1.206	1.028
M4	0.141	0.060	0.922	0.000	2.732	0.686	0.142	0.066	1.600	0.168	0.189	1.052	0.700	0.504	1.059	0.780	0.151	0.022	0.291	0.107
M5	2.872	2.792	1.811	2.732	0.000	2.047	2.594	2.666	3.251	2.578	2.913	2.410	2.324	2.271	1.676	1.965	2.582	2.755	3.017	2.838
M6	0.826	0.745	0.238	0.686	2.047	0.000	0.548	0.620	1.779	0.535	0.868	0.940	0.564	0.283	0.376	0.145	0.535	0.708	0.972	0.792
M7	0.282	0.199	0.784	0.142	2.594	0.548	0.000	0.079	1.644	0.098	0.330	1.022	0.643	0.394	0.923	0.638	0.027	0.163	0.423	0.244
M8	0.206	0.126	0.856	0.066	2.666	0.620	0.079	0.000	1.603	0.110	0.252	1.021	0.656	0.442	0.993	0.715	0.085	0.088	0.356	0.173
M9	1.580	1.604	1.919	1.600	3.251	1.779	1.644	1.603	0.000	1.552	1.544	0.906	1.216	1.523	1.922	1.922	1.622	1.601	1.672	1.615
M10	0.299	0.227	0.772	0.168	2.578	0.535	0.098	0.110	1.552	0.000	0.336	0.926	0.552	0.335	0.902	0.642	0.072	0.190	0.458	0.274
M11	0.056	0.136	1.105	0.189	2.913	0.868	0.330	0.252	1.544	0.336	0.000	1.106	0.798	0.662	1.237	0.967	0.337	0.168	0.158	0.105
M12	1.112	1.088	1.038	1.052	2.410	0.940	1.022	1.021	0.906	0.926	1.106	0.000	0.404	0.740	1.022	1.073	0.995	1.066	1.265	1.122
M13	0.789	0.746	0.712	0.700	2.324	0.564	0.643	0.656	1.216	0.552	0.798	0.404	0.000	0.338	0.747	0.707	0.615	0.717	0.953	0.787
M14	0.631	0.562	0.499	0.504	2.271	0.283	0.394	0.442	1.523	0.335	0.662	0.740	0.338	0.000	0.600	0.426	0.371	0.526	0.793	0.609
M15	1.197	1.119	0.162	1.059	1.676	0.376	0.923	0.993	1.922	0.902	1.237	1.022	0.747	0.600	0.000	0.338	0.909	1.081	1.347	1.165
M16	0.920	0.838	0.176	0.780	1.965	0.145	0.638	0.715	1.922	0.642	0.967	1.073	0.707	0.426	0.338	0.000	0.630	0.801	1.056	0.882
M17	0.291	0.210	0.772	0.151	2.582	0.535	0.027	0.085	1.622	0.072	0.337	0.995	0.615	0.371	0.909	0.630	0.000	0.173	0.438	0.256
M18	0.119	0.037	0.944	0.022	2.755	0.708	0.163	0.088	1.601	0.190	0.168	1.066	0.717	0.526	1.081	0.801	0.173	0.000	0.269	0.085
M19	0.166	0.232	1.206	0.291	3.017	0.972	0.423	0.356	1.672	0.458	0.158	1.265	0.953	0.793	1.347	1.056	0.438	0.269	0.000	0.184
M20	0.049	0.048	1.028	0.107	2.838	0.792	0.244	0.173	1.615	0.274	0.105	1.122	0.787	0.609	1.165	0.882	0.256	0.085	0.184	0.000

Table A. 16: Matrix for distance values between indices for all materials used in color index analysis taxonomy attempts for the V2-IR1 versus V2-IR13 color-color diagram.

	M1	M2	M3	M4	M5	M6	M7	M8	M9	M10	M11	M12	M13	M14	M15	M16	M17	M18	M19	M20
M1	0.000	0.315	1.377	0.203	2.794	0.735	0.897	0.352	3.092	1.789	0.576	1.399	2.039	0.863	1.794	0.750	0.354	0.315	0.107	0.092
M2	0.315	0.000	1.584	0.412	2.965	0.809	0.586	0.212	3.400	2.065	0.883	1.469	2.263	1.030	1.987	0.866	0.532	0.104	0.299	0.342
M3	1.377	1.584	0.000	1.194	1.433	0.875	1.967	1.419	2.230	0.737	0.981	0.714	0.683	0.568	0.422	0.772	1.055	1.501	1.480	1.296
M4	0.203	0.412	1.194	0.000	2.601	0.537	0.936	0.328	3.008	1.654	0.508	1.198	1.865	0.664	1.606	0.547	0.151	0.356	0.310	0.112
M5	2.794	2.965	1.433	2.601	0.000	2.174	3.238	2.776	2.347	1.497	2.408	1.611	0.906	1.939	1.011	2.102	2.454	2.872	2.900	2.709
M6	0.735	0.809	0.875	0.537	2.174	0.000	1.096	0.608	2.985	1.517	0.776	0.669	1.552	0.326	1.233	0.115	0.399	0.710	0.839	0.644
M7	0.897	0.586	1.967	0.936	3.238	1.096	0.000	0.611	3.941	2.546	1.440	1.641	2.647	1.401	2.328	1.195	1.003	0.590	0.883	0.903
M8	0.352	0.212	1.419	0.328	2.776	0.608	0.611	0.000	3.329	1.948	0.835	1.260	2.102	0.855	1.811	0.675	0.397	0.109	0.398	0.320
M9	3.092	3.400	2.230	3.008	2.347	2.985	3.941	3.329	0.000	1.495	2.517	2.930	1.828	2.665	2.155	2.870	2.940	3.363	3.151	3.059
M10	1.789	2.065	0.737	1.654	1.497	1.517	2.546	1.948	1.495	0.000	1.239	1.447	0.609	1.192	0.773	1.403	1.552	2.005	1.872	1.731
M11	0.576	0.883	0.981	0.508	2.408	0.776	1.440	0.835	2.517	1.239	0.000	1.287	1.575	0.658	1.398	0.705	0.492	0.852	0.645	0.543
M12	1.399	1.469	0.714	1.198	1.611	0.669	1.641	1.260	2.930	1.447	1.287	0.000	1.214	0.628	0.847	0.654	1.051	1.367	1.505	1.308
M13	2.039	2.263	0.683	1.865	0.906	1.552	2.647	2.102	1.828	0.609	1.575	1.214	0.000	1.251	0.368	1.453	1.731	2.182	2.138	1.963
M14	0.863	1.030	0.568	0.664	1.939	0.326	1.401	0.855	2.665	1.192	0.658	0.628	1.251	0.000	0.957	0.213	0.516	0.942	0.970	0.774
M15	1.794	1.987	0.422	1.606	1.011	1.233	2.328	1.811	2.155	0.773	1.398	0.847	0.368	0.957	0.000	1.143	1.464	1.900	1.898	1.711
M16	0.750	0.866	0.772	0.547	2.102	0.115	1.195	0.675	2.870	1.403	0.705	0.654	1.453	0.213	1.143	0.000	0.398	0.770	0.856	0.658
M17	0.354	0.532	1.055	0.151	2.454	0.399	1.003	0.397	2.940	1.552	0.492	1.051	1.731	0.516	1.464	0.398	0.000	0.458	0.461	0.262
M18	0.315	0.104	1.501	0.356	2.872	0.710	0.590	0.109	3.363	2.005	0.852	1.367	2.182	0.942	1.900	0.770	0.458	0.000	0.333	0.313
M19	0.107	0.299	1.480	0.310	2.900	0.839	0.883	0.398	3.151	1.872	0.645	1.505	2.138	0.970	1.898	0.856	0.461	0.333	0.000	0.198
M20	0.092	0.342	1.296	0.112	2.709	0.644	0.903	0.320	3.059	1.731	0.543	1.308	1.963	0.774	1.711	0.658	0.262	0.313	0.198	0.000

Table A. 17: Matrix for distance values between indices for all materials used in color index analysis taxonomy attempts for the V2-IR5 versus V2-IR13 color-color diagram.

	M1	M2	M3	M4	M5	M6	M7	M8	M9	M10	M11	M12	M13	M14	M15	M16	M17	M18	M19	M20
M1	0.000	0.309	1.333	0.097	2.710	0.596	0.852	0.256	4.505	1.690	0.582	1.619	2.111	0.961	1.800	0.482	0.231	0.271	0.329	0.081
M2	0.309	0.000	1.580	0.396	2.928	0.744	0.547	0.128	4.717	1.999	0.887	1.724	2.357	1.148	2.028	0.709	0.497	0.042	0.416	0.351
M3	1.333	1.580	0.000	1.238	1.396	0.896	2.004	1.462	3.186	1.119	0.880	0.918	0.778	0.527	0.484	0.872	1.103	1.538	1.596	1.357
M4	0.097	0.396	1.238	0.000	2.618	0.531	0.931	0.324	4.412	1.607	0.491	1.553	2.015	0.878	1.706	0.396	0.141	0.356	0.396	0.131
M5	2.710	2.928	1.396	2.618	0.000	2.192	3.273	2.803	1.794	2.023	2.272	1.483	0.682	1.783	0.914	2.232	2.479	2.888	2.988	2.742
M6	0.596	0.744	0.896	0.531	2.192	0.000	1.110	0.616	3.978	1.636	0.619	1.023	1.652	0.410	1.306	0.216	0.404	0.705	0.923	0.658
M7	0.852	0.547	2.004	0.931	3.273	1.110	0.000	0.610	5.037	2.538	1.417	1.921	2.760	1.511	2.410	1.160	1.004	0.582	0.908	0.898
M8	0.256	0.128	1.462	0.324	2.803	0.616	0.610	0.000	4.591	1.928	0.807	1.598	2.236	1.022	1.905	0.591	0.398	0.093	0.468	0.322
M9	4.505	4.717	3.186	4.412	1.794	3.978	5.037	4.591	0.000	3.615	4.057	3.156	2.434	3.569	2.708	4.026	4.273	4.678	4.781	4.536
M10	1.690	1.999	1.119	1.607	2.023	1.636	2.538	1.928	3.615	0.000	1.125	2.036	1.369	1.473	1.372	1.467	1.543	1.961	1.765	1.656
M11	0.582	0.887	0.880	0.491	2.272	0.619	1.417	0.807	4.057	1.125	0.000	1.468	1.627	0.728	1.364	0.407	0.419	0.847	0.756	0.567
M12	1.619	1.724	0.918	1.553	1.483	1.023	1.921	1.598	3.156	2.036	1.468	0.000	1.231	0.740	0.895	1.182	1.420	1.692	1.946	1.681
M13	2.111	2.357	0.778	2.015	0.682	1.652	2.760	2.236	2.434	1.369	1.627	1.231	0.000	1.251	0.368	1.648	1.881	2.315	2.365	2.132
M14	0.961	1.148	0.527	0.878	1.783	0.410	1.511	1.022	3.569	1.473	0.728	0.740	1.251	0.000	0.899	0.483	0.737	1.109	1.271	1.008
M15	1.800	2.028	0.484	1.706	0.914	1.306	2.410	1.905	2.708	1.372	1.364	0.895	0.368	0.899	0.000	1.325	1.568	1.987	2.074	1.829
M16	0.482	0.709	0.872	0.396	2.232	0.216	1.160	0.591	4.026	1.467	0.407	1.182	1.648	0.483	1.325	0.000	0.254	0.667	0.789	0.526
M17	0.231	0.497	1.103	0.141	2.479	0.404	1.004	0.398	4.273	1.543	0.419	1.420	1.881	0.737	1.568	0.254	0.000	0.454	0.535	0.271
M18	0.271	0.042	1.538	0.356	2.888	0.705	0.582	0.093	4.678	1.961	0.847	1.692	2.315	1.109	1.987	0.667	0.454	0.000	0.409	0.318
M19	0.329	0.416	1.596	0.396	2.988	0.923	0.908	0.468	4.781	1.765	0.756	1.946	2.365	1.271	2.074	0.789	0.535	0.409	0.000	0.265
M20	0.081	0.351	1.357	0.131	2.742	0.658	0.898	0.322	4.536	1.656	0.567	1.681	2.132	1.008	1.829	0.526	0.271	0.318	0.265	0.000

Table A. 18: Matrix for distance values between indices for all materials used in color index analysis taxonomy attempts for the V1-IR1 versus V1-IR3 color-color diagram.

	M1	M2	M3	M4	M5	M6	M7	M8	M9	M10	M11	M12	M13	M14	M15	M16	M17	M18	M19	M20
M1	0.000	0.112	1.663	0.220	4.474	1.649	0.463	0.358	2.418	0.599	0.038	2.276	1.579	1.208	1.822	1.597	0.453	0.184	0.367	0.085
M2	0.112	0.000	1.551	0.112	4.363	1.538	0.351	0.246	2.352	0.497	0.141	2.167	1.469	1.098	1.711	1.485	0.340	0.080	0.469	0.127
M3	1.663	1.551	0.000	1.453	2.812	0.014	1.207	1.314	1.767	1.175	1.692	0.655	0.121	0.467	0.168	0.099	1.215	1.493	2.008	1.657
M4	0.220	0.112	1.453	0.000	4.265	1.439	0.247	0.140	2.328	0.387	0.243	2.076	1.374	1.005	1.614	1.385	0.238	0.040	0.556	0.205
M5	4.474	4.363	2.812	4.265	0.000	2.826	4.019	4.126	3.261	3.970	4.503	2.216	2.895	3.267	2.652	2.883	4.027	4.305	4.820	4.469
M6	1.649	1.538	0.014	1.439	2.826	0.000	1.194	1.300	1.764	1.162	1.678	0.667	0.109	0.453	0.180	0.092	1.201	1.479	1.994	1.644
M7	0.463	0.351	1.207	0.247	4.019	1.194	0.000	0.107	2.192	0.228	0.489	1.834	1.130	0.765	1.369	1.138	0.019	0.286	0.801	0.450
M8	0.358	0.246	1.314	0.140	4.126	1.300	0.107	0.000	2.248	0.282	0.382	1.939	1.235	0.868	1.475	1.245	0.099	0.180	0.695	0.344
M9	2.418	2.352	1.767	2.328	3.261	1.764	2.192	2.248	0.000	2.345	2.455	1.617	1.684	1.733	1.719	1.840	2.182	2.355	2.754	2.475
M10	0.599	0.497	1.175	0.387	3.970	1.162	0.228	0.282	2.345	0.000	0.613	1.824	1.117	0.780	1.342	1.093	0.247	0.418	0.878	0.556
M11	0.038	0.141	1.692	0.243	4.503	1.678	0.489	0.382	2.455	0.613	0.000	2.308	1.609	1.239	1.852	1.625	0.479	0.204	0.331	0.070
M12	2.276	2.167	0.655	2.076	2.216	0.667	1.834	1.939	1.617	1.824	2.308	0.000	0.708	1.070	0.488	0.747	1.839	2.115	2.632	2.280
M13	1.579	1.469	0.121	1.374	2.895	0.109	1.130	1.235	1.684	1.117	1.609	0.708	0.000	0.372	0.246	0.158	1.136	1.414	1.930	1.578
M14	1.208	1.098	0.467	1.005	3.267	0.453	0.765	0.868	1.733	0.780	1.239	1.070	0.372	0.000	0.617	0.424	0.769	1.045	1.562	1.210
M15	1.822	1.711	0.168	1.614	2.652	0.180	1.369	1.475	1.719	1.342	1.852	0.488	0.246	0.617	0.000	0.260	1.376	1.654	2.170	1.819
M16	1.597	1.485	0.099	1.385	2.883	0.092	1.138	1.245	1.840	1.093	1.625	0.747	0.158	0.424	0.260	0.000	1.147	1.424	1.937	1.588
M17	0.453	0.340	1.215	0.238	4.027	1.201	0.019	0.099	2.182	0.247	0.479	1.839	1.136	0.769	1.376	1.147	0.000	0.278	0.794	0.443
M18	0.184	0.080	1.493	0.040	4.305	1.479	0.286	0.180	2.355	0.418	0.204	2.115	1.414	1.045	1.654	1.424	0.278	0.000	0.517	0.165
M19	0.367	0.469	2.008	0.556	4.820	1.994	0.801	0.695	2.754	0.878	0.331	2.632	1.930	1.562	2.170	1.937	0.794	0.517	0.000	0.352
M20	0.085	0.127	1.657	0.205	4.469	1.644	0.450	0.344	2.475	0.556	0.070	2.280	1.578	1.210	1.819	1.588	0.443	0.165	0.352	0.000

Table A. 19: Matrix for distance values between indices for all materials used in color index analysis taxonomy attempts for the g'-z' versus g'-Y color-color diagram.

	M1	M2	M3	M4	M5	M6	M7	M8	M9	M10	M11	M12	M13	M14	M15	M16	M17	M18	M19	M20
M1	0.000	0.078	1.460	0.159	4.124	1.153	0.310	0.254	2.621	0.397	0.014	2.207	1.580	1.123	1.791	1.093	0.369	0.123	0.362	0.035
M2	0.078	0.000	1.382	0.082	4.046	1.075	0.232	0.176	2.545	0.322	0.090	2.129	1.502	1.045	1.713	1.015	0.291	0.046	0.439	0.104
M3	1.460	1.382	0.000	1.302	2.664	0.307	1.151	1.207	1.198	1.083	1.472	0.748	0.122	0.338	0.331	0.369	1.092	1.338	1.820	1.484
M4	0.159	0.082	1.302	0.000	3.966	0.995	0.151	0.095	2.468	0.241	0.171	2.049	1.422	0.965	1.633	0.934	0.210	0.036	0.518	0.183
M5	4.124	4.046	2.664	3.966	0.000	2.971	3.815	3.871	1.575	3.744	4.136	1.918	2.544	3.001	2.333	3.032	3.756	4.002	4.484	4.148
M6	1.153	1.075	0.307	0.995	2.971	0.000	0.844	0.901	1.493	0.778	1.166	1.055	0.428	0.044	0.638	0.065	0.785	1.031	1.513	1.178
M7	0.310	0.232	1.151	0.151	3.815	0.844	0.000	0.057	2.320	0.112	0.322	1.898	1.271	0.815	1.482	0.783	0.059	0.188	0.669	0.334
M8	0.254	0.176	1.207	0.095	3.871	0.901	0.057	0.000	2.375	0.156	0.266	1.955	1.328	0.871	1.538	0.840	0.116	0.131	0.612	0.277
M9	2.621	2.545	1.198	2.468	1.575	1.493	2.320	2.375	0.000	2.266	2.634	0.517	1.077	1.515	0.886	1.558	2.261	2.504	2.983	2.649
M10	0.397	0.322	1.083	0.241	3.744	0.778	0.112	0.156	2.266	0.000	0.408	1.831	1.205	0.753	1.414	0.715	0.094	0.275	0.744	0.415
M11	0.014	0.090	1.472	0.171	4.136	1.166	0.322	0.266	2.634	0.408	0.000	2.219	1.592	1.135	1.803	1.105	0.381	0.135	0.349	0.023
M12	2.207	2.129	0.748	2.049	1.918	1.055	1.898	1.955	0.517	1.831	2.219	0.000	0.627	1.084	0.417	1.117	1.839	2.086	2.567	2.232
M13	1.580	1.502	0.122	1.422	2.544	0.428	1.271	1.328	1.077	1.205	1.592	0.627	0.000	0.457	0.211	0.490	1.212	1.458	1.940	1.605
M14	1.123	1.045	0.338	0.965	3.001	0.044	0.815	0.871	1.515	0.753	1.135	1.084	0.457	0.000	0.668	0.062	0.755	1.002	1.483	1.148
M15	1.791	1.713	0.331	1.633	2.333	0.638	1.482	1.538	0.886	1.414	1.803	0.417	0.211	0.668	0.000	0.700	1.423	1.669	2.151	1.816
M16	1.093	1.015	0.369	0.934	3.032	0.065	0.783	0.840	1.558	0.715	1.105	1.117	0.490	0.062	0.700	0.000	0.724	0.971	1.452	1.117
M17	0.369	0.291	1.092	0.210	3.756	0.785	0.059	0.116	2.261	0.094	0.381	1.839	1.212	0.755	1.423	0.724	0.000	0.246	0.728	0.393
M18	0.123	0.046	1.338	0.036	4.002	1.031	0.188	0.131	2.504	0.275	0.135	2.086	1.458	1.002	1.669	0.971	0.246	0.000	0.482	0.146
M19	0.362	0.439	1.820	0.518	4.484	1.513	0.669	0.612	2.983	0.744	0.349	2.567	1.940	1.483	2.151	1.452	0.728	0.482	0.000	0.335
M20	0.035	0.104	1.484	0.183	4.148	1.178	0.334	0.277	2.649	0.415	0.023	2.232	1.605	1.148	1.816	1.117	0.393	0.146	0.335	0.000

Table A. 20: Matrix for distance values between indices for all materials used in color index analysis taxonomy attempts for the IR8-IR13 versus V1-IR4 color-color diagram.

	M1	M2	M3	M4	M5	M6	M7	M8	M9	M10	M11	M12	M13	M14	M15	M16	M17	M18	M19	M20
M1	0.000	0.148	1.180	0.088	3.101	1.098	0.692	0.334	3.181	1.108	0.298	1.891	1.176	0.968	1.285	0.971	0.242	0.345	0.438	0.113
M2	0.148	0.000	1.145	0.173	3.042	1.022	0.545	0.187	3.117	1.244	0.435	1.777	1.145	0.870	1.230	0.921	0.229	0.206	0.569	0.258
M3	1.180	1.145	0.000	1.097	1.934	0.345	1.273	1.093	2.026	1.515	1.162	1.127	0.037	0.551	0.187	0.242	0.940	1.217	1.538	1.252
M4	0.088	0.173	1.097	0.000	3.021	1.028	0.711	0.338	3.103	1.073	0.267	1.838	1.092	0.909	1.206	0.892	0.165	0.379	0.489	0.165
M5	3.101	3.042	1.934	3.021	0.000	2.027	2.987	2.947	0.159	3.290	3.095	1.656	1.947	2.220	1.816	2.129	2.859	3.064	3.473	3.181
M6	1.098	1.022	0.345	1.028	2.027	0.000	1.013	0.920	2.096	1.687	1.168	0.901	0.377	0.231	0.274	0.226	0.863	1.038	1.509	1.192
M7	0.692	0.545	1.273	0.711	2.987	1.013	0.000	0.377	3.036	1.783	0.978	1.508	1.289	0.789	1.280	1.033	0.673	0.351	1.064	0.793
M8	0.334	0.187	1.093	0.338	2.947	0.920	0.377	0.000	3.014	1.406	0.605	1.620	1.099	0.741	1.152	0.856	0.304	0.124	0.753	0.445
M9	3.181	3.117	2.026	3.103	0.159	2.096	3.036	3.014	0.000	3.411	3.188	1.658	2.041	2.280	1.898	2.212	2.940	3.129	3.562	3.264
M10	1.108	1.244	1.515	1.073	3.290	1.687	1.783	1.406	3.411	0.000	0.810	2.588	1.485	1.706	1.698	1.465	1.128	1.449	0.938	1.030
M11	0.298	0.435	1.162	0.267	3.095	1.168	0.978	0.605	3.188	0.810	0.000	2.027	1.148	1.092	1.300	0.994	0.367	0.639	0.387	0.238
M12	1.891	1.777	1.127	1.838	1.656	0.901	1.508	1.620	1.658	2.588	2.027	0.000	1.162	0.935	0.943	1.123	1.682	1.710	2.326	1.998
M13	1.176	1.145	0.037	1.092	1.947	0.377	1.289	1.099	2.041	1.485	1.148	1.162	0.000	0.578	0.222	0.256	0.937	1.223	1.527	1.245
M14	0.968	0.870	0.551	0.909	2.220	0.231	0.789	0.741	2.280	1.706	1.092	0.935	0.578	0.000	0.504	0.353	0.749	0.852	1.398	1.072
M15	1.285	1.230	0.187	1.206	1.816	0.274	1.280	1.152	1.898	1.698	1.300	0.943	0.222	0.504	0.000	0.314	1.043	1.275	1.667	1.366
M16	0.971	0.921	0.242	0.892	2.129	0.226	1.033	0.856	2.212	1.465	0.994	1.123	0.256	0.353	0.314	0.000	0.729	0.980	1.355	1.053
M17	0.242	0.229	0.940	0.165	2.859	0.863	0.673	0.304	2.940	1.128	0.367	1.682	0.937	0.749	1.043	0.729	0.000	0.393	0.651	0.329
M18	0.345	0.206	1.217	0.379	3.064	1.038	0.351	0.124	3.129	1.449	0.639	1.710	1.223	0.852	1.275	0.980	0.393	0.000	0.719	0.443
M19	0.438	0.569	1.538	0.489	3.473	1.509	1.064	0.753	3.562	0.938	0.387	2.326	1.527	1.398	1.667	1.355	0.651	0.719	0.000	0.328
M20	0.113	0.258	1.252	0.165	3.181	1.192	0.793	0.445	3.264	1.030	0.238	1.998	1.245	1.072	1.366	1.053	0.329	0.443	0.328	0.000

Table A. 21: Matrix for distance values between indices for all materials used in color index analysis taxonomy attempts for the V1-IR16 versus IR4-IR16 color-color diagram.

	M1	M2	M3	M4	M5	M6	M7	M8	M9	M10	M11	M12	M13	M14	M15	M16	M17	M18	M19	M20
M1	0.000	0.393	1.317	0.060	2.916	0.765	1.384	0.588	3.023	2.305	0.739	1.379	1.601	0.638	1.297	0.840	0.174	0.321	0.339	0.060
M2	0.393	0.000	1.619	0.411	3.158	0.842	0.991	0.200	3.269	2.695	1.130	1.185	1.929	0.715	1.576	1.086	0.441	0.072	0.682	0.424
M3	1.317	1.619	0.000	1.267	1.633	0.982	2.502	1.751	1.734	1.520	0.861	1.767	0.349	1.036	0.125	0.559	1.191	1.560	1.348	1.336
M4	0.060	0.411	1.267	0.000	2.860	0.707	1.400	0.599	2.968	2.285	0.720	1.342	1.555	0.582	1.243	0.782	0.115	0.340	0.372	0.112
M5	2.916	3.158	1.633	2.860	0.000	2.360	3.893	3.249	0.114	2.215	2.477	2.817	1.475	2.468	1.625	2.083	2.768	3.110	2.980	2.943
M6	0.765	0.842	0.982	0.707	2.360	0.000	1.557	0.896	2.473	2.382	1.020	0.861	1.330	0.131	0.894	0.446	0.593	0.813	1.034	0.819
M7	1.384	0.991	2.502	1.400	3.893	1.557	0.000	0.802	4.007	3.684	2.120	1.251	2.837	1.474	2.433	1.943	1.410	1.062	1.646	1.412
M8	0.588	0.200	1.751	0.599	3.249	0.896	0.802	0.000	3.361	2.882	1.319	1.076	2.073	0.781	1.698	1.203	0.610	0.269	0.881	0.623
M9	3.023	3.269	1.734	2.968	0.114	2.473	4.007	3.361	0.000	2.253	2.573	2.930	1.564	2.580	1.730	2.192	2.877	3.220	3.082	3.049
M10	2.305	2.695	1.520	2.285	2.215	2.382	3.684	2.882	2.253	0.000	1.565	3.232	1.236	2.384	1.645	1.942	2.279	2.624	2.098	2.283
M11	0.739	1.130	0.861	0.720	2.477	1.020	2.120	1.319	2.573	1.565	0.000	1.859	1.026	0.962	0.911	0.717	0.724	1.059	0.583	0.720
M12	1.379	1.185	1.767	1.342	2.817	0.861	1.251	1.076	2.930	3.232	1.859	0.000	2.111	0.897	1.657	1.290	1.254	1.212	1.713	1.438
M13	1.601	1.929	0.349	1.555	1.475	1.330	2.837	2.073	1.564	1.236	1.026	2.111	0.000	1.380	0.455	0.900	1.492	1.866	1.576	1.611
M14	0.638	0.715	1.036	0.582	2.468	0.131	1.474	0.781	2.580	2.384	0.962	0.897	1.380	0.000	0.960	0.481	0.468	0.684	0.920	0.694
M15	1.297	1.576	0.125	1.243	1.625	0.894	2.433	1.698	1.730	1.645	0.911	1.657	0.455	0.960	0.000	0.495	1.160	1.520	1.359	1.321
M16	0.840	1.086	0.559	0.782	2.083	0.446	1.943	1.203	2.192	1.942	0.717	1.290	0.900	0.481	0.495	0.000	0.686	1.033	0.977	0.873
M17	0.174	0.441	1.191	0.115	2.768	0.593	1.410	0.610	2.877	2.279	0.724	1.254	1.492	0.468	1.160	0.686	0.000	0.376	0.467	0.226
M18	0.321	0.072	1.560	0.340	3.110	0.813	1.062	0.269	3.220	2.624	1.059	1.212	1.866	0.684	1.520	1.033	0.376	0.000	0.616	0.354
M19	0.339	0.682	1.348	0.372	2.980	1.034	1.646	0.881	3.082	2.098	0.583	1.713	1.576	0.920	1.359	0.977	0.467	0.616	0.000	0.283
M20	0.060	0.424	1.336	0.112	2.943	0.819	1.412	0.623	3.049	2.283	0.720	1.438	1.611	0.694	1.321	0.873	0.226	0.354	0.283	0.000

Table A. 22: Matrix for distance values between indices for all materials used in color index analysis taxonomy attempts for the V3-IR16 versus IR4-IR16 color-color diagram.

	M1	M2	M3	M4	M5	M6	M7	M8	M9	M10	M11	M12	M13	M14	M15	M16	M17	M18	M19	M20
M1	0.000	0.450	0.244	0.046	0.191	0.708	1.570	0.693	3.107	2.202	0.831	1.339	1.570	0.454	0.233	0.375	0.143	0.370	0.379	0.055
M2	0.450	0.000	0.692	0.405	0.351	0.260	1.120	0.244	3.436	2.650	1.280	1.104	1.977	0.292	0.646	0.163	0.306	0.080	0.816	0.489
M3	0.244	0.692	0.000	0.289	0.384	0.948	1.811	0.933	2.917	1.965	0.588	1.481	1.343	0.647	0.129	0.616	0.386	0.612	0.203	0.217
M4	0.046	0.405	0.289	0.000	0.170	0.663	1.525	0.648	3.144	2.246	0.877	1.316	1.613	0.424	0.273	0.331	0.098	0.324	0.420	0.089
M5	0.191	0.351	0.384	0.170	0.000	0.588	1.449	0.576	3.101	2.344	0.959	1.148	1.626	0.268	0.308	0.352	0.140	0.280	0.555	0.246
M6	0.708	0.260	0.948	0.663	0.588	0.000	0.864	0.019	3.612	2.909	1.535	0.998	2.204	0.423	0.893	0.393	0.564	0.339	1.075	0.748
M7	1.570	1.120	1.811	1.525	1.449	0.864	0.000	0.878	4.353	3.768	2.399	1.249	3.044	1.244	1.756	1.225	1.427	1.200	1.929	1.608
M8	0.693	0.244	0.933	0.648	0.576	0.019	0.878	0.000	3.608	2.894	1.521	1.013	2.194	0.418	0.880	0.374	0.549	0.323	1.059	0.733
M9	3.107	3.436	2.917	3.144	3.101	3.612	4.353	3.608	0.000	2.402	2.537	3.260	1.674	3.190	2.875	3.450	3.208	3.376	2.974	3.110
M10	2.202	2.650	1.965	2.246	2.344	2.909	3.768	2.894	2.402	0.000	1.389	3.284	1.234	2.593	2.041	2.547	2.345	2.570	1.840	2.161
M11	0.831	1.280	0.588	0.877	0.959	1.535	2.399	1.521	2.537	1.389	0.000	1.940	0.874	1.205	0.654	1.197	0.974	1.200	0.515	0.799
M12	1.339	1.104	1.481	1.316	1.148	0.998	1.249	1.013	3.260	3.284	1.940	0.000	2.258	0.900	1.360	1.262	1.250	1.137	1.679	1.394
M13	1.570	1.977	1.343	1.613	1.626	2.204	3.044	2.194	1.674	1.234	0.874	2.258	0.000	1.801	1.342	1.942	1.696	1.903	1.351	1.557
M14	0.454	0.292	0.647	0.424	0.268	0.423	1.244	0.418	3.190	2.593	1.205	0.900	1.801	0.000	0.553	0.409	0.350	0.279	0.823	0.508
M15	0.233	0.646	0.129	0.273	0.308	0.893	1.756	0.880	2.875	2.041	0.654	1.360	1.342	0.553	0.000	0.600	0.355	0.569	0.331	0.236
M16	0.375	0.163	0.616	0.331	0.352	0.393	1.225	0.374	3.450	2.547	1.197	1.262	1.942	0.409	0.600	0.000	0.247	0.131	0.707	0.400
M17	0.143	0.306	0.386	0.098	0.140	0.564	1.427	0.549	3.208	2.345	0.974	1.250	1.696	0.350	0.355	0.247	0.000	0.226	0.516	0.186
M18	0.370	0.080	0.612	0.324	0.280	0.339	1.200	0.323	3.376	2.570	1.200	1.137	1.903	0.279	0.569	0.131	0.226	0.000	0.737	0.409
M19	0.379	0.816	0.203	0.420	0.555	1.075	1.929	1.059	2.974	1.840	0.515	1.679	1.351	0.823	0.331	0.707	0.516	0.737	0.000	0.331
M20	0.055	0.489	0.217	0.089	0.246	0.748	1.608	0.733	3.110	2.161	0.799	1.394	1.557	0.508	0.236	0.400	0.186	0.409	0.331	0.000

Table A. 23: Matrix for distance values between indices for all materials used in color index analysis taxonomy attempts for the V1-IR16 versus IR2-IR16 color-color diagram.

	M1	M2	M3	M4	M5	M6	M7	M8	M9	M10	M11	M12	M13	M14	M15	M16	M17	M18	M19	M20
M1	0.000	0.400	1.319	0.093	2.920	0.815	1.481	0.641	4.141	2.139	0.789	1.409	1.615	0.603	1.297	0.873	0.210	0.361	0.240	0.024
M2	0.400	0.000	1.626	0.384	3.157	0.860	1.082	0.250	4.536	2.531	1.188	1.204	1.952	0.706	1.580	1.074	0.421	0.048	0.597	0.381
M3	1.319	1.626	0.000	1.277	1.649	1.042	2.572	1.781	3.178	1.265	0.885	1.807	0.377	1.017	0.130	0.648	1.207	1.577	1.336	1.343
M4	0.093	0.384	1.277	0.000	2.860	0.722	1.455	0.608	4.154	2.148	0.813	1.323	1.586	0.512	1.247	0.799	0.118	0.339	0.325	0.104
M5	2.920	3.157	1.649	2.860	0.000	2.362	3.909	3.249	3.082	2.062	2.515	2.807	1.522	2.459	1.635	2.082	2.768	3.110	2.972	2.943
M6	0.815	0.860	1.042	0.722	2.362	0.000	1.577	0.897	4.202	2.229	1.162	0.821	1.418	0.219	0.945	0.397	0.604	0.821	1.012	0.827
M7	1.481	1.082	2.572	1.455	3.909	1.577	0.000	0.847	5.605	3.596	2.267	1.234	2.932	1.556	2.496	1.938	1.457	1.121	1.667	1.462
M8	0.641	0.250	1.781	0.608	3.249	0.897	0.847	0.000	4.759	2.751	1.421	1.051	2.125	0.796	1.722	1.185	0.614	0.281	0.847	0.624
M9	4.141	4.536	3.178	4.154	3.082	4.202	5.605	4.759	0.000	2.009	3.354	4.985	2.805	4.123	3.295	3.806	4.147	4.493	3.998	4.162
M10	2.139	2.531	1.265	2.148	2.062	2.229	3.596	2.751	2.009	0.000	1.360	3.037	0.937	2.130	1.394	1.842	2.139	2.488	2.012	2.161
M11	0.789	1.188	0.885	0.813	2.515	1.162	2.267	1.421	3.354	1.360	0.000	1.958	1.028	0.979	0.944	0.907	0.832	1.147	0.653	0.809
M12	1.409	1.204	1.807	1.323	2.807	0.821	1.234	1.051	4.985	3.037	1.958	0.000	2.181	0.980	1.692	1.195	1.229	1.195	1.647	1.409
M13	1.615	1.952	0.377	1.586	1.522	1.418	2.932	2.125	2.805	0.937	1.028	2.181	0.000	1.381	0.490	1.023	1.531	1.904	1.588	1.639
M14	0.603	0.706	1.017	0.512	2.459	0.219	1.556	0.796	4.123	2.130	0.979	0.980	1.381	0.000	0.941	0.391	0.394	0.662	0.794	0.616
M15	1.297	1.580	0.130	1.247	1.635	0.945	2.496	1.722	3.295	1.394	0.944	1.692	0.490	0.941	0.000	0.559	1.168	1.532	1.337	1.321
M16	0.873	1.074	0.648	0.799	2.082	0.397	1.938	1.185	3.806	1.842	0.907	1.195	1.023	0.391	0.559	0.000	0.696	1.028	0.995	0.893
M17	0.210	0.421	1.207	0.118	2.768	0.604	1.457	0.614	4.147	2.139	0.832	1.229	1.531	0.394	1.168	0.696	0.000	0.373	0.427	0.222
M18	0.361	0.048	1.577	0.339	3.110	0.821	1.121	0.281	4.493	2.488	1.147	1.195	1.904	0.662	1.532	1.028	0.373	0.000	0.568	0.344
M19	0.240	0.597	1.336	0.325	2.972	1.012	1.667	0.847	3.998	2.012	0.653	1.647	1.588	0.794	1.337	0.995	0.427	0.568	0.000	0.246
M20	0.024	0.381	1.343	0.104	2.943	0.827	1.462	0.624	4.162	2.161	0.809	1.409	1.639	0.616	1.321	0.893	0.222	0.344	0.246	0.000

Table A. 24: Matrix for distance values between indices for all materials used in color index analysis taxonomy attempts for the V3-IR10 versus V3-IR16 color-color diagram.

	M1	M2	M3	M4	M5	M6	M7	M8	M9	M10	M11	M12	M13	M14	M15	M16	M17	M18	M19	M20
M1	0.000	0.470	0.263	0.041	0.189	0.689	1.171	0.502	4.521	2.121	0.830	0.987	2.138	0.420	0.401	0.494	0.104	0.274	0.182	0.021
M2	0.470	0.000	0.732	0.432	0.619	0.220	0.835	0.276	4.991	2.591	1.297	1.377	2.607	0.790	0.868	0.025	0.402	0.377	0.570	0.455
M3	0.263	0.732	0.000	0.302	0.200	0.952	1.405	0.746	4.260	1.859	0.567	0.827	1.875	0.368	0.160	0.757	0.350	0.490	0.233	0.277
M4	0.041	0.432	0.302	0.000	0.208	0.652	1.131	0.462	4.558	2.159	0.870	1.006	2.175	0.430	0.436	0.457	0.067	0.239	0.214	0.039
M5	0.189	0.619	0.200	0.208	0.000	0.833	1.220	0.576	4.384	1.990	0.728	0.799	2.008	0.237	0.269	0.644	0.218	0.312	0.302	0.210
M6	0.689	0.220	0.952	0.652	0.833	0.000	0.720	0.372	5.210	2.810	1.517	1.570	2.827	0.989	1.087	0.195	0.618	0.565	0.786	0.675
M7	1.171	0.835	1.405	1.131	1.220	0.720	0.000	0.670	5.504	3.149	1.944	1.700	3.171	1.243	1.484	0.821	1.069	0.915	1.332	1.168
M8	0.502	0.276	0.746	0.462	0.576	0.372	0.670	0.000	4.946	2.558	1.303	1.227	2.577	0.669	0.845	0.281	0.401	0.264	0.663	0.498
M9	4.521	4.991	4.260	4.558	4.384	5.210	5.504	4.946	0.000	2.401	3.703	3.813	2.386	4.285	4.124	5.015	4.594	4.685	4.451	4.537
M10	2.121	2.591	1.859	2.159	1.990	2.810	3.149	2.558	2.401	0.000	1.303	1.518	0.033	1.910	1.726	2.615	2.197	2.295	2.051	2.136
M11	0.830	1.297	0.567	0.870	0.728	1.517	1.944	1.303	3.703	1.303	0.000	0.759	1.317	0.736	0.461	1.322	0.916	1.040	0.749	0.843
M12	0.987	1.377	0.827	1.006	0.799	1.570	1.700	1.227	3.813	1.518	0.759	0.000	1.546	0.588	0.679	1.399	1.001	1.005	1.052	1.008
M13	2.138	2.607	1.875	2.175	2.008	2.827	3.171	2.577	2.386	0.033	1.317	1.546	0.000	1.931	1.744	2.632	2.214	2.314	2.065	2.153
M14	0.420	0.790	0.368	0.430	0.237	0.989	1.243	0.669	4.285	1.910	0.736	0.588	1.931	0.000	0.319	0.813	0.416	0.424	0.534	0.441
M15	0.401	0.868	0.160	0.436	0.269	1.087	1.484	0.845	4.124	1.726	0.461	0.679	1.744	0.319	0.000	0.893	0.471	0.581	0.393	0.419
M16	0.494	0.025	0.757	0.457	0.644	0.195	0.821	0.281	5.015	2.615	1.322	1.399	2.632	0.813	0.893	0.000	0.426	0.397	0.594	0.479
M17	0.104	0.402	0.350	0.067	0.218	0.618	1.069	0.401	4.594	2.197	0.916	1.001	2.214	0.416	0.471	0.426	0.000	0.172	0.281	0.106
M18	0.274	0.377	0.490	0.239	0.312	0.565	0.915	0.264	4.685	2.295	1.040	1.005	2.314	0.424	0.581	0.397	0.172	0.000	0.453	0.278
M19	0.182	0.570	0.233	0.214	0.302	0.786	1.332	0.663	4.451	2.051	0.749	1.052	2.065	0.534	0.393	0.594	0.281	0.453	0.000	0.175
M20	0.021	0.455	0.277	0.039	0.210	0.675	1.168	0.498	4.537	2.136	0.843	1.008	2.153	0.441	0.419	0.479	0.106	0.278	0.175	0.000

Table A. 25: Matrix for distance values between indices for all materials used in color index analysis taxonomy attempts for the V1-IR7 versus V4-IR11 color-color diagram.

	M1	M2	M3	M4	M5	M6	M7	M8	M9	M10	M11	M12	M13	M14	M15	M16	M17	M18	M19	M20
M1	0.000	0.387	1.198	0.062	3.085	1.063	0.586	0.241	4.587	1.519	0.563	1.732	1.823	1.045	1.383	0.917	0.215	0.159	0.389	0.095
M2	0.387	0.000	1.406	0.371	3.219	1.030	0.354	0.295	4.936	1.902	0.950	1.973	2.165	1.272	1.594	0.953	0.432	0.284	0.441	0.333
M3	1.198	1.406	0.000	1.154	1.907	0.792	1.231	1.119	3.720	1.671	1.082	0.576	1.075	0.162	0.188	0.637	1.013	1.167	1.586	1.290
M4	0.062	0.371	1.154	0.000	3.035	1.001	0.537	0.185	4.579	1.550	0.586	1.695	1.811	1.003	1.340	0.856	0.157	0.111	0.439	0.138
M5	3.085	3.219	1.907	3.035	0.000	2.259	2.947	2.961	3.318	3.269	2.966	1.512	2.135	2.069	1.737	2.274	2.884	3.026	3.473	3.172
M6	1.063	1.030	0.792	1.001	2.259	0.000	0.709	0.850	4.500	2.196	1.325	1.310	1.855	0.777	0.925	0.211	0.854	0.937	1.396	1.120
M7	0.586	0.354	1.231	0.537	2.947	0.709	0.000	0.356	4.885	2.062	1.092	1.807	2.127	1.125	1.413	0.677	0.480	0.427	0.783	0.586
M8	0.241	0.295	1.119	0.185	2.961	0.850	0.356	0.000	4.650	1.712	0.742	1.681	1.879	0.981	1.307	0.728	0.147	0.089	0.548	0.274
M9	4.587	4.936	3.720	4.579	3.318	4.500	4.885	4.650	0.000	3.490	4.090	3.197	2.771	3.784	3.574	4.357	4.506	4.653	4.882	4.675
M10	1.519	1.902	1.671	1.550	3.269	2.196	2.062	1.712	3.490	0.000	0.971	1.786	1.190	1.557	1.737	1.985	1.583	1.659	1.638	1.570
M11	0.563	0.950	1.082	0.586	2.966	1.325	1.092	0.742	4.090	0.971	0.000	1.491	1.365	0.922	1.234	1.126	0.613	0.692	0.792	0.629
M12	1.732	1.973	0.576	1.695	1.512	1.310	1.807	1.681	3.197	1.786	1.491	0.000	0.799	0.701	0.398	1.190	1.565	1.722	2.113	1.827
M13	1.823	2.165	1.075	1.811	2.135	1.855	2.127	1.879	2.771	1.190	1.365	0.799	0.000	1.082	1.002	1.676	1.735	1.882	2.141	1.913
M14	1.045	1.272	0.162	1.003	2.069	0.777	1.125	0.981	3.784	1.557	0.922	0.701	1.082	0.000	0.339	0.593	0.868	1.023	1.432	1.138
M15	1.383	1.594	0.188	1.340	1.737	0.925	1.413	1.307	3.574	1.737	1.234	0.398	1.002	0.339	0.000	0.794	1.201	1.355	1.771	1.476
M16	0.917	0.953	0.637	0.856	2.274	0.211	0.677	0.728	4.357	1.985	1.126	1.190	1.676	0.593	0.794	0.000	0.702	0.809	1.275	0.984
M17	0.215	0.432	1.013	0.157	2.884	0.854	0.480	0.147	4.506	1.583	0.613	1.565	1.735	0.868	1.201	0.702	0.000	0.157	0.592	0.292
M18	0.159	0.284	1.167	0.111	3.026	0.937	0.427	0.089	4.653	1.659	0.692	1.722	1.882	1.023	1.355	0.809	0.157	0.000	0.467	0.185
M19	0.389	0.441	1.586	0.439	3.473	1.396	0.783	0.548	4.882	1.638	0.792	2.113	2.141	1.432	1.771	1.275	0.592	0.467	0.000	0.301
M20	0.095	0.333	1.290	0.138	3.172	1.120	0.586	0.274	4.675	1.570	0.629	1.827	1.913	1.138	1.476	0.984	0.292	0.185	0.301	0.000

Vita

Jacqueline Andrea Reyes served as a graduate student in the Materials Science and Engineering graduate school program at the University of Texas at El Paso (UTEP) between 2017 and 2022. She received a Bachelor of Science degree in Metallurgical and Materials Engineering from UTEP in May 2017. She has participated in internship positions serving the National Aeronautics and Space Administration (NASA) under the Jacobs JETS contract from 2017 to 2020. She has also served in the Space Vehicles Directorate of the Air Force Research Labs as an AFRL Scholar intern for two consecutive summers between 2019 and 2020. Reyes then accepted the opportunity to be a NASA Fellow since the onset of 2021 and has conducted her dissertation research under this NASA Fellowship Activity Award (Award #80NSSC18K1702).

Reyes published her previous work in the *Acta Astronautica* journal in 2021 with the manuscript titled "Spectroscopic behavior of various materials in a GEO simulated environment," and in *The Journal of the Astronautical Sciences* with the paper titled "Optical Characterization of DebriSat Fragments in Support of Orbital Debris Environmental Models," also in 2021. Reyes has contributed many manuscripts to conference proceedings, including manuscripts for the Advanced Maui Optical and Space Surveillance Technologies Conference (AMOS) conference in 2018, the International Association for the Advancement of Space Safety (IAASS) conference in 2019, the 1st International Orbital Debris conference in 2019, and SPIE conferences in 2019 and 2021.

Much of her work for these agencies involved material characterization of commonly used spacecraft materials to contribute to remote observations and risk assessment of resident space objects positioned and traveling in space domains near Earth.

Contact Information: jareyes10@miners.utep.edu